

Frequency Selective Surfaces

Integrated with Phased Array Antennas

Analysis and Design using Multimode Equivalent Networks

Frequency Selective Surfaces

Integrated with Phased Array Antennas

Analysis and Design using Multimode Equivalent Networks

PROEFSCHRIFT

ter verkrijging van de graad van doctor aan de
Technische Universiteit Eindhoven, op gezag van de
Rector Magnificus, prof.dr.ir. C. J. van Duijn, voor een
commissie aangewezen door het College voor
Promoties in het openbaar te verdedigen
op maandag 27 juni 2005 om 16.00 uur

door

Stefania Monni

geboren te Cagliari, Italië

Dit proefschrift is goedgekeurd door de promotor:

prof.dr. A.G. Tijhuis

Copromotor:

dr. G. Gerini

CIP-DATA LIBRARY TECHNISCHE UNIVERSITEIT EINDHOVEN

Monni, Stefania

Frequency selective surfaces integrated with phased array antennas :
analysis and design using multimode equivalent networks

/ by Stefania Monni. - Eindhoven : Technische Universiteit Eindhoven, 2005.

Proefschrift. - ISBN 90-386-1713-5

NUR 959

Trefw.: frequentiefilters / fasegestuurde antennestelsels /
microgolfantenne / golfgeleiders / elektromagnetisme ; numerieke methoden.

Subject headings: frequency selective surfaces / antenna phased arrays /
microwave antenna arrays / waveguides / computational electromagnetics.

Copyright ©2005 by S. Monni, TNO, The Hague, The Netherlands

Cover design: S. Monni, implemented by P. Verspaget (Grafische Vormgeving)

Press: Universiteitsdrukkerij, TUE

The work presented in this thesis has been performed at TNO and financed by TNO with support of the Dutch Ministry of Defense.

To my parents

To Michel

Abbreviations

BCMM	Boundary Contour Mode Matching
EBG	Electronic Band Gap
EFIE	Electric Field Integral Equation
EMC	Electromagnetic Compatibility
EMI	Electromagnetic Interference
FSS	Frequency Selective Surface
FT	Fourier Transform
GAM	Generalized Admittance Matrix
GF	Green's Function
GIM	Generalized Impedance Matrix
GSM	Generalized Scattering Matrix
GTM	Generalized Transmission Matrix
HPB	Half Power Beamwidth
IE	Integral Equation
IEMEN	Integral Equation's method for the derivation of Multimode Equivalent Networks
IPD	Insertion Phase Delay
ITD	Integrated Topside Design
MAC	Microwave Anechoic Chamber
MEN	Multimode Equivalent Network
MFIE	Magnetic Field Integral Equation
MFR	Multi-Frequency Radar
MoM	Method of Moment
PEC	Perfect Electric Conductor
PSWW	Phase Shift Wall Waveguide
PWL	Piece Wise Linear
PWS	Piece Wise Sinusoidal
RAM	Radar Absorbing Material

RCS	Radar Cross Section
RNLN	Royal Netherlands Navy
RX	Receiving Antenna
TE	Transverse Electric
TEM	Transverse ElectroMagnetic
TFW	Truncated Floquet Waves
TL	Transmission Line
TM	Transverse Magnetic
TX	Transmitting Antenna
WAIM	Wide Angle Impedance Matching

Contents

Abbreviations	i
1 Introduction	1
1.1 Frequency Selective Surfaces: historical context	3
1.1.1 Applications of frequency selective surfaces	5
1.2 Analysis techniques for FSS's	10
1.3 Design techniques for FSS's	13
1.4 Outline of the thesis	15
2 Multimode Equivalent Networks: the IEMEN method	17
2.1 Multimode equivalent networks for waveguides	19
2.1.1 The microwave network formalism	20
2.1.2 MEN of a waveguide junction	26
2.1.3 MEN of a rectangular waveguide section	36
2.1.4 MEN of a cascade of uniform waveguides	37
2.2 Multimode equivalent network formulation for infinite periodic arrays	40
2.2.1 MEN of the junction waveguide-PSWW	41
2.2.2 Numerical results	48
2.3 Thick FSS	50
2.4 Conclusions	53
3 IEMEN approach for aperture- and patch-based FSS's	57
3.1 Theoretical basis	58
3.2 Patch-based FSS	60
3.2.1 Formulation	60
3.2.2 Multimode Equivalent Network	63
3.3 Aperture-based FSS	65
3.3.1 Formulation	65

3.3.2	Multimode Equivalent Network	68
3.4	Thin layer problem	69
3.5	Solution of the integral equation	72
3.6	Numerical results	76
3.6.1	Free-standing FSS	77
3.6.2	Multi-layer FSS	80
3.7	Conclusions	81
4	FSS design	83
4.1	Description of the design problem	83
4.1.1	Single-mode design	85
4.1.2	Full-wave refinement	94
4.1.3	Discussion of the results	96
4.2	Conclusions	98
5	Experimental validation	101
5.1	Manufacturing	102
5.1.1	Modified design: thin layer problem	105
5.2	Measurements	106
5.2.1	Far field of the TX and far field of the FSS measurement setup . . .	108
5.2.2	Far field of the TX and the near field of the FSS measurement setup	112
5.2.3	Quasi far field of the TX and near field of the FSS measurement setup	116
5.2.4	Discussion of the results	118
5.3	Conclusions	121
6	Reduced kernel integral equation	123
6.1	Two-dimensional TM problem	124
6.1.1	Geometry and IE formulation	124
6.1.2	Non-accessible Green's function	126
6.1.3	Ill conditioning of the sub-domain expansion	129
6.1.4	Eigenvalues and eigenfunctions	131
6.2	Truncated Floquet waves	135
6.2.1	Convergence study	140
6.3	Conclusions	141

7	Conclusions and recommendations	147
7.1	Conclusions by chapter	148
7.2	General conclusions and recommendations	155
A	Modal representation of the electromagnetic field	161
A.1	Maxwell's equations	161
A.1.1	Time domain	161
A.1.2	Frequency domain	163
A.1.3	Plane waves	165
A.2	Electromagnetic field in uniform waveguide regions	168
A.2.1	Modal representation of the fields and their sources	169
A.2.2	Solution of the uniform transmission-line equations	178
A.3	Application of the modal representation	179
A.3.1	Homogeneously filled rectangular waveguide	179
A.3.2	Electromagnetic field in free space	182
B	Electromagnetic field in proximity of a periodic array	185
B.1	Bloch-Floquet theorem for crystals	185
B.1.1	Some basics about crystals	185
B.1.2	The Bloch-Floquet theorem	187
B.2	Bloch-Floquet theorem for periodic phased arrays	188
B.2.1	Rectangular lattice	191
B.2.2	Triangular lattice	191
C	Infinite array Green's function in a periodic environment	199
C.1	General formulation	199
C.2	Green's function in terms of Floquet modes	206
C.3	Green's function in Cartesian coordinates	210
D	Measurement of the dielectric properties of the foam Bisco HT-820	213
D.1	Rogers measurements	213
D.2	Coaxial probe measurements	215
E	Non-accessible Green's function	217
E.1	Approximated g_{na} for large N_a	217
E.2	Approximated non-accessible field for large N_a	220
E.3	Fourier transform of pws-shaped currents	222

E.4	Approximated integral equation for large N_a	222
E.4.1	Right hand side	223
E.4.2	Left hand side	224
E.4.3	Summary	225
E.5	Fourier transform of truncated Floquet waves	227
Summary		243
Samenvatting		247
Biography		251
Acknowledgements		253

Chapter 1

Introduction

*If we want to solve a problem that we have never solved before,
we must leave the door to the unknown ajar.*

Richard P. Feynman(1918-1988)

A Frequency Selective Surface (FSS) is an array of periodically arranged patches or apertures, showing a particular filtering behavior with respect to frequency. Its selectivity in frequency is obtained by the design and allows the transmission of signals in a certain frequency range only. Typical applications of FSS's exploit their filtering properties, to prevent for example Electromagnetic Interference (EMI) between two antennas operating in overlapping frequency bands, to improve the Electromagnetic Compatibility (EMC) of a system of sensors, to reduce the Radar Cross Section (RCS) of antennas located on a ship topside or in the nose of an aircraft, or to make an antenna weather-resistant and protect it from ballistic threats (to reduce its vulnerability). These properties are defined in more detail in the text box at the top of the next page.

FSS's are also used to shape the frequency or angular response of an antenna. An appropriate FSS can be associated to a broadband antenna to obtain a reduction of the bandwidth. Moreover, the beam of an antenna with a wide scan range can be suitably oriented by means of an FSS that introduces a notch in its angular response.

The analysis and design of FSS's has been a very popular research topic in the last decades and a large amount of literature is available on this subject, both for the case of single periodic screen and for the case of cascaded screens interleaved with dielectric slabs (the interested reader can find many references in [94]). Historically, the research in this field has been aimed at the design and analysis of stand-alone FSS's, without taking into account the effect of the interactions with the antenna.

Radar Cross Section (RCS). For a target illuminated by a monostatic radar, whose receive and transmit antennas are pointed such that the pattern maxima are directed toward the target, the RCS is defined as the ratio between the power scattered by the target and the power density incident on the target. It represents the equivalent area of the target, provided that the incident power is scattered isotropically [133].

Vulnerability. It is defined as the characteristics of a system that cause it to suffer a definite degradation (incapability to perform the designated mission) as a result of having been subjected to a certain level of environmental effects (for example electromagnetic vulnerability or ballistic vulnerability).

Electromagnetic Interference (EMI). It is defined as the degradation of the performance of an equipment, transmission channel or system caused by an electromagnetic disturbance [70].

Electromagnetic Compatibility (EMC). It is defined as the ability of an equipment or system to function satisfactorily in its electromagnetic environment without introducing intolerable electromagnetic disturbances to anything in that environment [70].

As a consequence, since a great deal of work is necessary afterwards to tune the FSS with the antenna, the tendency has been often to locate the FSS as far as possible from the antenna, with the purpose of minimizing the mutual interactions. This is clearly inefficient and time consuming. Moreover, in view of the latest technological trends, which go for highly integrated and compact structures, it is no longer adequate. The integration of the FSS with the target antenna is convenient also from the structural point of view, since it results in a more compact configuration and consequently in a reduction of the RCS. Another advantage is that the FSS can be used as an Electronic Band Gap material, to enlarge the bandwidth of printed array antennas [47]. In fact, very compact antennas can be manufactured in printed technology, on a dielectric substrate surface. However, typical substrate configurations are usually narrow band, while thicker substrates, which allow increasing the bandwidth of the antenna, lead to a reduction of the efficiency because of surface-wave excitation. As proposed in [47], an approach to improve the bandwidth characteristics of the antenna, while reducing the influence of surface waves, is to use frequency-dependent substrates, in other words, to integrate the antenna with multi-layer FSS's.

The design of such an integrated system requires the availability of a CAD package that

is able to take into account in the same framework both the antenna and the (multi-layer) FSS. In this respect, the purpose of this thesis is to develop a unified approach for the analysis of waveguide phased arrays integrated with multi-layer FSS's, consisting of periodic distributions of patches and/or slots etched in a metal plate, and sandwiched between dielectric slabs. The developed methodology must also be capable of being used as basis for the design.

Techniques based on microwave network representations are very suitable for the analysis of layered structures, because of their inherent modularity. The starting point of our research is a methodology originally proposed in [53] to characterize a waveguide junction in terms of a multimode generalized impedance matrix. By extending this methodology to the analysis of waveguide arrays radiating in free space, multi-layer FSS's and array antennas integrated with FSS's, we have developed a powerful analysis tool, which can also take into account feeding and filtering elements inside the waveguides of the array, modeled as waveguide junctions.

In the following, we will briefly describe the context in which this research project was originated. In Sec. 1.1 some historical references are given about FSS's and examples of cutting-edge applications are listed. The state of the art in FSS analysis and design is presented in Sec. 1.2 and Sec. 1.3, respectively. The objectives of our research work and the organization of the thesis are outlined in Sec. 1.4.

1.1 Frequency Selective Surfaces: historical context

The ancestor of the FSS is the radome. Radomes, or radar antenna dome covers, are structures that enclose or are placed in front of the antenna to ensure protection from environmental exposure and to reduce its ballistic vulnerability. To minimize the impedance mismatch, they are usually designed with an optimal thickness of about half a wavelength at the resonance frequency of the antenna. Since this design is often based on the approximation of single-mode incidence, the obtained configuration does not guarantee a perfect matching. In general, the presence of the radome changes the electrical characteristics of the antenna. Parameters typically used to quantify this effect are beam squint, pattern distortion, transmission loss, reflected power and Insertion Phase Delay (IPD) [42]. The IPD is defined as the phase of the transmitted wave in presence of the radome, relative to the phase of the wave at the same point if the radome was removed. This parameter is critical in the evaluation of radome's electrical performances. A high IPD causes a high gain loss, a large bandwidth change, a high beam deflection and an increased side-lobe

level, and is therefore particularly troublesome for tracking radars.

Initially, radomes consisted of homogeneous dielectric materials, in a single- or multi-layer configuration [42]. In this case, the electrical thickness, and therefore the matching properties, are heavily influenced by the angle of incidence, the polarization and the frequency of the impinging wave. Scanning the beam of the enclosed antenna results in a variation of the insertion loss and insertion phase introduced by the radome. To reduce the angular dependence of the radome behavior, dielectric radomes were sometimes made of very hard materials, like fiberglass and ceramic, which have a high dielectric constant. However, tolerances related to thickness and dielectric constant variations become more critical for high values of the dielectric constant. Moreover, this kind of material is in general not suitable for outdoor exposure because it is extremely fragile from the mechanical point of view. Therefore, it is particularly vulnerable to hail, rain, and lightning. Moreover, it is subject to static discharge noise.

In view of this, the studies performed in the 50's to investigate the effects of metal inclusions in the radome structure represented a breakthrough. It was shown that matching in a broader frequency band could be achieved by embedding arrays of metal wires or thin strips in the dielectric; this allowed at the same time a reduction of the required thickness of the dielectric layer [73]. The metal elements were modeled as lumped circuit elements shunted across the transmission line representing the propagation into the dielectric sheet. However, only in the late 60's a systematic study was performed into the properties of the so-called *metallic radomes* or *hybrid radomes*, consisting of periodic arrays of conducting elements printed on a very thin dielectric sheet. Periodic arrays of slots or patches had already been studied in detail in [33, 74, 107], but Lee [80] and Munk *et al.* [113] separately demonstrated for the first time that a radome made of a periodic screen sandwiched between two dielectric layers would improve the mechanical strength, with respect to conventional configurations based only on dielectrics, as well as the selectivity of the transmission of the electromagnetic waves. The design proposed by Lee was based on a trial-and-error method for determining the parameters of the metallic radome, while Munk published the first systematic studies on the effect of different kinds of printed elements and different types of layout on the radome performances. He also introduced a tripolar geometry to reduce the angular dependence of the radome response [113].

In the first stages of their development, metallic radomes were mainly used as matching and protecting structures for antennas. It was in the 70's that their filtering properties started to be investigated and, correspondingly, the designation of Frequency Selective Surface was introduced. Unlike conventional radio-frequency filters, FSS's can perform the filtering of the signal not only in the frequency domain but also in the angular domain and therefore

can be used as space filters [51, 76, 100]. Correspondingly, new possible applications in different frequency ranges of the electromagnetic spectrum have emerged. Some examples are presented in the following section and an excellent review of the literature can be found in [94, 106].

1.1.1 Applications of frequency selective surfaces

As mentioned above, in the *microwave region*, FSS's were originally used as *radomes*, to protect radar antennas and to reduce their RCS outside the operating band. In fact, periodic screens combined with dielectric layers can be designed to be transparent in a certain frequency band and opaque at any other frequency. Fig. 1.1 shows two typical applications, described in [100], for a naval and an airborne FSS. In Fig. 1.1a, a planar FSS is mounted on a ship mast, covering a compartment in which a radar antenna is located. In Fig. 1.1b, a conical FSS is mounted on an aircraft nose hosting a planar radar antenna. In both cases, the FSS is designed to be transparent for a signal in the antenna operating band while it acts as a perfectly conducting plate outside that band. Moreover, the out-of-band incident electromagnetic wave is reflected with a certain angle with respect to the direction of incidence (bi-static direction), while the backscattered signal is weak. An example of conical FSS measured at the Loughborough University is shown in Fig. 1.2.

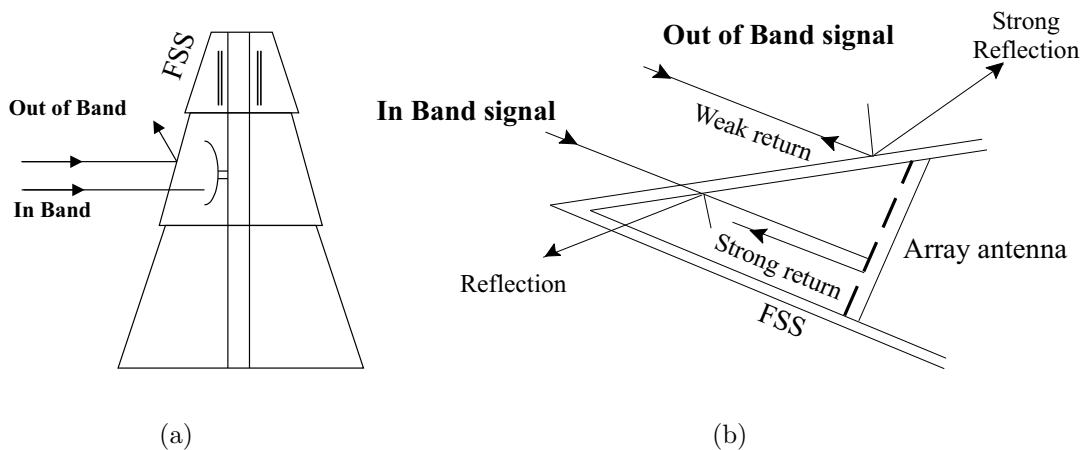


Figure 1.1: Application of an FSS to limit the Radar Cross Section of an antenna: (a) FSS mounted on a ship mast, (b) FSS mounted on a aircraft nose.

More recently, FSS's are used in the design of absorbers and dichroic reflectors. A *circuit analog absorber* consists of a periodic screen made of resistive material, backed by a ground

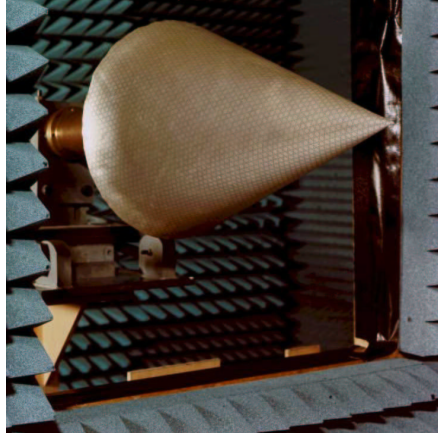


Figure 1.2: Conical FSS. Courtesy of the Loughborough University, UK.

plane to achieve a larger bandwidth for a given thickness than what allowed in most of the other absorbers [100]. In a Cassegrain system [4] the subreflector is a *dichroic structure*, which is a periodic surface transparent at a given frequency band and opaque at another frequency band [24]. The use of an FSS as subreflector (in the hyperboloid configuration for standard systems and in the flat configuration for offset systems) allows two independent feeds to share the same reflector antenna simultaneously, [120,145]. As shown in Fig. 1.3a, if the dichroic surface is transparent at the frequency f_1 and opaque at the frequency f_2 , it is possible to place one feed horn at the focal point of the main reflector, operating at frequency f_1 , and another feed at the Cassegrain focal point, operating at frequency f_2 . In this way, the manufacturing costs and the required space are reduced. Fig. 1.3b shows the S/X-band dichroic mirror designed by the University of Pavia for a deep space antenna system [19]. More examples of FSS's built for dichroic subreflectors are reported in [9, 100, 127].

In the microwave region FSS's are also used as *polarizers*. A *polarizer* is a diffraction grating, such that the fields with polarization parallel to the grating are reflected, while those with perpendicular polarization are transmitted [46]. Fig. 1.4a shows a dielectric polarizer presented in [141]; it operates in X-band and is used to rotate the polarization plane of a linearly polarized wave. An analogous polarizer, but operating in the 7-18 GHz range and obtained by cascading slanted strip grating plates, is described in [57]. Meander line polarizers can also be seen as FSS's and are typically used to convert horizontal to vertical polarization [22,29,100]. For example in [29] an application is described concerning a synthetic aperture radar that has to transmit for a single linear polarization and to receive

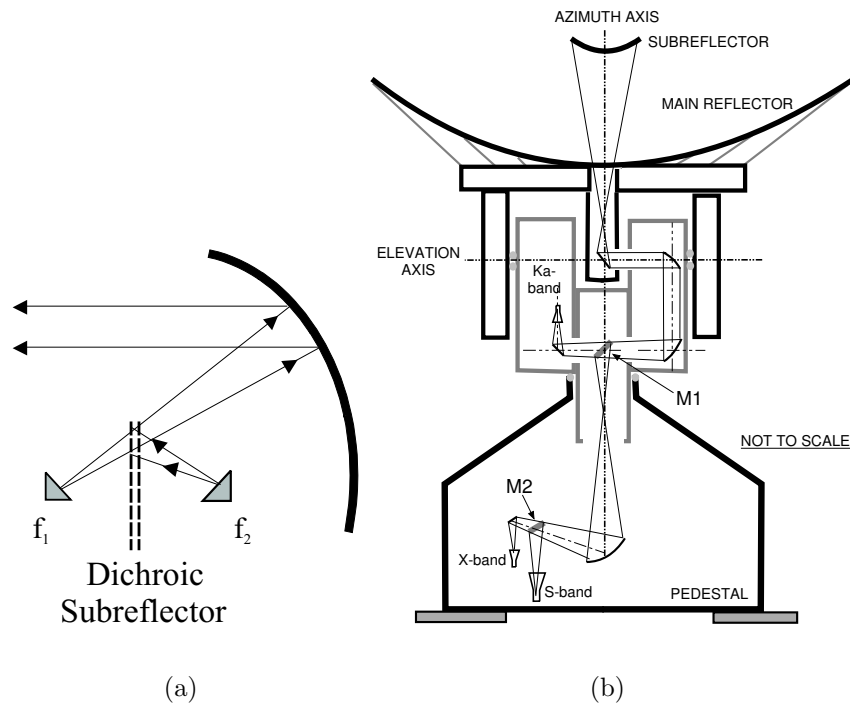


Figure 1.3: Use of an FSS as a Cassegrain subreflector. (a) Offset Cassegrain system. (b) Schematic of the deep space antenna system that uses an FSS as S/X-band dichroic mirror [19]. Courtesy of the University of Pavia, Italy.

for both linear polarizations. The proposed configuration consists of two horizontally polarized antennas and a meander line polarizer that changes the polarization of one of them. Meander line polarizers are also placed over the apertures of horns or flat plate arrays to convert linear to circular polarization, as the one for C-band applications shown in Fig. 1.4b.

A multi-layer FSS can be used as a frequency-dependent *magnetic ground plane* if the different layers are designed such that the phase is maintained near zero degrees in a certain frequency range. Some recent applications exploit this fact to enhance the radiation properties of printed antennas placed over the FSS, since the reflected field will be in phase with that directly radiated by the antenna itself, and to obtain *multi/wide-frequency antennas*, [47, 127].

Another interesting application consists in using FSS's to load the elements of an array with the purpose to increase their effective area. For example, for telecommunication reflector antennas the need is to maximize the number of reflectors and minimize the number of

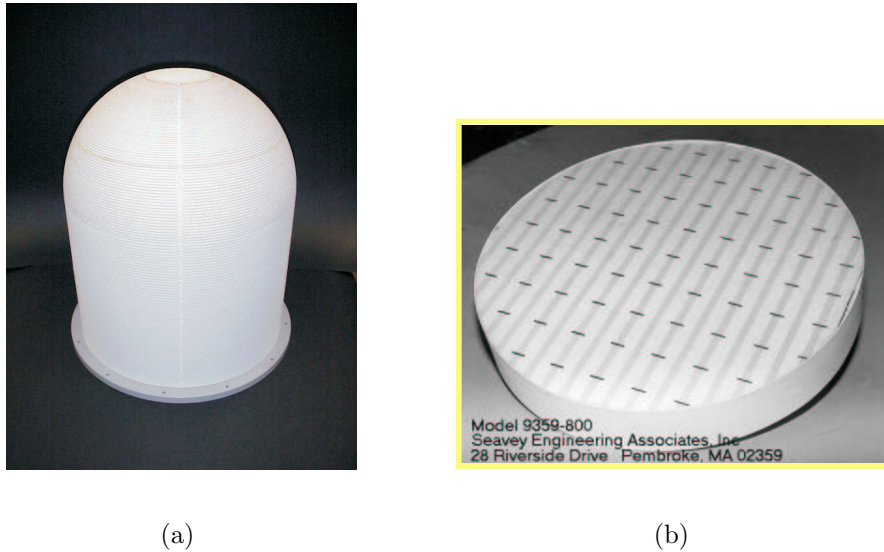


Figure 1.4: Examples of FSS's used as polarizers for microwave antennas. (a) Dielectric polarizer operating in X-band, presented in [141]. (b) Meander line polarizer operating in C-band, produced by Seavey Engineering [128].

feeds. Using small feeds, located close to each other, would lead to low spill over efficiency due to the low directivity of each feed. A possible configuration to avoid this problem, already adopted in 1956 in the Von Trentin antenna shown in Fig. 1.5a, consists in placing partially reflecting screens on the aperture of each feed to increase their directivity beyond what allowed by the physical area. As a result, for example in the case of horns, the physical cross section of the feeding antennas can be smaller and therefore the feeds can be placed closer to the focal point. Fig. 1.5b illustrates the functioning of overlapped feeds, as envisaged by Alcatel Space.

FSS's can also be designed to act as *frequency or angular filters* [51, 76]. An FSS can be used to block a certain frequency band, for example with the purpose of reducing the interference between two antennas [93, 99]. Moreover, the beam of an antenna with a wide scan range can be suitably oriented by means of an FSS that introduces a notch in its angular response. In this respect, FSS's are used as diplexer within complex antenna systems to separate closely spaced channels [30] and have proved to be suitable for spatial demultiplexing of a Gaussian beam at high frequencies [142].

Wide Angle Impedance Matching (WAIM) layers are structures cascaded to a phased array to improve the matching for a broad range of scan angles [86]. Typically, they consist of

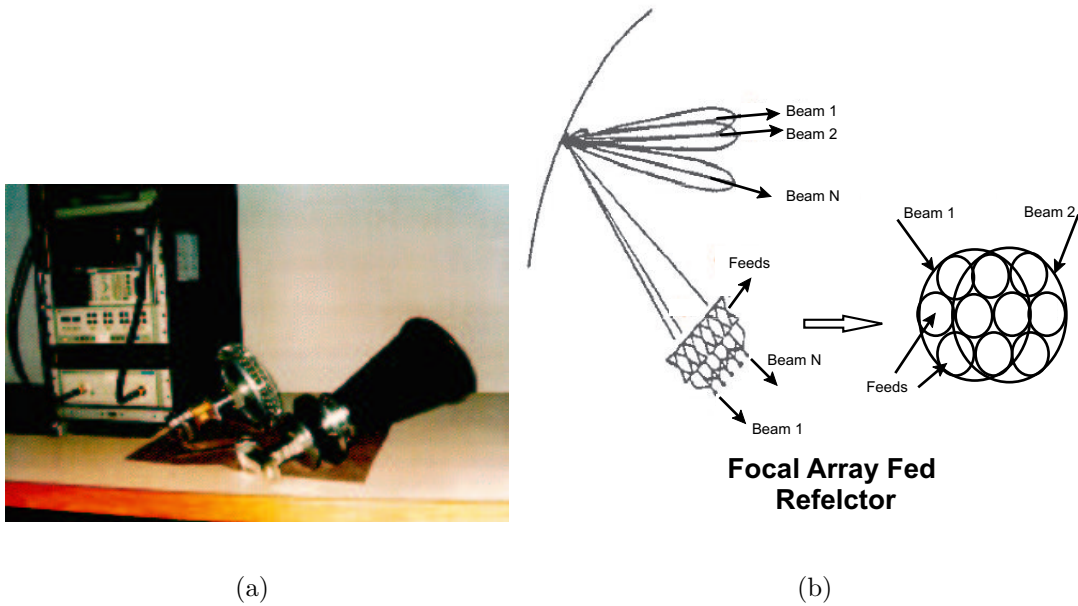


Figure 1.5: Use of FSS's to obtain overlapped feeds in a reflector antenna for telecommunication applications. (a) Von Trentin antenna. (b) Overlapped-feeds configuration. Courtesy of Alcatel Space.

dielectric slabs and guarantee the matching only in one scan plane. Another application of FSS's could be to design WAIM's that should work for different scan planes.

In the millimeter wave region, FSS's are obtained via photo etching of conducting sheets, vapor deposition onto photo-resist, or laser milling [98]. For example, in [17] FSS's manufactured by means of the wet-etch technique are employed as bandpass filters for Terahertz lasers.

In the *far-infrared region* periodic screens are used for example as polarizers, mirrors and infrared sensors. A *cavity mirror* for a molecular laser can be constructed from an FSS to be totally reflecting at the wavelength of the energy used to pump the cavity and partially transmitting at the lasing wavelength; an example is presented in [139]. *Infrared sensors* can use an FSS combined with dielectric layers to absorb the desired frequencies in the substrate material, on the back of the periodic screen, and to reject the out-of-band frequencies, as described in [45]. A detailed literature review on infrared applications of FSS's can be found in [98].

In the *near-infrared* and *visible region* FSS's have been proposed as solar selective surfaces:

screens that are transparent in the frequency band where the solar cells are more efficient, and opaque outside that band, can be exploited to collect solar energy, as explained in [68]. Finally, natural periodic screens have been identified in the corneas of insects (the fly-eye lens), as reported in [92].

1.2 Analysis techniques for FSS's

In 2000 the Royal Netherlands Navy (RNLN) founded the Integrated Topside Design (ITD) program for the next generation of frigates [43]. The aim was to optimize the performance of a ship with respect to four key parameters: RCS, EMI, EMC and vulnerability, by an appropriate combination of the sensors and of the communication systems housed on the ship topside. In the frame of this program, we focused on the development of an analysis technique for FSS's to be integrated with waveguide phased arrays.

The response of the FSS to plane-wave incidence is usually described in terms of reflection and transmission coefficients. To calculate this response it is necessary to relate the field scattered by the FSS to the incident field. This is done by writing boundary conditions for the electromagnetic field on the radiating elements of the FSS (apertures or patches). These boundary conditions are imposed on the integral representation for the scattered field in terms of the currents induced on the radiating elements and the Green's function (GF) of the periodic structure, including the layered background medium. This results in an Integral equation (IE) for these currents, which are treated as the fundamental unknowns. This equation cannot be solved in closed form, but must be tackled by numerical techniques; in particular we use the Method of Moments (MoM) [23, 66, 118]. If the FSS consists of the cascade of a number of periodic surfaces, sandwiched between dielectric slabs, this approach implies enforcing the appropriate boundary condition at each surface and solving the corresponding system of coupled integral equations [117]. Once the unknown currents have been determined, the scattered field can be easily determined from the same integral representation.

The described procedure provides global information about the electromagnetic response of the complete layered structure, but not about the field distribution at each internal discontinuity.

In the analysis of multi-layer structures, it is convenient to adopt a modular approach that characterizes separately each layer and transition between layers. As argued in [21], the obtained problem is computationally easier to handle than when analyzing the structure as a whole, because the maximum number of unknowns is limited by the number of unknowns

required to study each transition and because the Green's function used for the single transition has in general a much simpler form. Further, in the modular approach the computation time depends linearly on the number of layers, while it increases exponentially with that number if a global approach is adopted. Finally, a modular approach can be implemented in a general-purpose software tool that allows analyzing an arbitrary number of layers and appears therefore as a good basis for the design.

Because of these advantages, microwave network techniques are very suitable for the analysis of multi-layer structures because of their inherent modularity. They are based on a modal expansion of the fields in each layer and resort to a representation of the layer and of the transition between two adjacent layers in terms of an equivalent network; the different networks are then cascaded to represent the entire structure. Originally, microwave network techniques were developed for the analysis of discontinuities in waveguide and waveguide junctions [72, 96]. Subsequently, they have been extended to layered periodic structures, like for example FSS's. In fact, by virtue of the Bloch-Floquet theorem [26, 49], the propagation of the electromagnetic field in proximity of an infinite phased array, under the periodic boundary conditions dictated by the array, can be described as the propagation in an equivalent waveguide with a cross section equal to the unit cell. In this way, the scattering problem of an array under plane-wave incidence is reduced to a junction problem between the array waveguide and the unit-cell waveguide (the so-called unit cell approach [44]). The specific implementation of these techniques depends on the type of parameters chosen to characterize the structure: the Generalized Scattering Matrix (GSM) method [20, 72, 94, 106], the Generalized Transmission Matrix (GTM) method [105], the Generalized Impedance Matrix (GIM) [62, 67, 90] and the Generalized Admittance Matrix (GAM) [5, 61, 90] method. To derive the corresponding equivalent network, the scattering problem at each transition can be solved by means of different methods, as for example the MoM, the mode-matching method, the finite-element method or other hybrid methods [13]. In their conventional implementation, all techniques resort to an equivalent network with a large number of ports, corresponding to the number of propagating and evanescent modes used to represent the fields at the transitions. To limit the computational effort required to characterize the multi-layer structure when many matrices have to be cascaded to each other, a reduced form is calculated from the general network, including only those that actually contribute to the interaction with adjacent transitions (the accessible modes introduced in [126]). In the GAM method, the use of the reduced form of the equivalent network is necessary, as argued in [5], to prevent instability problems that arise in the cascade of matrices with a high number of evanescent modes (numerical underflow and overflow). The same kind of problem can be envisaged for the GIM method, while the

GSM representation is always stable.

Taking all these aspects into account, leads to the conclusion that the different microwave network techniques, in their conventional implementation, are almost equivalent from the point of view of the computational effort required to characterize structures consisting of the cascade of many layers [13]. In this respect, the GIM-based method proposed by Guglielmi in [36, 53] has an important advantage: it identifies the accessible modes as the only ones that are actually significant for representing the fields in the discontinuity region enclosed by the terminal planes, and *directly* resorts to an equivalent impedance matrix representation in terms of those modes only. Correspondingly, the problem is formalized in terms of a single IE with a fixed kernel, containing only localized modes (reduced kernel), and with multiple forcing terms, one for each accessible mode. In this thesis, we will indicate it as the Integral Equation method for the derivation of Multimode Equivalent Networks, or the IEMEN method. An approach based on the separation of interacting and localized modes was already proposed in [20] for the calculation of a reduced form of the GSM representing a waveguide junction. However, the IEMEN method requires a smaller number of matrix operations and therefore seems to be more efficient from the computational point of view. Hence, this method overcomes the problems of the conventional GIM and GAM-based techniques and offers a valid alternative to the consolidated GSM method for the analysis of multi-layer structures.

The first goal of our research was to develop a complete model for the analysis of waveguide array antennas integrated with multi-layer FSS's, also including feeding waveguides and filtering elements inside the waveguides. For this purpose, the IEMEN method, originally proposed for waveguide junctions [36, 53] and conformal arrays [56], has been extended to the analysis of multi-layer planar structures, consisting of infinite waveguide phased arrays and FSS's, composed by thick metal screens, or zero-thickness slots and patches, with an arbitrary shape and layout. This extension was simplified by the introduction of a GF formalism and the concept of non-accessible GF, only implicit until now. The other specifically addressed aspect was the appropriate combination of the newly developed equivalent networks with the networks already available for waveguide junctions.

Fig. 1.6 shows an example of structure that can be studied with the aid of the methodology described in this thesis. It consists of an infinite waveguide phased array integrated with a multi-layer FSS, composed by a periodic distribution of slots and an array of patches sandwiched between three dielectric slabs. Moreover, filtering, tuning and feeding elements inside the waveguide (like for example the matching iris in the waveguide apertures, as shown in the figure) can be included in the analysis.

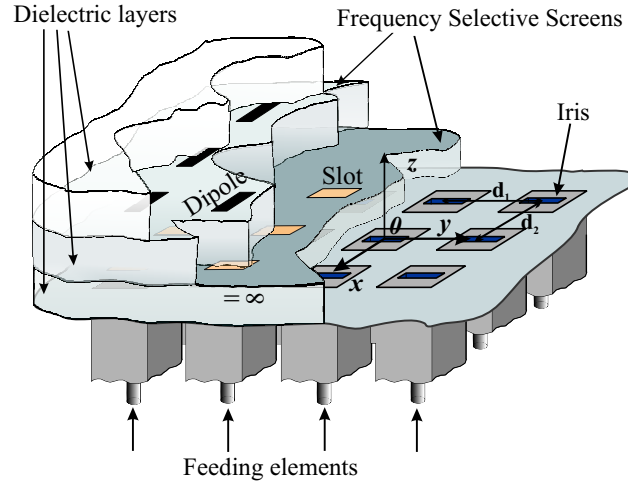


Figure 1.6: Geometry of a typical structure that can be studied with the methodology proposed in this thesis.

1.3 Design techniques for FSS's

An analysis methodology should be efficient enough to provide a reliable and flexible basis for the design.

The second goal of our work was to demonstrate that the IEMEN method is suitable as basis for an integrated antenna design procedure, where many aspects related to the functioning of the antenna are taken into account since the very beginning of the design: feeding and filtering structures, waveguide array, multi-layer FSS's.

The traditional design approach assumes the FSS to be a stand-alone structure. Therefore, the FSS and the antenna are designed independently, on the basis of the requirements set on the antenna performance (in terms of frequency bandwidth, return loss, scanning angle, etc.), but the effect of the mutual interactions is not considered. The design approach we are aiming for should allow the development of new configurations, where the FSS is directly integrated with the array (Fig. 1.6). This actually would offer several and new interesting features.

- The IPD is drastically reduced with respect to the traditional large FSS radomes covering the array antenna.
- The resulting structure is more compact and follows the profile of the platform, which can be designed to achieve a low RCS. Moreover, the RCS of the platform can be further improved by an appropriate design of the FSS.

- The engineer has more degrees of freedom in the optimization of the overall structure (the array-FSS system is now optimized as a whole). This allows new system functionalities: the FSS can also be used to reduce the interference between adjacent antennas or as matching structure, to improve the antenna return loss and to increase the frequency bandwidth.

In the early stages of FSS's development, when the available calculation power was rather limited, single-mode transmission-line (TL) models were the main instrument for the analysis and the design. The FSS was characterized in terms of an equivalent circuit of lumped components, typically LCR , connected in parallel to the TL corresponding to the only propagating mode. Langley and Parker [77–79] calculated the parameters of this circuit for the case of a strip grating in free space, by starting from the basic inductance and capacitance equations presented in [88]. The design approach was often based on filter synthesis techniques, which were already used for dielectric radomes [87], and then were directly extended to metal grids by replacing the frequency variable with the angular variable [51]. In [76], a single-mode TL model accounted for both the angular and the frequency dependence of the structure.

Nowadays, the availability of powerful computers, makes the use of equivalent circuits less interesting for analysis purposes, while they still represent a relevant instrument for the synthesis. Since full-wave simulations are time-consuming, a suitable design approach for multi-layer FSS's cannot completely rely on them. For this reason, the usually adopted design strategy consists of two phases [37,106]. A preliminary design is obtained by optimizing the single-mode TL equivalent to the fundamental propagating Floquet mode. Tuning very efficiently the relevant parameters allows reaching the requested performances. In a second stage, the analysis is refined by means of full-wave simulations. In the single-mode model, the FSS is usually still represented in terms of an LC circuit in parallel to the TL, where the L and C values can be obtained in different ways. In [47] they are calculated by comparing the full-wave simulations of the FSS reflection coefficient with the simulations of the LC single-mode model by means of a curve-fitting algorithm. Alternatively, as shown in [84], from the knowledge of the full-wave FSS reflection coefficient, the LC circuit parameters can be obtained in a straightforward way by deriving the poles and zeros of the equivalent FSS admittance or impedance and applying simple circuit theory [135]. In fact, it has been demonstrated in [35] that the input impedance of a lossless waveguide is purely reactive and that the reactance respects the Foster's reactance theorem. Therefore it can be approximated as a sum of rational functions with as coefficients the residues of the poles of the impedance. This theorem can also be applied to the waveguide equivalent

to the unit cell of an FSS. However, until now the approximation has been performed for the *single-mode* case only.

In this thesis it will be shown that the IEMEN formulation *directly* leads to a representation of an FSS's patch (slot) transition in terms of a shunt admittance (impedance) matrix, avoiding a preliminary derivation of an equivalent *LC* circuit. Moreover, since in this approach the modes that vary most rapidly as a function of the frequency are extracted from the kernel of the corresponding IE, only slowly elements are left in the impedance matrix as a function of that frequency. As a consequence, these elements can be calculated in a few frequency points of the operating frequency range. This is true for an *arbitrary number of accessible modes* and therefore an arbitrary number of elements in the impedance matrix and allows a significant reduction in the calculation time.

To validate the described design approach, based on the IEMEN method, in this thesis we will tackle a realistic interference problem, similar to the one reported in [93], concerning an array and a satellite communication antenna that operate on the topside of a ship. In our case, we will suppose that the signal transmitted by an X-band array antenna saturates the low-noise amplifiers in the receiver of a satellite communication antenna, located close to the array. Among the possible solutions for this problem, we will focus on the design and analysis of an appropriate FSS, which will have to operate as narrow roll-off (high-order) low-pass filter. For the sake of compactness, the FSS will be integrated with the array antenna.

1.4 Outline of the thesis

The thesis is structured as follows.

In *Chapter 2* the IEMEN approach is formulated in detail and is applied to the analysis of a waveguide junction. The formulation is then extended to the analysis of waveguide phased arrays radiating in free space. The concept of thick and thin screen is introduced and the new formulation for the case of a thick FSS is presented. To demonstrate the analysis capabilities of the method some representative examples are reported; they consist of comparisons with both literature results and simulations performed using other methods (direct method described in [144]).

In *Chapter 3* the new IEMEN formulation for the analysis of planar, patch-based and slot-based FSS's is presented. This chapter also contains considerations on the numerical implementation of the method, with emphasis on the solution of the pertinent IE. The theoretical formulation has been implemented in a software tool that has been validated

versus test cases available in literature and structures simulated by means of two commercial packages, based on the finite-element method (HFSS) and on the MoM (Ansoft Designer) [10, 11].

In *Chapter 4* the procedure to design a band-stop multi-layer FSS to be integrated with an X-band phased array is introduced. The starting point is a single-mode TL representation of all the cascaded components, which in turn results in a simple Smith-chart design. The design is then refined in a second phase by means of full-wave IEMEN-based simulations, where all the relevant accessible modes are included. The results of the analysis of the designed structure are compared with the simulations performed using HFSS.

In *Chapter 5* various aspects of the realization of the designed FSS panel are described and the results of the measurements of reflection and transmission coefficients performed using different setups are presented and discussed.

In *Chapter 6* we present the ill-conditioning problem that arises in a MoM-based solution of the reduced kernel IE derived by means of the IEMEN method, using sub-domain functions to expand the unknowns currents. In particular, when the frequency filtering performances required from the FSS include steep roll offs and wide scan angles, the number of accessible (interacting) modes to be included in the analysis grows and the MoM matrix becomes ill conditioned. This problem is circumvented by changing to a MoM that uses a special class of entire domain basis functions. Representative test cases are presented, which show the convenience of these functions with respect to sub-domain functions for the solution of reduced kernel IE's.

In *Chapter 7* the conclusions of this research work are drawn and recommendations are provided for future developments of the proposed analysis and design methodology.

Chapter 2

Multimode Equivalent Networks: the IEMEN method

A waveguide array antenna, with filtering and feeding elements in the radiating apertures, integrated with a Frequency Selective Surface (FSS) of arbitrary complexity, like the one shown in Fig. 2.1, can be analyzed as a multi-layer structure.

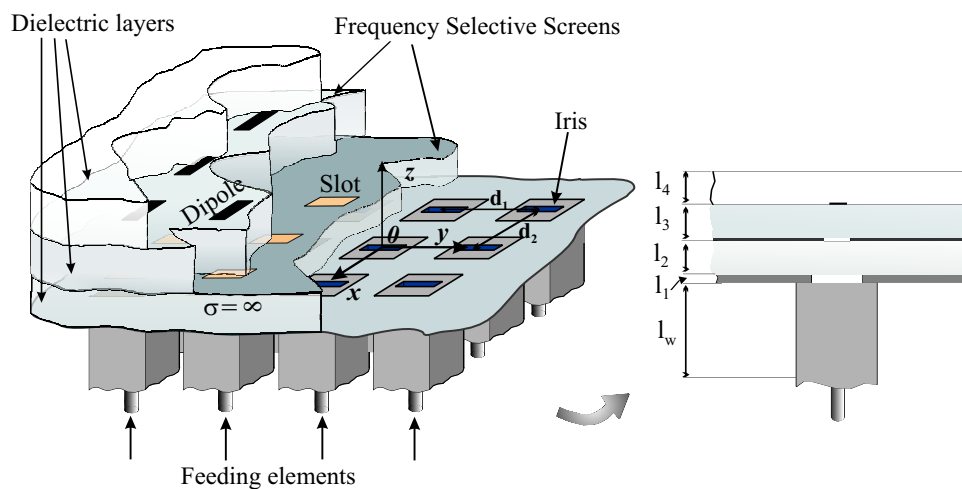


Figure 2.1: Multi-layer structure.

Two main approaches can be distinguished to perform this analysis. One of the approaches *studied the multi-layer structure as a whole*, by calculating the fields reflected at the first transition and transmitted at the last one. The other one *separately characterizes each layer and each transition between adjacent layers* by means of an appropriate microwave network and obtains the representation of the complete structure as a cascade of equivalent

networks. The latter approach retains the information about the behavior of the electromagnetic field at each internal discontinuity and it is a particularly suitable basis for the design because of its modularity. Moreover, it allows gaining a better feeling of the behavior of the various layers. In fact, if this approach is adopted for the design of a structure consisting of many different layers, a change in one of the layers requires recalculating only its equivalent network and the networks representing the transitions with the two adjacent layers. This results in a significant saving in calculation time.

Different techniques are available in literature for the characterization of waveguides and waveguide junctions in terms of microwave networks [13, 72]. Some of them calculate the scattering parameters to derive the equivalent Generalized Scattering Matrix (GSM), or the Generalized Transmission Matrix (GTM). Other techniques resort to a representation in terms of Generalized Admittance Matrix (GAM) or Generalized Impedance Matrix (GIM). In most implementations, the obtained matrices have a large number of ports and the computational effort required for their calculation is roughly the same [13, 72]. Instead, the methodology introduced in [36, 53], by identifying the modes that are truly significant in the representation of the fields at the junction (accessible modes), directly results in an equivalent GIM with a reduced number of ports compared to a conventional GIM representation. This approach requires the solution of a single Integral Equation (IE) with a fixed kernel, reduced to the contribution of the localized modes only, and with as many forcing terms as the number of accessible modes. It will be further referred as Integral Equation method for the derivation of Multimode Equivalent Networks, or IEMEN method.

Microwave network techniques that were originally developed for waveguides are also well suited for the analysis of multi-layer, infinitely extended, periodic structures. Based on the Bloch-Floquet theorem [26, 49], the unit cell approach [44] reduces the problem of an infinite periodic array radiating in free space to a waveguide junction problem. The extension of the IEMEN approach to planar phased arrays and thick FSS's is the subject of this chapter.

From now on the following terminology will be used:

1. *waveguide junction*: the junction between two conventional waveguides, for example between the waveguides cascaded to design a multi-cavity filter;
2. *waveguide discontinuity*: a discontinuity inside a waveguide, obtained for example by inserting a thin diaphragm;
3. *waveguide transition*: the junction between two nonconventional waveguides, for ex-

ample the junction between the waveguide equivalent to an array unit cell and the array waveguide.

The expression *discontinuity region* will be used to indicate the region, comprised between the selected terminal planes, containing a junction or a transition or a discontinuity.

In Sec. 2.1 the general procedure for deriving the microwave network representation of a waveguide and of a junction between two waveguides is described. The relevant theoretical formulation of the IEMEN approach for a waveguide junction and for a uniform waveguide section is outlined in Sec. 2.1.2 and in Sec. 2.1.3, respectively. The novel extension of the IEMEN formalism to the analysis of infinite phased arrays radiating in free space is described in Sec. 2.2; this section also contains numerical results. In Sec. 2.3 the representation derived for arrays of waveguides is used to study aperture-based FSS's with the apertures cut from a thick metal plate; some examples of applications are also reported. Finally, in Sec. 2.4, the distinguishing and innovative characteristics of the MEN approach are highlighted in comparison with other microwave network-based methodologies.

2.1 Multimode equivalent networks for waveguides

Microwave networks have been widely used for representing waveguide junctions, especially in filter modeling, [52, 60]. In this case, a configuration consisting of different cavities is represented as the cascade of their corresponding networks and the filter can be efficiently tuned by changing the parameters of each network separately. In the classical literature about waveguides [81, 88], the equivalent networks were derived under the single-mode assumption, by placing the terminal planes far from the discontinuity. For example, in [88] the problem of a discontinuity in a waveguide is formulated in terms of a single integral equation (IE) for the fundamental propagating mode, while the higher-order modes are considered terminated by their characteristic impedance; the obtained model is a lumped-element circuit. This approach is valid only for insulated waveguides, and it is not capable of modeling a sequence of waveguide junctions very close to each other, since, in this case, the interaction between adjacent junctions no longer proceed via single mode. Lately, different methods have been proposed for deriving multimode equivalent networks for waveguide junctions and some references will be provided in the following section.

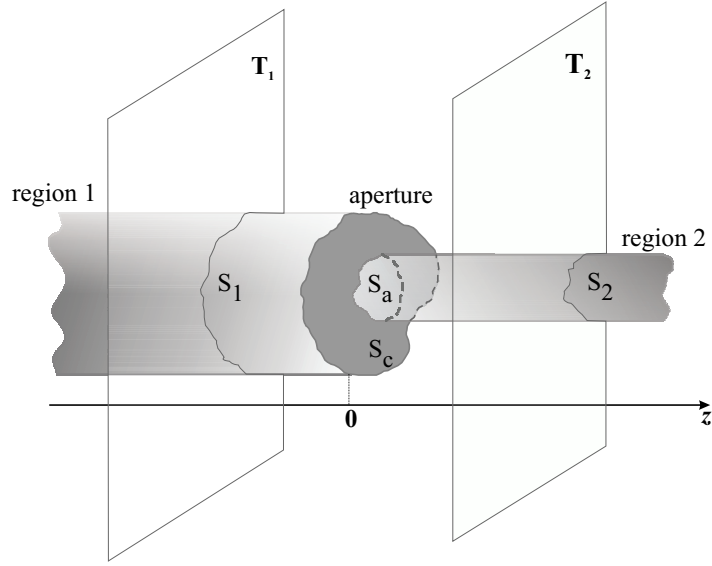


Figure 2.2: Junction between two waveguides of surfaces S_1 and S_2 respectively. S_a is the cross section of the smaller waveguide and S_c is the part of the cross section of the larger waveguide after subtracting S_a .

2.1.1 The microwave network formalism

In this section, the basic concepts underlying the use of the microwave network formalism for representing waveguide structures are introduced. In particular, we have used the formalism proposed in [36] by Sorrentino *et al.* Fig. 2.2 shows a *waveguide junction* between two uniform waveguides, with cross sections S_1 and S_2 , indicated in the figure as region 1 and region 2, respectively. The terminal planes T_1 and T_2 define the boundaries between the discontinuity region and the two uniform waveguides; S_a is the common aperture and S_c is the metallic wall at the junction.

In the formulation of the pertinent electromagnetic boundary value problem, the fields in a uniform waveguide region can be expressed in terms of modes, defined with respect to the waveguide axis (Appendix A). The first step to derive the microwave network representation of a waveguide junction consists then in expanding the unknown fields at the junction plane in terms of the modal basis defined in each one of the two uniform regions. Conventionally, the electromagnetic field in an infinitely long, uniform waveguide is described by a single propagating mode, studied by means of its equivalent transmission line, while the evanescent modes are closed by their characteristic impedances. In the proximity of a discontinuity, for example the junction depicted in Fig. 2.2, a complete representation of

the transverse field requires taking into account, in addition to the propagating mode, an infinite number of evanescent ones:

$$\mathbf{E}_t^{(\delta)}(\mathbf{r}) = \sum_{i=1}^{\infty} V_i^{(\delta)}(z) \mathbf{e}_i^{(\delta)}(\mathbf{r}_t), \quad (2.1a)$$

$$\mathbf{H}_t^{(\delta)}(\mathbf{r}) = \sum_{i=1}^{\infty} I_i^{(\delta)}(z) \mathbf{h}_i^{(\delta)}(\mathbf{r}_t), \quad (2.1b)$$

where $\delta = 1, 2$ indicates one of the two regions and the subscript t refers to the field component transverse to the z axis. The vector $\mathbf{r}_t = x\mathbf{u}_x + y\mathbf{u}_y$ identifies a point on the plane transverse to the z -axis, with respect to a Cartesian reference system defined by the unit vectors \mathbf{u}_x , \mathbf{u}_y and \mathbf{u}_z . The vectors $\mathbf{e}_i^{(\delta)}$ and $\mathbf{h}_i^{(\delta)}$ are the electric and magnetic vector mode functions, with $\mathbf{h}_i^{(\delta)} = \mathbf{u}_z \times \mathbf{e}_i^{(\delta)}$, and $V_i^{(\delta)}$ and $I_i^{(\delta)}$ are the modal voltages and currents respectively (Appendix A). In practice, instead of considering the modal representation of the unknown fields at the junction plane, this representation is derived at a pair of reference planes T_1 and T_2 located very close to the junction, so that only a finite number of modes need to be included in Eq. (2.1). By virtue of the linearity of Maxwell's equations (Appendix A Eq. (A.5)), the tangential electric and magnetic fields are linearly related on the boundary. The modal currents can then be calculated from the corresponding modal voltages (or vice versa) by solving the following system of linear equations [36]:

$$\begin{bmatrix} [V^{(1)}] \\ [V^{(2)}] \end{bmatrix} = \begin{bmatrix} [Z_{11}] & [Z_{12}] \\ [Z_{21}] & [Z_{22}] \end{bmatrix} \cdot \begin{bmatrix} [I^{(1)}] \\ [I^{(2)}] \end{bmatrix}, \quad (2.2)$$

where the subvectors $[I^{(\delta)}]$ and $[V^{(\delta)}]$ contain the modal currents and voltages at the δ -terminal plane ($\delta = 1, 2$). $[Z]$ is the Generalized Impedance Matrix that describes the waveguide discontinuity and its network interpretation is shown in Fig. 2.3. The adjective *generalized* emphasizes the fact that the network includes not only the propagating modes, as in the conventional microwave networks, but also the evanescent ones [96].

Using a modal approach to characterize the fields in the vicinity of a waveguide junction leads to a description of the junction in terms of a multi-port network, where each input port corresponds to a mode at the terminal plane T_1 and each output port to a mode at the terminal plane T_2 . The number of input and output ports depends therefore on the distance of these reference planes from the junction plane: the closer they are to the junction, the higher is the required number of modes. The network matrix is in this case the GIM described by Eq. (2.2). The relation between voltages and currents in this network can also be expressed in terms of a GAM, while the GSM and the GTM relate the complex

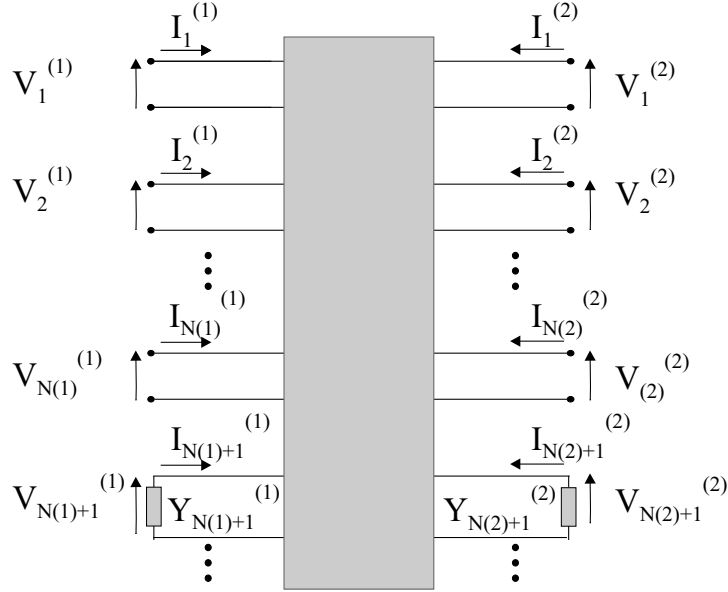


Figure 2.3: Equivalent multi-port network of the junction between two waveguides shown in Fig. 2.2, derived with respect to the terminal planes T_1 and T_2 .

amplitudes of the incident and reflected modes. The transform formulas between all these representations are the same as for standard microwave networks.

To build the relevant network matrices, the corresponding modal amplitudes are calculated by solving the equation derived from the pertinent boundary conditions for the fields at the discontinuity. Tangential magnetic and electric fields are continuous across the aperture and the tangential electric field vanishes on the metallic wall:

$$\mathbf{E}_t^{(2)}(\mathbf{r}) = \begin{cases} \mathbf{E}_t^{(1)}(\mathbf{r}) & \text{on } S_a, \\ 0 & \text{on } S_c, \end{cases} \quad (2.3a)$$

$$\mathbf{H}_t^{(2)}(\mathbf{r}) = \mathbf{H}_t^{(1)}(\mathbf{r}) \quad \text{on } S_a. \quad (2.3b)$$

Depending on the expressions used for the fields, different types of equations can be derived from these continuity conditions, which can be solved by applying various techniques, as for example the finite-element method, the integral equation method, the mode-matching method and hybrid methods as the boundary contour/mode-matching method and the mode-matching/finite-element method. An excellent review of the available methods can be found in [13, 72]. The mode-matching technique, for example, is often used to obtain a representation in terms of GSM. In this case, the fields in the continuity conditions (2.3) are expanded in terms of as many waveguide modes as the number of modes used in the

representation of the fields in the terminal planes. Then, the orthogonality of the vector mode functions is used to obtain a system in the modal coefficients $V_m^{(\delta)}$ and $I_m^{(\delta)}$, which is handled by resorting to approximation techniques, such as truncation and iteration [72]. Note that the number of modes actually used to represent the fields at the terminal planes 1 and 2 determines the accuracy with which the scattering problem is solved. As shown in [95], these two numbers cannot be chosen independently if a mode-matching technique is used, because of the relative convergence phenomenon. This problem is encountered as well when, from Eq. (2.3), an IE is derived and solved via the Method of Moments (MoM). In this case the convergence of the kernel depends on the number of evanescent modes summed in the kernel and on the discretization of the unknown currents.

The reader can find some examples of applications of the GSM in [16, 20, 72, 96, 97, 110], of the GTM in [105], of the GAM in [5, 61, 90] and of the GIM in [67, 90]. In particular, in this thesis we will focus on impedance and admittance matrix representations. Already in [126] waveguide junctions were represented in terms of equivalent lumped multi-port circuits, characterized by a reactance matrix, and the proposed method was not affected by the relative convergence phenomenon. In [5], the technique of boundary reduction/boundary enlargement was applied to derive a GAM representation of two grouped waveguide junctions, involving waveguides of different cross section. However, the network elements were frequency dependent and had to be recalculated at every frequency point. In [61] a GIM representation was derived by extending to waveguide junctions the method presented in [62] for the analysis of zero-thickness metal strip gratings. In this case, the generic element of the equivalent impedance matrix did not depend on the frequency (except for a multiplicative factor), and, for the cascade of a number of waveguides, the frequency dependence in the behavior of this multi-layer structure was accounted for by the transmission lines that represent the propagation of the modes in the discontinuity-free regions. The network is derived by solving the IE obtained from the continuity conditions (2.3) with the MoM. In [90], the GIM elements were directly calculated from the definition of the admittance matrix (designated as *direct method*). This led to a simple procedure, where only one entry of the matrix requires an infinite summation; thus, relative convergence problems were avoided. However, the matrix elements in this case were frequency dependent.

In the representation of the cascade of many waveguides, if the number of evanescent modes used to expand the fields in each junction is too large, it has been shown in [105], for the case of a GTM representation, that a numerical instability arises. In fact, in this case the product between the attenuation constant and the waveguide length becomes excessively large, which may lead to overflow in the calculation of the elements of the GTM characterizing a waveguide section. This kind of numerical instability has been observed also

in cascading admittance matrices. According to [5], the problem can be circumvented by deriving, from the general GAM representation of a certain junction, which has the same number of input and output ports as the number of modes included in the calculations, a reduced form corresponding to only the modes that contribute to the interaction with adjacent junctions. The reduced GAM is obtained by closing the non-interacting modes with their characteristic admittances. In its practical implementation, this requires performing one additional matrix inversion and two additional matrix multiplications.

The GSM representation is not affected by this stability problem [16, 112] and its reduced version is merely used to limit the calculation time and increase the efficiency in the solution of problems that involve the cascade of many waveguides. In fact, the accuracy of a GSM representation is related to the number of evanescent modes included in the calculation of the coupling matrix (or the kernel of the integral equations, depending on the adopted approach), but the number of input and output ports of the derived GSM is not necessarily the same as the number of those evanescent modes [16, 111].

The *computational efficiency* of a microwave network-based method can be evaluated on the basis of the number of matrix inversions required, the number of matrix multiplications, the size of the matrix to be inverted or multiplied and the time required to build this matrix. In the technique proposed in [61], one matrix inversion is required to build the GIM, while in the method of [5] no matrix inversion is needed to derive the GAM representation. This holds also for the GTM representation, if the same number of evanescent modes are used at the two sides of the discontinuity, as explained in [105]. To obtain the GSM representation, in general only one matrix inversion has to be performed.

As argued in [13, 111], for an appropriate choice of the analysis technique, the computational effort required to characterize complex structures consisting of many cascaded waveguides is actually about the same for the GSM, GAM or GIM representation. However, the calculation of the reduced version of the GAM or of the GIM, which is necessary for a large number of evanescent modes, involves one additional matrix inversion.

In this respect, the IEMEN method introduced in [36, 53] has an important advantage. It resorts directly to a reduced GIM representation, associated only to the interacting modes. To better understand the *basic idea* underlying the IEMEN approach, we shall now return to the waveguide junction problem depicted in Fig. 2.2. The uniqueness property of the electromagnetic field guarantees that, if the region enclosed by the terminal planes is source-free, the knowledge of either the tangential electric or the tangential magnetic field at the terminal planes characterizes uniquely the electromagnetic field within that region [48, 132]. Therefore, to derive an equivalent network of this junction, it is sufficient to describe the field distribution at the junction in terms of as many modes as those needed

to represent the field at the two terminal planes, which are located in proximity of the next two junctions. This allows us, from the beginning of the characterization of the junction, to reduce the number of modes to be included in the field representation to the *accessible modes* only [126]. The latter are the modes, propagating or below cut off, which, excited at a certain junction, reach the next junction and therefore contribute to the interaction between the different discontinuities in the structure. They are defined as the modes required to achieve a prescribed accuracy in the field representation at the terminal planes. This accuracy can be specified by setting a maximum acceptable value of attenuation of the modes when they reach the terminal planes; only those exhibiting an attenuation lower than that value are included in the representation. *Localized* or *non-accessible* modes, on the contrary, are higher-order modes that are confined to the discontinuity area and store reactive energy. For the case of only one junction, the terminal planes can be chosen at a distance such that only a few evanescent modes are still significant; at the limit of infinite distance, only the propagating modes contribute to the field representation, while all the evanescent ones become negligible. Instead, if the terminal planes separate the junction from other, nearby junctions, an higher number of accessible modes has to be taken into account, to properly characterize the interaction between the different discontinuities. In Fig. 2.2, the terminal planes are chosen at a distance from the discontinuity such that the tangential electric and magnetic fields at the terminal planes T_1 and T_2 can be described by means of only $N^{(1)}$ and $N^{(2)}$ accessible modes respectively (for a certain accuracy on the field representation) [36]. In the field expressions (2.1), the two series are correspondingly truncated to the first $N^{(\delta)}$ modes, with $\delta = 1, 2$ indicating one of the two regions:

$$\mathbf{E}_t^{(\delta)}(\mathbf{r}) = \sum_{i=1}^{N^{(\delta)}} V_i^{(\delta)}(z) \mathbf{e}_i^{(\delta)}(\mathbf{r}_t), \quad (2.4a)$$

$$\mathbf{H}_t^{(\delta)}(\mathbf{r}) = \sum_{i=1}^{N^{(\delta)}} I_i^{(\delta)}(z) \mathbf{h}_i^{(\delta)}(\mathbf{r}_t), \quad (2.4b)$$

Therefore, the description of the fields at the terminal planes, and by virtue of the uniqueness theorem also at the junction, involves $N^{(1)} + N^{(2)}$ modal voltages and the same number of modal currents, related by $N^{(1)} + N^{(2)}$ linear equations (2.2).

These quantities are identified as the *fundamental unknowns* of the problem, in the sense that, for the purpose of deriving the equivalent network representation of the junction, all the fields in the discontinuity region can be expressed in terms of these quantities only. In this sense, each accessible mode is considered as an independent input/output channel. In particular, we treat the modal amplitudes $I_i^{(\delta)}(z)$ and $V_i^{(\delta)}(z)$ at the interface $z = 0$ as the fundamental unknowns. This is actually the characterizing feature of the IEMEN method,

which results, to the author's best knowledge, in an absolutely original formulation. In fact, it results in a single IE with a fixed kernel and with a different forcing term for each accessible mode. The characteristics of this approach will become clearer in the following section, where the theoretical formulation will be explained in detail.

2.1.2 MEN of a waveguide junction

We shall consider again the waveguide junction shown in Fig. 2.2. According to the IEMEN formulation, a limited number of the modal coefficients (modal voltages and modal currents) suffice to represent the tangential electric and magnetic fields at the terminal planes to the required degree of accuracy. With respect to Fig. 2.2, they are the coefficients of the $N^{(1)}$ accessible modes on the terminal plane T_1 and of the $N^{(2)}$ accessible modes on the terminal plane T_2 , as in Eqs. (2.4). These modal coefficients are the *fundamental unknowns* of the problem. Hence, all the fields in the discontinuity region can be expressed as a linear combination of these quantities. In particular, in view of the relation (2.2) between modal currents and voltages, the fundamental unknowns for an aperture-type formulation (boundary condition for the magnetic field on the common aperture S_a) are the modal currents $I_i^{(\delta)}$, and for an obstacle-type formulation (boundary condition for the electric field on the metal surface S_c) are the modal voltages $V_i^{(\delta)}$, where $i : 1, \dots, N^{(\delta)}$ and $\delta = 1, 2$. The problem is treated here as of aperture type, with, as input variables, the $N^{(1)} + N^{(2)}$ modal currents $I_i^{(\delta)}$. Consequently, it is appropriate to express the unknown total transverse electric field in the common aperture S_a as a linear combination of these modal currents, with, as coefficients, $N^{(1)} + N^{(2)}$ suitable vector functions $\mathbf{m}_m^{(\delta)}$ that remain to be determined:

$$\left(\mathbf{u}_z \times \mathbf{E}_t(\mathbf{r})\right) = \sum_{m=1}^{N^{(1)}} I_m^{(1)}(z) \mathbf{m}_m^{(1)}(\mathbf{r}_t) - \sum_{m=1}^{N^{(2)}} I_m^{(2)}(z) \mathbf{m}_m^{(2)}(\mathbf{r}_t), \quad (2.5)$$

where $\mathbf{r} = x\mathbf{u}_x + y\mathbf{u}_y + z\mathbf{u}_z$. To determine these functions we utilize the physics of the problem. The magnetic fields at the common aperture can be written in terms of modes as:

$$\mathbf{H}_t^{(1)}(\mathbf{r}) = \sum_{n=1}^{\infty} I_n^{(1)} \mathbf{h}_n^{(1)}(\mathbf{r}_t), \quad \mathbf{r}_t \in S_1, \quad (2.6a)$$

$$\mathbf{H}_t^{(2)}(\mathbf{r}) = \sum_{n=1}^{\infty} I_n^{(2)} \mathbf{h}_n^{(2)}(\mathbf{r}_t), \quad \mathbf{r}_t \in S_2. \quad (2.6b)$$

The modal currents are evaluated at the discontinuity and, for the sake of simplicity, we consider the discontinuity plane at $z = 0$. Hence, we also introduce the short notation

$I_n^{(\delta)}(z=0) = I_n^{(\delta)}$. In this representation of the magnetic fields, only the first $N^{(1)}$ (for $\mathbf{H}_t^{(1)}(\mathbf{r})$) and $N^{(2)}$ (for $\mathbf{H}_t^{(2)}(\mathbf{r})$) modal coefficients are the independent ones, associated to the accessible modes, while the higher-order modes, which do not contribute to the energy exchange with other discontinuities, can be considered closed by an almost static modal characteristic admittance $Y_n^{(\delta)}$:

$$I_n^{(1)} = -Y_n^{(1)}V_n^{(1)}, \quad I_n^{(2)} = Y_n^{(2)}V_n^{(2)} \quad \text{for } n > N^{(\delta)}, \quad (2.7)$$

with

$$Y_n^{(\delta)} = \begin{cases} \frac{\kappa_n^{(\delta)}}{\omega\mu} & , \text{ TE,} \\ \frac{\omega\varepsilon^{(\delta)}}{\kappa_n^{(\delta)}} & , \text{ TM,} \end{cases} \quad (2.8)$$

where $\kappa^{(\delta)}$ is the modal propagation constant, with $\delta = 1, 2$. The TE and TM modes are defined with respect to the z direction identified by the vector \mathbf{u}_z . The localized modes contribute only to the reflected field in region 1 and to the transmitted field in region 2. The signs of the modal currents are taken accordingly, as shown in Fig. 2.4.

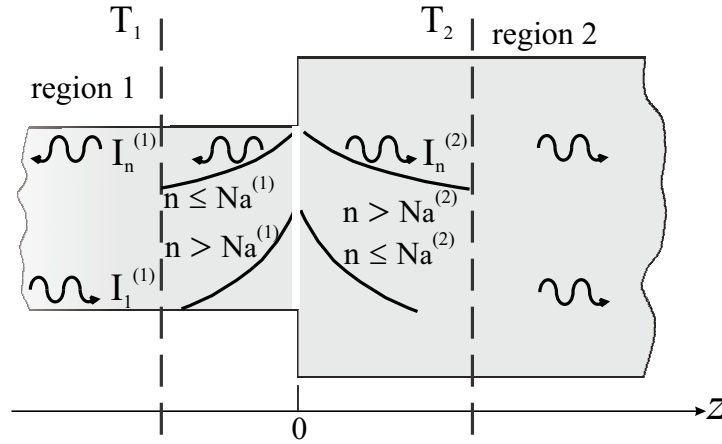


Figure 2.4: Accessible and localized modes in a waveguide discontinuity.

At the aperture S_a the boundary condition (2.3) for the tangential magnetic field holds:

$$\sum_{n=1}^{\infty} I_n^{(1)} \mathbf{h}_n^{(1)}(\mathbf{r}_t) = \sum_{n=1}^{\infty} I_n^{(2)} \mathbf{h}_n^{(2)}(\mathbf{r}_t), \quad \mathbf{r}_t \in S_a, \quad (2.9)$$

where the index n covers both *TE* and *TM* modes in each waveguide. Separating accessible

and localized modes, and using the definitions (2.7), we can write this equation as:

$$\begin{aligned} \sum_{n=1}^{N^{(1)}} I_n^{(1)} \mathbf{h}_n^{(1)}(\mathbf{r}_t) - \sum_{n=1}^{N^{(2)}} I_n^{(2)} \mathbf{h}_n^{(2)}(\mathbf{r}_t) &= \sum_{n=N^{(1)+1}}^{\infty} V_n^{(1)} Y_n^{(1)} \mathbf{h}_n^{(1)}(\mathbf{r}_t) \\ &+ \sum_{n=N^{(2)+1}}^{\infty} V_n^{(2)} Y_n^{(2)} \mathbf{h}_n^{(2)}(\mathbf{r}_t), \quad \mathbf{r}_t \in S_a. \end{aligned} \quad (2.10)$$

Let us now use Eq. (A.43) of Appendix A, which expresses the relation between the modal voltages and the transverse electric field given in:

$$V_n^{(\delta)}(z) = \iint_{S_\delta} \mathbf{E}_t(\mathbf{r}') \cdot \mathbf{e}_n^{(\delta)*}(\mathbf{r}') d\mathbf{r}' = \iint_{S_\delta} (\mathbf{u}_z \times \mathbf{E}_t(\mathbf{r}')) \cdot \mathbf{h}_n^{(\delta)*}(\mathbf{r}') d\mathbf{r}', \quad \delta = 1, 2, \quad (2.11)$$

where the integration is restricted to the waveguide cross section S_δ of the δ waveguide indicated in Fig. 2.2, and where the transverse electric field is the same on the two sides of the discontinuity. Recalling the expression (2.5) for the unknown electric field at the aperture, and substituting in Eq. (2.10), leads to:

$$\begin{aligned} \sum_{m=1}^{N^{(1)}} I_m^{(1)} \left[\mathbf{h}_n^{(1)}(\mathbf{r}_t) - \left(\sum_{n=N^{(1)+1}}^{\infty} Y_n^{(1)} \iint_{S_a} \mathbf{m}_m^{(1)}(\mathbf{r}') \cdot \mathbf{h}_n^{(1)}(\mathbf{r}_t) \mathbf{h}_n^{(1)*}(\mathbf{r}') d\mathbf{r}' \right. \right. \\ \left. \left. + \sum_{n=N^{(2)+1}}^{\infty} Y_n^{(2)} \iint_{S_a} \mathbf{m}_m^{(1)}(\mathbf{r}') \cdot \mathbf{h}_n^{(2)}(\mathbf{r}_t) \mathbf{h}_n^{(2)*}(\mathbf{r}') d\mathbf{r}' \right) \right] - \\ \sum_{m=1}^{N^{(2)}} I_m^{(2)} \left[\mathbf{h}_n^{(2)}(\mathbf{r}_t) - \left(\sum_{n=N^{(1)+1}}^{\infty} Y_n^{(1)} \iint_{S_a} \mathbf{m}_m^{(2)}(\mathbf{r}') \cdot \mathbf{h}_n^{(1)}(\mathbf{r}_t) \mathbf{h}_n^{(1)*}(\mathbf{r}') d\mathbf{r}' + \right. \right. \\ \left. \left. \sum_{n=N^{(2)+1}}^{\infty} Y_n^{(2)} \iint_{S_a} \mathbf{m}_m^{(2)}(\mathbf{r}') \cdot \mathbf{h}_n^{(2)}(\mathbf{r}_t) \mathbf{h}_n^{(2)*}(\mathbf{r}') d\mathbf{r}' \right) \right] = 0, \quad (2.12) \\ \mathbf{r}_t \in S_a, \quad \forall \{I_n^{(\delta)} | 1 < n < N^{(\delta)}, \delta = 1, 2\}, \end{aligned}$$

where the domain of integration is now restricted to the common aperture area S_a , since the tangential electric field $\mathbf{E}_t(\mathbf{r})$ vanishes on the metal wall S_c .

This system of linear equations has the form $\sum_j A_{ij} x_j = 0$. A result of functional algebra ensures that $A_{ij} = 0 \quad \forall (i, j)$ if and only if the equation holds for every possible combination of x_j . In our case, the x_j can be identified with the modal currents $I_m^{(\delta)}$, $m = 1, \dots, N^{(\delta)}$, where the index j corresponds to the double index (m, δ) , the terms A_{ij} are the coefficients of these modal currents, $\mathbf{m}_m^{(\delta)}(\mathbf{r}_t)$, and the index i corresponds to the spatial dependence \mathbf{r}_t . Since the $I_m^{(\delta)}$ are the fundamental unknowns of our problem, the mentioned condition is certainly satisfied and the only solution of Eq. (2.12) can be obtained by equating the

coefficients of $I_m^{(1)}$ and $I_m^{(2)}$ separately to zero. This leads to one IE, with fixed kernel and multiple forcing terms corresponding to the accessible modes in the two waveguides:

$$\mathbf{h}_n^{(\delta)}(\mathbf{r}_t) = \iint_{S_a} \mathbf{m}_n^{(\delta)}(\mathbf{r}'_t) \cdot \left[\sum_{m=N^{(1)}+1}^{\infty} Y_m^{(1)} \mathbf{h}_m^{(1)}(\mathbf{r}_t) \mathbf{h}_m^{(1)*}(\mathbf{r}'_t) + \sum_{m=N^{(2)}+1}^{\infty} Y_m^{(2)} \mathbf{h}_m^{(2)}(\mathbf{r}_t) \mathbf{h}_m^{(2)*}(\mathbf{r}'_t) \right] d\mathbf{r}'_t, \quad \mathbf{r}_t \in S_a. \quad (2.13)$$

The kernel of this equation depends only on the localized modes and it is therefore indicated as *reduced kernel integral equation*. We would like to stress once more that the result in (2.13) constitutes the peculiarity of the IEMEN method with respect to other approaches. In [20], Bhattacharyaa formalizes the waveguide junction problem through an IE with reduced kernel, from which he derives a GSM representation involving only the accessible modes, is derived. However, in [20] the unknown scattered field is expressed in terms of the all modal amplitudes (those of the accessible incident modes and those of all the reflected modes). As a consequence, the obtained IE contains all the accessible modes in both regions and it is not possible to separately consider their contribution. Instead, the IEMEN method, by introducing the concept of fundamental unknowns, resorts to a single IE with a fixed kernel and with a different forcing term for each accessible mode; the application of the MoM results then in a fixed system of linear equations with multiple right-hand sides, whose solution is therefore very fast. Moreover, the number of matrix operations required to derive the equivalent network of a waveguide junction is smaller when using the IEMEN method (only one matrix inversion has to be performed with the IEMEN approach, while four inversions are required with the method in [20]).

A further feature of the IEMEN approach is that, since the IE has different forcing terms, associated to different accessible modes, it can be solved by using a different set of expansion functions for each mode. This property will turn out to be particularly convenient when applying the IEMEN method to the analysis of FSS's, as it will be further discussed in Chapter 6.

Equivalent Network If we recall the definition of modal voltage amplitudes (2.11), we can now introduce a network formalism:

$$\begin{aligned} V_m^{(\gamma)}(z=0) &= \iint_{S_a} \left[\sum_{n=1}^{N^{(1)}} I_n^{(1)} \mathbf{m}_n^{(1)}(\mathbf{r}'_t) - \sum_{n=1}^{N^{(2)}} I_n^{(2)} \mathbf{m}_n^{(2)}(\mathbf{r}'_t) \right] \cdot \mathbf{h}_m^{(\gamma)*}(\mathbf{r}'_t) d\mathbf{r}'_t \\ &= \sum_{n=1}^{N^{(1)}} I_n^{(1)} Z_{m,n}^{(\gamma,1)} - \sum_{n=1}^{N^{(2)}} I_n^{(2)} Z_{m,n}^{(\gamma,2)}, \end{aligned} \quad (2.14)$$

where

$$Z_{m,n}^{(\gamma,\delta)} = \iint_{S_a} \mathbf{m}_n^{(\delta)}(\mathbf{r}'_t) \cdot \mathbf{h}_m^{(\gamma)*}(\mathbf{r}'_t) d\mathbf{r}'_t, \quad (2.15)$$

is the *multimode impedance matrix* of the transition. Equation (2.13) together with (2.15) provides the description of the scattering problem at the junction in terms of a multimode equivalent network, (analogous to the one shown in Fig. 2.3 but with $N^{(1)}$ inputs and $N^{(2)}$ outputs only), since the network parameters completely describe the field behavior at the junction plane in Fig. 2.2.

Note that, because of the choice made in Eq. (2.10) for the positive direction of the wave ingoing and outgoing the two waveguides, the currents in the equivalent network would be entering the input ports and leaving the output ports. However, the definition of the tangential electric field in Eq. (2.5) corresponds to a change in the sign of the output currents, which become ingoing in the description of the equivalent network's terminal conditions (2.14), as it is usual in microwave network formalism.

Solution of the IE with extraction of the frequency dependence

The IE (2.13) is solved with the aid of the Method of Moments (MoM) [66]. The unknown functions are expanded in terms of the first N_f vector mode functions of the smaller of the two rectangular waveguides, which are real valued ($\mathbf{h}_m^{(2)} = \mathbf{h}_m^{(2)*}$):

$$\mathbf{m}_n^{(\delta)}(\mathbf{r}_t) = \sum_{i=1}^{N_f} \alpha_{i,n}^{(\delta)} \mathbf{h}_i^{(\delta)}(\mathbf{r}_t). \quad (2.16)$$

In the case of an X-junction, the modes of a waveguide having as cross section the common intersection between the two waveguides are used as basis functions. The test functions are chosen equal to the basis functions (Galerkin's procedure).

We shall now consider the last two series in the kernel of the IE (2.13):

$$\sum_{m=N^{(\delta)}+1}^{\infty} Y_m^{(\delta)} \mathbf{h}_m^{(\delta)}(\mathbf{r}_t) \mathbf{h}_m^{(\delta)*}(\mathbf{r}'_t), \quad \delta = 1, 2. \quad (2.17)$$

The application of the Galerkin procedure to solve the IE, using the first N_f modes of the smaller waveguide $\mathbf{h}_i^{(1)*}(\mathbf{r}_t)$, would change these series into:

$$\sum_{m=N^{(\delta)}+1}^{\infty} Y_m^{(\delta)} \int \int_{S_a} \mathbf{h}_m^{(\delta)}(\mathbf{r}_t) \cdot \mathbf{h}_i^{(1)*}(\mathbf{r}_t) \int \int_{S_a} \mathbf{h}_n^{(1)}(\mathbf{r}'_t) \cdot \mathbf{h}_m^{(\delta)*}(\mathbf{r}'_t), \quad \delta = 1, 2, \quad (2.18)$$

where $i, n = 1, \dots, N_f$. For relatively large values of the number $N^{(\delta)}$ of accessible modes extracted from the IE kernel the behavior of the basis and test functions is very different from that of the localized modes in the kernel, which may lead to an instability problem. To circumvent this problem, we need to include in the kernel of (2.13) also terms behaving like the extracted accessible modes.

With this purpose, we shall go back to Eq. (2.10) and add to both sides the static series:

$$\sum_{n=1}^{\infty} V_n^{(1)} \hat{Y}_n^{(1)} \mathbf{h}_n^{(1)}(\mathbf{r}_t) + \sum_{n=1}^{\infty} V_n^{(2)} \hat{Y}_n^{(2)} \mathbf{h}_n^{(2)}(\mathbf{r}_t), \quad (2.19)$$

where $\hat{Y}_n^{(\delta)}$ with $\delta = 1, 2$ are the modal characteristic admittances evaluated in the quasi-static limit, for large values of the modal index n :

$$Y_n^{(\delta)} \stackrel{\text{a.e.}}{=} \hat{Y}_n^{(\delta)} = \hat{Y}_{-n}^{(\delta)} = \begin{cases} \frac{-j|k_{t_n}^{(\delta)}|}{\omega\mu} & , \text{ TE modes,} \\ \frac{\omega\varepsilon}{-j|k_{t_n}^{(\delta)}|} & , \text{ TM modes,} \end{cases} \quad n \rightarrow \infty, \quad (2.20)$$

where the symbol $\stackrel{\text{a.e.}}{=}$ means *asymptotically equal to* and where κ_{n_s} is the static modal propagation constant introduced in [88] and used also in [63]:

$$\kappa_n^{(\delta)} = \sqrt{k^{(\delta)} - k_{t_n}^{(\delta)}} \stackrel{\text{a.e.}}{=} -j|k_{t_n}^{(\delta)}| = \kappa_{n_s}^{(\delta)}, \quad n \rightarrow \infty, \quad \delta = 1, 2. \quad (2.21)$$

The modified current definitions:

$$\bar{I}_n^{(1)} = I_n^{(1)} + V_n^{(1)} \hat{Y}_n^{(1)}, \quad (2.22a)$$

$$\bar{I}_n^{(2)} = I_n^{(2)} - V_n^{(2)} \hat{Y}_n^{(2)}, \quad (2.22b)$$

are then introduced to make the notation more compact; their network interpretation is shown in Fig. 2.5.

The tangential electric field is redefined in terms of these new currents $\bar{I}_n^{(\delta)}$, $n = 1..N^{(\delta)}$ as:

$$\left(\mathbf{u}_z \times \mathbf{E}_t(\mathbf{r}) \right) = \sum_{m=1}^{N^{(1)}} \bar{I}_m^{(1)}(z) \mathbf{m}_m^{(1)}(\mathbf{r}_t) - \sum_{m=1}^{N^{(2)}} \bar{I}_m^{(2)}(z) \mathbf{m}_m^{(2)}(\mathbf{r}_t). \quad (2.23)$$

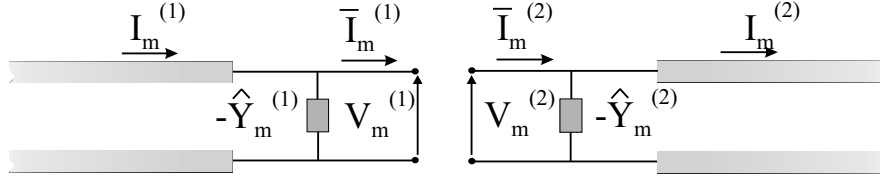


Figure 2.5: Network interpretation of the current definitions in Eq. (2.22).

This leads to the following IE:

$$\mathbf{h}_n^{(\delta)}(\mathbf{r}_t) = \iint_{S_a} \mathbf{m}_n^{(\delta)}(\mathbf{r}'_t) \cdot \left[\sum_{m=1}^{N^{(1)}} \hat{Y}_m^{(1)} \mathbf{h}_m^{(1)}(\mathbf{r}_t) \mathbf{h}_m^{(1)*}(\mathbf{r}'_t) + \sum_{m=N^{(1)+1}}^{\infty} Y_m^{(1)} \mathbf{h}_m^{(1)}(\mathbf{r}_t) \mathbf{h}_m^{(1)*}(\mathbf{r}'_t) \right. \\ \left. + \sum_{m=1}^{N^{(2)}} \hat{Y}_m^{(2)} \mathbf{h}_m^{(2)}(\mathbf{r}_t) \mathbf{h}_m^{(2)*}(\mathbf{r}'_t) + \sum_{m=N^{(2)+1}}^{\infty} Y_m^{(2)} \mathbf{h}_m^{(2)}(\mathbf{r}_t) \mathbf{h}_m^{(2)*}(\mathbf{r}'_t) \right] d\mathbf{r}'_t, \quad (2.24)$$

where $\mathbf{r}_t \in S_a$. The kernel contains now also two almost static series, which include contributions of the accessible modes in the two waveguides. Before proceeding to the solution, we would like to point out that the last two series in the kernel of Eqs. (2.24)

$$\sum_{m=N^{(\delta)+1}}^{\infty} Y_m^{(\delta)} \mathbf{h}_m^{(\delta)}(\mathbf{r}_t) \mathbf{h}_m^{(\delta)*}(\mathbf{r}'_t), \quad \delta = 1, 2, \quad (2.25)$$

depend on the frequency through the modal characteristic admittance $Y_m^{(\delta)}$ only, and are slowly converging. A way to accelerate the convergence is to apply a technique based on the Kummer transformation [2]. The basic idea consists in adding and subtracting from a given, slowly convergent series $\sum a_k$, its asymptotic form, which is another convergent series $\sum \hat{a}_k$ with known sum \hat{a} , such that:

$$\lim_{k \rightarrow \infty} \frac{a_k}{\hat{a}_k} = \lambda \neq 0. \quad (2.26)$$

The series $\sum a_k$ can then be rewritten as

$$\sum a_k = \lambda \hat{a} + \sum a_k \left(1 - \lambda \frac{\hat{a}_k}{a_k} \right), \quad (2.27)$$

where the series on the right-hand side converges faster than the original one.

The asymptotic form of the series (2.25) corresponds to its quasi-static limit, for large values of the modal index n . Therefore, since vector mode functions are frequency independent

in the case of waveguide modes, only the quasi-static limit of the modal characteristic admittances (2.8) has to be calculated according to Eq. (2.20). Let us evaluate the rate of convergence of the accelerated series, for a simple two-dimensional case, for example the case of a parallel-plate waveguide defined with respect to the x -axis. The modal admittance and its quasi-static version are such that:

$$\begin{aligned} Y_n &\propto \sqrt{k^2 - k_{t_n}^2} = \sqrt{k^2 - \left(\frac{n\pi}{a}\right)^2} = -j\frac{n\pi}{a} \sqrt{1 - \left(\frac{ka}{n\pi}\right)^2} \\ &= -j\frac{n\pi}{a} \left(1 - \frac{k}{2n^2} + O\left(\frac{1}{n^4}\right)\right), \end{aligned} \quad (2.28a)$$

$$\hat{Y}_n \propto -j\frac{n\pi}{a}, \quad (2.28b)$$

$$(Y_n - \hat{Y}_n) \propto j\frac{\pi}{a} \left(\frac{k}{2n} - O\left(\frac{1}{n^3}\right)\right). \quad (2.28c)$$

Therefore, the difference series converges faster than the original one by two orders of $1/n$. By introducing these definitions in the series (2.25), their asymptotic forms can be readily obtained:

$$\sum_{m=N^{(\delta)}+1}^{\infty} \hat{Y}_m^{(\delta)} \mathbf{h}_m^{(\delta)}(\mathbf{r}_t) \mathbf{h}_m^{(\delta)*}(\mathbf{r}'_t), \quad \delta = 1, 2. \quad (2.29)$$

The sum of this series is not analytically known. However, even in this case, the Kummer transformation can still be a convenient instrument to accelerate the convergence of a series, provided that the following two conditions are satisfied:

1. the sum of the series of the asymptotic terms (2.28b) should be relatively cheap to compute numerically, (only a few terms needed to extrapolate it, or the terms to be computed are very simple);
2. the number of terms (2.28c) summed in difference series to obtain convergence should be much smaller than the number of terms needed in the original series.

In the present case, it can be readily demonstrated that those conditions are satisfied for the series (2.29). In fact, after applying the Kummer transformation, the dyadic kernel of

Eqs. (2.24) becomes:

$$\begin{aligned}
\bar{\mathbf{K}}(\mathbf{r}_t, \mathbf{r}'_t) &= \sum_{m=1}^{\infty} \hat{Y}_m^{(1)} \mathbf{h}_m^{(1)}(\mathbf{r}_t) \mathbf{h}_m^{(1)*}(\mathbf{r}'_t) + \sum_{m=1}^{\infty} \hat{Y}_m^{(2)} \mathbf{h}_m^{(2)}(\mathbf{r}_t) \mathbf{h}_m^{(2)*}(\mathbf{r}'_t) \\
&- \sum_{m=N^{(1)}+1}^{\infty} \hat{Y}_m^{(1)} \left(1 - \frac{Y_m^{(1)}}{\hat{Y}_m^{(1)}} \right) \mathbf{h}_m^{(1)}(\mathbf{r}_t) \mathbf{h}_m^{(1)*}(\mathbf{r}'_t) \\
&- \sum_{m=N^{(2)}+1}^{\infty} \hat{Y}_m^{(2)} \left(1 - \frac{Y_m^{(2)}}{\hat{Y}_m^{(2)}} \right) \mathbf{h}_m^{(2)}(\mathbf{r}_t) \mathbf{h}_m^{(2)*}(\mathbf{r}'_t).
\end{aligned} \tag{2.30}$$

The first two terms can be considered static, because the admittances $\hat{Y}_m^{(\delta)}$ depend on the frequency only through a factor of $\omega = 2\pi f$ that can be accounted for at the end of the calculations. For the last two terms the following relation holds:

$$\left(1 - \frac{Y_m^{(\delta)}}{\hat{Y}_m^{(\delta)}} \right) \simeq \sum_{p=1}^P B_{(2p)} \left(\frac{k_0}{k_{t_m}^{(\delta)}} \right)^{(2p)}, \tag{2.31}$$

where the expansion coefficients B_p are tabulated in [36]. This expression is particularly convenient because only few terms need to be calculated to obtain an accurate result. The described procedure allows the extraction of the frequency dependence from the kernel, since it leads to the following quasi-static form, which depends on the frequency only through a factor ω :

$$\begin{aligned}
\bar{\mathbf{K}}(\mathbf{r}_t, \mathbf{r}'_t) &= \sum_{m=1}^{\infty} \hat{Y}_m^{(1)} \mathbf{h}_m^{(1)}(\mathbf{r}_t) \mathbf{h}_m^{(1)*}(\mathbf{r}'_t) + \sum_{m=1}^{\infty} \hat{Y}_m^{(2)} \mathbf{h}_m^{(2)}(\mathbf{r}_t) \mathbf{h}_m^{(2)*}(\mathbf{r}'_t) \\
&- \sum_{p=1}^P (k_0)^{2p} \cdot \left(\sum_{m=N^{(1)}+1}^{\infty} \frac{B_p}{(k_{t_m}^{(1)})^p} \hat{Y}_m^{(1)} \mathbf{h}_m^{(1)}(\mathbf{r}_t) \mathbf{h}_m^{(1)*}(\mathbf{r}'_t) \right. \\
&\quad \left. + \sum_{m=N^{(2)}+1}^{\infty} \frac{B_p}{(k_{t_m}^{(2)})^p} \hat{Y}_m^{(2)} \mathbf{h}_m^{(2)}(\mathbf{r}_t) \mathbf{h}_m^{(2)*}(\mathbf{r}'_t) \right) \\
&= \hat{\mathbf{K}}(\mathbf{r}_t, \mathbf{r}'_t) - \sum_{p=1}^P (k_0)^{2p} \check{\mathbf{K}}_{2p}(\mathbf{r}_t, \mathbf{r}'_t).
\end{aligned} \tag{2.32}$$

Introducing this kernel expression in the IE (2.13) and truncating the sum to a finite

number of terms, indicated with N_{ker} , results in

$$\mathbf{h}_n^{(\delta)}(\mathbf{r}_t) = \iint_{S_a} \mathbf{m}_n^{(\delta)}(\mathbf{r}'_t) \cdot \left[\sum_{\gamma=1}^2 \sum_{m=1}^{N_{ker}} \hat{Y}_m^{(\gamma)} \mathbf{h}_m^{(\gamma)}(\mathbf{r}_t) \mathbf{h}_m^{(\gamma)*}(\mathbf{r}'_t) - \sum_{p=1}^P (k_0)^{2p} \left(\sum_{\gamma=1}^2 \sum_{m=N(\gamma)+1}^{N_{ker}} \frac{B_p}{(k_{t_m}^{(\gamma)})^p} \hat{Y}_m^{(\gamma)} \mathbf{h}_m^{(\gamma)}(\mathbf{r}_t) \mathbf{h}_m^{(\gamma)*}(\mathbf{r}'_t) \right) \right] d\mathbf{r}'_t. \quad (2.33)$$

The application of the MoM with a Galerkin's procedure yields the system of linear equations:

$$\nu_{n,l}^{(\delta)} = \sum_{i=1}^{N_f} \eta_{l,i} \alpha_{i,n}^{(\delta)}, \quad (2.34)$$

where

$$\nu_{n,l}^{(\delta)} = \iint_{S_a} \mathbf{h}_n^{(\delta)} \cdot \mathbf{h}_l^{(2)*} d\mathbf{r}_t, \quad (2.35)$$

are the coupling integrals (known terms), while

$$\eta_{l,i} = \sum_{\gamma=1}^2 \sum_{m=1}^{N_{ker}} \hat{Y}_m^{(\gamma)} \nu_{m,l}^{(\gamma)} \nu_{i,m}^{(\gamma)} - \sum_{p=1}^P (k_0)^{2p} \left(\sum_{\gamma=1}^2 \sum_{m=N(\gamma)+1}^{N_{ker}} \frac{B_p}{(k_{t_m}^{(\gamma)})^p} \hat{Y}_m^{(\gamma)} \nu_{m,l}^{(\gamma)} \nu_{i,m}^{(\gamma)} \right), \quad (2.36)$$

is the generic element of the system's MoM matrix.

The corresponding multimode equivalent network is illustrated in Fig. 2.6, where the voltages are:

$$\begin{aligned} V_m^{(\gamma)}(z=0) &= \iint_{S_a} \left[\sum_{n=1}^{N^{(1)}} \bar{I}_n^{(1)} \mathbf{m}_n^{(1)}(\mathbf{r}'_t) - \sum_{n=1}^{N^{(2)}} \bar{I}_n^{(2)} \mathbf{m}_n^{(2)}(\mathbf{r}'_t) \right] \cdot \mathbf{h}_m^{(\gamma)*}(\mathbf{r}'_t) d\mathbf{r}'_t \\ &= \sum_{n=1}^{N^{(1)}} \bar{I}_n^{(1)} Z_{m,n}^{(\gamma,1)} - \sum_{n=1}^{N^{(2)}} \bar{I}_n^{(2)} Z_{m,n}^{(\gamma,2)}, \quad \gamma = 1, 2. \end{aligned} \quad (2.37)$$

Note again that the sign of the currents at the output ports of the network in Fig. 2.6 are opposite with respect to the signs in Fig. 2.5. The latter are coherent with the initial choice of positive direction as indicated in Fig. 2.4, but the use of the tangential electric field definition in Eq. (2.5) results in a change of sign of the output currents, which become outgoing according to Eq. (2.37).

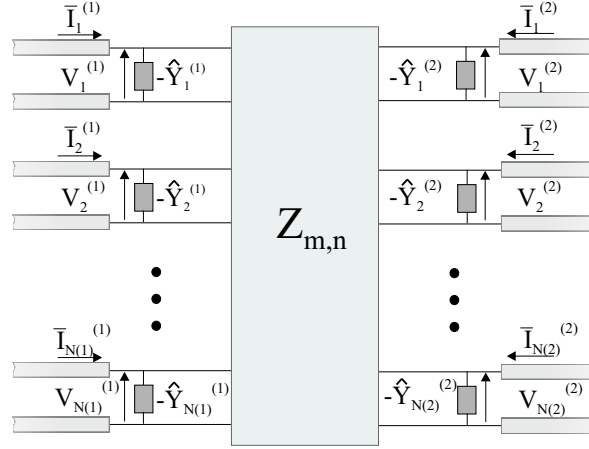


Figure 2.6: Multimode Equivalent Network for the waveguide junction in Fig. 2.2, derived using the IEMEN approach.

2.1.3 MEN of a rectangular waveguide section

Fig. 2.7a shows a rectangular waveguide of length ℓ and cross sectional dimension a and b with respect to the x and y axes of the indicated Cartesian reference system.

An uniform waveguide section can be represented in terms of an equivalent π -network, as indicated in Fig. 2.7b. The corresponding admittance values for the m -th mode are:

$$Y_{1m} = Y_{3m} = jY_m \tan\left(\frac{\kappa_m \ell}{2}\right), \quad (2.38a)$$

$$Y_{2m} = -jY_m \csc(\kappa_m \ell), \quad (2.38b)$$

where Y_m is the characteristic modal admittance of the m -th mode, as given by Eq. (2.8). The admittance in Eq. (2.38) are related to the parameters of the equivalent impedance matrix representations by [88]:

$$Z_m^{(1,1)} = (Y_{2m} + Y_{3m})/\Delta, \quad (2.39a)$$

$$Z_m^{(1,2)} = Z_m^{(2,1)} = Y_{2m}/\Delta, \quad (2.39b)$$

$$Z_m^{(2,2)} = (Y_{2m} + Y_{1m})/\Delta, \quad (2.39c)$$

where the denominator is defined as $\Delta = y_{1m}y_{2m} + y_{2m}y_{3m} + y_{1m}y_{3m}$. Note that the matrix representation of a uniform waveguide is always block diagonal because the modes do not interact while propagating inside a uniform waveguide.

The amplitudes of the current at the input and output ports of the impedance matrix describing a waveguide discontinuity in (Fig. 2.6) are defined as the summation of the

original modal current amplitude and of a static contribution, according to Eq. (2.22). However, when solving the problem of cascaded uniform waveguides, it is more convenient to include the static admittance in the network representation of the two uniform waveguide sections involved in a junction, instead of inserting it in the equivalent network of the junction itself.

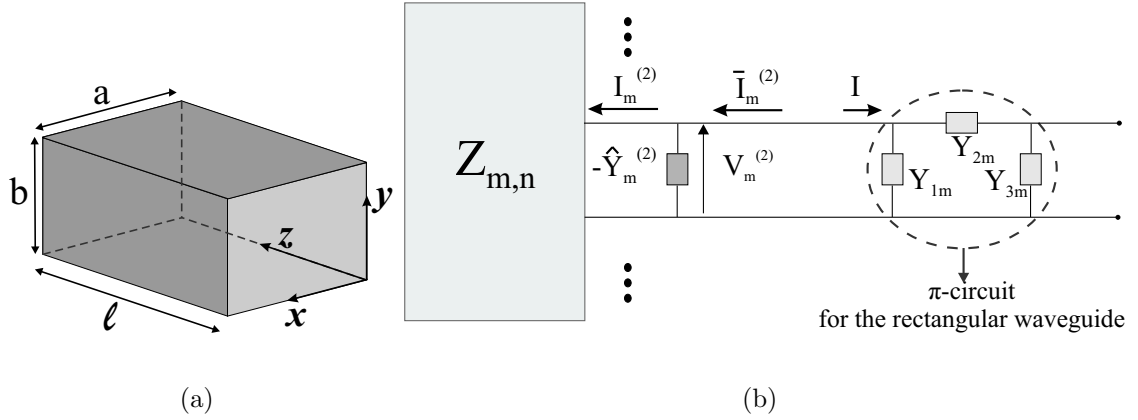


Figure 2.7: Section of a uniform waveguide. (a) Geometry. (b) Equivalent π -network.

Fig. 2.7b shows for example how the static admittance on the output ports of the the matrix $[Z]$, representing the equivalent circuit of a junction between uniform waveguides, is connected to the input ports of the π -circuit of the output waveguide. The input admittance value to be used is:

$$Y_{1m} = Y_{1m} - \hat{Y}_m. \quad (2.40)$$

The same observation holds for the output admittance of the π -circuit connected to the input port of the $[Z]$ matrix, which becomes:

$$Y_{3m} = Y_{3m} - \hat{Y}_m. \quad (2.41)$$

2.1.4 MEN of a cascade of uniform waveguides

The matrix representation of a cascade of N waveguides can be derived by means of different techniques. The technique presented in [27] for GAM representations (which can easily be extended to the case of GIM representations), results in a banded linear system of $2N$ equations. This is here briefly described for a simple case, consisting of the

cascade of three waveguides, which are indicated in Fig. 2.8 as $(TL1)$, $(TL2)$ and $(TL3)$. The waveguide $(TL1)$ is excited with its fundamental mode, with current amplitude $I_{TL1}^{(1)}$, while all the other modes are closed with their characteristic impedances. The network is loaded with the characteristic impedance of each mode of the output waveguide.

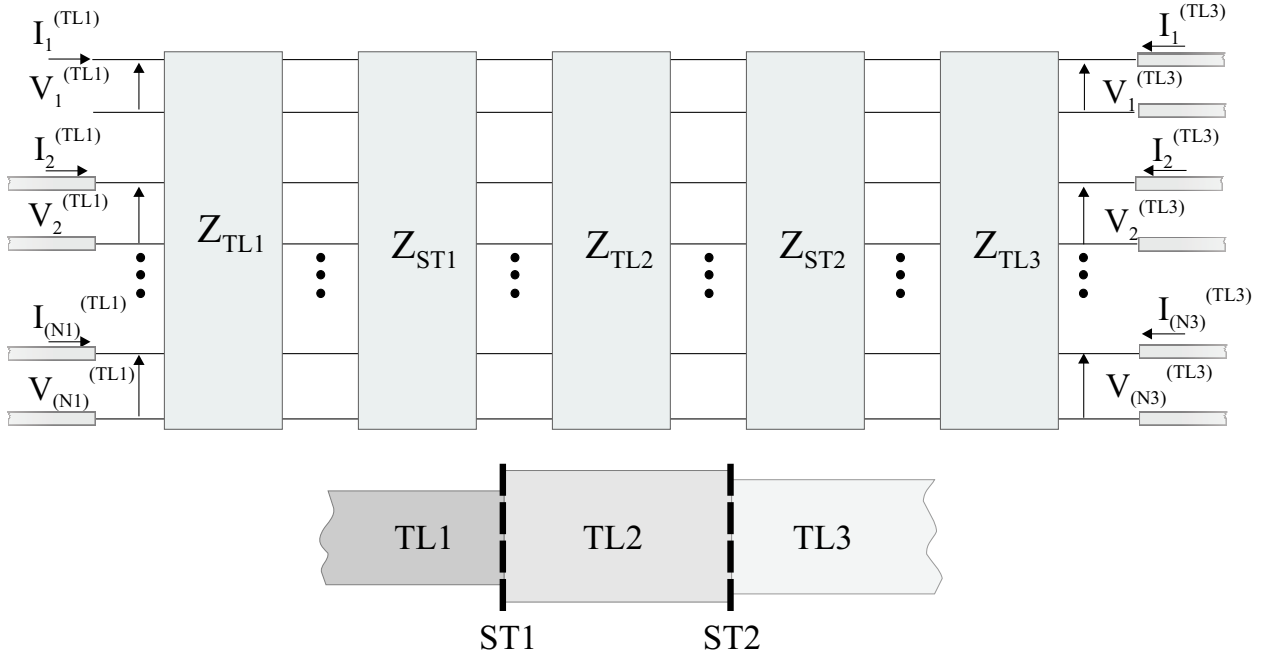


Figure 2.8: MEN for the cascade of three waveguides.

The equivalent impedance matrix of the i -th waveguide has been indicated with Z_{TLi} and the equivalent impedance matrix of the j -th waveguide step with Z_{STj} . It should be noted that, in this representation, the static admittances are not explicitly indicated, because they are included in the impedance matrix representation of each uniform waveguide section, as described in Sec. 2.1.3. Forcing the continuity conditions for voltages and currents at the junctions, leads to a banded linear system of six vectorial equations:

$$\left\{ \begin{array}{l} (Z_{TL1}^{(1,1)} + Z_{01}) \cdot Y_{TL1}^{(1)} + Z_{TL1}^{(1,2)} \cdot Y_{TL1}^{(2)} = I^{(1)}, \\ Z_{TL1}^{(2,1)} \cdot Y_{TL1}^{(1)} + (Z_{TL1}^{(2,2)} + Z_{ST1}^{(1,1)}) \cdot Y_{TL1}^{(2)} + Z_{ST1}^{(1,2)} \cdot Y_{TL2}^{(1)} = 0^{(1)}, \\ Z_{ST1}^{(2,1)} \cdot Y_{TL1}^{(2)} + (Z_{ST1}^{(2,2)} + Z_{TL2}^{(1,1)}) \cdot Y_{TL2}^{(1)} + Z_{TL2}^{(1,2)} \cdot Y_{TL2}^{(2)} = 0^{(2)}, \\ Z_{TL2}^{(2,1)} \cdot Y_{TL2}^{(1)} + (Z_{TL2}^{(2,2)} + Z_{ST2}^{(1,1)}) \cdot Y_{TL2}^{(2)} + Z_{ST2}^{(1,2)} \cdot Y_{TL3}^{(1)} = 0^{(2)}, \\ Z_{ST2}^{(2,1)} \cdot Y_{TL2}^{(2)} + (Z_{ST2}^{(2,2)} + Z_{TL3}^{(1,1)}) \cdot Y_{TL3}^{(1)} + Z_{TL3}^{(1,2)} \cdot Y_{TL3}^{(2)} = 0^{(3)}, \\ Z_{TL3}^{(2,1)} \cdot Y_{TL3}^{(1)} + (Z_{TL3}^{(2,2)} + Z_{03}) \cdot Y_{TL3}^{(2)} = 0^{(3)}, \end{array} \right. \quad (2.42)$$

where $I^{(1)}$ is a vector of dimension equal to the number of accessible modes in the first

waveguide, with all zero elements except for the first element, which is equal to 1; Z_{01} is a diagonal square matrix in which the first element is zero and the others are the characteristic impedances of the accessible modes of the first waveguide; $0^{(i)}$ is a null vector of dimension equal to the number of accessible modes in the i -th waveguide; Z_{03} is a diagonal square matrix containing the characteristic impedances of the accessible modes of the first and the last waveguide; $Y_{TLi}^{(\gamma)}$ (where $\gamma = 1, 2$ correspond to the input and output quantities) is an unknown vector whose elements are defined with respect to the voltage amplitudes of the accessible modes on the first waveguide (forcing terms): $Y_{TLi}^{(\gamma)} = I_{TLi}^{(\gamma)} / V_{TL1}^{(1)}$. The matrix of the system is a block diagonal matrix, where each block represents either a junction or a uniform waveguide section. The derivation of the matrix is illustrated in Fig. 2.9.

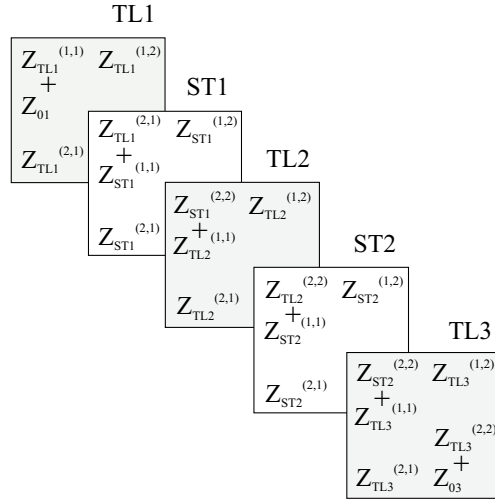


Figure 2.9: Derivation of the total equivalent impedance matrix for the cascade of three waveguides in Fig. 2.8.

From the sixth equation of the system (2.42) we obtain:

$$Y_{TL3}^{(2)} = -Z'_6 \cdot Y_{TL3}^{(1)}, \quad (2.43)$$

where

$$Z'_6 = (Z_{TL3}^{(2,2)} + Z_{03})^{-1} \cdot Z_{TL3}^{(2,1)}. \quad (2.44)$$

In Z'_α the subscript α indicates the number of the equation in the system (2.42) from which Z' is calculated. Substituting these expressions in the fifth equation of the system (2.42) leads to:

$$Y_{TL3}^{(1)} = -Z'_5 \cdot Y_{TL2}^{(2)}, \quad (2.45)$$

with

$$Z'_5 = (Z_{ST2}^{(2,2)} + Z_{TL3}^{(1,1)} - Z_{TL3}^{(1,2)} \cdot Z'_6)^{-1} \cdot Z_{ST2}^{(2,1)}. \quad (2.46)$$

Using a standard recursive solution procedure, we repeat this calculation to obtain all unknown values $Y_{TLi}^{(\gamma)}$.

This solution technique has been compared in [27] with the standard Gaussian elimination procedure and with the method of reduction to a single admittance matrix introduced in [112] for GSM representations. Considering the cascade of N waveguides, it results that the reduction technique requires $6(2N-2)$ matrix multiplications and $2N-1$ matrix inversions, while the recursive technique adopted here requires $3(2N-1)$ matrix multiplications and $2N$ matrix inversions. The maximum dimension of the blocks to be inverted corresponds to the maximum number of accessible modes considered for the three waveguides. Moreover, in the implementation described in [27], the used CPU time with the Gaussian method was one and half time longer than with the recursive method.

2.2 Multimode equivalent network formulation for infinite periodic arrays

In this thesis we will concentrate on the analysis of infinitely extended periodic structures. In fact, if an array is well designed, only the fundamental Floquet mode is propagating and the next higher-order mode is far from cut-off for all the scan angles of interest. In this case, for a large array (at least 10×10 elements), with maximum bandwidth of about 30%, the analysis of the corresponding infinite array is sufficient to retrieve its relevant behavior in terms of the input impedance [102, 103]. For example, the phased array antennas used for military ship radars fall onto this category. In the case of arrays with larger bandwidth, as for example the Square Kilometer Array under development for astronomical applications, for very low frequencies at the extreme of its operating bandwidth, the effect of the edges cannot be neglected [38]. However, also in this case, the infinite array approximation would fail only when the antenna is almost outside its operating range. The finiteness effects, instead, should always be taken into account when calculating the radiation pattern, although this could be done by simply applying windowing techniques.

Therefore, for well designed, large, narrow band arrays, the computational effort required to include the effect of the edges in full-wave calculations is often way too heavy with respect to the gain of information. The main advantage of treating infinitely extended periodic arrays is that the application of the Bloch-Floquet theorem [26, 49] leads to a

representation of the electromagnetic field radiated by the array in terms of Floquet modes (Appendix B). In particular, according to [44, 88], free-space propagation in proximity of the array can be treated as propagation in a uniform waveguide, infinitely extended, having cross sectional dimensions equal to those of the array unit cell. Because of the periodic boundary conditions dictated by the phased array, the electric and magnetic fields in all the unit cells have the same amplitude and differ by a phase shift. For broadside radiation, the unit cell waveguide is bounded by electric and magnetic walls while, when the array is scanned, opposite walls present a phase difference associated to the scan angle. For this reason, the unit cell waveguide is referred to as Phase Shift Wall Waveguide (PSWW). Based on this concept, in [44] the problem of a waveguide phased array radiating in free space was formulated as a junction problem between the array waveguide and the unit cell waveguide, resorting to an equivalent circuit for the only fundamental propagating Floquet mode. Afterwards, a multimode admittance network representation was derived for a metal grating under plane-wave incidence, in free space [109] and placed at a dielectric interface [63]. In [75], this representation was extended to the case of more than one strip in the grating unit cell. A GAM formalism was also used in [144], where the *direct method*, originally introduced in [90] for waveguide junctions, was extended to the case of planar phased array radiating in free space. The problem of scattering from an infinite periodic distribution of radiating elements has been tackled also by using GSM representations and the interested reader can find many references in [37, 94, 106]. All these methods resorted to an equivalent network with a large number of ports. To obtain a representation reduced to the accessible modes, the IEMEN method, which was already applied to cylindrical geometries in [55, 56], has been extended in this thesis to the analysis of planar waveguide phased arrays.

2.2.1 MEN of the junction waveguide-PSWW

The multimode equivalent network representation for the junction between a rectangular waveguide and a PSWW shown in Fig. 2.10 can be derived by following the same procedure described in Sec. 2.1.2 for the junction between two standard uniform waveguides. In the present case, however, the Floquet modes transverse wavenumber is frequency dependent and, therefore, the extraction of the frequency dependence can only be partially performed. Let us consider the boundary condition for the tangential magnetic field at the transition between waveguide and free space:

$$\sum_{n=1}^{\infty} I_n^{(1)} \mathbf{h}_n^{(1)}(\mathbf{r}_t) = \sum_{n=1}^{\infty} I_n^{(2)} \mathbf{h}_n^{(2)}(\mathbf{r}_t), \quad \mathbf{r}_t \in S_w, \quad (2.47)$$

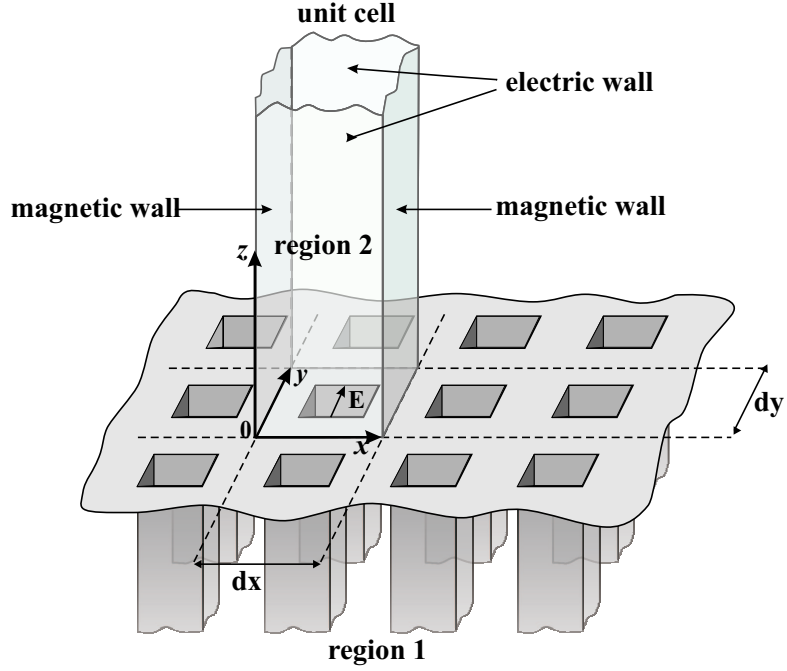


Figure 2.10: Geometry of the junction between the rectangular waveguide of a phased array and a Phase Shift Wall Waveguide.

where now we indicate with $\mathbf{h}_n^{(2)}(\mathbf{r}_t)$ the Floquet magnetic vector mode functions and S_w is the area of the waveguide aperture. Separating accessible and localized modes leads to

$$\sum_{n=1}^{N^{(1)}} I_n^{(1)} \mathbf{h}_n^{(1)}(\mathbf{r}_t) - \sum_{n=1}^{N^{(2)}} I_n^{(2)} \mathbf{h}_n^{(2)}(\mathbf{r}_t) = \sum_{n=N^{(1)+1}}^{\infty} V_n^{(1)} Y_n^{(1)} \mathbf{h}_n^{(1)}(\mathbf{r}_t) + \sum_{n=N^{(2)+1}}^{\infty} V_n^{(2)} Y_n^{(2)} \mathbf{h}_n^{(2)}(\mathbf{r}_t), \quad (2.48)$$

where $\mathbf{r}_t \in S_w$. By proceeding analogously to the derivation given in Sec. 2.1.2 for a waveguide junction, we would obtain one IE similar to Eq. (2.13). To improve the stability in the kernel calculation, it is useful, also in this case, to first add and subtract the static terms

$$\sum_{n=1}^{\infty} V_n^{(1)} \hat{Y}_n^{(1)} \mathbf{h}_n^{(1)}(\mathbf{r}_t), \quad (2.49)$$

from Eq. (2.48), which becomes

$$\begin{aligned} \sum_{n=1}^{N^{(1)}} \bar{I}_n^{(1)} \mathbf{h}_n^{(1)}(\mathbf{r}_t) - \sum_{n=1}^{N^{(2)}} I_n^{(2)} \mathbf{h}_n^{(2)}(\mathbf{r}_t) &= \sum_{n=1}^{N^{(1)}} V_n^{(1)} \hat{Y}_n^{(1)} \mathbf{h}_n^{(1)}(\mathbf{r}_t) + \sum_{n=N^{(1)}+1}^{\infty} V_n^{(1)} Y_n^{(1)} \mathbf{h}_n^{(1)}(\mathbf{r}_t) \\ &+ \sum_{n=N^{(2)}+1}^{\infty} V_n^{(2)} Y_n^{(2)} \mathbf{h}_n^{(2)}(\mathbf{r}_t), \quad \mathbf{r}_t \in S_w, \end{aligned} \quad (2.50)$$

where we have introduced the modified current definition:

$$\bar{I}_n^{(1)} = I_n^{(1)} + V_n^{(1)} \hat{Y}_n^{(1)}. \quad (2.51)$$

The fundamental unknowns of this problem are identified in the modal currents associated to the accessible modes of both waveguides and, for the array waveguide, they are defined as in Eq. (2.51). On account of the linearity of Maxwell's equations, the unknown tangential electric field at the interface can be then expressed as:

$$\left(\mathbf{u}_z \times \mathbf{E}_t(\mathbf{r}) \right) = \sum_{m=1}^{N^{(1)}} \bar{I}_m^{(1)}(z) \mathbf{m}_m^{(1)}(\mathbf{r}_t) - \sum_{m=1}^{N^{(2)}} I_m^{(2)}(z) \mathbf{m}_m^{(2)}(\mathbf{r}_t). \quad (2.52)$$

The corresponding modal voltages are derived by substituting this expression in (2.11). Introducing these voltages in Eq. (2.50) and equating the coefficients of the modal currents as explained in Sec. 2.1.2, leads to the following IE:

$$\begin{aligned} \mathbf{h}_n^{(\delta)}(\mathbf{r}_t) &= \iint_{S_w} \mathbf{m}_n^{(\delta)}(\mathbf{r}') \cdot \left[\sum_{m=1}^{N^{(1)}} \hat{Y}_m^{(1)} \mathbf{h}_m^{(1)}(\mathbf{r}_t) \mathbf{h}_m^{(1)*}(\mathbf{r}') + \sum_{m=N^{(1)}+1}^{\infty} Y_m^{(1)} \mathbf{h}_m^{(1)}(\mathbf{r}_t) \mathbf{h}_m^{(1)*}(\mathbf{r}') \right. \\ &\left. + \sum_{m=N^{(2)}+1}^{\infty} Y_m^{(2)} \mathbf{h}_m^{(2)}(\mathbf{r}_t) \mathbf{h}_m^{(2)*}(\mathbf{r}') \right] d\mathbf{r}', \quad \mathbf{r}_t \in S_w, \end{aligned} \quad (2.53)$$

which has a fixed kernel and multiple forcing terms, consisting of the accessible modes in the array and in the unit-cell waveguides. Let us now have a closer look at the dyadic kernel of this IE:

$$\begin{aligned} \bar{\mathbf{K}}(\mathbf{r}_t, \mathbf{r}'_t) &= \left[\sum_{m=1}^{N^{(1)}} \hat{Y}_m^{(1)} \mathbf{h}_m^{(1)}(\mathbf{r}_t) \mathbf{h}_m^{(1)*}(\mathbf{r}'_t) + \sum_{m=N^{(1)}+1}^{\infty} Y_m^{(1)} \mathbf{h}_m^{(1)}(\mathbf{r}_t) \mathbf{h}_m^{(1)*}(\mathbf{r}'_t) \right. \\ &\left. + \sum_{m=N^{(2)}+1}^{\infty} Y_m^{(2)} \mathbf{h}_m^{(2)}(\mathbf{r}_t) \mathbf{h}_m^{(2)*}(\mathbf{r}'_t) \right]. \end{aligned} \quad (2.54)$$

The third series depends on the frequency not only through the modal admittance but also through the Floquet vector mode functions $\mathbf{h}_m^{(2)}$. Therefore, the frequency extraction technique, described in Sec. 2.1.2 for the problem of waveguide junction, and consisting in applying the Kummer transformation and in exploiting the result (2.31) to express the obtained difference term, can be used here only for the second series in (2.54). This leads to the following expression:

$$\begin{aligned} \bar{\mathbf{K}}(\mathbf{r}_t, \mathbf{r}'_t) &= \sum_{m=1}^{\infty} \hat{Y}_m^{(1)} \mathbf{h}_m^{(1)}(\mathbf{r}_t) \mathbf{h}_m^{(1)*}(\mathbf{r}'_t) - \sum_{p=1}^P (k_0)^{2p} \sum_{m=N^{(1)}+1}^{\infty} \frac{B_p}{(k_{t_m}^{(1)})^p} \hat{Y}_m^{(1)} \mathbf{h}_m^{(1)}(\mathbf{r}_t) \mathbf{h}_m^{(1)*}(\mathbf{r}'_t) \\ &\quad + \sum_{m=N^{(2)}+1}^{\infty} Y_m^{(2)} \mathbf{h}_m^{(2)}(\mathbf{r}_t) \mathbf{h}_m^{(2)*}(\mathbf{r}'_t) \\ &= \hat{\mathbf{K}}(\mathbf{r}_t, \mathbf{r}'_t) - \sum_{p=1}^P (k_0)^{2p} \check{\mathbf{K}}_{2p}(\mathbf{r}_t, \mathbf{r}'_t) + \sum_{m=N^{(2)}+1}^{\infty} Y_m^{(2)} \mathbf{h}_m^{(2)}(\mathbf{r}_t) \mathbf{h}_m^{(2)*}(\mathbf{r}'_t). \end{aligned} \quad (2.55)$$

Nevertheless, the Kummer transformation can also be separately applied to accelerate the third series in the kernel (2.54). The asymptotic form of this series in the quasi-static limit is:

$$\sum_{m=N^{(2)}+1}^{\infty} \hat{Y}_m^{(2)} \hat{\mathbf{h}}_m^{(2)}(\mathbf{r}_t) \hat{\mathbf{h}}_m^{(2)*}(\mathbf{r}'_t) = \tilde{\mathbf{K}}(\mathbf{r}_t, \mathbf{r}'_t), \quad (2.56)$$

where the admittance $\hat{Y}_m^{(2)}$ is

$$Y_m^{(2)} \stackrel{\text{a.e.}}{=} \hat{Y}_m^{(2)} = \hat{Y}_{-m}^{(2)} = \begin{cases} \frac{-j|\hat{k}_{t_m}^{(2)}|}{\omega\mu} & , \text{ TE modes,} \\ \frac{\omega\varepsilon}{-j|\hat{k}_{t_m}^{(2)}|} & , \text{ TM modes,} \end{cases} \quad m \rightarrow \infty, \quad (2.57)$$

where the static modal propagation constant for the m -th Floquet mode, identified by the pair of integer (p, q) can be obtained from Eq. (B.25) of Appendix B:

$$\hat{k}_{x_m} = -\frac{2\pi p}{d_1}, \quad (2.58a)$$

$$\hat{k}_{y_m} = \frac{2\pi p}{d_1 \tan \Omega} - \frac{2\pi q}{d_2 \sin \Omega}, \quad (2.58b)$$

$$\hat{k}_{t_m} = \sqrt{\hat{k}_{x_m}^2 + \hat{k}_{y_m}^2} = \sqrt{\left(-\frac{2\pi p}{d_1}\right)^2 + \left(\frac{2\pi p}{d_1 \tan \Omega} - \frac{2\pi q}{d_2 \sin \Omega}\right)^2}. \quad (2.58c)$$

The vector functions $\hat{\mathbf{h}}_m^{(2)}(\mathbf{r}'_t)$ are the quasi-static forms of the Floquet vector mode functions for the magnetic field given in Eqs. (B.29b) and (B.31b) for TM and TE modes, respectively,

defined by:

$$\hat{\mathbf{h}}_m(\mathbf{r}_t) = \frac{1}{\hat{k}_{t_m}} \frac{1}{\sqrt{d_1 d_2 \sin \Omega}} (-\hat{k}_{y_m} \mathbf{u}_x + \hat{k}_{x_m} \mathbf{u}_y) e^{-j(\hat{k}_{x_m} x + \hat{k}_{y_m} y)} \quad \text{TM modes,} \quad (2.59a)$$

$$\hat{\mathbf{h}}_m(\mathbf{r}_t) = \frac{1}{\hat{k}_{t_m}} \frac{1}{\sqrt{d_1 d_2 \sin \Omega}} (\hat{k}_{x_m} \mathbf{u}_x + \hat{k}_{y_m} \mathbf{u}_y) e^{-j(\hat{k}_{x_m} x + \hat{k}_{y_m} y)} \quad \text{TE modes.} \quad (2.59b)$$

Adding and subtracting the static term in Eq. (2.56) from the kernel $\bar{\mathbf{K}}(\mathbf{r}_t, \mathbf{r}'_t)$ in Eq. (2.55) results in

$$\begin{aligned} \bar{\mathbf{K}}(\mathbf{r}_t, \mathbf{r}'_t) &= \hat{\mathbf{K}}(\mathbf{r}_t, \mathbf{r}'_t) + \check{\mathbf{K}}(\mathbf{r}_t, \mathbf{r}'_t) - \sum_{p=1}^P (k_0)^{2p} \check{\mathbf{K}}_{2p}(\mathbf{r}_t, \mathbf{r}'_t) \\ &\quad - \sum_{m=N^{(2)}+1}^{\infty} \left(\hat{Y}_m^{(2)} \hat{\mathbf{h}}_m^{(2)}(\mathbf{r}_t) \hat{\mathbf{h}}_m^{(2)*}(\mathbf{r}'_t) - Y_m^{(2)} \mathbf{h}_m^{(2)}(\mathbf{r}_t) \mathbf{h}_m^{(2)*}(\mathbf{r}'_t) \right), \end{aligned} \quad (2.60)$$

where the terms $\hat{\mathbf{K}}$, $\check{\mathbf{K}}_{2p}$, $\check{\mathbf{K}}$ and the coupling integrals in the first term of the last series can be calculated outside the frequency loop. The coupling integrals in the last term of Eq. (2.60) are frequency dependent and their sum has to be calculated inside the frequency loop, but the difference between each coupling integral and its asymptotic form converges faster than in the original expression (2.55). The kernel of the IE (2.53) now contains a static and a dynamic part, which have to be calculated separately. Since the vector mode functions are ordered with respect to their cut-off wavenumber, the identification of the accessible modes, which is based on the same parameter, depends on the frequency. To calculate the static part of the kernel, the modes are ordered at a fixed frequency, for example the center of the frequency range that we want to study, while, to calculate the dynamic part, they are reordered for every frequency point in the range. Consequently, the number and type of modal contributions required to calculate the sum of the static series with the desired accuracy is in general different than that required to calculate the sum of the dynamic series with the same accuracy.

If the problem is solved in only one frequency point, the mode ordering used to calculate the static and dynamic part of the kernel is the same. Instead, if the analysis of the transition is performed over a wide frequency range, we should expect that the modes involved in the calculation of the static part of the kernel, ordered at the central frequency of the range, are different from those contributing to the dynamic part, which are recalculated at every frequency point. The same kind of problem arises when the array is scanned in a certain range of angles. In this case, to be able to include the same accessible modes in the static and dynamic parts of the kernel, the modes should be reordered for every frequency and scan angle, also in the calculation of the static term; the acceleration technique would

become useless, though. To circumvent this problem, if the frequency or angle range of study is too wide with respect to the dynamic of the Floquet modes, this range is split into smaller bands, where the ordering of the modes does not change significantly. The width of the band depends on the maximum relative error on the approximated result that we are willing to accept.

Introducing the kernel expression (2.60) into the IE (2.53), we obtain

$$\begin{aligned} \mathbf{h}_n^{(\delta)}(\mathbf{r}_t) = & \iint_{S_w} \mathbf{m}_n^{(\delta)}(\mathbf{r}'_t) \cdot \left[\sum_{m=1}^{N_{ker}} \hat{Y}_m^{(1)} \mathbf{h}_m^{(1)}(\mathbf{r}_t) \mathbf{h}_m^{(1)*}(\mathbf{r}'_t) + \sum_{m=N^{(2)+1}}^{N_{kerf}} \hat{Y}_m^{(2)} \hat{\mathbf{h}}_m^{(2)}(\mathbf{r}_t) \hat{\mathbf{h}}_m^{(2)*}(\mathbf{r}'_t) \right. \\ & - \sum_{p=1}^P (k_0)^{2p} \sum_{m=N^{(1)+1}}^{N_{ker}} \frac{B_p}{(k_{t_m}^{(1)})^p} \hat{Y}_m^{(1)} \mathbf{h}_m^{(1)}(\mathbf{r}_t) \mathbf{h}_m^{(1)*}(\mathbf{r}'_t) \\ & \left. - \sum_{m=N^{(2)+1}}^{N_{kerf}} \left(\hat{Y}_m^{(2)} \hat{\mathbf{h}}_m^{(2)}(\mathbf{r}_t) \hat{\mathbf{h}}_m^{(2)*}(\mathbf{r}'_t) - Y_m^{(2)} \mathbf{h}_m^{(2)}(\mathbf{r}_t) \mathbf{h}_m^{(2)*}(\mathbf{r}'_t) \right) \right] d\mathbf{r}'_t, \end{aligned} \quad (2.61)$$

where the summations over rectangular waveguide modes have been truncated to the first N_{ker} terms and the summations over the Floquet modes of the PSWW to the first N_{kerf} terms. Also in this case, the IE is solved by applying the MoM with a Galerkin's procedure and using as basis and test functions the first N_f vector mode functions of the rectangular waveguide:

$$\mathbf{m}_n^{(\delta)}(\mathbf{r}_t) = \sum_{i=1}^{N_f} \alpha_{i,n}^{(\delta)} \mathbf{h}_i^{(1)}(\mathbf{r}_t). \quad (2.62)$$

The result is a linear system of equations that can still be expressed in compact form as in Eq. (2.34):

$$\nu_{n,l}^{(\delta)} = \sum_{i=1}^{N_f} \eta_{l,i} \alpha_{i,n}^{(\delta)}, \quad (2.63)$$

where the matrix of the system is now:

$$\begin{aligned} \eta_{p,i} = & \sum_{m=1}^{N_{ker}} \hat{Y}_m^{(1)} \nu_{m,p}^{(1)} \nu_{i,m}^{(1)} + \sum_{m=1}^{N_{kerf}} \hat{Y}_m^{(2)} \hat{\nu}_{m,p}^{(2)} \hat{\nu}_{i,m}^{(2)} - \sum_{p=1}^P (k_0)^{2p} \sum_{m=N^{(1)+1}}^{N_{ker}} \frac{B_p}{(k_{t_m}^{(1)})^p} \hat{Y}_m^{(1)} \nu_{m,p}^{(1)} \nu_{i,m}^{(1)} \\ & - \sum_{m=N^{(2)+1}}^{N_{kerf}} \left(\hat{Y}_m^{(2)} \hat{\nu}_{m,p}^{(2)} \hat{\nu}_{i,m}^{(2)} - Y_m^{(2)} \nu_{m,p}^{(2)} \nu_{i,m}^{(2)} \right). \end{aligned} \quad (2.64)$$

The coupling integrals $\nu_{m,p}^{(\delta)}$ are expressed as:

$$\nu_{m,p}^{(\delta)} = \iint_{S_a} \mathbf{h}_m^{(\delta)}(\mathbf{r}_t) \cdot \mathbf{h}_p^{(1)*}(\mathbf{r}_t) d\mathbf{r}_t, \quad (2.65)$$

and the static coupling integrals $\hat{v}_{m,p}^{(2)}$ are:

$$\hat{v}_{m,p}^{(2)} = \iint_{S_a} \hat{\mathbf{h}}_m^{(2)}(\mathbf{r}_t) \cdot \mathbf{h}_p^{(1)*}(\mathbf{r}_t) d\mathbf{r}_t. \quad (2.66)$$

The expression of the generic element of the multimode impedance matrix derived for a waveguide junctions (2.15) is still valid, but the modal voltages are now defined as:

$$\begin{aligned} V_m^{(\gamma)}(z=0) &= \iint_{S_a} \left[\sum_{n=1}^{N^{(1)}} \bar{I}_n^{(1)} \mathbf{m}_n^{(1)}(\mathbf{r}'_t) - \sum_{n=1}^{N^{(2)}} I_n^{(2)} \mathbf{m}_n^{(2)}(\mathbf{r}'_t) \right] \cdot \mathbf{h}_m^{(\gamma)*}(\mathbf{r}'_t) d\mathbf{r}'_t \\ &= \sum_{n=1}^{N^{(1)}} \bar{I}_n^{(1)} Z_{m,n}^{(\gamma,1)} - \sum_{n=1}^{N^{(2)}} I_n^{(2)} Z_{m,n}^{(\gamma,2)}. \end{aligned} \quad (2.67)$$

As shown in Fig. 2.11, in this case the static admittance is connected in parallel only to the input ports of the equivalent network. Therefore, the input currents of the transition multimode impedance matrix are still the equivalent currents $\bar{I}_n^{(1)}$ in Eq. (2.22)a and in Eq. (2.51), while the output currents are the modal currents in input to the PSWW equivalent network, taken with opposite sign.

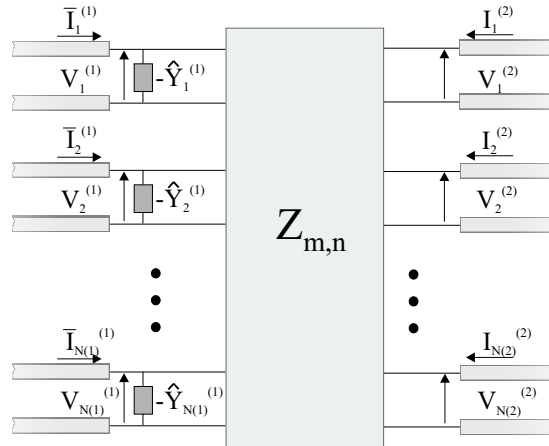


Figure 2.11: Multimode equivalent network for the junction between the rectangular waveguide of a phased array and a Phase Shift Wall Waveguide shown in Fig. 2.10, derived by applying the IEMEN approach.

In [21], Bhattacharyaa derives a GSM representation of an array of slots by solving an IE with reduced kernel, obtained by following a procedure analogous to the one described in [22] for waveguide junctions. With respect to the IEMEN approach outlined in this thesis, however, the method in [21] seems computationally heavier, because it requires a

larger number of matrix inversion to derive the equivalent network and because neither frequency extraction or acceleration technique is implemented.

The multimode equivalent network for a section of PSWW is the same as the one derived in Sec. 2.1.3 for a uniform waveguide section, but in this case the current amplitudes are only redefined at the side of the array waveguide.

Multimode equivalent network of the junction PSWW-PSWW

The tangential fields at the transition between two planar dielectric slabs are continuous; therefore, the modal transverse wavenumbers in the two dielectrics are equal, implying the equality of the Floquet vector mode functions. Since there is no coupling between these modes, the multimode impedance matrix representation of the PSWW-PSWW transition is a unit matrix and it does not need to be explicitly included in the calculations.

2.2.2 Numerical results

The IEMEN method for the analysis of planar phased arrays has been implemented in a software tool. Several examples from the literature have been considered for validation purposes and the results are described in this paragraph. The analysis were performed on an Intel Pentium 4 PC, with CPU of 1.6 GHz and RAM of 256 MB. The calculation time for all the presented examples was about two minutes for ten frequency points.

The parallel-plate waveguide phased array in Fig. 2.12 has been used by Amitay in [7] to study the effect of changing the relative wall thickness on the array performances.

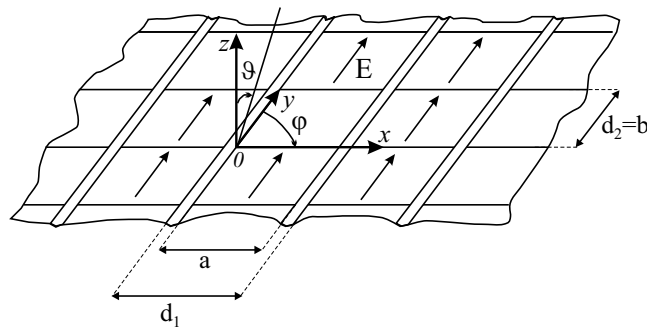


Figure 2.12: Geometry of the parallel-plate array in [7]

Fig. 2.13 shows the magnitude and the phase of the reflection coefficient, when scanning on the H -plane, for different values of the relative waveguide wall thickness $tp = (d_1 - a)/d_1$, where $d_1 = 0.5714\lambda$. The analysis was performed by including as accessible four Floquet

modes (which are all above cut off when the scan angle is 60°). The results obtained in [7] are also displayed for comparison, and the agreement with the IEMEN-based results is very good.

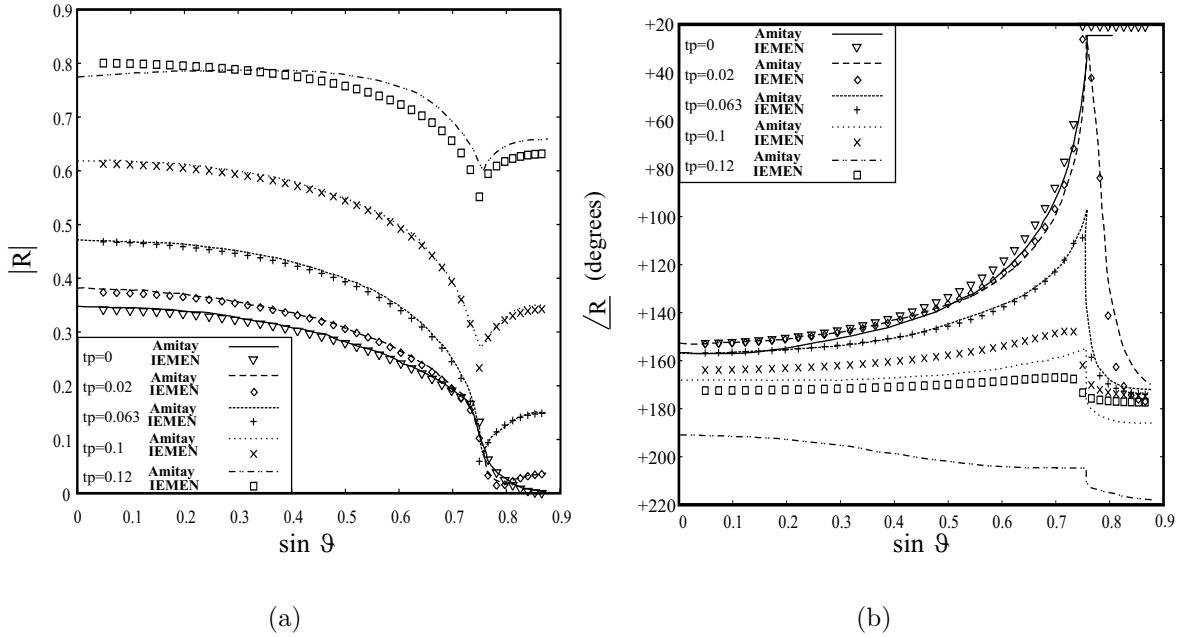


Figure 2.13: Parametric study of the reflection coefficient of the array in Fig. 2.12 for different values of the wall thickness: comparison between the IEMEN-base results and those reported by Amitay in [7]. The reflection coefficient is plotted versus the scan angle for scanning in the H-plane. (a) Magnitude. (b) Phase.

The results provided by the IEMEN method have also been compared with those obtained using a software package based on the *direct method* [144]. Excellent agreement was obtained between the two methods, as shown in Fig. 2.15 for the magnitude of the reflection coefficient of a planar phased array of standard X-band waveguides (the dimensions are: $a=22.86$ mm, $b=10.16$ mm); the waveguides are excited by means of the TE_{10} mode and they are arranged in a rectangular lattice of dimensions $d_1=31$ mm, $d_2=20$ mm, with respect to the reference system reported in Fig. 2.1. The array radiates in free space at broadside and only the fundamental TEM Floquet mode is above cut off. The same figure also shows the results concerning a cylindrical waveguide array, with radiating elements having the same cross section as in the planar array, and with a very large radius with respect to the wavelength to approximate the planar case (about 4 m radius for a wavelength

of 3 cm in X-band); the dimensions of the array are indicated in the caption of Fig. 2.15, according to the reference system in Fig. 2.14. These results were obtained by using the extension of the IEMEN approach to the analysis of conformal arrays described in [56]. Fig. 2.16 shows the magnitude of the reflection coefficient of a planar and of a cylindrical array of standard X-band waveguides loaded with a dielectric layer of permittivity $\varepsilon_1 = 1.4$ and thickness $l_1 = 26.3$ mm. The relevant dimensions are indicated in the caption.

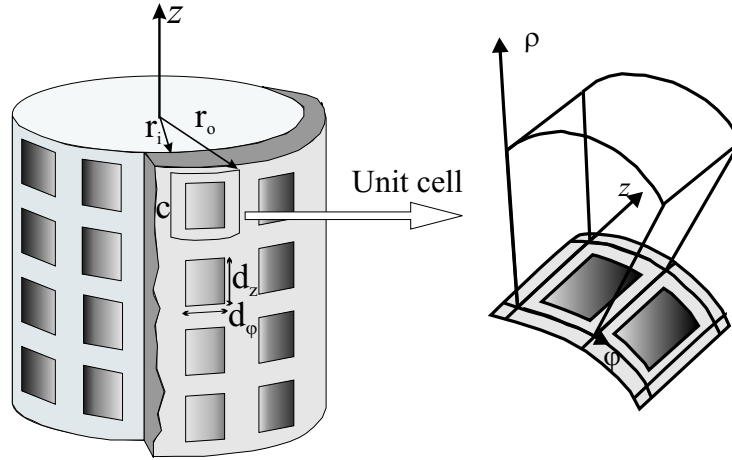


Figure 2.14: Cylindrical array geometry used also in [56].

2.3 Thick FSS

An infinite aperture-based FSS, cut from a thick metal plate, can be analyzed as an infinite waveguide phased array. The corresponding multimode equivalent network is then derived by applying the procedure described in Sec 2.2.1. Note that the suitability of this procedure to study aperture-based FSS depends on its thickness, which determines how many accessible waveguide modes should be included in the calculations. If the FSS is etched on a thin plate, an overwhelming number of accessible modes would be needed to correctly represent the transitions at the input and output of the corresponding FSS waveguides. In this case, the procedure described in Chapter 3 for zero-thickness FSS's should be preferred.

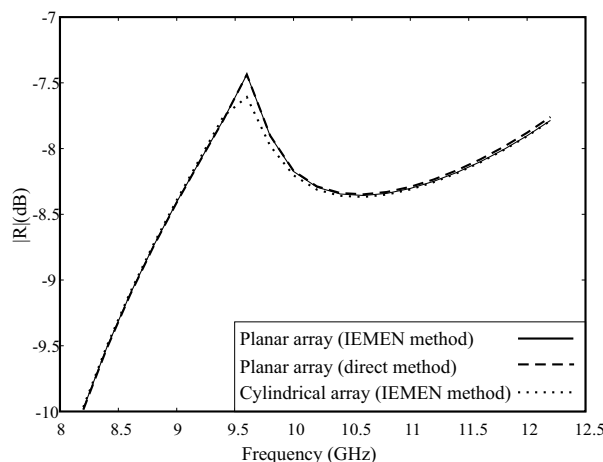


Figure 2.15: Comparison between a planar and a cylindrical waveguide phased array: magnitude of the reflection coefficient obtained by applying the IEMEN method and the *direct method*. The dimensions of the unit cell for the planar array are: $d_1=31$ mm, $d_2=20$ mm; the cylindrical array has 810 elements on each row and dimensions $c=20$ mm, $r_i=4000$ mm, $r_o=5000$ mm.

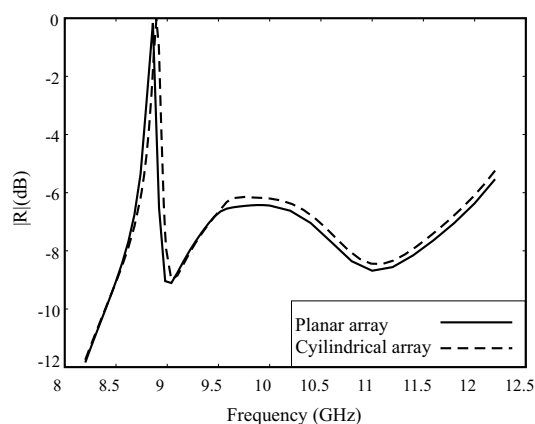


Figure 2.16: Comparison between a planar and a cylindrical waveguide phased array: magnitude of the reflection coefficient obtained by applying the IEMEN method. The unit cell size for the planar array is: $d_1=31$ mm, $d_2=20$ mm; the cylindrical array has 810 elements on each row and dimensions $c=20$ mm, $r_i=4000$ mm, $r_o=4026$ mm.

Numerical results

Fig. 2.18 shows the magnitude of the reflection coefficient of an infinite waveguide phased array cascaded with an aperture-based FSS. The array operates in X-band and consists

of standard waveguides of dimensions $a=22.86$ mm, $b=10.16$ mm arranged in a rectangular lattice of dimensions $d_1=24.247$ mm, $d_2=20$ mm. The FSS elements are rectangular apertures cut from a metal plate of thickness $l_2=2.5$ mm and the lattice is the same as for the array. The aperture dimensions, a_x and a_y along the x and y axes are indicated in the caption with respect to the reference system in Fig. 2.17. The distance array-FSS and the dimensions of the FSS apertures affect the frequency response of the structure. Figs. 2.18a and 2.18b show, for example, the effect of distance between FSS and array. Moreover, the size of the FSS aperture influences the position of the resonance, as can be seen in Fig. 2.19, where increasing the shorter dimension of the FSS apertures results in a lower resonance frequency. This aspect will be further investigated in Chapter 4. The inclusion of ten accessible Floquet modes was sufficient to obtain an accurate result for all three structures. The corresponding highest order mode arrives at the terminal plane with an attenuation factor of 4.5 when the FSS is located at a distance of 10 mm from the array and of 1.8 when this distance is 24.3 mm; this factor is defined as $1/e^{-\alpha l} = e^{\alpha l}$, where $k_z = j\alpha l$ is the propagation constant of a mode under cut-off and l is the distance between the terminal plane and the discontinuity plane.

Fig. 2.20 shows the magnitude of the reflection coefficient of a planar array of standard X-band waveguides cascaded with a thick aperture-based FSS, compared with the result obtained for a cylindrical waveguide array with the same waveguide cross section and a very large radius. The relevant dimensions are indicated in the caption of the figure and, for the cylindrical case, they refer to the geometry indicated in Fig. (2.14).

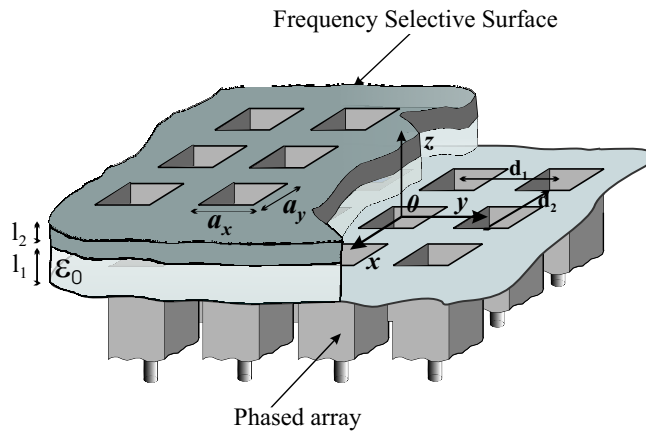


Figure 2.17: FSS geometry for the examples in Figs. 2.18 and Fig. 2.19.

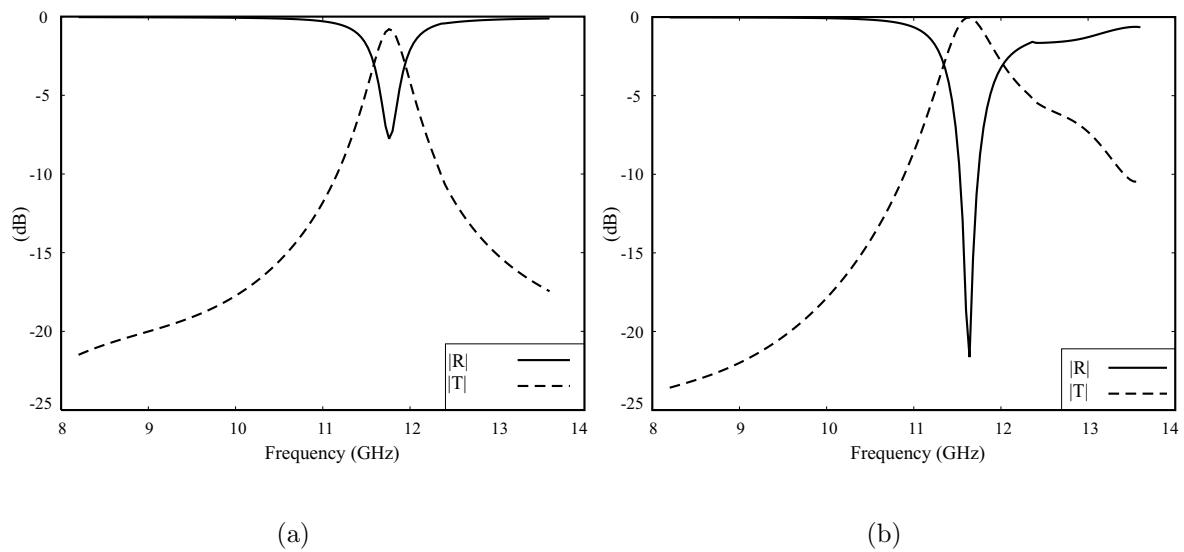


Figure 2.18: Filtering behavior of an open-ended waveguide array operating at X-band loaded with an aperture-based FSS. The dimensions of the FSS apertures are: $a_x=12$ mm, $a_y=2$ mm. The distance l_1 between array and FSS is (a) 10 mm, (b) 24.3 mm.

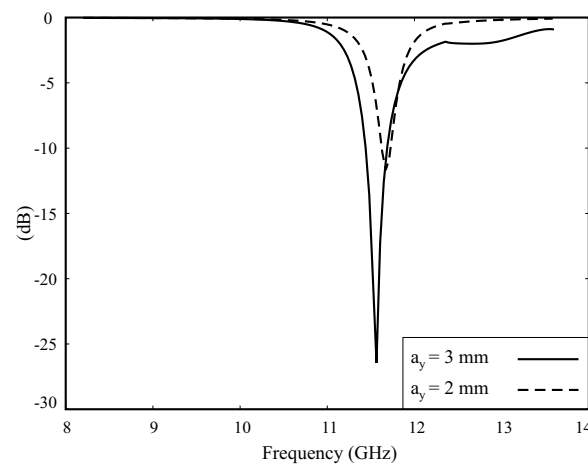


Figure 2.19: Filtering behavior of an open-ended waveguide array operating at X-band cascaded with an aperture-based FSS. Effect of the change of the shorter aperture's dimension a_y . The distance l_1 between array and FSS is 10 mm.

2.4 Conclusions

The usual procedure followed to derive the equivalent network of a waveguide junction is based on the expansion of the tangential unknown electric (or magnetic) field at the

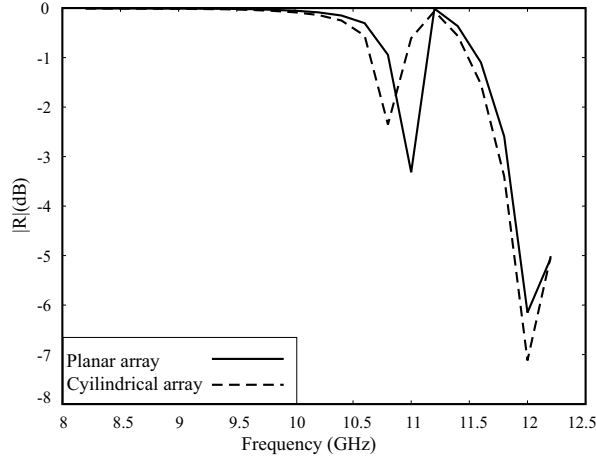


Figure 2.20: Comparison between a planar and a cylindrical waveguide phased array loaded with an aperture-based FSS: magnitude of the reflection coefficient. The cylindrical array has 810 elements on each row and dimensions $c=20$ mm, $r_i=4000$ mm, $r_o=4026$ mm; the unit cell size for the planar array is: $d_1=31$ mm, $d_2=20$ mm; the distance between array and FSS is $l_1=26.3$ mm; the size of the FSS apertures is $a_x=12$ mm, $a_y=2$ mm, with thickness $l_2=2.5$ mm for the planar case, and $d_\varphi=12$ mm, $d_z=2$ mm, $r_i=4026.3$ mm, $r_o=4028.8$ mm for the radial case.

junction in terms of an infinite number of evanescent waveguide modes, and it resorts to a network with a theoretically infinite number of input and output ports [37, 94, 106]. Depending on the adopted technique, the obtained representation consists in a GSM, a GTM, a GAM, or a GIM. In their practical implementation, however, only a finite number of modes, for each one of the two waveguides involved in the junction, is included in the calculations; these two numbers are not independent and have to be chosen taking into account the relative convergence phenomenon [95]. Moreover, if a conventional GAM or GIM representation is adopted, the originally calculated full matrix, associated to a large number of evanescent modes, has to be reduced to the accessible ones to avoid numerical instability problems in the computation of the equivalent network parameters of the cascade of uniform waveguides [5]. This requires two additional matrix multiplications and one matrix inversion. The key feature of the IEMEN approach in comparison with other microwave network techniques is that it pushes the concept of accessible modes to its extreme consequences and resorts directly to a reduced GIM representation of the junction, where the ports of the equivalent network correspond to the accessible modes only. In fact, this method recognizes a finite number of modes, the accessible ones defined

at the terminal planes, as the only modes that are really needed to represent all the fields in the discontinuity region with a prescribed accuracy. The corresponding modal amplitudes become the fundamental unknowns of the problem. This leads to a single IE with a fixed kernel and a different forcing function for each accessible mode. The application of the MoM with a Galerkin's procedure results in a system of linear equations with multiple right-hand side corresponding to the projection of the accessible modes on the test functions. As a consequence, an expansion of the unknowns that uses as basis and test functions waveguide modes of order at least equal to the highest accessible mode guarantees the convergence of the solution without conditioning problems. The IE's kernel, as derived in the basis formulation, contained only localized modes; to improve the stability, quasi-static terms corresponding to the accessible modes were added in the kernel. The frequency extraction technique described in [36] was implemented to further reduce the calculation time. It consists in applying of the Kummer transformation to the slowly converging series of the IE's kernel and, subsequently, in using a convenient expansion of the obtained difference series. For the problem of the junction between two uniform waveguides, this technique lead to a frequency independent kernel (except for a multiplying factor), which had to be calculated only once when performing the simulations over a certain frequency range. As a consequence, the elements of the corresponding equivalent network were also frequency independent. For the problem of the array radiating in free space, thanks to the frequency extraction technique, only one series in the kernel of the pertinent IE had to be calculated inside the frequency loop, and its convergence was accelerated by means of the Kummer transformation.

The computational effort required when using microwave network formalisms to represent the cascade of waveguides depends essentially on two factors:

- the computation of the equivalent network for each junction;
- the computation of the cascade of the equivalent networks, which requires at least one matrix inversion.

For conventional microwave networks techniques, which resort to a matrix representation of each junction with as many ports as the number of modes included in the calculations, the cascade of the matrices is the critical aspect. This is for example the case of the GAM method in [5] or the GTM method [105]. The calculation of the transition network with this two techniques is in general fast and, in the implementations of [5, 105] does not involve matrix inversions. However, when many evanescent modes are taken into account,

to prevent instability problems in the cascade of a number of waveguides, a reduced form of the matrix has to be calculated. This requires additional matrix operations.

For reduced techniques, which directly resort to a network representation of the junction with only the ports corresponding to the accessible modes, the effort required to obtain the reduced matrix plays a decisive role. The reduced GSM method, presented in [22] for waveguide junctions and in [21] for arrays of slots, from the solution of a reduced IE resorts to an equivalent matrix involving only the accessible modes. However, to achieve this representation four matrix inversions and eleven matrix multiplications have to be performed (sixteen for the analysis of slot arrays), versus only one inversion and six multiplications needed with the IEMEN technique. Moreover, the IEMEN formalism allows reusing the reaction integrals that appear in the MoM matrix to build the equivalent network matrix entries, with a consequent reduction in the computation time. The application of the frequency extraction technique makes the IEMEN approach even more appealing. Therefore, the IEMEN method not only allows circumventing the instability problems typical of GIM/GAM representations, but it is in general an appropriate choice for the characterization of a waveguide junction in terms of a reduced multimode equivalent network.

Furthermore, when cascading more waveguides to each other, the calculation time that is needed to solve the corresponding linear system of equations (see Eq. (2.42)) depends on the size of the system matrix to be inverted. The IEMEN method resorts to the inversion of the smallest possible matrix: the one associated to the accessible modes only. In fact, the system is solved by means of a highly efficient technique, which exploits the fact that the system matrix is banded. With this technique, only small sub-blocks have to be inverted, of maximum dimension equal to the maximum number of accessible modes included in the representation.

Chapter 3

IEMEN approach for aperture- and patch-based FSS's

In Chapter 2, Sec. 2.1, we have described in detail the theoretical basis of the Integral Equation formulation for deriving a Multimode Equivalent Network (MEN) representation of cascaded waveguides (IEMEN); additionally, we have outlined the relevant steps for the analysis of waveguide junctions and we have extended the IEMEN method to the analysis of the transition between an infinite waveguide phased array and free space. In Sec. 2.3, we have shown how this network can be also used to represent a thick aperture-based Frequency Selective Surface (FSS), under plane-wave incidence. In this chapter, the general theoretical formulation for FSS's, consisting of periodic distributions of patches and slots etched on an infinitesimally thin metal plane, is described in Sec. 3.1. Our study has been directed to large FSS's, approximated as infinite periodic arrays, because, by virtue of the Bloch-Floquet theorem (Appendix B, Sec. B.2), the problem can be reduced to the analysis of a single periodic cell [44,88]. A vast amount of literature is available about the finiteness effects for an array of radiating elements (the interested reader could refer for example to [18,38–40,102,103]) but these aspects have not been further investigated in the present work. The specific application of the IEMEN method to patch- and aperture-based FSS's is treated in Sec. 3.2 and Sec. 3.3, respectively. If a number of FSS's are sandwiched between thin dielectric slabs, and a large number of accessible modes is required to characterize the transition, it might be convenient to directly include the effect of the dielectric layers in the analysis of the junction. This implies substituting the periodic free-space Green's functions (GF) with the periodic multi-layer GF, as it will be explained in detail in Sec. 3.4. The Integral Equation (IE) that formalizes the patch and the aperture problems is solved in Sec. 3.5 by using the Method of Moments (MoM). The technique adopted to accelerate the

convergence of the infinite series appearing in the IE kernel is also described. Numerical results are presented and discussed in Sec. 3.6.

3.1 Theoretical basis

We consider an infinite periodic array of open-ended waveguides integrated with an FSS, consisting of multiple planar dielectric layers loaded by patch- and slot-based resonant elements (in the example of Fig. 3.1 the lattice is rectangular). A Cartesian coordinate system is chosen, with x and y axes in the plane of the waveguide apertures and z orthogonal to this plane. We will associate the internal and external regions with $z < 0$ and $z > 0$, respectively.

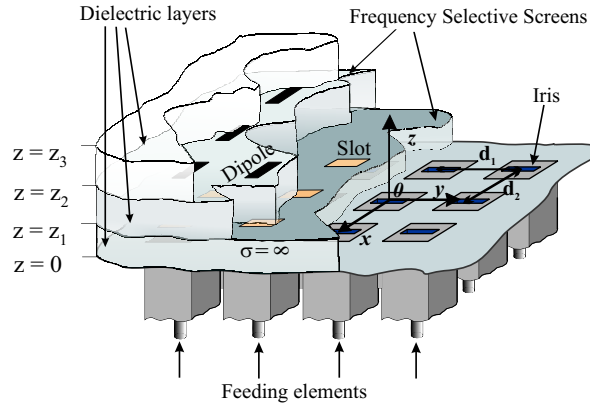


Figure 3.1: Geometry of an iris loaded waveguide array integrated with a generic FSS structure, comprising a slot-based FSS and a patch-based FSS sandwiched between different dielectric layers

The analysis of this kind of structures starts by enforcing the appropriate boundary conditions for the electromagnetic field at each transition. From these conditions, the problem can be formalized in different ways, depending on the expression used for the fields. Most common numerical approaches adopt an integral representation, and resort to an IE that is solved by means of the MoM [22, 66, 118]. For a multi-layer structure, either the scattering problem is tackled simultaneously at all the layers by solving the corresponding system of IE's, as in [100, 117], or it is treated separately at each layer, as it is typical for microwave network-based techniques. The latter have been extensively used for the analysis of FSS's. A detailed description of the application of the Generalized Scattering Matrix (GSM) method is given by Mittra in the review paper [94] and by Orta and Tas-

cone in [37, 106]. A Generalized Admittance Matrix (GAM) is derived in [109] by Oliner for metallic-strip gratings in free space under plane wave incidence; this GAM method is extended in [75, 109] to the analysis of gratings at a dielectric interface.

The first step, in a microwave network technique, consists in expressing the fields in terms of Floquet modes and identifying their pertinent transmission-line (TL) representations (along z) for all z -invariant regions between the transitions. These transitions are here localized at the planes $z = 0$, $z = z_1$, $z = z_2$, $z = z_3$. Each region and each transition between regions is then represented in terms of a multi-port equivalent network. If more dielectric slabs are cascaded to the FSS, each slab can be separately characterized by its equivalent network representation, although there is no intermodal coupling between two adjacent slabs. An alternative way of proceeding is to derive the equivalent network only of those transitions where there is actual mode coupling (at the metallic FSS's), and to include the effect of the dielectric slabs directly in the calculation of the field interaction at the FSS interface. In this case, a smaller number of equivalent networks has to be cascaded to obtain a representation of the entire structure, and therefore, a smaller number of matrix inversions is required. This is the approach usually adopted in the implementation of the GSM method, (for example in [16, 37, 94]).

The general procedure followed in the application of the IEMEN method is aimed at modularity, which is especially important for design purposes. Therefore, the information about the behavior of the electromagnetic field at the internal dielectric steps is preserved by characterizing each slab with its equivalent network. However, when the dielectric slabs become very thin, and a high number of accessible modes is required to appropriately represent the fields at the FSS transition, the analysis can be performed more efficiently if the effect of the dielectric is included directly in the network representation of the FSS; an example will be given in Chapter 5. The equivalent impedance and admittance matrix associated with every layer in Fig. 3.1 is in general multimode, with one port per accessible mode. The equivalent networks for each transition are also multimode and are obtained by solving a single IE with fixed kernel and multiple forcing terms, which represents the specific interface problem. In general, given an array of zero thickness patches, two different IE's can be obtained, in which either the induced currents on the patches or the tangential electric fields in the complementary apertures are treated as the unknowns of the problem [62, 106]. In a three-dimensional problem, the former is more convenient when the patches have a simple shape (patch-based FSS), and the latter when the apertures have a more regular form (aperture-based FSS) [106]. In both cases, the equivalent circuit is in parallel with respect to the z -oriented TL's because the electric field and the pertinent modal voltages are continuous at the interface. In the *patch formulation*, the problem is formalized

in terms of an Electric Field Integral Equation (EFIE) and the unknown quantities are the differences between the tangential magnetic fields in the half spaces defined by the FSS. Accordingly, these differences can be seen as currents flowing in a generalized load, parallel to the transmission lines associated to the Floquet modes, defined above and below the FSS discontinuity (shunt multimode admittance network). In the *aperture formulation*, instead, the problem is formalized in terms of a Magnetic Field Integral Equation (MFIE). In this case, the unknowns are the equivalent magnetic currents (tangential electric field in the aperture), and the equivalent network is again in parallel (shunt multimode impedance network). In the following, we will explicitly derive the equivalent network representation for these two transitions only, shown in Fig. 3.2.

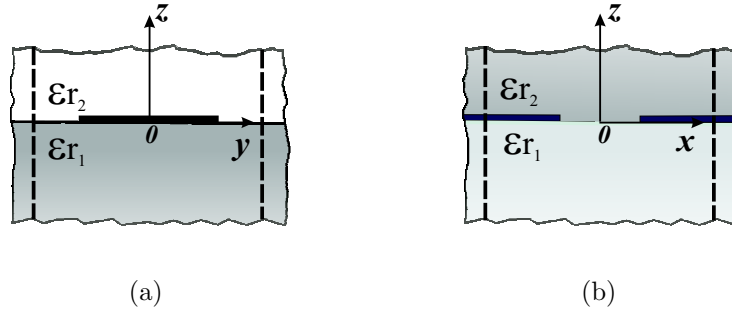


Figure 3.2: Unit cell of a planar FSS, seen as (a) a patch transition for the patch formulation, (b) a slot transition for the aperture formulation.

3.2 Patch-based FSS

3.2.1 Formulation

Fig. 3.2a shows the unit cell of an infinite doubly periodic distribution of metallic patches between two different dielectric half spaces. On each elementary cell of the array, the total tangential electric field must vanish on the surface of the patches, which are assumed perfectly conducting and infinitesimally thin. Since the tangential electric and magnetic fields are continuous at the interface between the two dielectric half spaces, their representation in terms of Floquet vector mode functions, \mathbf{e}_i and \mathbf{h}_i (Appendix B, Sec. B.2.2), is the same on the two half spaces. Accordingly, the overall Electric Field Integral Equation (EFIE)

for the patch located at the origin of the reference system, ($z = 0$), can be expressed as

$$\mathbf{E}_t(\mathbf{r}_t) = \sum_{i=1}^{\infty} V_i \mathbf{e}_i(\mathbf{r}_t) = 0, \quad \mathbf{r}_t \in S_p, \quad (3.1)$$

where $\mathbf{r}_t = x\mathbf{u}_x + y\mathbf{u}_y$ identifies a point on the FSS plane, with respect to the Cartesian reference system indicated in Fig. 3.2, and S_p is the surface of the patch. The IE (3.1) is valid for the tangential electric field in both regions. The modal voltages are here evaluated at the discontinuity and, for sake of simplicity, we have indicated $V_n(z = 0) = V_n$. The first step in the definition of a MEN of the transition is the identification of the subsets of Floquet modes that are considered accessible in the two dielectric half spaces, with respect to the chosen terminal planes, as indicated in Fig. 3.3. In absence of other discontinuities, the terminal planes can be located arbitrarily far from the transition itself and, therefore, the only accessible modes are the propagating ones. Otherwise, the significance of the modes in the description of the fields at the terminal planes depends on the distance of these planes from the transition plane.

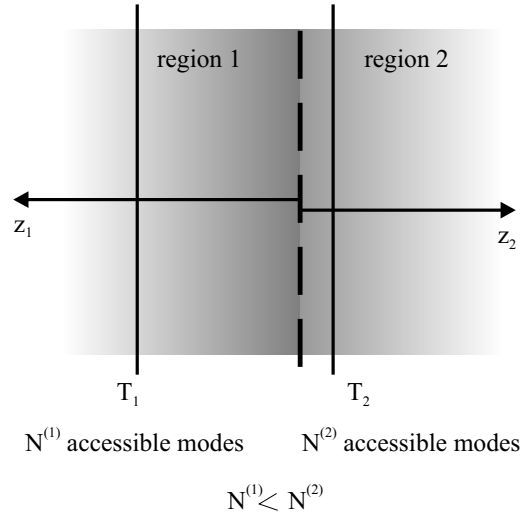


Figure 3.3: Infinite array of metallic conductors between two semi-infinite half-spaces: choice of the terminal planes for the definition of the accessible modes.

Let us suppose that the FSS in Fig. 3.1a is part of a multi-layer structure and is sandwiched between two dielectric slabs of different thickness; as a consequence, the number of accessible modes $N^{(1)}$ defined with respect to the terminal plane T_1 is in general different from the number $N^{(2)}$ defined with respect to the terminal plane T_2 . We use now the idea, introduced in Chapter 2, Sec. 2.1, of fundamental unknowns of the scattering problem, as

those values in terms of which all the relevant field quantities between the terminal planes can be expressed. When the fields in the two regions defined by the transition plane are represented in a different modal base, the fundamental unknowns are all the accessible modes at the two terminal planes. This is the case, for example, of the waveguide-to-waveguide junction or the array waveguide-to-free space transition. However if, like in the present case, the fields are expressed in both regions in terms of Floquet modes, the number of fundamental unknowns actually needed to express the fields at the transition is equal to the maximum number of accessible modes between those relevant at the terminal plane T_1 and those at the terminal plane T_2 .

For the patch approach, the fundamental unknowns are the $M = \max(N^{(1)}, N^{(2)})$ accessible modal voltages V_i . As a consequence, the equivalent electric current distribution on the metallic conductors $\mathbf{J}(\mathbf{r}) = \mathbf{u}_z \times (\mathbf{H}_t^{(2)}(\mathbf{r}) - \mathbf{H}_t^{(1)}(\mathbf{r}))$, which is the unknown physical quantities of the problem, can be expressed in terms of these modal voltages as:

$$\mathbf{J}(\mathbf{r}_t) = \sum_{i=1}^M V_i \mathbf{j}_i(\mathbf{r}_t), \quad (3.2)$$

where $\mathbf{j}_i(\mathbf{r}_t)$ are M unknown functions. Similarly, the total electric field in (3.1) can be rewritten as a superposition of accessible (the first M) and localized contributions:

$$\mathbf{E}_t(\mathbf{r}_t) = \mathbf{E}_{t_a}(\mathbf{r}_t) + \mathbf{E}_{t_{na}}(\mathbf{r}_t) = \sum_{i=1}^M V_i \mathbf{e}_i(\mathbf{r}_t) + \sum_{i=M+1}^{\infty} V_i \mathbf{e}_i(\mathbf{r}_t). \quad (3.3)$$

In particular, the incident field is expressed by definition in terms of only accessible modes, while the constituent of the field associated to the localized modes at the transition plane $\mathbf{E}_{t_{na}}(\mathbf{r}_t)$ does not interact with any other part of the circuit (it does not reach the terminal planes) and stores the reactive energy. In view of this, it is convenient to define the non-accessible (na) constituent of the infinite array dyadic GF for the electric field, $\bar{\mathbf{G}}_{na}^e$, as derived in Appendix C Sec. C.2:

$$\bar{\mathbf{G}}_{na}^e(\mathbf{r}_t; \mathbf{r}'_t) = - \sum_{i=M+1}^{\infty} \left(Z_i(\mathbf{k}_{t_i}, 0) \mathbf{e}_i(\mathbf{r}_t) \mathbf{e}_i^*(\mathbf{r}'_t) \right) \quad \text{non-accessible GF}, \quad (3.4)$$

where $Z_i(\mathbf{k}_{t_i}, 0)$ are the impedances at the section $z = 0$ in the equivalent circuit of Fig. C.3, equal to the parallel of the characteristic impedances of the two media:

$$Z_i(\mathbf{k}_{t_i}, 0) = \frac{Z_{01i}(\mathbf{k}_{t_i}, 0) Z_{02i}(\mathbf{k}_{t_i}, 0)}{Z_{01i}(\mathbf{k}_{t_i}, 0) + Z_{02i}(\mathbf{k}_{t_i}, 0)}, \quad (3.5)$$

for both TM and TE transmission lines. By using this concept, $\mathbf{E}_{na}^t(\mathbf{r}_t)$ can be expressed as

$$\mathbf{E}_{tna}(\mathbf{r}_t) = \sum_{i=M+1}^{\infty} V_i \mathbf{e}_i(\mathbf{r}_t) = \int_{S_p} \bar{\mathbf{G}}_{na}^e(\mathbf{r}_t; \mathbf{r}'_t) \cdot \mathbf{J}(\mathbf{r}'_t) d\mathbf{r}'_t. \quad (3.6)$$

Note that, for the case of a stacked FSS, the IEMEN formulation is applied to each patch transition separately and $\mathbf{J}(\mathbf{r}'_t)$ indicates therefore the equivalent current distribution pertinent to the patch layer under analysis. Inserting (3.6) and (3.3) in Eq. (3.1) changes the EFIE into

$$\sum_{i=1}^M V_i \mathbf{e}_i(\mathbf{r}_t) = - \int_{S_p} \bar{\mathbf{G}}_{na}^e(\mathbf{r}_t; \mathbf{r}'_t) \cdot \mathbf{J}(\mathbf{r}'_t) d\mathbf{r}'_t \quad \mathbf{r}_t \in S_p. \quad (3.7)$$

This equation relates the accessible modes to the equivalent currents on the patch. With respect to a standard procedure based on the MoM [118], in which the unknowns are expanded in terms of an appropriate set of basis functions selected a priori, the IEMEN formulation resorts to a linear combination of fundamental quantities and unknown functions, as explained in Chapter 2, Sec. 2.1.2 for waveguide junctions. In the present case, the unknown equivalent currents are represented as in Eq. (3.2). Inserting this expression in (3.7) leads to

$$\sum_{i=1}^M V_i \mathbf{e}_i(\mathbf{r}_t) = - \sum_{i=1}^M V_i \int_{S_p} \bar{\mathbf{G}}_{na}^e(\mathbf{r}_t; \mathbf{r}'_t) \cdot \mathbf{j}_i(\mathbf{r}'_t) d\mathbf{r}'_t \quad \mathbf{r}_t \in S_p. \quad (3.8)$$

By virtue of the nature of the accessible modal voltages, this equation is valid for all V_i , with $i = 1..M$. As a consequence, we can equate the coefficients of V_i on both sides of the equation and obtain a single IE, with fixed kernel and multiple forcing terms consisting of the accessible vector mode functions $\mathbf{e}_i(\mathbf{r}_t)$:

$$\mathbf{e}_i(\mathbf{r}_t) = - \int_{S_p} \bar{\mathbf{G}}_{na}^e(\mathbf{r}_t; \mathbf{r}'_t) \cdot \mathbf{j}_i(\mathbf{r}'_t) d\mathbf{r}'_t \quad \mathbf{r}_t \in S_p \quad i = 1, \dots, M. \quad (3.9)$$

The IE (3.9) can be solved resorting to a MoM procedure, in which the kernel of the operator contains the non-accessible GF, $\bar{\mathbf{G}}_{na}^e$, rather than the standard periodic array GF. Therefore, we refer to this equation as *reduced-kernel IE*. The specific implementation of the MoM will be described in Sec. 3.5.

3.2.2 Multimode Equivalent Network

The unknown functions $\mathbf{j}_i(\mathbf{r}'_t)$, obtained by solving the IE (3.9), and weighted by proper coefficients as in (3.2), provide a representation of the equivalent current and consequently

of the total tangential magnetic field difference at the interface containing the patch $-\mathbf{u}_z \times \mathbf{J}(\mathbf{r}_t) = (\mathbf{H}_t^{(2)}(\mathbf{r}) - \mathbf{H}_t^{(1)}(\mathbf{r}))$.

The Floquet expansion of the magnetic fields: $\mathbf{H}_t^{(\gamma)}(\mathbf{r}) = \sum_{m=1}^{\infty} I_m^{(\gamma)} \mathbf{h}_m(\mathbf{r}_t)$, with $\gamma = 1, 2$, can then be invoked to derive a relation between the modal currents in the two media and the solutions $\mathbf{j}_i(\mathbf{r}_t)$:

$$\sum_{m=1}^{\infty} (I_m^{(2)} - I_m^{(1)}) \mathbf{h}_m(\mathbf{r}_t) = -\mathbf{u}_z \times \sum_{j=1}^M V_j \mathbf{j}_j(\mathbf{r}_t) \quad \mathbf{r}_t \in S_p. \quad (3.10)$$

To achieve the terminal conditions on the M modal voltages and currents in input to the equivalent network representing the transition, we perform the integral projection of both sides of Eq. (3.10) on the set of accessible modes $\mathbf{h}_i(\mathbf{r}_t)$, with $i = 1, \dots, M$:

$$\begin{aligned} & \int_{U_c} \left(\sum_{m=1}^M (I_m^{(2)} + \check{I}_m^{(1)}) \mathbf{h}_m(\mathbf{r}_t) + \sum_{m=M+1}^{\infty} (I_m^{(2)} - I_m^{(1)}) \mathbf{h}_m(\mathbf{r}_t) \right) \cdot \mathbf{h}_i^*(\mathbf{r}_t) d\mathbf{r}_t = \\ & \int_{U_c} \left(-\mathbf{u}_z \times \sum_{j=1}^M V_j \mathbf{j}_j(\mathbf{r}_t) \right) \cdot \mathbf{h}_i^*(\mathbf{r}_t) d\mathbf{r}_t, \end{aligned} \quad (3.11)$$

where U_c indicates the surface of the unit cell. Note that the signs of the accessible modal currents $I_m^{(1)}$ and $I_m^{(2)}$, in output from the MEN of region 1 and in input to the MEN of region 2, are chosen to comply with the usual microwave rule (the current has positive sign when entering the network terminals), as shown in Fig. 3.3, so that $\check{I}_m^{(1)} = -I_m^{(1)}$. Using the orthogonality of the Floquet modes on the unit cell (see Appendix B, Sec. B.2) and some straightforward algebraic manipulations, results in the following terminal conditions:

$$I_i = \sum_{j=1}^M V_j Y_{ij}, \quad i = 1..M, \quad (3.12)$$

where $I_i = -(\check{I}_i^{(1)} + I_i^{(2)})$ and

$$Y_{ij} = \int_{U_c} \mathbf{j}_j(\mathbf{r}_t) \cdot \mathbf{e}_i^*(\mathbf{r}_t) d\mathbf{r}_t, \quad i, j = 1, M. \quad (3.13)$$

Thus, the multimode equivalent network of the patch transition, obtained by applying the IEMEN formulation, can be envisaged as a multimode admittance in parallel to the transmission lines associated to the accessible modes in the two different dielectric regions. It is worth to note that if $N^{(1)} < N^{(2)}$, as it would be for the transition depicted in Fig. 3.3, then $\check{I}_i^{(1)} = Y_{0i}^{(1)} V_i$ for $i > N^{(1)}$, which means closing the corresponding $N^{(2)} - N^{(1)}$ ports of the equivalent network with the characteristic admittance of those modes $Y_{0i}^{(1)}$, as shown in Fig. 3.4. The same holds for the case of $N^{(2)} < N^{(1)}$.

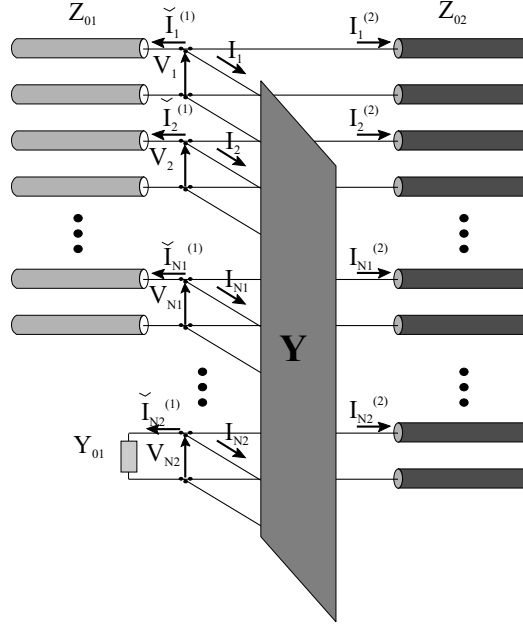


Figure 3.4: Multimode Equivalent Network of an FSS, made of metal patches, for which the patch formulation of the IEMEN method has been used; the elements of the admittance matrix $[Y]$ are defined in Eq. (3.13)

3.3 Aperture-based FSS

3.3.1 Formulation

Fig. 3.2b shows the unit cell of an infinite doubly periodic distribution of slots, etched on a screen of perfect electric conductor separating two different semi-infinite dielectric half spaces. We assume the screen to be infinitesimally thin. The problem of an aperture-based FSS, obtained from a thick metal plate, can be formulated as transition problem between a waveguide array and free space, and has already been treated in Chapter 2, Sec. 2.3.

The Magnetic Field Integral Equation (MFIE), expressing the continuity of the tangential magnetic field in the aperture, located at $z = 0$, is

$$\mathbf{H}_t^{(1)}(\mathbf{r}_t) = \mathbf{H}_t^{(2)}(\mathbf{r}_t), \quad \mathbf{r}_t \in S_a, \quad (3.14)$$

where S_a is the surface of the aperture and $\mathbf{H}_t^{(1)}$ and $\mathbf{H}_t^{(2)}$ are the magnetic fields, tangent to the FSS plane, in region 1 and 2, respectively. As already noticed in the description of the patch approach, the fields in both regions are expressed in terms of the same modal

base, the Floquet modes:

$$\sum_{i=1}^{\infty} I_i^{(1)} \mathbf{h}_i(\mathbf{r}_t) = \sum_{i=1}^{\infty} I_i^{(2)} \mathbf{h}_i(\mathbf{r}_t), \quad \mathbf{r}_t \in S_a. \quad (3.15)$$

To derive the equivalent network representation of this transition, we have to define a pair of terminal planes and identify the accessible modes that should be included in the representation of the fields in each one of the two regions. Referring again to Fig. 3.3, $N^{(1)}$ is the number of accessible modes at the terminal plane T_1 and $N^{(2)}$ at the terminal plane T_2 . Eq. (3.15) becomes:

$$\sum_{i=1}^{N^{(1)}} -\check{I}_i^{(1)} \mathbf{h}_i(\mathbf{r}_t) + \sum_{i=N^{(1)}+1}^{\infty} I_i^{(1)} \mathbf{h}_i(\mathbf{r}_t) = \sum_{i=1}^{N^{(2)}} I_i^{(2)} \mathbf{h}_i(\mathbf{r}_t) + \sum_{i=N^{(2)}+1}^{\infty} I_i^{(2)} \mathbf{h}_i(\mathbf{r}_t), \quad \mathbf{r}_t \in S_a, \quad (3.16)$$

The positive direction of the modal currents $I_i^{(1)}$ in region 1, indicated in Fig. 3.3 by the vector \mathbf{z}_1 , is chosen such that they are entering the terminals of the equivalent impedance matrix of this dielectric slab, to comply with the usual microwave rule (the current has positive sign when entering the network terminals), so that $\check{I}_i^{(1)} = -I_i^{(1)}$.

Since the terminal planes are not symmetrical with respect to the transition plane, the number of accessible modes is different, as indicated in Fig. 3.3, where $N^{(1)} < N^{(2)}$. However, as a consequence of the continuity of the tangential fields at the transition and of the fact that they are expressed in the same modal base, the relevant quantities at the FSS interface have to be represented using the same fundamental unknowns in the two regions. For the present aperture formulation, they are the $M = \max(N^{(1)}, N^{(2)})$ sum of the accessible modal currents in the two regions $-(\check{I}_i^{(1)} + I_i^{(2)})$. As a consequence, using the linearity of the fields, the tangential electric field in the aperture $\mathbf{E}_t(\mathbf{r}_t)$ can be expressed in terms of these quantities only, as well as the corresponding equivalent magnetic currents:

$$\mathbf{M}(\mathbf{r}_t) = \sum_{m=1}^M -(\check{I}_m^{(1)} + I_m^{(2)}) \mathbf{m}_m(\mathbf{r}_t), \quad (3.17)$$

where $\mathbf{m}_m(\mathbf{r}_t)$ are unknown functions to be determined. Explicitly separating these fundamental unknowns from the other modal currents in Eq. (3.16) yields:

$$\sum_{i=1}^M -(\check{I}_i^{(1)} + I_i^{(2)}) \mathbf{h}_i(\mathbf{r}_t) = - \sum_{i=M+1}^{\infty} I_i^{(1)} \mathbf{h}_i(\mathbf{r}_t) + \sum_{i=M+1}^{\infty} I_i^{(2)} \mathbf{h}_i(\mathbf{r}_t), \quad \mathbf{r}_t \in S_a, \quad (3.18)$$

in the aperture. If we apply the equivalence theorem and subsequently the image theorem in the region comprised between two planes just above and just below the transition plane,

the original aperture problem is transformed into two separate problems, one for an homogeneous infinite medium like region 1 and the other for an homogeneous infinite medium like region 2, where the effect of the aperture is accounted for by the magnetic currents $2\mathbf{M}^{(1)}(\mathbf{r}_t)$ and $2\mathbf{M}^{(2)}(\mathbf{r}_t)$, respectively. The electric field tangent to the original aperture plane in each one of the two problems is related to these two currents by:

$$\hat{\mathbf{z}} \times 2\mathbf{M}(\mathbf{r}_t)^{(\gamma)} = \mathbf{E}_t(\mathbf{r}_t), \quad \gamma = 1, 2. \quad (3.19)$$

At this point, one can introduce the non-accessible constituent of the infinite array periodic GF, for the case of magnetic source and magnetic observation, $\bar{\mathbf{G}}_{na}^h$, as derived in Appendix C, Sec. C.2:

$$\bar{\mathbf{G}}^{h(\gamma)}(\mathbf{r}_t; \mathbf{r}'_t) = -2 \sum_{i=M+1}^{\infty} \left(Y_i^{(\gamma)}(\mathbf{k}_{t_i}, 0) \mathbf{h}_i(\mathbf{r}_t) \mathbf{h}_i^*(\mathbf{r}'_t) \right), \quad (3.20)$$

where $Y_i^{(\gamma)} = 1/(2Z_i^{(\gamma)})$ and $Z_i^{(\gamma)} = Z_{TE}^{(\gamma)} + Z_{TM}^{(\gamma)}$. In this case $Z_{TE}^{(\gamma)}$ and $Z_{TM}^{(\gamma)}$ are the modal characteristic impedances for the TE and TM modes in region $\gamma = 1, 2$.

Therefore, the non-accessible tangential magnetic field is:

$$\mathbf{H}_{na}^{(\gamma)} = \sum_{i=M+1}^{\infty} I_i^{(\gamma)} \mathbf{h}_i(\mathbf{r}_t) = \int_{S_a} 2\bar{\mathbf{G}}_{na}^{h(\gamma)}(\mathbf{r}_t; \mathbf{r}'_t) \cdot \mathbf{M}^{(\gamma)}(\mathbf{r}'_t) d\mathbf{r}'_t, \quad (3.21)$$

where $\gamma = 1, 2$. Substituting in Eq. (3.18) and using the fact that in (3.21) the magnetic currents on the two sides of the slots, $2\mathbf{M}^{(1)}(\mathbf{r}_t)$ and $2\mathbf{M}^{(2)}(\mathbf{r}_t)$, are equal in amplitude and opposite in sign ($2\mathbf{M}^{(1)}(\mathbf{r}_t) = -2\mathbf{M}^{(2)}(\mathbf{r}_t) = -2\mathbf{M}(\mathbf{r}_t)$), leads to

$$\begin{aligned} \sum_{i=1}^M -(\check{I}_i^{(1)} + I_i^{(2)}) \mathbf{h}_i(\mathbf{r}_t) &= -2 \int_{S_a} \bar{\mathbf{G}}_{na}^{h(1)}(\mathbf{r}_t; \mathbf{r}'_t) \cdot \mathbf{M}(\mathbf{r}'_t) d\mathbf{r}'_t - \\ &\quad - \int_{S_a} \bar{\mathbf{G}}_{na}^{h(2)}(\mathbf{r}_t; \mathbf{r}'_t) \cdot 2\mathbf{M}(\mathbf{r}'_t) d\mathbf{r}'_t, \quad \mathbf{r}_t \in S_a. \end{aligned} \quad (3.22)$$

Eq. (3.15) can then be expressed in a form that resembles Eq. (3.7), written for the patch FSS case:

$$\sum_{i=1}^M (\check{I}_i^{(1)} + I_i^{(2)}) \mathbf{h}_i(\mathbf{r}_t) = 2 \int_{S_a} \bar{\mathbf{G}}_{na}^h(\mathbf{r}_t; \mathbf{r}'_t) \cdot \mathbf{M}(\mathbf{r}'_t) d\mathbf{r}'_t, \quad \mathbf{r}_t \in S_a, \quad (3.23)$$

where $\bar{\mathbf{G}}_{na}^h(\mathbf{r}_t; \mathbf{r}'_t) = \left(\bar{\mathbf{G}}_{na}^{h(1)}(\mathbf{r}_t; \mathbf{r}'_t) + \bar{\mathbf{G}}_{na}^{h(2)}(\mathbf{r}_t; \mathbf{r}'_t) \right)$ is the sum of the GF of the two homogeneous infinite spaces, while in Eq. (3.8) it indicated the GF of the single half-space; this is the reason why in Eq. (3.23) a factor 2 appears.

Introducing the expression (3.17) for the equivalent magnetic current in terms of the modal current sums $-(\check{I}_i^{(1)} + I_i^{(2)})$, for $i = 1, \dots, M$, finally leads to:

$$\sum_{m=1}^M (\check{I}_i^{(1)} + I_i^{(2)}) \mathbf{h}_i(\mathbf{r}_t) = \sum_{m=1}^M -(\check{I}_i^{(1)} + I_i^{(2)}) \int_{S_a} 2\bar{\mathbf{G}}_{na}^h(\mathbf{r}_t; \mathbf{r}'_t) \cdot \mathbf{m}_i(\mathbf{r}'_t) d\mathbf{r}'_t, \quad \mathbf{r}_t \in S_a. \quad (3.24)$$

From this equation, which is valid over the entire domain of the slot, by equating the coefficients of the modal currents sums $(\check{I}_m^{(1)} + I_m^{(2)})$ with $m = 1, \dots, M$ one may obtain a single IE with a fixed kernel and as many forcing terms as the number of accessible modes:

$$\mathbf{h}_i(\mathbf{r}_t) = - \int_{S_a} 2\bar{\mathbf{G}}_{na}^h(\mathbf{r}_t; \mathbf{r}'_t) \cdot \mathbf{m}_i(\mathbf{r}'_t) d\mathbf{r}'_t, \quad \mathbf{r}_t \in S_a, \quad i = 1, \dots, M. \quad (3.25)$$

This IE is similar to the one obtained for the patch case (3.9), but the GF is now the one of homogeneous infinite spaces and the currents are doubled.

3.3.2 Multimode Equivalent Network

The solution of the IE in (3.25) provides the unknown functions $\mathbf{m}_m(\mathbf{r}_t)$. These functions, weighted by the coefficients (3.17), in each of the two homogeneous infinite spaces identified by applying the equivalence and image theorem, provide a representation of the equivalent magnetic current and consequently of the total tangential electric field in the aperture plane:

$$\mathbf{u}_z \times 2\mathbf{M}^{(\gamma)}(\mathbf{r}_t) = \mathbf{E}_t(\mathbf{r}_t), \quad \gamma = 1, 2. \quad (3.26)$$

The Floquet expansion of the electric fields can then be invoked to obtain a relationship between the modal voltages in the two media and the solutions $\mathbf{m}_j(\mathbf{r}_t)$:

$$\mathbf{E}_t(\mathbf{r}_t) = \sum_{m=1}^{\infty} V_m \mathbf{e}_m(\mathbf{r}_t) = -\mathbf{u}_z \times 2 \sum_{j=1}^M (\check{I}_j^{(1)} + I_j^{(2)}) \mathbf{m}_j(\mathbf{r}_t), \quad \text{in the aperture.} \quad (3.27)$$

To obtain the terminal conditions for the $N^{(1)}$ and $N^{(2)}$ mode lines of the transition, we perform the integral projection of Eq. (3.27) on the accessible modes \mathbf{e}_i with $i = 1..M$. After some algebraic manipulations, the accessible voltages and currents at the two sides of the FSS can be linked by an equivalent network characterized by a multimode impedance matrix connected in parallel to the TL's associated to the accessible modes. The conditions for voltages and currents at the terminal planes are expressed as:

$$V_i = - \sum_{j=1}^M Z_{ij} (\check{I}_j^{(1)} + I_j^{(2)}), \quad i = 1, \dots, M, \quad (3.28)$$

with

$$Z_{ij} = 2 \int_{U_c} \mathbf{m}_j(\mathbf{r}_t) \cdot \mathbf{h}_i^*(\mathbf{r}_t) d\mathbf{r}_t, \quad (3.29)$$

where U_c is the surface of the unit cell. If $N^{(1)} < N^{(2)}$ as in Fig. 3.3, the modes with index higher than $N^{(1)}$ arrive too attenuated to the terminal plane T_1 and can be considered as seeing an infinite transmission line terminated by a characteristic impedance. Consequently, the last $N^{(2)} - N^{(1)}$ ports of the equivalent impedance matrix are closed on the characteristic impedance of the corresponding modes of region 1, as shown in Fig. 3.5.

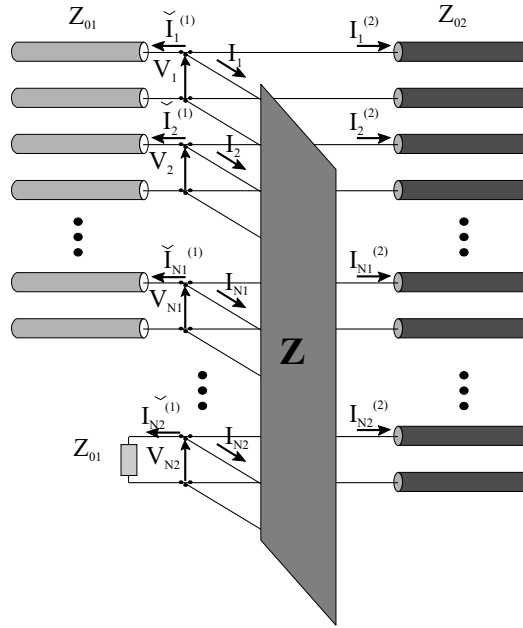


Figure 3.5: Multimode Equivalent Network of an FSS, made of infinitesimally thin slots, for which the aperture formulation of the IEMEN method has been used; the elements of the impedance matrix $[Z]$ are defined in Eq. (3.29).

The equivalent networks provided by Eq. (3.29) and Eq. (3.13) for the planar FSS, as admittance network and as impedance network, respectively, are not independent and can be obtained from each other by using well known microwave transformation formulas.

3.4 Thin layer problem

According to the IEMEN formulation, to derive the equivalent network of a patch transition, only the modes responsible for the energy exchange with the next discontinuity,

propagating or below cut-off, have to be accounted for as accessible at the ports of the network. These modes are extracted from the kernel of the corresponding IE and the information about their behavior in the z -direction is given at TL level, in terms of the equivalent network of the slab. The non-accessible modes, which appear in the kernel of the IE, are localized at the transition and see an infinite transmission line; therefore, the corresponding spectral GF is the one associated to two semi-infinite half-spaces in the patch approach (Sec. 3.2), and to the infinite space in the aperture approach (Sec. 3.3). In Chapter 6, it will be demonstrated that, for small domain basis function expansion in the frame of a MoM solution of the IE, the conditioning of the MoM system matrix deteriorates for an increasing number of accessible modes. Therefore, it is in general desirable to restrict the number of accessible modes; in the IEMEN formulation, this is possible for thick dielectric layers or terminal planes far from the discontinuity. To tackle the problem of a very thin slab, where a large number of accessible modes should be included in the analysis, instead of extracting from the kernel of the IE all the modes that behave like accessible, we select only a few of them, and include the information about the finiteness of the dielectric directly in a multi-layer spectral GF. This approach was already suggested in [94] for the GSM formulation and is implemented here to the reduced kernel IE obtained by applying the IEMEN method. It is clear that the minimum number of modes to be still treated as accessible is the number of propagating ones.

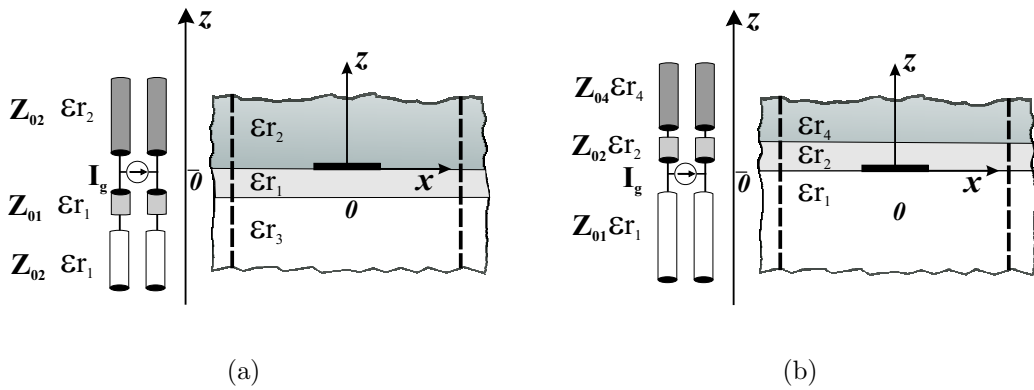


Figure 3.6: Unit cell of a patch FSS etched on a thin dielectric slab and corresponding equivalent transmission line circuit. (a) Patch etched above the slab. (b) Patch etched below the slab.

Let us consider, for example, a patch FSS etched on a very thin board; a unit cell is shown

in Fig. 3.6a. Usually, this transition is described as in Sec. 3.2 by means of Eq. (3.7):

$$\sum_{i=1}^N V_i \mathbf{e}_i(\mathbf{r}_t) = - \int_{S_p} \bar{\mathbf{G}}_{na}^e(\mathbf{r}_t; \mathbf{r}'_t) \cdot \mathbf{J}(\mathbf{r}'_t) d\mathbf{r}'_t, \quad (3.30)$$

where N is now the number of accessible modes in the thin slab. $\bar{\mathbf{G}}_{na}^e$ is the periodic non-accessible GF (semi-infinite half-space), for the case of electric source and electric observation, whose expression in terms of Floquet modes has been derived in Appendix C, Sec. C.2:

$$\bar{\mathbf{G}}_{na}^e(\mathbf{r}; \mathbf{r}') = - \sum_{i=N+1}^{\infty} \left(Z_i(\mathbf{k}_{t_i}, 0) \mathbf{e}_i(\mathbf{r}_t) \mathbf{e}_i^*(\mathbf{r}'_t) \right). \quad (3.31)$$

Alternatively, we can write the left-hand side of Eq. (3.30) as dependent only on the first N_r accessible modes and include the remaining accessible modes in the kernel:

$$\sum_{i=1}^{N_r} V_i \mathbf{e}_i(\mathbf{r}_t) = - \int_{S_p} \bar{\mathbf{G}}_{na(r)}^e(\mathbf{r}_t; \mathbf{r}'_t) \cdot \mathbf{J}(\mathbf{r}'_t) d\mathbf{r}'_t, \quad (3.32)$$

where now

$$\bar{\mathbf{G}}_{na(r)}^e(\mathbf{r}; \mathbf{r}') = - \sum_{i=N_r+1}^{\infty} \left(Z_i(\mathbf{k}_{t_i}, 0) \mathbf{e}_i(\mathbf{r}_t) \mathbf{e}_i^*(\mathbf{r}'_t) \right). \quad (3.33)$$

The impedances $Z_i(\mathbf{k}_{t_i}, 0)$ are obtained by connecting in parallel the input impedances on the left and right of the FSS, as shown in the equivalent circuit at the side of Fig. 3.6a:

$$Z_i(\mathbf{k}_{t_i}, 0) = \frac{Z_{1i}(\mathbf{k}_{t_i}, 0) Z_{2i}(\mathbf{k}_{t_i}, 0)}{Z_{1i}(\mathbf{k}_{t_i}, 0) + Z_{2i}(\mathbf{k}_{t_i}, 0)}, \quad (3.34)$$

in which

$$Z_{1i}(\mathbf{k}_{t_i}, 0) = Z_{01i}(\mathbf{k}_{t_i}, 0) \frac{Z_{03i}(\mathbf{k}_{t_i}, 0) + j Z_{01i}(\mathbf{k}_{t_i}, 0) \tan(\kappa_{1i} l_1)}{Z_{01i}(\mathbf{k}_{t_i}, 0) + j Z_{03i}(\mathbf{k}_{t_i}, 0) \tan(\kappa_{1i} l_1)}, \quad (3.35a)$$

$$Z_{2i} = Z_{02i}. \quad (3.35b)$$

The GF now depends on the input impedance at the two sides of the transition. The same procedure can be followed to model the case in Fig. 3.6b, where the patch is etched on a semi-infinite dielectric half-space and is covered by a thin dielectric slab. In this case, the impedances $Z_i(\mathbf{k}_{t_i}, 0)$ in the expression of the multi-layer spectral GF become:

$$Z_i(\mathbf{k}_{t_i}, 0) = \frac{Z_{1i}(\mathbf{k}_{t_i}, 0) Z_{2i}(\mathbf{k}_{t_i}, 0)}{Z_{1i}(\mathbf{k}_{t_i}, 0) + Z_{2i}(\mathbf{k}_{t_i}, 0)}, \quad (3.36)$$

in which

$$Z_{1i}(\mathbf{k}_{t_i}, 0) = Z_{01i}(\mathbf{k}_{t_i}, 0), \quad (3.37a)$$

$$Z_{2i}(\mathbf{k}_{t_i}, 0) = Z_{02i}(\mathbf{k}_{t_i}, 0) \frac{Z_{04i}(\mathbf{k}_{t_i}, 0) + j Z_{02i}(\mathbf{k}_{t_i}, 0) \tan(\kappa_{2i} l_2)}{Z_{02i}(\mathbf{k}_{t_i}, 0) + j Z_{04i}(\mathbf{k}_{t_i}, 0) \tan(\kappa_{2i} l_2)}, \quad (3.37b)$$

and the corresponding equivalent circuit is shown at the side of Fig. 3.6b.

3.5 Solution of the integral equation

The IE that characterizes transitions inside waveguides (Eq. (2.33) in Chapter 2) or transitions from waveguides to periodically loaded free spaces (Eq. (2.61) in Chapter 2), as well as those appearing in (3.9) and (3.25) can be solved with the aid of MoM procedures [66]. Depending on the specific geometries of the elements composing the FSS, different sets of basis functions can be adopted. In the case of waveguide transitions, it is convenient to adopt the waveguide modes of the smaller waveguide as basis functions. This choice has several advantages. First, techniques are available to extract the frequency dependence from the quasi-static part of the IE's kernel [62]. Second, the reaction integrals that appear in the MoM matrix can be reused to build the equivalent network matrix entries in Eq. (2.15), which reduces the required computation time. Third, a modal expansion of the unknowns, using modes of order at least equal to the highest accessible mode, guarantees the convergence of the solution without conditioning problems.

For more general structures, like patch- or slot-based FSS's that contain non canonical geometries, a sub domain basis functions approach turns out to be more convenient, since it is capable of representing sharp discontinuities [121]. For example, for the patch case described by the IE (3.9), each unknown current $\mathbf{j}_i(\mathbf{r}_t)$ is expanded in terms of N_f basis functions, centered in $\mathbf{r}_{t_k} \equiv (x_k, y_k)$ for $k = 1, \dots, N_f$:

$$\mathbf{j}_i(\mathbf{r}_t) = \sum_{k=1}^{N_f} I_k^{(i)} \mathbf{f}_k(\mathbf{r}_t - \mathbf{r}_{t_k}). \quad (3.38)$$

Applying the MoM with a Galerkin's procedure to Eq. (3.9) and substituting this expression of the unknowns leads to:

$$\int_{S_p} \mathbf{e}_i(\mathbf{r}_t) \cdot \mathbf{f}_l(\mathbf{r}_t - \mathbf{r}_{t_l}) = - \sum_{k=1}^{N_f} I_k^{(i)} \iint_{S_p} \mathbf{f}_k(\mathbf{r}'_t - \mathbf{r}_{t_k}) \cdot \bar{\mathbf{G}}_{na}^e(\mathbf{r}_t; \mathbf{r}'_t) \cdot \mathbf{f}_l(\mathbf{r}_t - \mathbf{r}_{t_l}) d\mathbf{r}'_t d\mathbf{r}_t, \quad (3.39)$$

where $i = 1, \dots, M$ and $l = 1, \dots, N_f$. Let us now introduce the expression of the electric field non-accessible GF in terms of the spectral coordinates (as derived in Appendix C, Sec. C.2), for $z = z' = 0$:

$$\begin{aligned} \bar{\mathbf{G}}_{na}^e(\mathbf{r}_t; \mathbf{r}'_t) &= \frac{1}{d_x d_y} \sum_{p=M+1}^{\infty} \left(G_{\text{TM}}^e(\mathbf{k}_{tp}, 0) \hat{\mathbf{k}}_{tp} \hat{\mathbf{k}}_{tp} + G_{\text{TE}}^e(\mathbf{k}_{tp}, 0) \hat{\boldsymbol{\alpha}}_p \hat{\boldsymbol{\alpha}}_p \right) e^{-j\mathbf{k}_{tp} \cdot (\mathbf{r}_t - \mathbf{r}'_t)}, \\ &= \frac{1}{d_x d_y} \sum_{p=M+1}^{\infty} \tilde{\mathbf{G}}^e(\mathbf{k}_{tp}, 0) e^{-j\mathbf{k}_{tp} \cdot (\mathbf{r}_t - \mathbf{r}'_t)}, \end{aligned} \quad (3.40)$$

where $\hat{\mathbf{k}}_t$, $\hat{\boldsymbol{\alpha}}$ and \mathbf{u}_z are the unit basis vectors of a polar reference system in the spectral domain, defined as:

$$\hat{\mathbf{k}}_t = \frac{1}{k_t}(k_x \mathbf{u}_x + k_y \mathbf{u}_y), \quad (3.41)$$

$$\hat{\boldsymbol{\alpha}} = \mathbf{u}_z \times \hat{\mathbf{k}}_t = \frac{1}{k_t}(k_x \mathbf{u}_y - k_y \mathbf{u}_x), \quad (3.42)$$

and where the spectral dyadic infinite array GF, for the case of electric source and electric observation, has been expressed in a compact form as (Appendix C, Sec. C.2):

$$\tilde{\mathbf{G}}^e(\mathbf{k}_{tp}, 0) = G_{\text{TM}}^e(\mathbf{k}_{tp}, 0) \hat{\mathbf{k}}_{tp} \hat{\mathbf{k}}_{tp} + G_{\text{TE}}^e(\mathbf{k}_{tp}, 0) \hat{\boldsymbol{\alpha}}_p \hat{\boldsymbol{\alpha}}_p. \quad (3.43)$$

If we write the Floquet vector mode functions as

$$\mathbf{e}_i(\mathbf{r}_t) = \mathbf{e}'_i e^{-j(\mathbf{k}_i \cdot \mathbf{r}_t)}, \quad (3.44)$$

and we use the definition of the spatial Fourier transform (Appendix A, Eq. (A.116a)):

$$\tilde{\mathbf{f}}(\mathbf{k}_t) = \int_{S_p} \mathbf{f}(\mathbf{r}_t) e^{j(\mathbf{k}_t \cdot \mathbf{r}_t)} d\mathbf{r}_t \quad (3.45)$$

and the definition of the non-accessible GF (3.40), the EFIE (3.39) becomes:

$$\begin{aligned} \mathbf{e}'_i \cdot \tilde{\mathbf{f}}_l(-\mathbf{k}_{t_i}) e^{-j(\mathbf{k}_{t_i} \cdot \mathbf{r}_{t_i})} = & \sum_{k=1}^{N_f} I_k^{(i)} \left[-\frac{1}{d_x d_y} \sum_{p=M+1}^{\infty} \tilde{\mathbf{f}}_l(-\mathbf{k}_{tp}) \cdot \tilde{\mathbf{G}}^e(\mathbf{k}_{tp}, 0) \right. \\ & \left. \cdot \tilde{\mathbf{f}}_k(\mathbf{k}_{tp}) e^{-j\mathbf{k}_{tp} \cdot (\mathbf{r}_{t_i} - \mathbf{r}_{t_k})} \right]. \end{aligned} \quad (3.46)$$

If sub-domain basis functions are used to expand the unknown currents, the evaluation of the MoM matrix entries can become cumbersome, essentially because of two reasons:

1. when the element geometry contains corners (for example crosses), a large number of sub-domain basis functions is necessary;
2. for high order accessible modes, and accordingly for an IE with spatially fast varying incident fields, a large number of unknowns are necessary to correctly represent the behavior of the currents induced on the patches or slots.

In these cases, the reaction integrals involve the calculation of the periodic (non-accessible) Green's functions for high values of the Floquet-mode indices. In the present implementation, these integrals have been greatly accelerated by extracting the quasi-static contribution of the mutual coupling itself. The followed procedure closely resembles the

one presented by Wilton et al. [130] and is based on the Kummer transformation [2]. This transformation separates the slowly converging quasi-static contributions from the rapidly converging (low spectrum) ones, in the IE kernel obtained after using the MoM for Eqs. (3.9) and (3.25). However, in [130] the acceleration method was developed for the case of scalar, free-space GF, while in [82] it has been extended to the dyadic multi-layer GF. In the following, the key points of this acceleration technique will be recalled, but the interested reader is encouraged to refer to [82] for further details.

Let us now write the kernel of Eq. (3.46) with the explicit dependence on the double mode index (m, n) corresponding to the p -th mode, for the case of a rectangular lattice:

$$\frac{1}{d_x d_y} \sum_{m=M+1}^{\infty} \sum_{n=M+1}^{\infty} \tilde{\mathbf{f}}_l(-k_{x_m}, -k_{y_n}) \cdot \tilde{\mathbf{G}}^e(k_{x_m}, k_{y_n}, 0) \cdot \tilde{\mathbf{f}}_k(k_{x_m}, k_{y_n}) e^{-jk_{x_m}(x_l-x_k)} e^{-jk_{y_n}(y_l-y_k)}. \quad (3.47)$$

To apply the Kummer transformation to this kernel, we have to calculate the asymptotic form of the dyadic GF of a stratified medium, for large values of the transverse wavenumber components k_{x_m} and k_{y_n} , such that

$$\kappa_p = \sqrt{k^2 - (k_{x_m}^2 + k_{y_n}^2)} \stackrel{\text{a.e.}}{=} -j|\mathbf{k}_t|, \quad m, n \rightarrow \infty. \quad (3.48)$$

For example, the GF of two semi-infinite dielectric layers approaches the GF of a homogeneous medium with a permittivity equal to the average of the two media permittivities: $\varepsilon_r = \frac{\varepsilon_{r1} + \varepsilon_{r2}}{2}$. Therefore, its expression in Cartesian coordinates (derived in Appendix C, Eq. (C.42a)), assumes the following asymptotic form:

$$\begin{aligned} G_{xx}^e &= -\frac{\zeta_0}{k_0} \left(\frac{k_0^2}{\kappa_1 + \kappa_2} - \frac{k_x^2}{\kappa_1 \varepsilon_{r2} + \kappa_2 \varepsilon_{r1}} \right) \rightarrow -j \frac{\zeta_0}{k_0} \left(-\frac{k_x^2}{k_t(\varepsilon_{r2} + \varepsilon_{r1})} \right) = G_{xx}^{ea}, \\ G_{xy}^e &= -\frac{\zeta_0}{k_0} \left(-\frac{k_x k_y}{\kappa_1 \varepsilon_{r2} + \kappa_2 \varepsilon_{r1}} \right) \rightarrow j \frac{\zeta_0}{k_0} \left(\frac{k_x k_y}{k_t(\varepsilon_{r2} + \varepsilon_{r1})} \right) = G_{xy}^{ea}, \end{aligned} \quad (3.49)$$

where the superscript a stands for asymptotic. Furthermore, following a procedure introduced in [130], a smoothing parameter has been introduced in the expression of the transverse wavenumber which affects the convergence of the IE kernel:

$$k_u^2 = k_{x_m}^2 + k_{y_n}^2 + u^2 = |k_{t_i}|^2 + u^2, \quad (3.50)$$

so that the asymptotic expression of κ_p becomes

$$\kappa_p = \sqrt{k^2 + u^2 - k_{t_p}^2 - u^2} \stackrel{\text{a.e.}}{=} -j\sqrt{k_u^2}, \quad m, n \rightarrow \infty. \quad (3.51)$$

The inclusion of the smoothing parameter u guarantees that the asymptotic approximation of the GF in the spacial domain decays exponentially. The choice of its value is the result of a trade-off: the higher is u , the faster is the convergence of the spatial series and the slower that of the spectral series, and viceversa.

If we now apply the Kummer transformation to the series in Eq. (3.47) and add and subtract the asymptotic expression for the kernel (containing the spectral asymptotic GF $\tilde{\mathbf{G}}^a(k_{x_m}, k_{y_n})$), we obtain:

$$\begin{aligned} & \frac{1}{d_x d_y} \sum_{m=-\infty}^{\infty} \sum_{n=-\infty}^{\infty} \tilde{\mathbf{f}}_l(-k_{x_m}, -k_{y_n}) \cdot (\tilde{\mathbf{G}}(k_{x_m}, k_{y_n}) - \tilde{\mathbf{G}}^a(k_{x_m}, k_{y_n})) \cdot \tilde{\mathbf{f}}_k(k_{x_m}, k_{y_n}) \\ & e^{-jk_{x_m}(x_l - x_k)} e^{-jk_{y_n}(y_l - y_k)} + \frac{1}{d_x d_y} \sum_{m=-\infty}^{\infty} \sum_{n=-\infty}^{\infty} \tilde{\mathbf{f}}_l(-k_{x_m}, -k_{y_n}) \\ & \cdot \tilde{\mathbf{G}}^a(k_{x_m}, k_{y_n}) \cdot \tilde{\mathbf{f}}_k(k_{x_m}, k_{y_n}) e^{-jk_{x_m}(x_l - x_k)} e^{-jk_{y_n}(y_l - y_k)}, \end{aligned} \quad (3.52)$$

where, to simplify the notation, we have omitted the superscript e . At this point, after that the inverse Poisson summation and the inverse Fourier transformation of the basis and test functions and of the asymptotic GF have been performed, the last term of Eq. (3.52) becomes the summation of quadruple convolution and projection integrals

$$\sum_{m=-\infty}^{\infty} \sum_{n=-\infty}^{\infty} (\mathcal{S}_x)^m (\mathcal{S}_y)^n \int_{D_{x_k}} \int_{D_{y_k}} \int_{D_{x_l}} \int_{D_{y_l}} \mathbf{f}_l(\mathbf{r}_t) \cdot \bar{\mathbf{G}}^a(\mathbf{r}_t, \mathbf{r}'_t) \cdot \mathbf{f}_k(\mathbf{r}'_t) d\mathbf{r}_t d\mathbf{r}'_t, \quad (3.53)$$

with the integration domains:

$$D_{x_k} = [(x_k + md_x) - l_x/2, (x_k + md_x) + l_x/2], \quad (3.54)$$

$$D_{y_k} = [(y_k + nd_y) - l_y/2, (y_k + nd_y) + l_y/2], \quad (3.55)$$

$$D_{x_l} = [x_l - l_x/2, x_l + l_x/2], \quad (3.56)$$

$$D_{y_l} = [y_l - l_y/2, y_l + l_y/2], \quad (3.57)$$

for an array of rectangular patches of dimensions l_x and l_y along the x and y directions, with unit cell dimensions d_x and d_y respectively (according to Fig. C.1 in Appendix C). In Eq. (3.53), the terms

$$(\mathcal{S}_x)^m (\mathcal{S}_y)^n = e^{-jmd_x k_{x_0}} e^{-jnd_y k_{y_0}}, \quad (3.58)$$

introduce the phase shift associated to the phased array, the functions $\mathbf{f}_k(\mathbf{r}_t)$ and $\mathbf{f}_l(\mathbf{r}_t)$ are the inverse Fourier transforms of $\tilde{\mathbf{f}}_k(k_x, k_y)$ and $\tilde{\mathbf{f}}_l(k_x, k_y)$, respectively, and the dyadic operator $\bar{\mathbf{G}}^a(\mathbf{r}_t, \mathbf{r}'_t)$ is the inverse Fourier transform of $\tilde{\mathbf{G}}^a(k_{x_m}, k_{y_n})$:

$$\bar{\mathbf{G}}^a(\mathbf{r}_t, \mathbf{r}'_t) = -j \frac{1}{4\pi} \frac{\zeta_0}{k_0} \frac{2}{\varepsilon_{r2} + \varepsilon_{r1}} \begin{pmatrix} \frac{\partial^2}{\partial x \partial x'} & \frac{\partial^2}{\partial x \partial y'} \\ \frac{\partial^2}{\partial y' \partial x'} & \frac{\partial^2}{\partial y' \partial y'} \end{pmatrix} \frac{e^{-u|\mathbf{r}_t - \mathbf{r}'_t|}}{|\mathbf{r}_t - \mathbf{r}'_t|}. \quad (3.59)$$

The quadruple convolution and projection integrals in (3.53) have been solved in [82], for the case in which the unknown is expanded by means of piecewise linear (pwl) functions, by applying a technique proposed in [25], which consists of transforming these quadruple integrals into a summation of double integrals.

For broadside incidence, the asymptotic form of the GF can be calculated for the static wavenumber ($k_{x_0}, k_{y_0} \rightarrow 0 \Rightarrow k_{x_m}^a = \frac{2\pi m}{d_x}$ and $k_{y_m}^a = \frac{2\pi n}{d_y}$), outside the frequency and angle loop. In this case, the exponentials (3.58) no longer depend on the mode indices m, n , and can be extracted from the series.

A more detailed discussion on the problem of identifying the most suitable basis functions for the solution of the reduced kernel IE will follow in Chapter 6.

3.6 Numerical results

The IEMEN approach has been implemented in a software tool that allows analyzing waveguide phased arrays integrated with multi-layer patch- and slot-based FSS's and dielectric radomes. Using the formulation for waveguide junctions, the tool is also able to analyze feeding and filtering elements inside the waveguide. Moreover, thanks to the modularity of the underlying IEMEN formulation, the developed software can also make use of the results provided by commercial packages based on other techniques. This feature is very useful when the structure to be analyzed contains complex radiating elements or components of the array feeding structure that cannot be easily interpreted in terms of waveguides and waveguide junctions. In this case, their equivalent network representation can be derived by means of other packages and then cascaded, in the IEMEN-based tool, to the equivalent network of the other elements of the structure.

In this section, the analysis capabilities of our tool are demonstrated by presenting some representative examples. They concern FSS's under plane-wave incidence. In fact, whatever is the source we are dealing with, we can always expand the radiated electromagnetic field in terms of plane waves. In particular, the TE_{00} and TM_{00} Floquet waves are used to simulate a TE or TM plane wave impinging on the FSS, respectively.

The unknown currents are expanded in terms of pwl functions. The expression of the pwl

centered in $x_c = 0$ is:

$$\text{pwl}(x) = \frac{2}{\ell} \left(\frac{\ell}{2} - |x| \right) \quad |x| \leq \frac{\ell}{2}, \quad (3.60)$$

where ℓ is length of the the pwl function. The Fourier transform is:

$$\text{PWL}(k_x) = \frac{\ell}{2} \left(\frac{\sin\left(\frac{k_x \ell}{4}\right)}{\left(\frac{k_x \ell}{4}\right)} \right)^2. \quad (3.61)$$

The analysis were performed on an Intel Pentium 4 PC, with CPU of 1.6 GHz and RAM of 256 MB. For the sake of completeness, the calculation time has been indicated for each example. However, it should be noticed that this time is strictly related to the technique adopted to solve the IE (accelerated MoM, as described in Sec. 3.5), and did not represent the main issue in the development of the IEMEN method.

3.6.1 Free-standing FSS

First, we have tested the program for free-standing FSS's; in this case, only one accessible mode had to be included in the analysis. Fig. 3.7 shows the magnitude and phase of the reflection coefficient of a free-standing infinite array of conducting patches, 13.3 mm long and 2.38 mm wide, arranged in a rectangular lattice of dimensions 15.2 mm \times 7.6 mm (the unit cell geometry is given in the inset), under TE plane-wave incidence. The incidence is almost broadside (to compare with [32], we have considered the same angle of incidence: $\vartheta = 1^\circ$). Twenty-four pwl functions were used to expand the unknown currents on the patch. The acceleration was performed with extraction of the quasi-static asymptotic part of the GF, and the kernel was calculated with a relative precision of $e_r = 10^{-6}$, which resulted in a MoM matrix with condition number¹ $n_c = 10^4$. This implies, according to [115], an accuracy on the result of $e_r * n_c = 10^{-2}$. The calculation time for ten frequency points was 16 minutes. The results obtained by [32] for the same kind of basis and testing functions are included for comparison and the agreement is very good.

In Fig. 3.8 the magnitude and phase of the reflection coefficient of a free-standing infinite array of Jerusalem cross patches is shown for normal plane-wave incidence. The element geometry is indicated in the inset of Fig. 3.8; the crosses are arranged in a square lattice

¹The condition number is calculated as product between the norm of the matrix and the estimated norm of the inverse matrix; as norm of a matrix we consider the maximum of the sum of the absolute value of the row elements

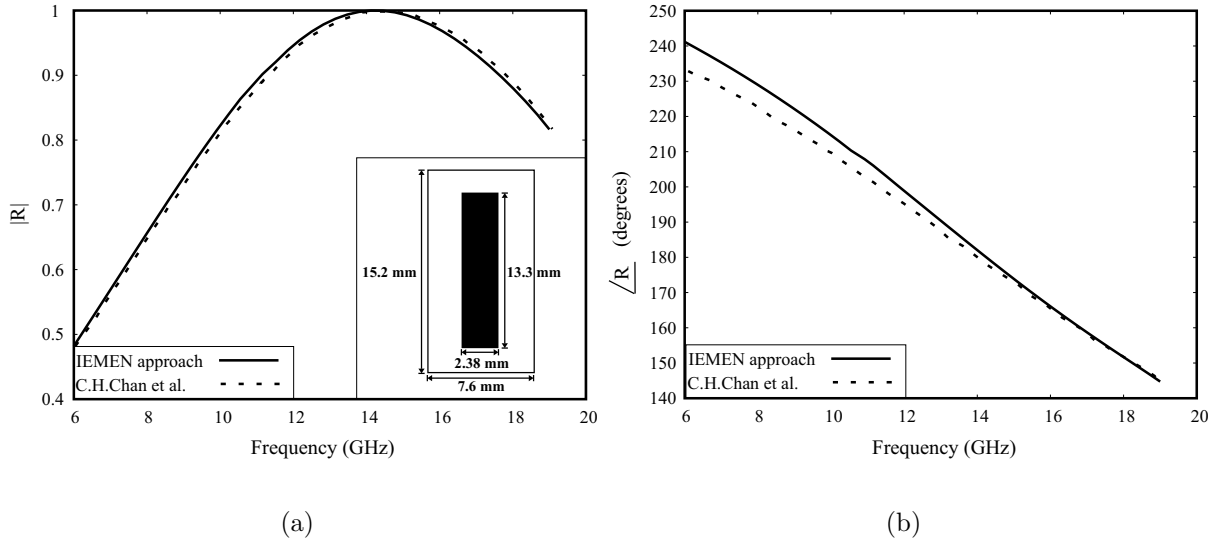


Figure 3.7: Reflection coefficient of the patch-based FSS in [32]: comparison between the IEMEN simulation results and the results reported by Chan *et al.* in [32], for a pwl-based expansion of the currents. (a) Magnitude of the reflection coefficient. (b) Phase of the reflection coefficient.

and the cell dimension is 1.52 mm. The results obtained by applying the IEMEN approach, using 20 pwl functions to expand the unknowns, are displayed together with those presented in [94], where a roof-top expansion with 584 unknowns was employed. The number of Floquet waves summed in the kernel was chosen such that a relative precision of $e_r = 10^{-6}$ is guaranteed, which leads to a MoM matrix with a condition number of $n_c = 10^5$. Hence, this result is accurate up to at least the first digit after the decimal point. The calculation time for ten frequency points was 43 minutes. The agreement with the results presented in [94] is excellent.

Fig. 3.9 shows the power reflection coefficient in log scale for a free-standing infinite cross-dipole FSS. The elements are arranged in a square lattice with cell dimension 2.44 mm, and the geometry is indicated in the inset. The results obtained with the IEMEN method, where 68 pwl functions were used to expand the unknowns, are compared with those obtained by expanding the currents on the patch with entire-domain basis functions derived by means of the Boundary Contour Mode Matching (BCMM) method [122]. These functions are defined as the eigenmodes of a uniform waveguide with the same cross section as the patch, and are expressed as a combination of Bessel and trigonometric functions [54]. The simulation of the FSS in Fig. 3.9 required 25 of these expanding eigenfunctions. The

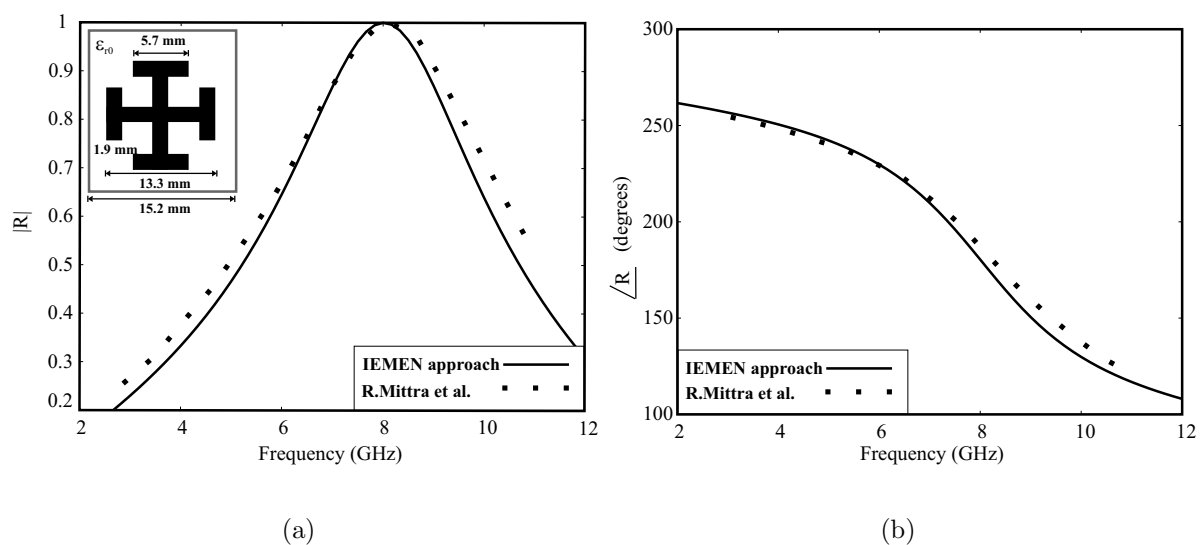


Figure 3.8: Reflection coefficient of a Jerusalem-cross based FSS: comparison between the IEMEN simulations results and those reported by Mittra in [94] for pwl expansion. (a) Magnitude of the reflection coefficient. (b) Phase of the reflection coefficient.

calculation time for ten frequency points when using the IEMEN method was 2 hours and 42 minutes. Again, agreement is excellent.

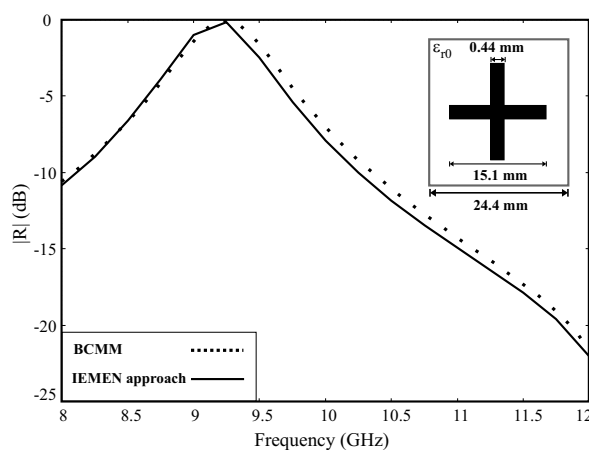


Figure 3.9: Magnitude of the reflection coefficient of a free-standing crossed-dipole FSS: comparison between the IEMEN simulation results, based on a pwl expansion of the unknown currents, and those obtained with the BCMM approach, using entire domain basis functions.

3.6.2 Multi-layer FSS

Subsequently, our approach was applied to the analysis of multi-layer FSS's, consisting of metal plates and dielectric slabs. In this case, the modeling of the structure required cascading the equivalent networks of each layer and the network of the transitions were mode coupling occurs, as explained in Sec. 3.1.

Fig. 3.10 shows the power reflection coefficient of an infinite array of crossed dipoles printed on a dielectric slab, versus the slab thickness indicated with a (the unit cell and element geometry is shown in the inset). The simulations were performed for three different permittivities of the slab, when a TE polarized plane wave is impinging on the FSS plate almost at broadside (the angle of incidence $\vartheta = 1^\circ$ has been used to compare with [94]). The unknown currents were expanded in terms of 20 pwl's, and one accessible mode was included in the analysis. The results based on the IEMEN method are displayed in Fig. 3.10, together with those obtained by expanding the unknowns with 25 entire-domain basis functions derived by means of the BCMM method, and with the results presented in [94], based on a GSM approach. The calculation time for ten frequency points when using the IEMEN method was 19 minutes for each permittivity value. The agreement is again remarkable.

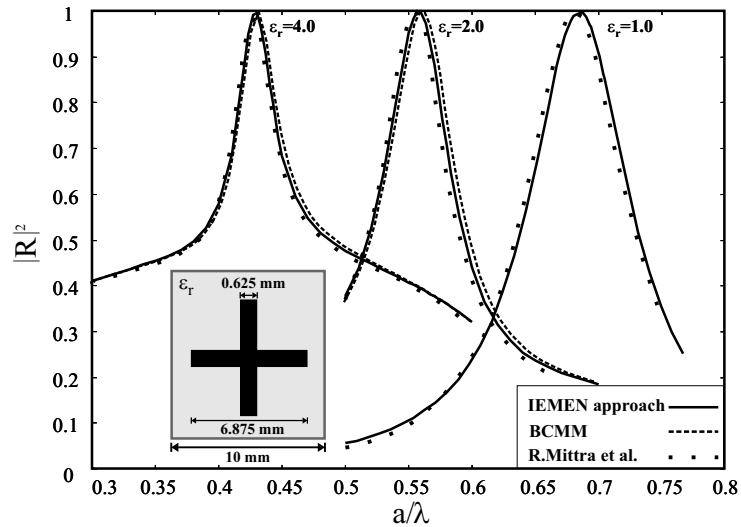


Figure 3.10: Power reflection coefficient of a crossed-dipole FSS printed on a dielectric slab: comparison between the IEMEN simulation results and those reported by Mittra in [94].

Furthermore, we have analyzed an FSS, proposed in [100], consisting of an infinite array of Jerusalem cross patches, arranged in square lattice, with cell dimension 5.091 mm, embedded in a dielectric slab of permittivity $\epsilon_r = 2.2$ and total thickness 1.016 mm.

The dimensions of the cross are specified in the inset of Fig. 3.11. This figure shows the magnitude of the reflection coefficient for TE and TM plane-wave incidence at an angle of $\vartheta = 45^\circ$ on the E -plane, obtained by using 104 pwl's to expand the unknown currents and by including 14 accessible modes in the analysis. At the end of the slab, the accessible modes are attenuated by a factor 1.37, defined as $1/e^{-\alpha l} = e^{\alpha l}$, where the propagation constant of a mode under cut-off is $k_z = j\alpha l$ and l is the thickness of the slab. Although this attenuation value is low, we have observed that considering more accessible modes does not lead to a significant change in the results. In fact, as shown in Fig. 3.11 excellent agreement is achieved with those presented by Munk in [100]. The IE kernel was calculated with a relative precision of $e_r = 10^{-6}$ and the calculation time for ten frequency points was about four hours.

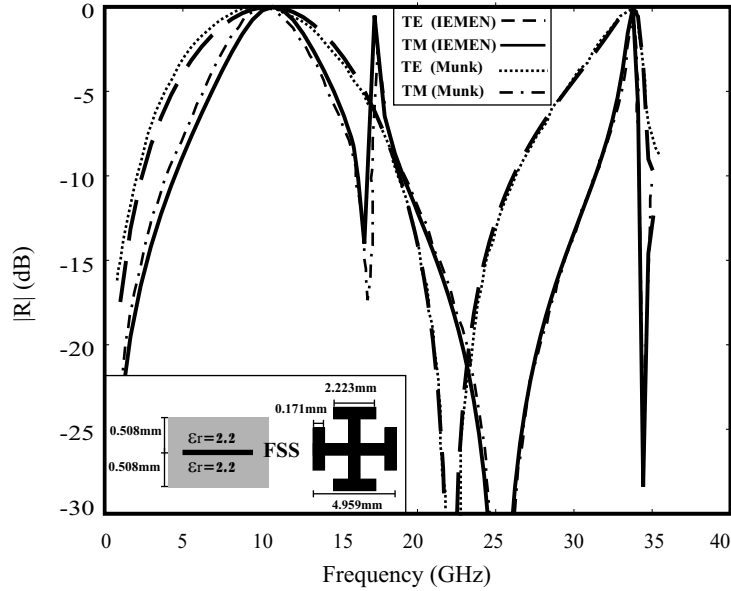


Figure 3.11: Magnitude of the reflection coefficient of a Jerusalem cross FSS embedded in a dielectric slab: comparison between the IEMEN simulation results and those reported by Munk in [100].

3.7 Conclusions

In this chapter we have described the IEMEN formulation for the derivation of a multimode equivalent network representation of patch- and slot-based FSS's, and we have applied this formulation to the analysis of some simple free-standing and multi-layer structures. Unlike

conventional microwave network techniques, the IEMEN method formulates the scattering problem in terms of a single IE with multiple forcing terms, one for each accessible mode, and with a fixed kernel, containing only the contribution of the localized modes. This original formulation leads *directly* to a reduced equivalent network, with the ports corresponding to the interacting modes only, which, to the authors best knowledge, constitutes the distinguishing feature of the IEMEN approach compared to other analysis techniques for FSS's.

The reduced kernel appearing in the IE is almost frequency independent for all kinds of discontinuities, since the contribution of the modes that vary strongly with the frequency has been extracted. Therefore, the full characterization of a transition in terms of its equivalent network can be performed only for a couple of frequency points and the results can then be interpolated in a broader frequency range. This aspect will be further discussed in Chapter 4, where we will show how it can be exploited for the design of an FSS.

Moreover, the IEMEN formulation has been extended to include the case of very thin layers. In a straightforward application of this method, an overwhelming number of accessible modes would be required to characterize a FSS sandwiched between these layers, which would lead to an ill-conditioned (reduced) MoM matrix. By exploiting the GF formulation introduced in Sec. 3.2, we have included the possibility of accounting for the finiteness of the slab also at the level of the the accessible modes kept inside the kernel, through the multi-layer (reduced) GF.

Furthermore, the calculation of the IE's kernel has been accelerated by following the technique proposed in [82], which is based on the Kummer transformation. The asymptotic form of the GF is calculated for large values of the modal transverse wavenumber, resorting for broadside incidence to the quasi-static limit. A fast convergence of the asymptotic term was insured by introducing a smoothing parameter, as already suggested in [130].

Chapter 4

FSS design

Historically, FSS's have been designed as stand-alone elements and only in a second phase they were used in antenna systems. Nowadays, stringent requirements for naval and airborne radar applications demand a change in the design strategy. In a ship's topside, for example, FSS's form an integral part of the antennas, both as additional protecting structures and as band-stop filters for the signals outside the antenna band. If two antennas, located close to each other, operate in overlapping frequency bands, an interference problem arises. In this chapter, the design of an appropriate FSS is proposed to circumvent this problem and the design procedure is described in detail in Sec. 4.1. A preliminary design, based on a single-mode transmission line (TL) circuit, is subsequently refined by applying the Integral Equation formulation for the derivation of a Multimode Equivalent Networks (IEMEN), described in Chapter 3, Sec. 3.2. Because of the inherent modularity, this method is a highly suitable instrument for the design. The distinguishing features of the IEMEN-based design procedure are outlined in Sec. 4.1.3 and conclusions are drawn in Sec. 4.2.

4.1 Description of the design problem

In this section, we present the design of an FSS structure that should be integrated with a waveguide phased array, representative of the complexity required in actual Multi Frequency Radar (MFR) arrays. The array, shown in Fig. 4.1a, consists of waveguide apertures of width $a=20$ mm and height $b=8$ mm, arranged in a triangular grid characterized by $d_1=21$ mm, $d_2=13.83$ mm and skew angle $\Omega = 40.6^\circ$. This antenna operates with a reflection coefficient of -10 dB over the entire X-band (8 - 12 GHz) and is capable of scanning in the H -plane until 30° . In Fig. 4.2, the reflection coefficient of the array antenna

is reported as a function of the frequency for various scan angles. The simulations were performed for an infinite array radiating in free space.

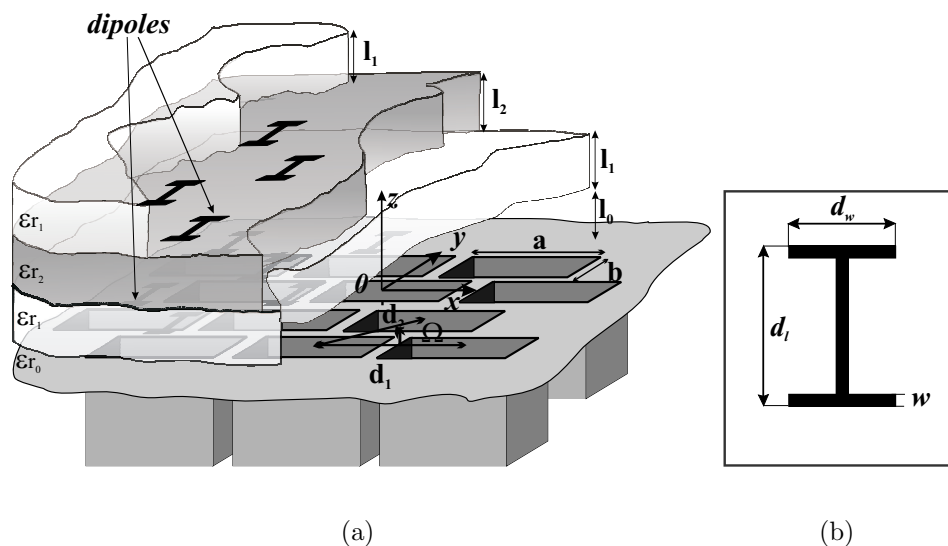


Figure 4.1: Geometry of the the waveguide phased array considered as basis for the FSS design described in this chapter. (a) The array integrated with a multi-layer dipole-based FSS. (b) Geometry of the FSS element.

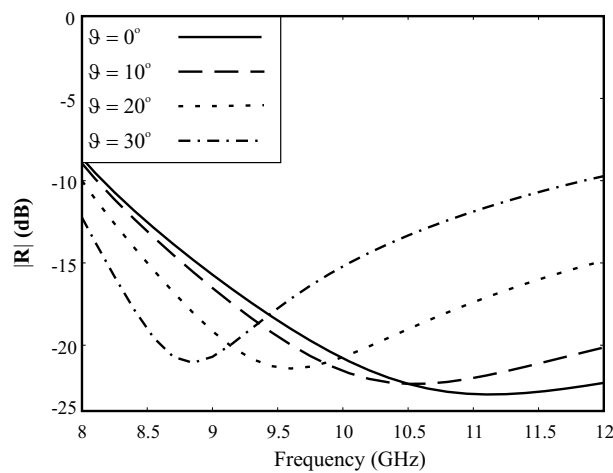


Figure 4.2: Magnitude of the reflection coefficient of the array only.

4.1.1 Single-mode design

The signal transmitted by the array saturates the low-noise amplifiers in the receiver of a satellite communication antenna, located close to the array. The FSS has to be designed to reduce this interference; the complete configuration is shown in Fig. 4.3.

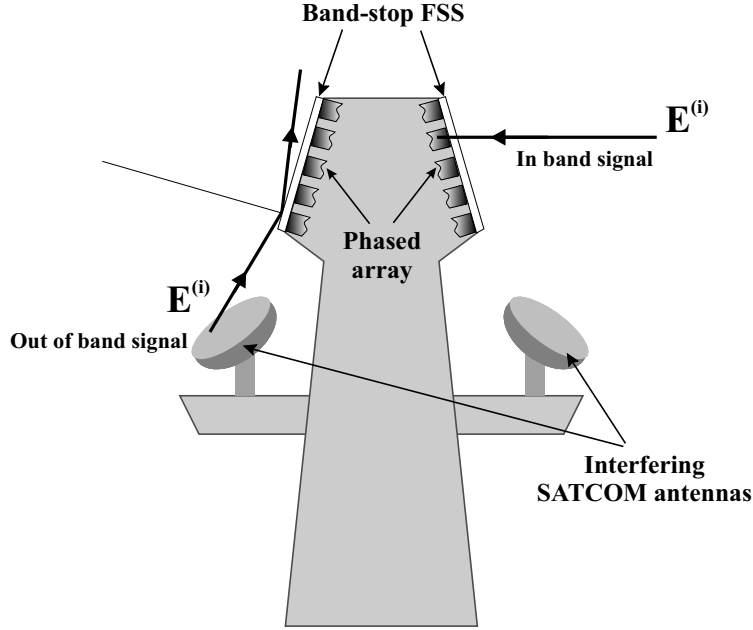


Figure 4.3: Application of band-stop FSS to reduce the interference between a MFR array and a satellite communication antenna, located on a ship mast.

In particular, the FSS has to realize a band-stop behavior in the frequency range 11 - 12 GHz, while preserving as much as possible the original performance in the range 8.2 - 11 GHz. The roll-off band should be limited to 0.5 GHz between -0.1 dB and -10 dB. Note that, once the FSS is integrated with the array, the maximum value of the reflection coefficient of the integrated structure in the pass-band of the FSS will be limited by the maximum value of the reflection coefficient of the array, which, in the present case, is about -10 dB. However, this limitation does not concern only the present array, but it is very general, related to the performances of a scanning array, as argued in [101]. In fact, as shown in more contributions, including [65], the resistance (the conductance) for an array of dipoles (slots) varies with the scan angle according to the expression:

$$C \cdot \left(\frac{1 - \sin^2 \vartheta \cos^2 \varphi}{\cos \vartheta} \right) \cdot \begin{cases} \zeta_0 & = R_{dipoles} \\ \frac{1}{\zeta_0} & = G_{slots} \end{cases} \quad (4.1)$$

where C is a normalization constant that depends on the array geometry for a fixed frequency. Expression (4.1) limits the maximum value that the reflection coefficient of an array can assume when scanning in a certain range. For example, if an array of dipoles is scanned up to 60° , the best matching that can be obtained for all angles is -9.55 dB. Improved performances for the scanning in one plane can be obtained by loading the array with a Wide Angle Impedance Matching (WAIM) layer, consisting of a dielectric slab of appropriate permittivity [86]. However, this option has not been considered in the present design case, since the FSS was aimed to realize a stop band in the array response, rather than enlarging its bandwidth.

FSS elements and layout

An FSS is characterized by its element type and layout. Different *type of elements* have been proposed in literature, both for patch- and slot-based FSS's. Following the classification proposed in [100] the FSS element types can be arranged in four groups:

- center-connected or N -poles (gangbuster element, three-legged unloaded element, anchor element, Jerusalem cross, square spiral);
- loop type (three- and four-legged loaded element, circular loop, square and hexagonal loop);
- solid interior or plate type (slot and patch);
- combinations of the previous types.

Each one of these groups shows a peculiar frequency behavior and has its corresponding specific applications. In general, the bandwidth of the element increases with an increasing physical width, (as it will become clearer in the following). *The layout* is defined as the way in which the elements are arranged on the periodic screen. It is characterized by the period of the grid, (the inter-element spacing), and the type of lattice, (rectangular or triangular).

For our design problem, since the transmission band is larger than the rejection band, a dipole-based FSS was the most convenient choice. In particular, we have chosen folded dipole elements in Fig. 4.1b, which resonate at 11.5 GHz, whose dimensions have been indicated as d_w and d_l along the axes x and y respectively, and whose width is w . In fact, this simple geometry allows meeting the requirements without causing major etching problems. For the sake of simplicity, the elements are arranged in a triangular lattice with the same periodicity as the array.

Design strategy

Since the very beginning of the study of FSS's, single-mode TL models have been extensively used for analysis and design purposes. Originally, when the available calculation power was quite limited, the circuit models were a valuable instrument for a simplified analysis. The first equivalent circuits were aimed to model free-standing grids under plane-wave incidence. In [8], the circuit for an infinite periodic array of narrow strips, derived from physical considerations, consisted of an admittance in parallel to the TL equivalent to the only propagating mode. Later, lossless FSS's were modeled in terms of a lumped element *LCR* circuit. In [77, 78] the parameters of this circuit were calculated by means of the basic circuit modeling equations presented in [88]; a correction term was then applied to extend the model to oblique angles of incidence [79]. This kind of circuit modeling was very useful when a full-wave analysis was not yet possible, because it allowed handling complex shaped FSS's as well. Based on this model, the design approach followed often filter synthesis techniques. These techniques, already used for dielectric radomes [87], were directly extended to metal grids by replacing the frequency variable with the angular variable [51]. In these early studies, the filtering behavior required from the FSS was obtained by an appropriate choice of the grating geometry. In the guided approach proposed in [76], instead, the frequency discrimination function is performed by the space between cascaded gratings, which act as a resonator; the use of a single-mode TL model allows then to separately control the angular and frequency behavior of the structure.

Nowadays, both the development of acceleration techniques which greatly reduce the computational resources required to perform full-wave simulations of FSS performances, and the availability of powerful computers, diminishes the relevance of the equivalent circuit for analysis purposes. However, these kinds of circuit are still a very appealing instrument for the design. Since full-wave simulations are time-consuming, a suitable design approach for multi-layer FSS's cannot completely rely on them. For this reason, a typical design strategy consists of two phases [106]: a first rough design is performed on the basis of a single-mode TL model; subsequently, full-wave simulations allow refining and finalizing this design. Usually, the FSS is represented in this model in terms of an *LC* circuit parallel to the TL's. The *L* and *C* values for this circuit can be obtained in different ways. In [47] they are calculated by comparing the full-wave simulations of the FSS reflection coefficient with the simulations of the *LC* single-mode model by means of a curve-fitting algorithm; moreover, by repeating the simulations for different values of the relevant dimensions of an FSS element, an empirical relation is derived between the circuit parameters and the FSS geometry. Alternatively, as shown in [84], from the knowledge of the full-wave FSS

reflection coefficient, the LC circuit parameters can be obtained in a straightforward way, by deriving the poles and zeros of the the equivalent FSS admittance or impedance and applying simple circuit theory [135]. It is also observed that the poles and zero of the FSS impedance are slowly varying functions of the frequency and, therefore, once the behavior of the array is known in a few frequency points, its dispersion properties in the Brillouin zone can be interpolated over a wider frequency range. This very interesting property could be directly used in our IEMEN formulation, described in Chapter 3, which naturally leads to a representation of an FSS patch (slot) transition in terms of shunt admittance (impedance), without having to pass through an equivalent LC circuit.

In the present design case, the procedure that we have adopted is rather classical [37] and consists first of a single-mode design, which is very fast, since it exploits the slow dependence of the admittance (impedance) on the frequency: the values are calculated in a few frequency points and then interpolated. The design is then tuned by performing a full-wave analysis were all the pertinent accessible modes are included. In the first phase, the FSS dipoles, under TE incidence, can be characterized by a simple parallel load (Y_p) with respect to the transmission line (TL) equivalent to the main propagating Floquet mode, whose modal characteristic admittance in free-space is $Y_0 = \frac{\cos \vartheta}{\sqrt{\mu_0/\epsilon_0}}$, where ϑ is the angle of incidence. The actual value of Y_p as a function of the frequency can be obtained with the IEMEN approach described in Chapter 3, Sec. 3.2.

Figs. 4.4–4.6 show the results of a parametric study of the imaginary part of the impedance $Z_p = 1/Y_p$ for various folded-dipole array configurations, under plane-wave incidence. Note that the real part of the impedance is always null, in the hypothesis of single-mode propagation and no losses, because the power scattered by the FSS is accounted for at TL-level. However, this is not true in general, when more than one element is retained as accessible besides the propagating one; in this case, the entries of the equivalent admittance matrix of the patch may have a non-zero real part, due to [37]:

- propagating modes that have not been included as accessible in the analysis;
- power dissipation due to surface waves;
- power dissipation in lossy dielectric slabs;
- power conversion between the principal polarizations (TE_{00} and TM_{00}).

In the three studied configurations, the dipole parameters were tuned to achieve a resonance frequency of 11.5 GHz. The resonance frequency is defined here as the frequency for which the imaginary part of the dipole impedance is zero.

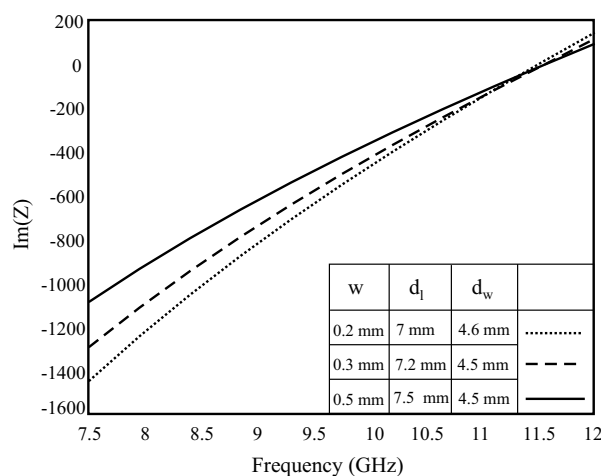


Figure 4.4: Parametric study of the imaginary part of the dipole impedance for different values of the dipole width.

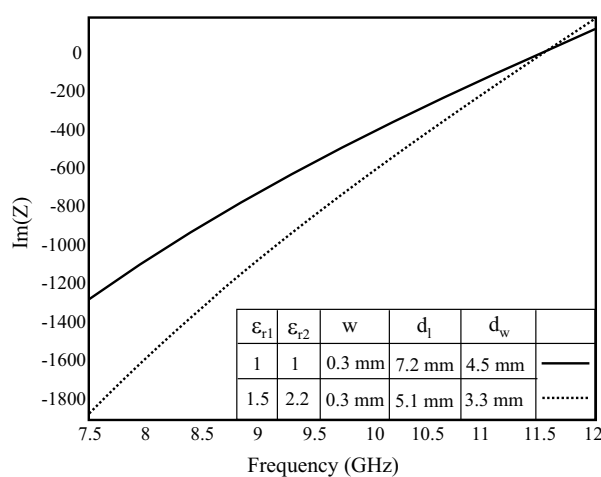


Figure 4.5: Parametric study of the imaginary part of the dipole impedance for different values of the dielectric constant (and a fixed dipole width $w=0.3$ mm).

Fig. 4.4 shows the influence of the width of the dipole ($w=0.2$ mm, $w=0.3$ mm, $w=0.5$ mm) on the bandwidth of the FSS for the case of a free-standing array. Correspondingly, as summarized in the table in the inset, three different values of d_w and d_l were considered, in order to obtain in all cases the same resonant frequency. It appears that narrower dipoles are associated to higher slopes of the impedance curves, i.e., to narrower bandwidths. However, the objective of the present application is more achieving a fast roll off than a large bandwidth. Fig. 4.5 shows that similar impedance curves can be obtained when

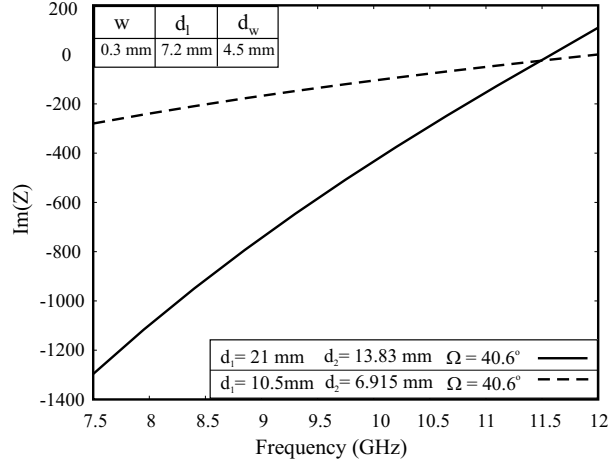


Figure 4.6: Parametric study of the imaginary part of the dipole impedance for different periods.

the dipoles are printed at the interface between two homogeneous dielectric half spaces ($\varepsilon_{r1} = 1.5$, $\varepsilon_{r2} = 2.2$). The desired resonance is achieved for smaller elements (see table in the inset), while the periods are preserved. Printing the dipoles on a dielectric slab results in a steeper roll off and a narrower bandwidth. However, since identical periods become larger in terms of the wavelength in the dielectric, Floquet modes of higher order can come close to cutoff (in the dielectric) for higher frequency ranges or wider observation angles. This effect will be accurately taken into account in Sec. 4.1.2, when, from a single-mode based design, we will move on to the IEMEN-based accurate analysis. Finally, we would like to point out that the FSS bandwidth decreases with the periods d_1 and d_2 , because of the mutual coupling among the metallic patches [37]. The impedance of a dipole array, having periods half of those in the array of Fig. 4.5, and the same element dimensions, is shown in Fig. 4.6; a much broader band is obtained. Therefore, for the present narrow-band application, it is convenient to use relatively large periods.

The slowly varying reactances in Figs. 4.4-4.6 can be approximated linearly with the aid of a first-order Taylor series expansion in the vicinity of the resonance f_r :

$$\begin{aligned}
 Z_p(f)_{f \approx f_r} &\approx Z_p(f_r) + Z'_p(f_r)(f - f_r) \Rightarrow \\
 Y_p(f)_{f \approx f_r} &\approx \frac{1}{Z'_p(f_r)} \cdot \frac{1}{f - f_r}.
 \end{aligned} \tag{4.2}$$

The advantage of this representation is that, once the resonance frequency is roughly known, a simple evaluation of the patch impedance for two frequency points enables an accurate approximation of the admittance over a wide frequency range. Fig. 4.7 shows the

reflection coefficient of a single free standing FSS for different scan angles (the dimensions of the FSS elements are indicated in the inset). It is clear that a single FSS panel does not guarantee a fast enough roll off between the stop band and the pass band and a constant stop band behavior, even for normal incidence.

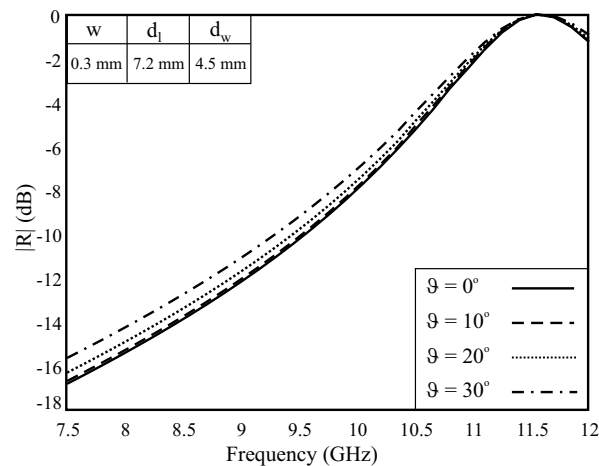


Figure 4.7: Magnitude of the reflection coefficient of the folded dipole FSS: single panel in free-space.

A second FSS plane, located in free-space at a distance of $\lambda_0/4$ from the first one, allows achieving a faster roll-off transition, as shown in Fig. 4.8 (dimensions in the inset).

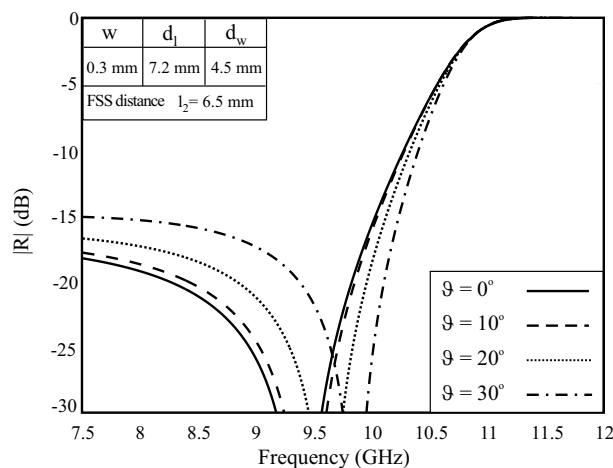


Figure 4.8: Magnitude of the reflection coefficient of the folded-dipole FSS: double panel in free-space.

We shall now consider the single-mode equivalent TL circuit for the fundamental propagating Floquet mode in Fig. 4.9a, which represents the double frequency selective structure, provided that all the higher-order Floquet modes are sufficiently attenuated. Note that this circuit corresponds to two identical FSS's sandwiched between three dielectric layers, where with Y_{ci} we have indicated the modal characteristic admittance of the i -th dielectric material, with $i = 1, 2$:

$$Y_{ci} = \sqrt{\varepsilon_{ri}} \frac{\cos \vartheta}{\sqrt{\frac{\mu_0}{\varepsilon_0}}}, \quad (4.3)$$

for an angle of incidence ϑ . We shall first consider the free-space case, for which $\varepsilon_{r0} = \varepsilon_{r1} = \varepsilon_{r2} = 1$. The Smith chart in Fig. 4.9b, normalized to the modal characteristic admittance in free-space Y_0 , allows us to readily evaluate how the input admittance of the structure is affected by the cascade of the additional layers. Moving from the right to the left of the chart, we add the normalized patch admittance $Yp_n = Yp/Y_0 = jBp_n$ to the normalized free-space admittance $Y_0/Y_0 = 1$, with $Yp_n \gg 1$, and obtain $Y_1 = Yp_n + 1$. This admittance is then rotated by $\lambda_0/4$, which is the length of the TL corresponding to the free-space distance between the two FSS's, and this leads to the transformed admittance $Y_2 \ll Yp_n$. The input admittance of the double FSS structure, Y_3 , obtained as parallel between this admittance Y_2 and the admittance Yp_n of the second FSS is now much larger, not only with respect to the free-space admittance on the left part of the circuit (1), but also with respect to the admittance on the right part (Y_2). Therefore, cascading a second, identical FSS at distance $\lambda_0/4$ from the initial FSS results in an enhanced blocking effect. From Fig. 4.8 it is clear that the double FSS still presents a too wide roll-off with respect to the given requirements and is too sensitive to the angle of incidence. A dielectric slab of permittivity $\varepsilon_{r2} = 2.2$ and $d_2 = \lambda_2/4$ inserted between the two FSS's guarantees that plane waves impinging from non orthogonal directions present similar reflection properties. Note that this particular value of the dielectric constant was chosen because a corresponding material for electromagnetic applications is available on the market (duroid from Rogers Corp. [124] or PTFE/glass from Taconic [134]). The introduction of this slab, however, degrades the transmission of the signal in the pass band. The requirements were then met by adding two further matching dielectric layers of dielectric constant $\varepsilon_{r1} = 1.5 \approx \sqrt{\varepsilon_{r2}}$ and thickness $d_1 = \lambda_1/4$, (at the center of the pass band), as indicated in Fig. 4.9a. Fig. 4.10 presents the reflection coefficients of the dielectric loaded double FSS, as a function of the frequency, for different scan angles (dimensions in the inset).

We would like again to recall that these simulations are obtained by resorting to a single-

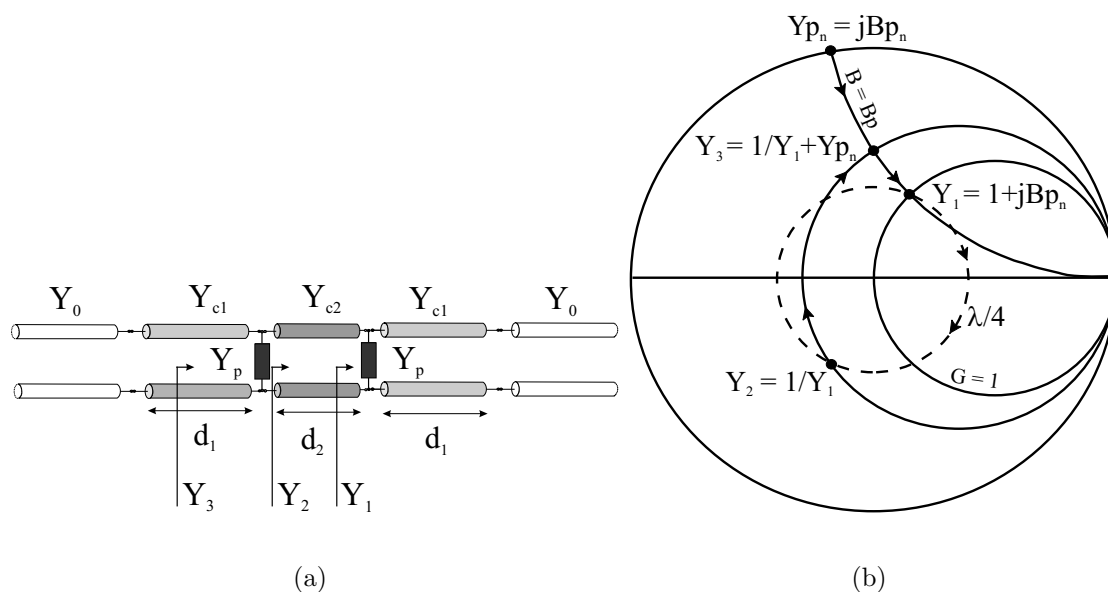


Figure 4.9: (a) Equivalent TL circuit and (b) Smith chart representing the interaction between the two dipole FSS panels as in Fig. 4.1 in the single mode approximation.

mode TL and are based on two interpolation points only to approximate the residue of the susceptance in (4.2). Thus, this first design phase is extremely fast.

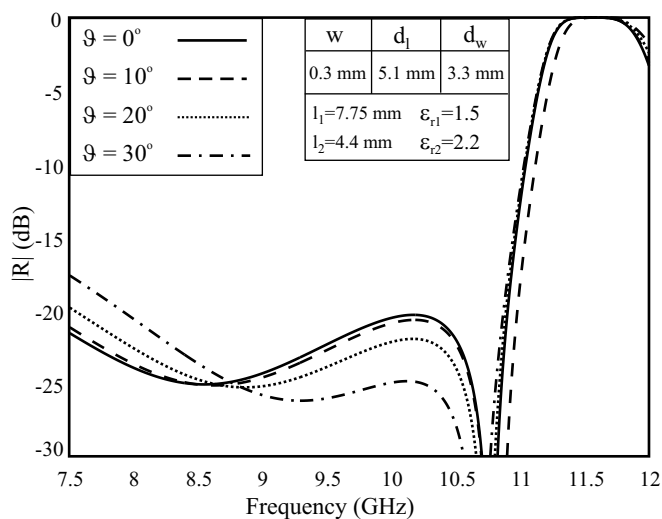


Figure 4.10: Magnitude of the reflection coefficient of the folded-dipole double FSS with dielectric loads.

4.1.2 Full-wave refinement

The design based on the single-mode TL model of Sec. 4.1.1 was tuned by performing a full-wave analysis based on the IEMEN formulation. Therefore, we had to identify which modes should be considered as accessible in each dielectric slab and for every incidence configuration. For this purpose, we have calculated the value of the attenuation factor of the modes excited in a certain slab, when they reach the next transition; this factor is defined as $1/e^{-\alpha l} = e^{\alpha l}$, where the propagation constant of a mode under cut-off is $k_z = j\alpha l$ and l is the thickness of the slab. In Tab. 4.1 the results are reported for the first 20 TE and TM modes in the FSS core and in the foam layer. The values were calculated at the maximum frequency in the operating band of the FSS (12 GHz), both for broadside incidence and for $\vartheta = 30^\circ$. The modes were ordered according to their cut-off frequency at $\vartheta = 30^\circ$ incidence. The kernel was calculated with a relative precision of $e_r = 10^{-6}$. If we retain, in the IEMEN analysis of the FSS, the modes with an attenuation factor less than 10, then, in the foam, only the fundamental mode is significant for normal incidence, while the first six modes should be selected for $\vartheta = 30^\circ$; in the FSS core instead, the first 14 TE and TM modes should be included in the calculations for broadside incidence and the first 12 for incidence at $\vartheta = 30^\circ$ (they are bold-faced in the table). Eventually, only the first 10 modes were retained in the analysis; correspondingly 150 piecewise linear (pwl) sub-domain basis functions were used to expand the unknown electric currents on the dipoles. In fact, the extraction of a higher number of modes from the IE's kernel would require a further refinement in the representation of the unknowns (a higher number of basis functions) to avoid an ill-conditioned MoM matrix. However, because of the available computation capabilities, we could account only for 10 accessible modes. The reflection coefficients predicted resorting to the full-wave analysis are shown in Fig. 4.11. In the same figure, the results achieved via the simple single-mode equivalent network are reported for comparison. The relatively small differences between the two simulation results confirm the Smith chart as a relevant instrument to predict the behavior of the structure in the first stage of the design.

Finally, the combination of the designed FSS with the waveguide array was investigated. The FSS was been located at a distance of 5.2 mm from the array antenna. In Fig. 4.12 we can observe that the requirements are met by the complete system for both broad-side radiation and for a scan angle of 30° . As further validation, the results were compared with those predicted by a commercial tool based on finite-element techniques HFSS [11]. Very good agreement was obtained, although the number of modes included as accessible in the analysis performed with the IEMEN method was lower than the number of modes

m	n	FSS core ($\vartheta = 0^\circ$)	FSS core ($\vartheta = 30^\circ$)	foam ($\vartheta = 0^\circ$)	foam ($\vartheta = 30^\circ$)
0	0	1	1	1	1
1	1	3.27	1.64	14.08	6.36
1	0	3.27	1.64	14.08	6.36
2	1	7.87	3.59	53.30	16.09
-1	-1	3.27	5.91	14.08	34.14
-1	0	3.27	5.91	14.08	34.14
0	1	13.42	14.28	128.45	141.47
0	-1	13.42	14.28	128.45	141.47
-2	-1	7.87	15.36	53.30	160.63
2	2	41.66	27.1	823.8	437.78

Table 4.1: Attenuation factors for the various modes as function of the index for a frequency of 12 GHz and scan angle of 30° .

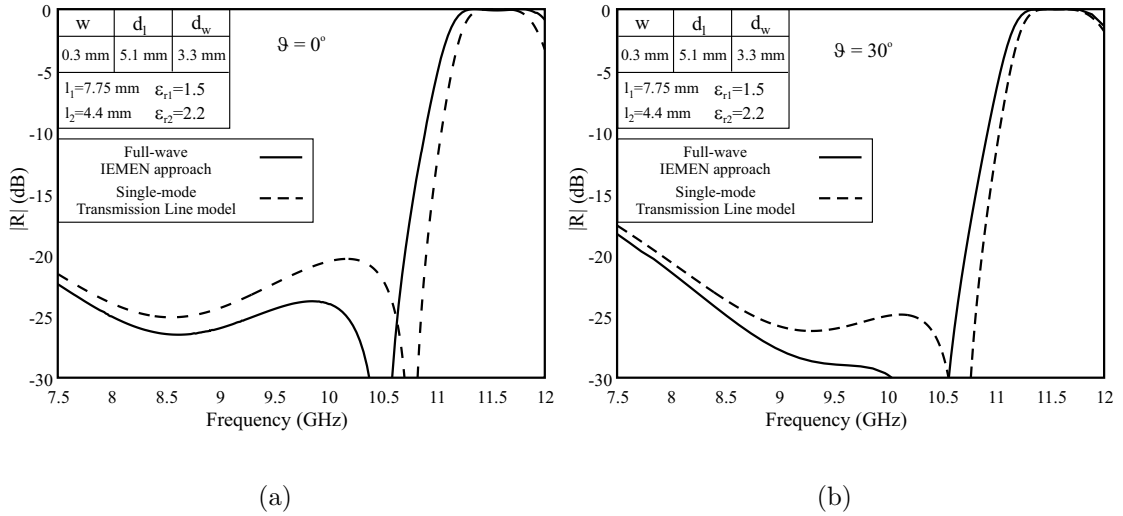


Figure 4.11: Magnitude of the reflection coefficient of the folded-dipole double FSS: comparison between the full-wave simulation (IEMEN formulation) and the single mode TL model for different angle of incidences. (a) Angle of incidence $\vartheta = 0^\circ$. (b) Angle of incidence $\vartheta = 30^\circ$.

showing the same attenuation level at the terminals of the network equivalent to the double FSS. Therefore, as already observed in Chapter 3, the evaluation of the attenuation factor

of each higher-order mode when it reaches the terminal planes gives only an indication of the number of accessible modes that should be considered in a IEMEN-based analysis. However, the number of modes actually needed to obtain a prescribed accuracy in the corresponding fields representation is probably smaller.

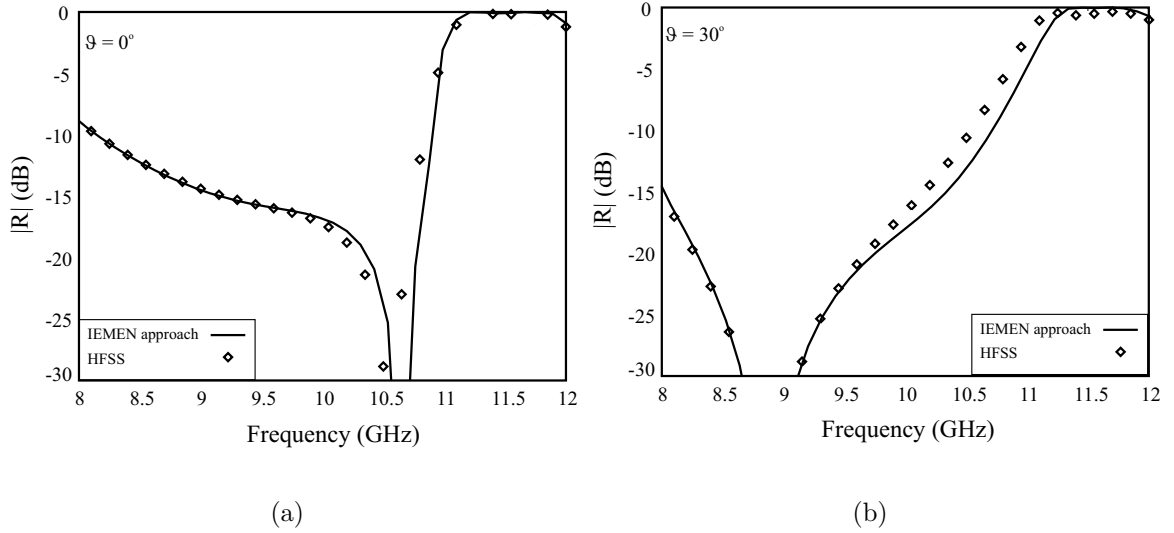


Figure 4.12: Magnitude of the reflection coefficient of the complete FSS cascaded with the array as in Fig. 4.1: comparison between the IEMEN-based simulations and the results obtained using HFSS for different angle of incidences. (a) Angle of incidence $\vartheta = 0^\circ$. (b) Angle of incidence $\vartheta = 30^\circ$.

4.1.3 Discussion of the results

The number of full-wave simulations that are necessary to characterize the complete FSS structure in a certain frequency range depends on how fast the observed parameters vary with the frequency. Fig. 4.13 shows that the input impedance of the whole multi-layer patch FSS, derived from the reflection coefficients in Fig. 4.11, has a singularity at the resonance, while the elements of the FSS impedance matrix (inverse of the multimode equivalent admittance matrix), displayed in Fig. 4.14, are slowly varying functions of the frequency and their interpolation is straightforward. In fact, all the fast frequency variations are associated to the TL-type interaction between the two FSS's, which in our approach is accounted for at equivalent-network level, rather than at full-wave analysis level. This property is systematic and occurs also for aperture based FSS's.

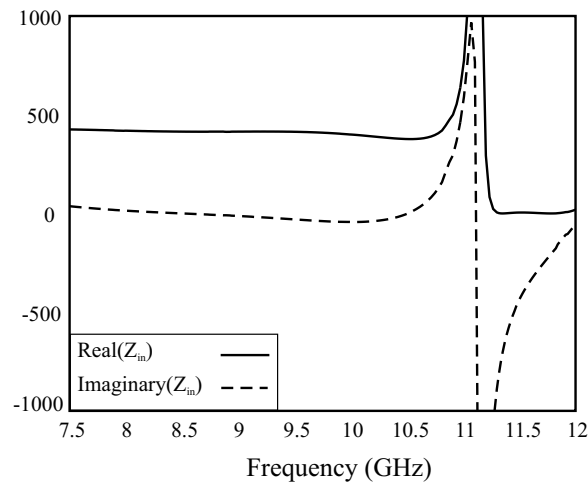


Figure 4.13: Input impedance of the FSS calculated from the reflection coefficient in Fig. 4.11.

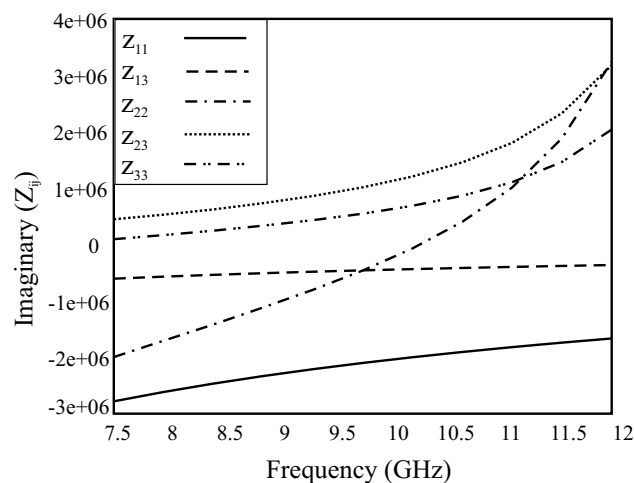


Figure 4.14: Imaginary part of some relevant elements of the multimode impedance matrix characterizing the patch transition.

At this point, knowing the resonance frequency of a multi-layer frequency selective structure, the problem is to identify which elements of the structure do contribute to the resonance. For this purpose, the knowledge of the equivalent impedance matrix of each FSS layer plays a key role. In fact, from the calculation of the eigenvalues of the matrix, it is possible to identify the causes of the resonant behavior, associated to the smallest eigenvalue.

4.2 Conclusions

In the previous sections we have described the design of an FSS directed to a specific application. In general, the following parameters have an essential influence on the behavior of the target, formulated in terms of resonance curve, resonance frequency, and bandwidth [37, 100]:

1. the number of periodic surfaces cascaded behind each other,
2. the number and type of dielectric slabs sandwiched between the periodic surfaces,
3. the element type,
4. the element layout (rectangular or triangular) and the configuration (flat or curved) of the periodic screen.

Cascading equal free-standing FSS's at a distance of $\lambda_0/4$ results in a flatter resonance curve and in a faster roll off, although the behavior of the obtained structure at the resonance still strongly depends on the polarization and angle of incidence of the impinging plane wave. In our problem we have observed that, by sandwiching the FSS's between properly chosen dielectric slabs, the bandwidth is stabilized with respect to angle of incidence and polarization and the roll off is improved. The resonance frequency (f_0) is shifted correspondingly toward lower values (f'_0), in the following way [100]:

- periodic surface embedded in an infinitely extended dielectric: $f'_0 = \frac{f_0}{\sqrt{\varepsilon_r}}$;
- periodic surface embedded in a finite dielectric slab: $f_0 < f'_0 < \frac{f_0}{\sqrt{\varepsilon_r}}$;
- periodic surface between two finite dielectric slabs: $f_0 < f'_0 < \frac{f_0}{\sqrt{\frac{\varepsilon_{r1} + \varepsilon_{r2}}{2}}}$;

where the slabs are $d \approx \frac{\lambda}{4}$ thick at the resonance frequency and act as quarter-wavelength transformers. For FSS's operating at different incidence angles, the true thickness seen by the impinging wave changes with the angle, and it has to be tuned depending also on the permittivity of the material. Moreover, we have noticed that, by appropriately choosing the slab permittivity, we can change the bandwidth of the frequency selective structure: the lower is the permittivity ε_r , the larger is the bandwidth. Cascading FSS's with slightly different resonance frequencies would allow the designer to obtain a larger

stop-band. However, since this way of proceeding would make the design more cumbersome and time consuming, the periodic surfaces cascaded in the structure are usually equal and the arrangement of the layers is symmetrical with respect to the central plane. Furthermore, according to classical filter theory, a higher number of cascaded filtering elements leads to a steeper roll off and a flatter response in the stop-band. However, filter theory does not account for variations with angle of incidence and polarization and its application to FSS design is not straightforward. In addition, the losses increase with the number of sandwiched dielectric layers and also the material and the manufacturing costs could become unacceptable. Therefore, even if in theory an arbitrary number of periodic surfaces could be cascaded, in practical applications, where the design and computation time are an issue, at most three or four FSS's are used [100]. Finally, the thickness of the whole FSS structure is usually also a relevant criterion for the design choices.

Another effect of sandwiching dielectric slabs between the FSS's is that the performances in the pass band are degraded and high *ears* (local maxima of the reflection coefficient) appear. A way to reduce them, is to use matching layers with a thickness of $\lambda/4$ at the center of the pass-band.

In the design case described in this chapter we have observed that the choice of the FSS geometry greatly affects its performance. In Sec. 4.1.1 it was shown that the FSS bandwidth increases with the element width. Moreover, we have noticed that, when the inter-element spacing is small with respect to the wavelength ($< \frac{\lambda}{2}$), the FSS bandwidth becomes larger while the grating lobes are delayed, and the resonance frequency is less dependent of the angle of incidence [100].

Chapter 5

Experimental validation

A design procedure has been developed on the basis of the Integral Equation formulation for the characterization of multi-layer Frequency Selective Surfaces (FSS) in terms of their Multimode Equivalent Networks (IEMEN), described in Chapter 2. This procedure has been applied in Chapter 4 to a realistic design problem, concerning an FSS to be integrated with a waveguide phased array to prevent interference from another antenna. The designed FSS has been manufactured and measured to validate the analysis capabilities of the IEMEN formulation and the developed design approach. The manufacturing process of the panel is described in Sec. 5.1. The design had to be slightly changed with respect to the one presented in Sec. 4.1 because of the limited availability of the selected materials and because of constraints imposed by the manufacturing process. In particular, a number of layers of the same material had to be stacked together by means of an adhesive to obtain a slab of the desired thickness. Consequently, the bonding film, which was not taken into account in the original design, played a significant role in this configuration and caused a shift of the resonance frequency with respect to the value expected from the analysis in Sec. 4.1.2. Simulations of the new structure needed to be carried out. For this purpose, we had to accurately model very thin dielectric layers, associated to the bonding material; in particular, to obtain an equivalent transmission line (TL) representation, an overwhelming number of accessible modes should have been included in the analysis. The best option was then to use, in the kernel of the reduced IE's, the multi-layer spectral Green's Function (GF), rather than the GF associated to the semi-infinite dielectric. While this is the usual way of proceeding of many planar tools based on the Method of Moments (MoM), it has been extended to the IEMEN method for the first time in Chapter 3, Sec. 3.4, thanks to the adopted GF formalism. The pertinent simulation results are reported in Sec. 5.1.1. The FSS was then experimentally characterized in terms of its reflection and transmission

coefficients, by means of measurements performed, with three different setups, in one of the anechoic chambers of TNO. The measurement setups are described in Sec. 5.2, where the experimental results are compared with the computed ones. Finally, conclusions are drawn in Sec. 5.3.

5.1 Manufacturing

The FSS has been manufactured as a square panel of $60 \text{ cm} \times 60 \text{ cm}$. For the FSS core, we have chosen a laminate made of woven fiberglass fabric, coated with PTFE (polytetrafluoroethylene). In particular, we have selected the Taconic TLY 5 material, whose main features are homogeneity and low losses. It has a dielectric constant of 2.2, (tolerance of ± 0.02) and a dissipation factor of $\tan \delta = 0.0004$ measured at 10 GHz, with electro-deposited copper clad on both sides (the data sheet is available at [134]).

For the external FSS layer, we could not find a material with a permittivity of 1.5 in X-band. The high-performance silicone foams produced by Rogers Corporation represented the closest approximation, although they are not originally meant for microwave applications [123]. Among these foams, we have selected the Bisco Cellular Silicone HT-820, with a permittivity of 1.5 at 60 Hz. Tests had to be performed to determine the dielectric properties of this foam in X-band. Fig. 5.1 shows a side view of the manufactured FSS where the foam is visible. It consists of a spongy core covered by a smooth uniform surface, and, since the material is not homogeneous, only an average dielectric constant can be measured. The range of possible permittivity values predicted by Rogers Corp. on the basis of the total density range was 1.52-1.76, with a medium value of 1.64. Furthermore, Rogers performed a test on two foam samples in the frequency range 0.78-14 GHz, using the IPC TM 650 2.5.5.5.1 method [69]. The complete sets of results are reported in Appendix D. The difference between the dielectric properties measured for these two samples can be attributed to the local density variation of the material. The medium value of the measured dielectric constant is 1.6 while the medium value of the dissipation factor is $\tan \delta = 0.0981$. At the time of the purchase, both the Taconic and the Bisco materials were available only in slabs of limited thicknesses. The fiberglass-PTFE material was supplied in two laminates, 2.2 mm thick, glued together with a bonding film of 0.089 mm, for a total thickness of 4.5 mm. The dielectric properties of this adhesive were not available at the time of the purchase. The foam was supplied in layers with a nominal thickness of 2.54 mm, and, also in this case, the slabs were dispatched with a layer of adhesive, without providing its electromagnetic data. Three slabs were stuck together using an additional bonding

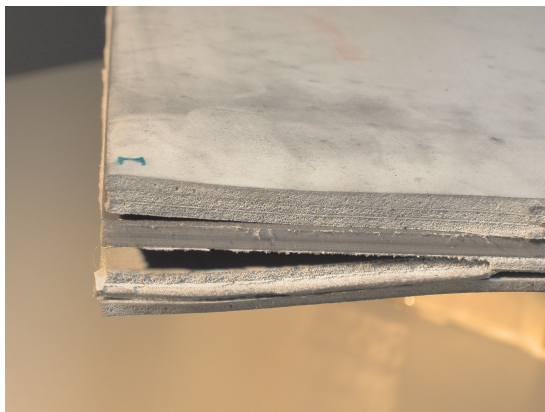


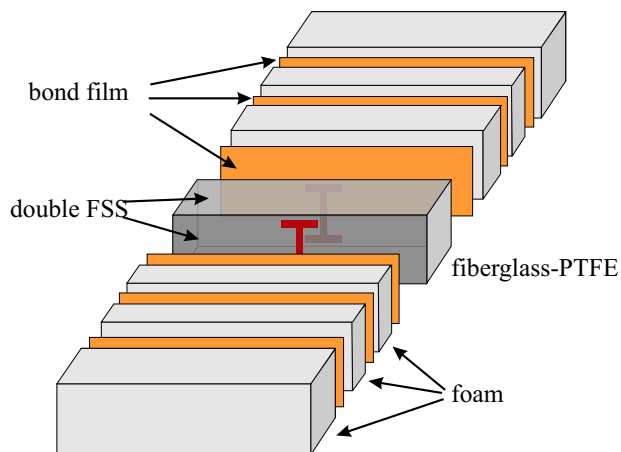
Figure 5.1: Side view of a corner of the manufactured FSS. The stratification is clearly visible: the external spongy layers are made of Bosco foam, while the internal hard core is a double Taconic laminate.

film, Arlon 6250, having nominal thickness of 0.0381 mm, dielectric constant $\epsilon_r = 2.32$ and dissipation factor $\tan \delta = 0.0013$ at 10 GHz. The same bonding film was used to bond the foam to the board. The resulting total thickness of the bonding film, due to the superposition of the Arlon to the pre-existing adhesive, was 0.1 mm as measured using a micrometer. The panels were vacuum pressed at 20 tons for 1 hour at a temperature of 150°C. Arlon bonding film is actually meant to be used for PTFE-based laminates and the typical temperature and pressure needed to flow the adhesive and ensure the bonding are 120°C and 6.4 tons respectively, applied for about 10 minutes [12]. However, while for the bonding of the foam to the Taconic board the FSS manufacturer could stick to these standard values, the foam-to-foam bonding required a higher temperature and pressure. As a consequence, the bonding process changed the thickness and therefore the density and the dielectric properties of the foam in a non-predictable way. For this reason, another test on the dielectric constant of the foam was performed at TNO on a number of samples cut from the slabs used in the actually manufactured FSS, by means of the Hewlett Packard coaxial probe kit HP85070A. The measurement results are described in Appendix D. The average value of the dielectric constant measured in X-band was about 1.67; taking into account a calibration error of $\pm 3\%$, we would resort to the medium value predicted by Rogers: 1.64. The dissipation factor could not be measured because the coaxial probe method does not give reliable results for dissipations lower than 0.01.

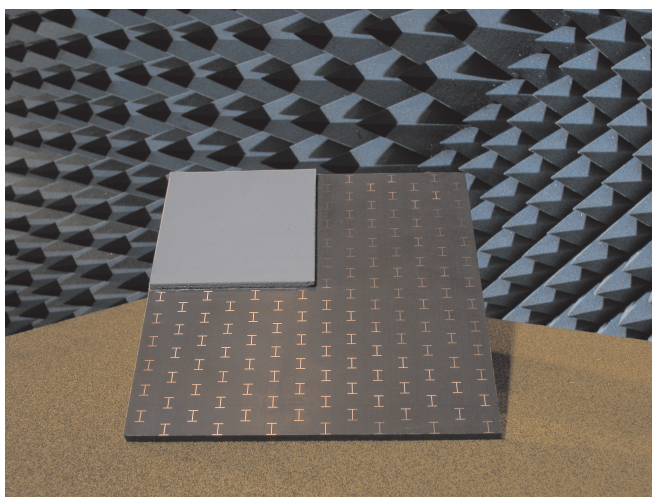
The actual values of the dielectric slabs thicknesses, measured by means of a micrometer, are reported in Tab. 5.1. Note that, because of the softness of the foam, the reproducibility

of the measurements was difficult to evaluate and these values should be considered merely as averages values. The final multi-layer structure is shown in Fig. 5.2a.

A 600 mm \times 600 mm screen has been etched on both sides of the double Taconic laminate, on a 17 μ m copper foil, with a nominal accuracy of 20 μ m. Fig. 5.2b shows a photograph of a portion of the manufactured FSS.



(a)



(b)

Figure 5.2: Manufactured multi-layer FSS. (a) Final structure of the manufactured FSS. (b) Photography of a portion of the manufactured FSS.

Layer	Thickness (mm)
Foam (Bisco HT-820)	3.1
Bonding film (Arlon 6250)	0.1
Foam (Bisco HT-820)	2.2
Bonding film (Arlon 6250)	0.1
Foam (Bisco HT-820)	2.2
Bonding film (Arlon 6250)	0.1
Fiberglass/PTFE (Taconic TLY5)	4.5
Bonding film (Arlon 6250)	0.1
Foam (Bisco HT-820)	2.4
Bonding film (Arlon 6250)	0.1
Foam (Bisco HT-820)	2.4
Bonding film (Arlon 6250)	0.1
Foam (Bisco HT-820)	3.1

Table 5.1: Thickness of the dielectric slabs in the manufactured FSS panel.

5.1.1 Modified design: thin layer problem

The actually manufactured FSS panel was different from the structure originally designed (Chapter 4, Sec. 4.1) as effect of the manufacturing process and of the changes imposed by the limited availability of the materials. In fact, since the bonding film was used systematically in the delivered structure, its effect had to be taken into account in the simulations. In Chapter 3, Sec. 3.4 we have extended the IEMEN formulation to the case of multi-layer structures where one or more layers are very thin with respect to the wavelength, by using in the kernel of the Integral Equations the GF of a stratified medium instead of the GF of the the semi-infinite half-space. In this way, the number of modes extracted from the kernel can be smaller than the actual number of accessible modes and this allows preventing ill conditioning problems. Based on this approach, new simulations have been carried out for the multi-layer FSS in Fig. 5.2a, using the permittivity values reported in Tab. 5.2. Since the dielectric constant of the adhesive already present on the foam was not made available by the manufacturer and permittivity measurements using the coaxial probe would have not been reliable for such a thin sample, in our simulations we have assumed the dielectric constant to be the same as that of the Arlon bonding film. As dielectric constant of the foam we have used the medium value indicated by Rogers,

which is equal to the medium value obtained by coaxial probe measurements, corrected for the calibration errors (Appendix D). When the simulations were performed, the effect of the dissipation factor could not yet be taken into account in the analysis. The results of the simulations, obtained by using the acceleration technique described in Sec. 3.5, are shown in Fig. 5.3a (reflection coefficient) and in Fig. 5.3b (transmission coefficient) for the angles of incidence 0° , 15° , 20° and 25° . For the broadside incidence case, we calculated the asymptotic form of the IE kernel in the quasi-static limit; for the self coupling 10^5 modes were summed to reach an accuracy of 10^{-6} ; the corresponding MoM matrix had a condition number of 10^4 . For other angles of incidence, the asymptotic term was calculated in the frequency loop; in this case, 10^6 modes were needed for the target accuracy of 10^{-6} ; the condition number of the MoM matrix was also in this case 10^4 , corresponding to a total accuracy on the results of 10^{-2} .

Dielectric	Permittivity and tolerance
Foam (Bisco HT-820)	1.64 ± 0.12
Bonding film (Arlon 6250)	2.32 ± 0.10
Fiberglass/PTFE (Taconic TLY5)	2.2 ± 0.02

Table 5.2: Permittivity of the dielectric slabs in the manufactured FSS panel.

5.2 Measurements

The experimental characterization of the FSS panel has been accomplished by means of reflection and transmission measurements in X-band, for different incidence conditions, carried out in one of the anechoic chambers of TNO. For this purpose, horn antennas with an aperture of $73.5 \text{ mm} \times 54.1 \text{ mm}$ were used. Their 3 dB half power beamwidth (HPB), calculated using the empirical expression in $\psi = 50.6^\circ \lambda/a$, where a indicates the dimension of one of the sides of the rectangular cross-section, is $\psi_1 = 20.6^\circ$ in the H -plane and $\psi_2 = 27.95^\circ$ in the E -plane. The relative position of transmitting and receiving antennas and FSS panel has been determined on the basis of the following considerations.

- The reflection measurements are calibrated against the reflection response of a copper plate having the same size as the FSS. Therefore, the measured panel has to be located in the far field of the transmitting horn antenna (TX), so that the phase front of the incident wave can be considered plane. In fact, only in this case the FSS response in its resonance band is approximately the same as the one of the metallic plate,

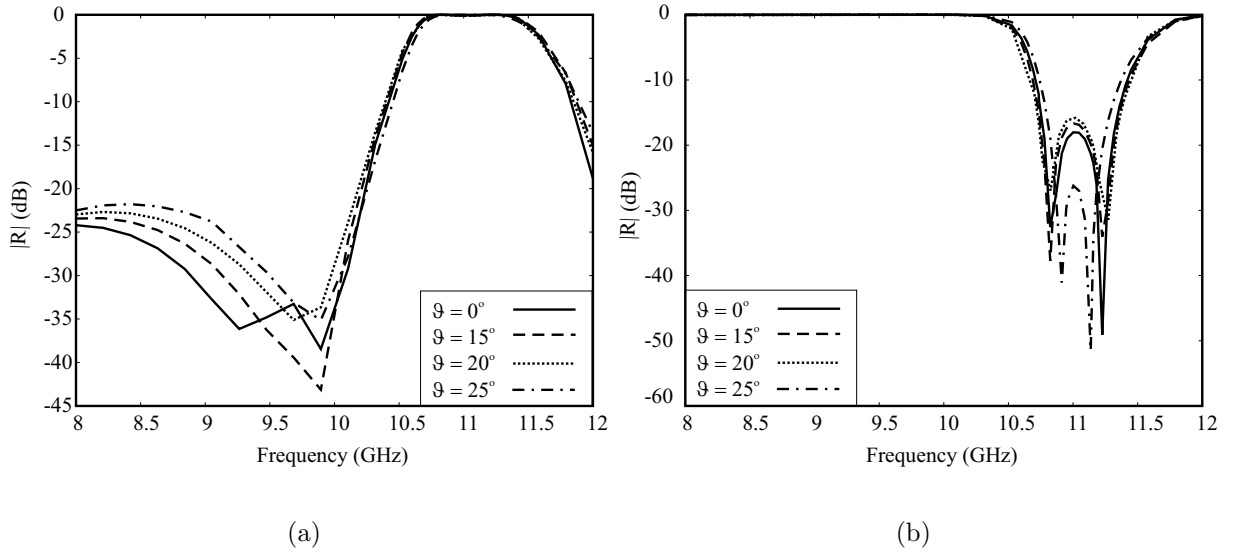


Figure 5.3: IEMEN simulation results of the manufactured FSS for the angles of incidence: 0° , 15° , 20° and 25° . (a) Amplitude of the reflection coefficient. (b) Amplitude of transmission coefficient.

which can then be used as reference for calibration purposes. The far-field distance from the antenna with respect to its largest dimension is [15] $R = 2d^2/\lambda = 36$ cm, calculated at 10 GHz (center of the operating band).

- The FSS transmission measurements are calibrated against the transmission measurement of the receiving horn antenna (RX) when the FSS was removed. Therefore, to be able to perform the calibration, the TX and the RX have to be located in each other's far field.

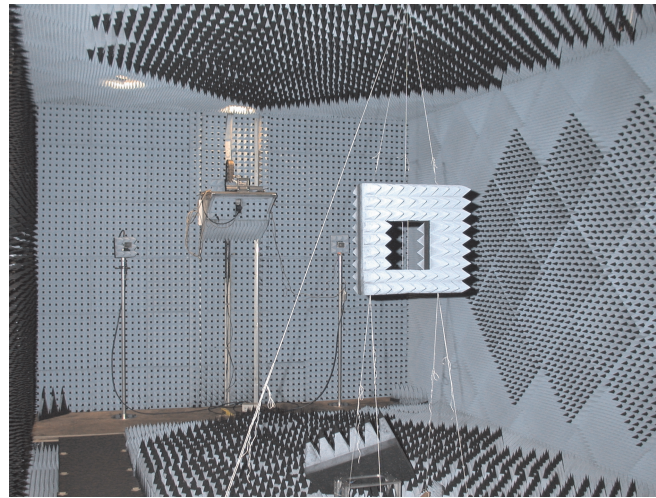
Moreover, since the simulations were performed under the hypothesis of plane-wave incidence and plane-wave back scattering, the ideal situation, to be able to correctly compare them with the measurements, would be to locate the FSS and the calibration panels in the far field of the TX and the RX in the far field of the FSS panel. While the first requirement can be easily met when using X-band horn antennas, the second one is in practice not achievable in an anechoic chamber, when the panel to be measured is large. For example, if we consider an FSS panel of $60\text{ cm} \times 60\text{ cm}$, its far field would begin at a distance of 24 m, while the largest chamber available at TNO is 10 m long!

Consequently, three measurements setups have been identified:

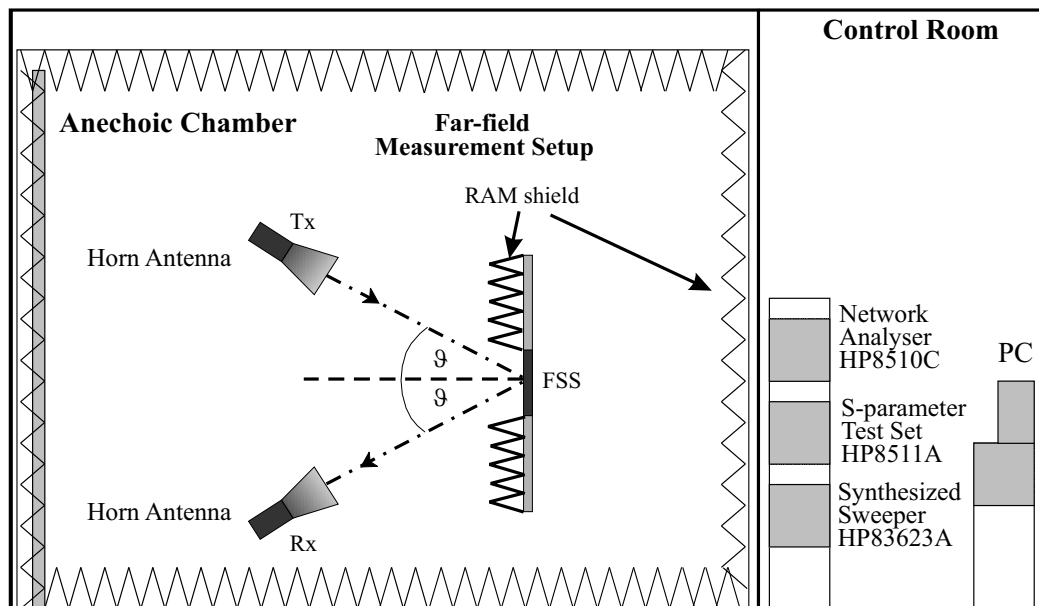
- FSS in the far field of the TX and RX in the far field of the FSS (a subpanel of the manufactured FSS), to perform bistatic reflection coefficient measurements with angle of incidence up to 25° (Sec. 5.2.1);
- FSS in the far field of the TX and RX in the near field of the FSS (entire panel), to perform monostatic reflection coefficient measurements at normal incidence (Sec. 5.2.2);
- FSS in the quasi far field of the TX and RX in the near field of the FSS (entire panel) for transmission measurements with angle of incidence up to 25° (Sec. 5.2.2).

5.2.1 Far field of the TX and far field of the FSS measurement setup

The microwave anechoic chamber (MAC) of TNO is 10 m long, but the maximum useful distance is 4.2 m; by considering a subpanel of the manufactured FSS of size $28\text{ cm} \times 28\text{ cm}$ we were able to locate the RX almost in the far field of the FSS. A schematic of the measurement setup is illustrated in Fig. 5.4b. The subpanel was obtained by inserting the original panel in a frame of radar absorbing material (RAM), having a square window of dimension 28 cm, as illustrated in Fig. 5.4a. To change the orientation of the panel with respect to the antennas, and to measure its reflection coefficient in different incidence condition, the panel was fixed, by means of Nylon wires, to a turntable, whose engine was analogically controlled. For non-normal incidence, the two antennas, mounted on poles, had to be moved correspondingly; however, because of logistic constraints, only a limited number of incidence configurations could be obtained: 0° , 15° , 20° and 25° . A laser beamer, mounted between the two antennas, was used for optical alignment between the FSS plate and the antennas. All the objects inside the anechoic room were shielded by means of RAM panels. The instruments used to collect and process the measurements were a calibrated automatic Network Analyzer HP8510C, a Frequency Converter Test Set HP11A and a Synthesized Sweeper HP83623A, all from Agilent Technologies [3]. They were located in the control room, next to the MAC, together with the PC, used to collect and process the data. The measured reflection response was calibrated against the reflection response of a copper plate, having the same size as the FSS panel, and also inserted in the frame of absorbing material. Empty-room measurements were performed before and after each FSS/calibration panel measurement. Time gating was used to separate the FSS back-scattered signal from the spurious signals due to multipath.



(a)



(b)

Figure 5.4: Far-field bistatic measurement setup. (a) Microwave anechoic chamber of TNO. (b) Outline of the setup.

Results and discussion

The measured reflection coefficient of the FSS plate, calibrated against the metal panel, is plotted in Fig. 5.5.

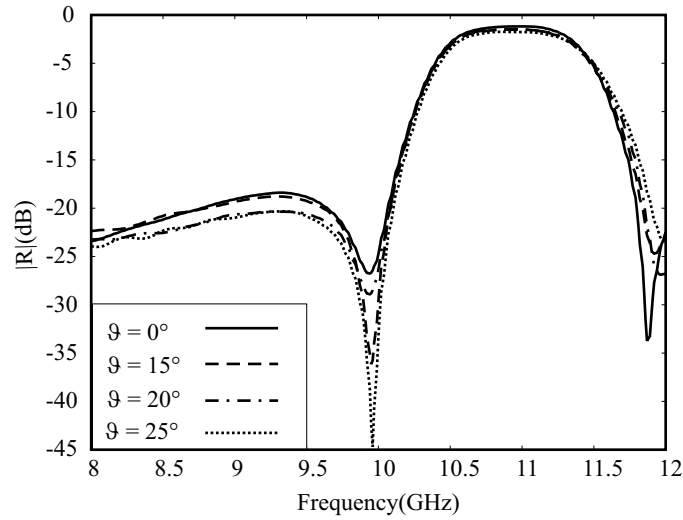


Figure 5.5: Amplitude of the reflection coefficient, measured with the bistatic far-field, setup for different angles of incidence: $\vartheta = 0^\circ$, 15° , 20° and 25° .

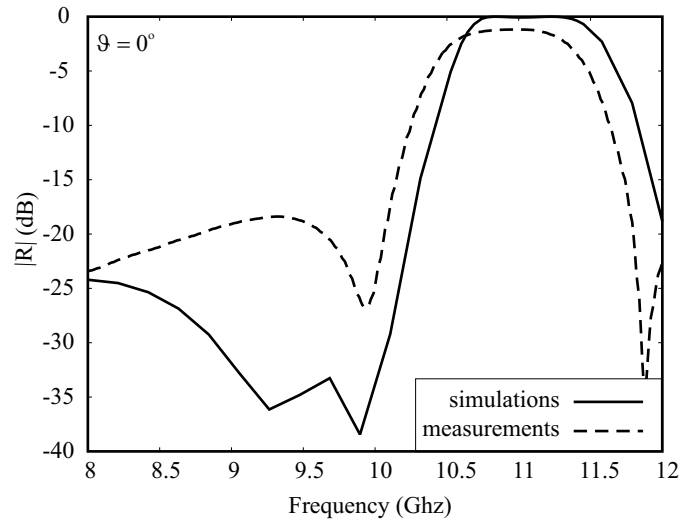


Figure 5.6: Amplitude of the FSS reflection coefficient for normal incidence; comparison between bistatic far-field measurements and full-wave IEMEN-based simulations.

As shown in Fig. 5.6 for the case of normal incidence, the behavior of the FSS at the resonance is in very good agreement with the simulations, but the out-of-band measured level is higher than the simulated one. This difference can be interpreted as mainly due to the contribution of two factors.

- The simulations were performed for an infinitely extended panel, without taking into account the effect of edge diffraction. The surface illuminated on the FSS panel can be estimated, on the basis of the antenna HPB, as approximately equal to $A \times B$, where $A = distance * \tan(\psi_1/2) * 2 = 1.53$ m and $B = distance * \tan(\psi_2/2) * 2 = 2.09$ m, with $distance = 4.2$ m. Therefore, the panel and the RAM frame were completely illuminated by the antenna and the diffraction from the frame was significant.
- Some sources of inaccuracy could be identified in the measurement setup, associated to mechanical problems. They were mainly due to the use of the RAM frame and affected the lower part of the FSS response. Since the RAM frame was supported by stretchable wires, and since the calibration plate and the FSS plate had different weights and were both heavier than the empty RAM frame, their relative position with respect to the antennas changed at every measurement. Additional mechanical problems were caused by the movable construction used for the antennas. These problems led to the following inaccuracies.

Repeatability. Inaccuracy in the repeatability of these measurements was associated to the effective FSS area, which depends on the distance between the outer FSS elements actually illuminated and therefore contributing to the back-scattered signal. Since the location of the FSS plate could not be exactly identified in the RAM frame, the effective area of the FSS was different at every measurement. The measurement repeatability was also affected by inaccuracies introduced in the calibration and in the alignment between the FSS and the antennas. The repeatability error, as measured for time domain responses, resulted to be about ± 0.07 dB.

Alignment. Alignment between the antennas and the FSS or the calibration plate had to be guaranteed in azimuth, elevation and height. The alignment procedure was repeated at every measurement and required using a laser beamer to retrieve the relative position of antennas-plate corresponding to the maximum measured signal in time domain (optimal position). The position of the plate in azimuth was varied by operating the turntable with a minimum step size of 0.001° . The accuracy of the azimuth alignment was about 0.04 dB/ 0.5° , measured around the optimal azimuth angle. Since the height and elevation angle of the plate could not be varied, the height of the antennas was changed instead. The accuracy of the height alignment was about 0.05 dB/cm measured around the optimal height, for an height step of 1 cm.

Calibration. The measurements were calibrated by using a standard S11 Network Analyzer. The empty-room back-scattered signal was coherently subtracted from the signal back-scattered in presence of the FSS, to remove spurious contributions (i.e. multipath due to the RAM covering the walls of the MAC, cable and antenna reflections). Further, in the time domain a time gate of 1.2 ns, centered at the location of the plate, was applied to the back-scattered signal to reduce the contributions due to non-fixed spurious signals (i.e. multipath from the empty RAM frame). After this first processing, the value of the FSS backscattered signal obtained from the measured backscattered signal was affected only by the contribution due to reflections from the RAM frame, when containing the FSS or the calibration plate. To calculate the reflection coefficient of the FSS from this corrected backscattered signal, a perfectly conducting plate was used as reference for total reflection. The measured backscattered signal, in presence of the reference plate, was also corrected for the empty-room scattering and for the RAM frame multipath. The calibration error due to the multipath contributions that could not be eliminated was estimated to be about 0.08 dB in the FSS stop band and about 1 dB in the FSS pass band.

In view of this, the extent of the inaccuracies associated to mechanical errors resulted to be negligible. Moreover, since the requirement for the FSS reflection coefficient in the out-of-band region was dictated by the array antenna and corresponded to a maximum of -10 dB, as explained in Chapter 4, Sec. 4.1.1, we can conclude that the agreement between simulations and far-field measurements is reasonably good in the entire frequency range 8 - 12 GHz.

5.2.2 Far field of the TX and the near field of the FSS measurement setup

To reduce the effect of edge diffraction, new measurements were performed with the TX and the RX located much closer to the FSS panel. Two measurement setups were constructed, to measure respectively:

- the monostatic reflection coefficient for normal incidence;
- the transmission coefficient.

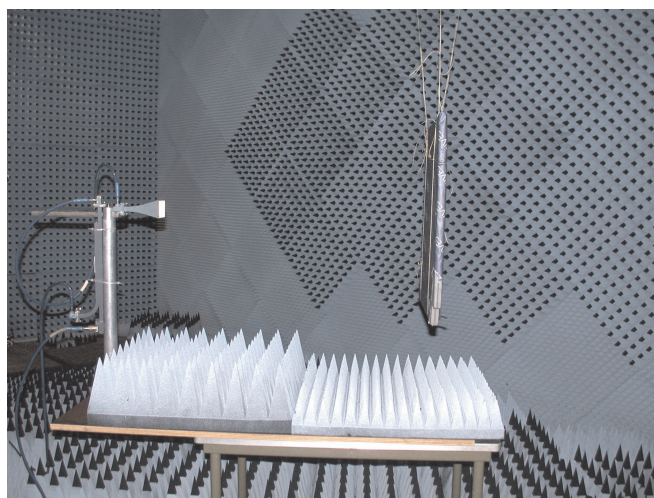
Also these measurements were performed at the MAC of TNO, using the equipment already described in Sec. 5.2.1. To reduce the sources of error, which affected the previous far-

field measurements, a new, computer-controlled turntable was used to select the incidence configuration, with an accuracy of 0.001° . The turntable was located outside the MAC, to avoid reflections from moving objects other than the FSS (or the reference plate) and the Kevlar wires.

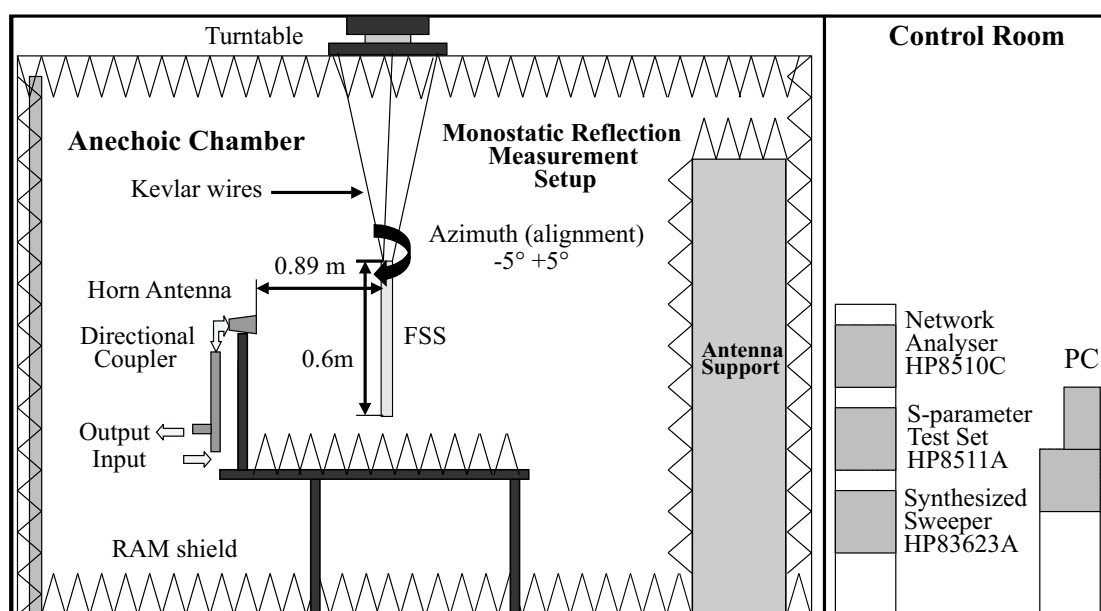
This measurement setup is shown in Fig. 5.7. To measure the monostatic reflection coefficient at broadside, the antenna and the combined directional coupler were fixed on a long pole (60 cm) at $distance = 89$ cm from the panel. The FSS was then located in the far field of the TX. The illuminated surface on the FSS panel can be estimated on the basis of the HPB of the TX as equal to $A \times B$ where $A = distance * \tan(\psi_1/2) * 2 = 32.3$ cm and $B = \tan(\psi_2/2) * 2 = 44.29$ cm. Therefore, most of the power of the TX falls in a region completely internal to the panel and we would expect that the edge diffraction effect on the measurements would be less critical for this setup than for the previous one (RX in the far field of the FSS). The coupling of the directional coupler was -10dB and its directivity was less than -40 dB. The transmitted signal was swept over the frequency band 7.5 GHz - 12.5 GHz. The measurements were calibrated by means of an aluminum plate with the same size as the FSS. Each FSS measurement was followed by a measurement of the reference plate and an empty-room measurement. In the FSS measurements, the signal back-scattered by the FSS consisted of the following contributions:

- the backscatter contribution from the FSS;
- the cable reflections;
- the directivity signal of the directional coupler;
- the reflections of the antenna with coax/waveguide adapter;
- the multipath signals from RAM on the table;
- the reflections from the Kevlar wires;
- the backscatter from all RAM in the room;
- the multiple reflections between antenna and FSS.

These contributions could be recognized in the time-domain response and they were all removed by applying a time gate around the FSS response (60 cm), except for the reflection from the Kevlar wires. The gated signal was then Fourier transformed to obtain the FSS reflection coefficient. The distance between antenna and FSS (89 cm) was such to guarantee that multiple reflections between antenna and FSS would be outside the chosen time gate.



(a)



(b)

Figure 5.7: Monostatic measurement set-up with the RX in the near field of the FSS. (a) Microwave anechoic chamber of TNO. (b) Outline of the setup.

At this distance, the FSS was in the far-field region of the RX (which corresponds to a distance $2d^2/\lambda = 33$ cm, where $d = 7.35$ cm is the longest side length of the waveguide horn

antenna). The monostatic reflection coefficient, measured for normal incidence, is shown in Fig. 5.8, together with the bistatic one measured with the setup described in Sec. 5.2.1.

Reflection measurements: comparison between the two setups

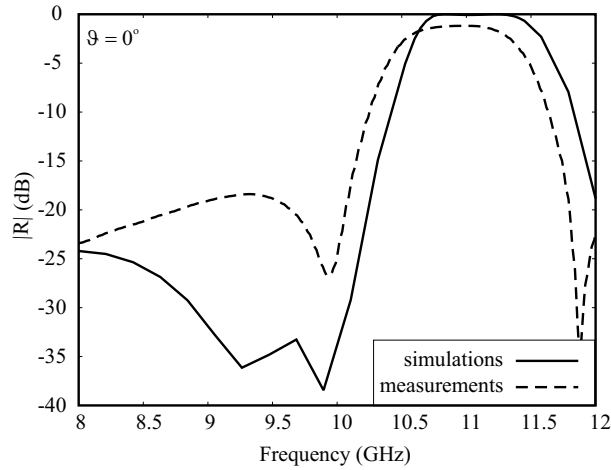


Figure 5.8: Amplitude of the measured reflection coefficient for normal incidence: comparison between the measurements performed with the RX located in the far field of the FSS plate (Fig. 5.4) and those performed with the RX located in the near field of the plate (Fig. 5.7).

Fig. 5.8 shows the amplitude of the reflection coefficient for broadside incidence, measured both with the RX in the far field of the FSS and with the RX in the near-field of the FSS. The differences in the results concern mainly the pass band and can be associated to:

- the differences between the two setups, since the phase front of the wave arriving to the RX can be considered flat in the first setup (RX in the far field of the FSS) but not in the second setup; moreover the measurement was bistatic in the first setup and monostatic in the second setup;
- the effect of edge diffraction, which is more relevant in the first setup (RX in the far field of the FSS);
- the contribution of the multipath propagation through the RAM frame, which could not be removed by time gating in the first setup.

However, since these differences are rather small and fall within the tolerances of the measurements, we can conclude that the fact that the RX is located in the near-field of the

FSS does not significantly affect the result. Moreover, since the realization of this second setup is more straightforward, it seems a better choice for reflection measurements with respect to the far-field setup.

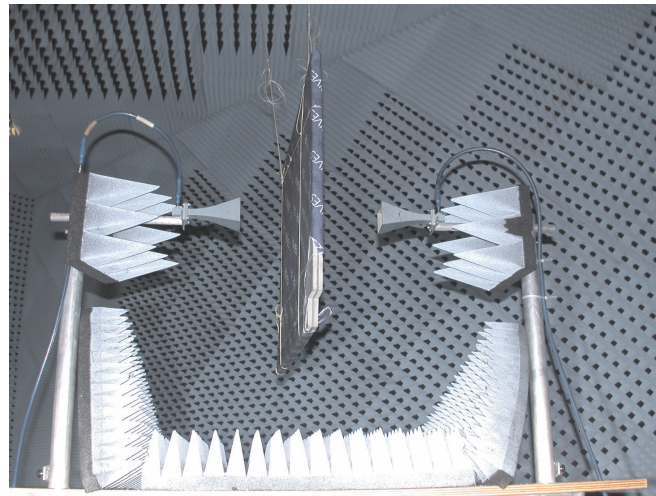
5.2.3 Quasi far field of the TX and near field of the FSS measurement setup

The transmission measurement setup is shown in Fig. 5.9. The two horn antennas, fixed on long poles, were located in each other's far field, at a distance of 33 cm; the FSS, in the middle, was then positioned at a distance about half of the far-field distance from both the TX and the RX. The distance of the two antennas was chosen on the basis of two considerations.

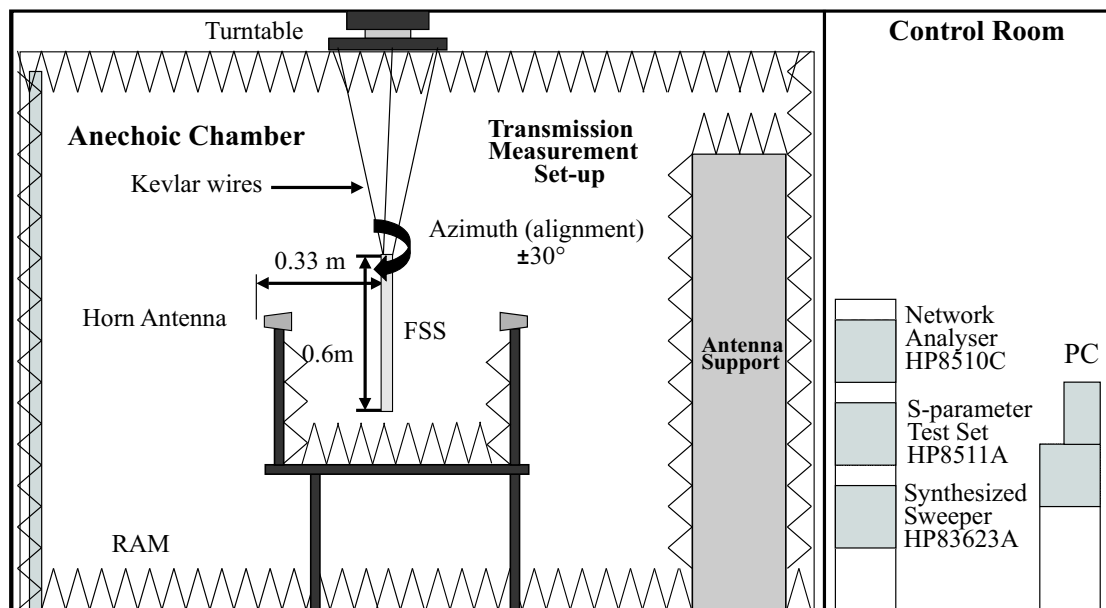
- The antennas had to be in the far field of each other to be able to perform the calibration measurement (the TX without the FSS panel).
- Coupling between the TX and the RX had to be prevented. In other setups proposed in literature, for example in [41, 91], this decoupling is realized by inserting the FSS panel in a wall of RAM which divides the anechoic chamber in two areas, one containing the TX and one containing the RX. To avoid errors due to multipath propagation through the RAM and due to the difficulty of maintaining the RAM wall in a stable position, we have not adopted this configuration. Instead, we have positioned the TX and RX close to the panel, so that the surface illuminated by the TX on the FSS panel was equal to $A \times B$ where $A = distance * \tan(\psi_1/2) * 2 = 5.68$ cm and $B = \tan(\psi_2/2) * 2 = 7.78$ cm, estimated on the basis of the HPB of the TX.

Empty-room measurements were used as reference for calibration purposes. The measurements were performed in the frequency band 7.5 GHz - 12.5 GHz and the angle of incidence on the panel was changed by rotating the turntable from -25° to 25° . The received frequency response consisted of the following contributions:

- the transmission contribution from the FSS;
- the multipath signals from the RAM on the table;
- the reflections of the Kevlar wires;
- the backscatter from all the RAM in the room.



(a)



(b)

Figure 5.9: Transmission measurement setup. (a) Microwave anechoic chamber of TNO. (b) Schematic of the setup.

Also in this case, a time gate was applied around the FSS response, which allowed removing all these spurious signals apart for the scattering of the Kevlar wires. The measured

transmission coefficient is shown in Fig. 5.10.

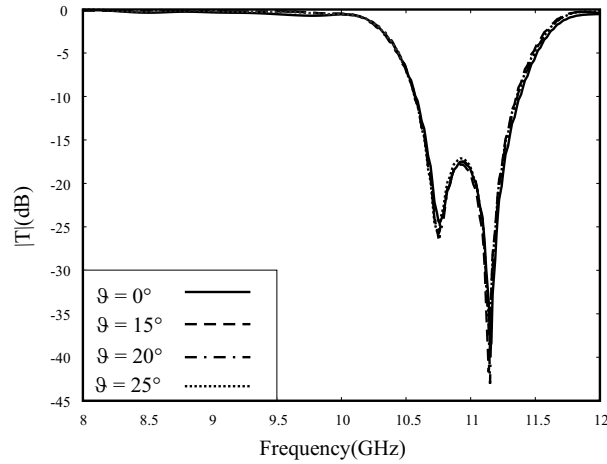


Figure 5.10: Amplitude of the transmission coefficient measured for different incidence angles, using the setup shown in Fig. 5.9, with the FSS plate located in the near field of the TX.

5.2.4 Discussion of the results

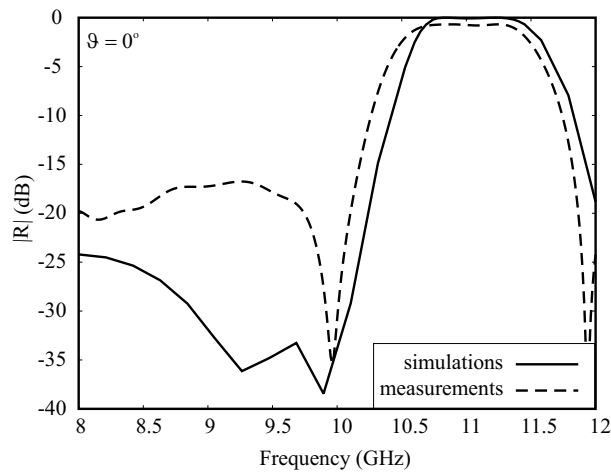


Figure 5.11: Amplitude of the FSS reflection coefficient for normal incidence: comparison between the IEMEN-based simulations and the measurements performed using the setup shown in Fig. 5.8, with the FSS plate located in the near field of the TX.

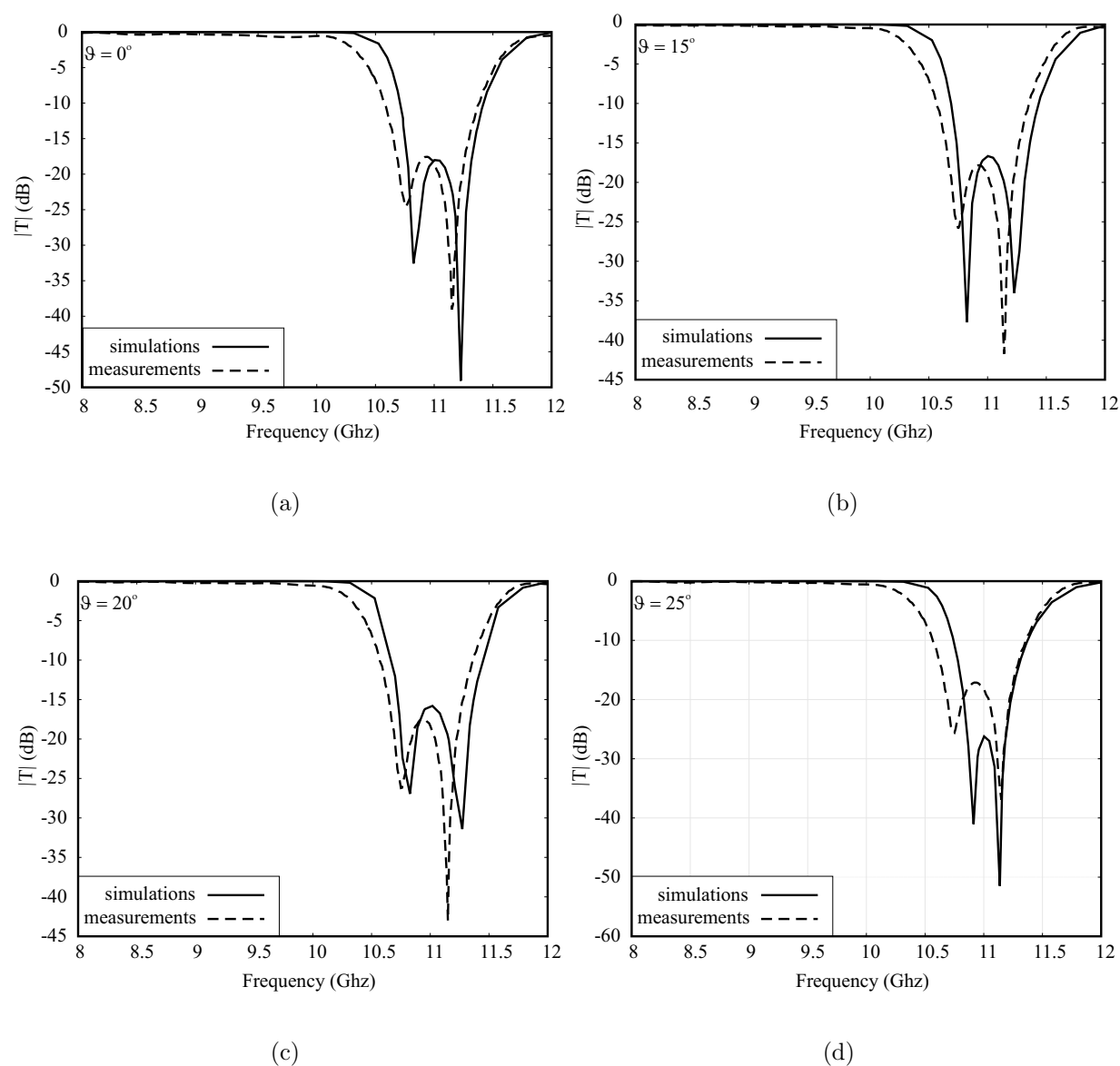


Figure 5.12: Amplitude of the FSS transmission coefficient: comparison between the full-wave IEMEN-based simulations and the near-field measurements for different angles of incidence: (a) $\vartheta = 0^\circ$, (b) $\vartheta = 15^\circ$, (c) $\vartheta = 20^\circ$, (d) $\vartheta = 25^\circ$.

In Fig. 5.11 we have reported for the sake of completeness the reflection coefficient simulated by means of our IEMEN formulation and the one measured using the setup described in Sec.5.2.2. The agreement between the two results is reasonably good, when we take into account that the comparison is interesting only in the stop band. In fact, as already

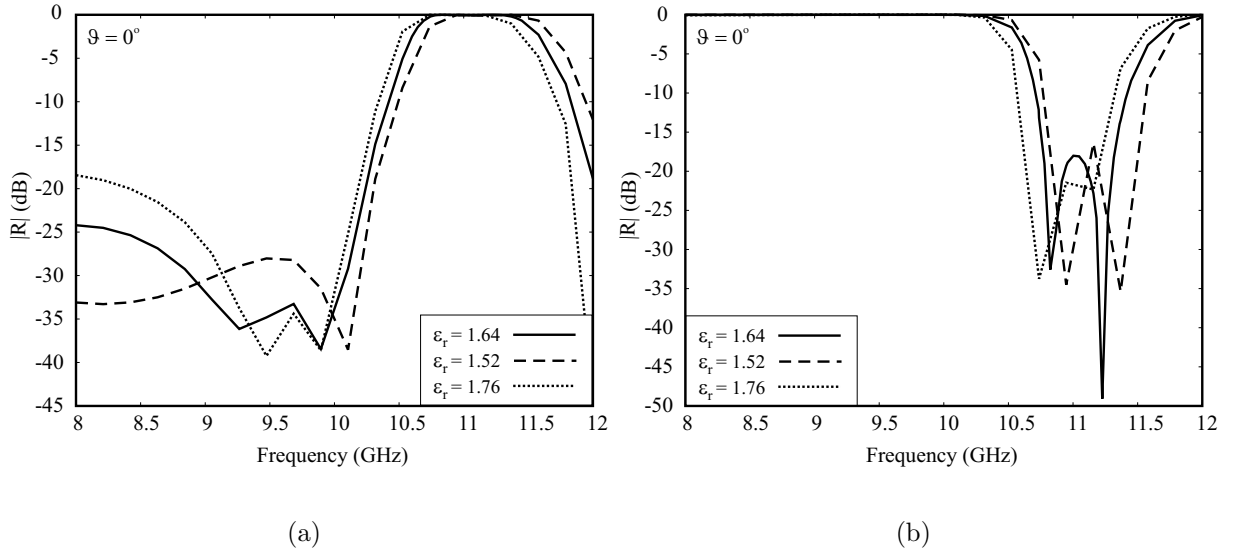


Figure 5.13: Effect of the foam permittivity on the FSS performances for normal incidence: (a) amplitude of the reflection coefficient and (b) amplitude of the transmission coefficient, for the permittivity values $\epsilon_r = 1.52$, $\epsilon_r = 1.64$ and $\epsilon_r = 1.76$.

observed for the comparison with the far-field measurements in Fig. 5.6, if we consider the order of magnitude of the reflection coefficient in the pass-band, the measured and simulated values are quite close to each other and they both satisfy the design requirements of being less or equal to -10 dB. In Figs. 5.12 the measured and the calculated transmission coefficient are compared for the angles of incidence 0° , 15° , 20° and 25° . In this case, a very good agreement is obtained and the small frequency shift of 0.1 GHz, which corresponds to about 0.9% with respect to the measured resonance frequency, is within the tolerances of the dielectric constant of the foam. To gain a feeling of the impact of the foam permittivity on the FSS performances, we have plotted in Fig. 5.13 the magnitude of the reflection and transmission coefficients for the same structure, where the permittivity assumes the minimum a maximum values indicated by Rogers, $\epsilon_r = 1.76$ and $\epsilon_r = 1.52$, compared to the medium value used for our simulations $\epsilon_r = 1.64$. The resonance frequency shifts about $\pm 1\%$. Also on the basis of the previous discussion, the evaluation of the FSS performances should be based on its transmission coefficient measurement results.

Finally, the losses of the materials, which were not taken into account in our simulations, have an effect on the level of the response. In Fig. 5.11 we can observe a difference of about 1 dB between the simulated and the measured reflection coefficient level at reso-

nance. Simulations performed with commercial tools have shown that this is the order of magnitude of the impact of the losses.

5.3 Conclusions

In this chapter we have described the steps that, from the FSS design of Chapter 4, Sec. 4.1, lead to the manufacturing of the panel and to the corresponding experimental verification. Because of the limited availability of the materials and of manufacturing constraints, the structure of the final panel was somewhat different from the initial design. In particular, a number of slabs of the same material had to be stacked together to obtain the desired thickness, for both the FSS core and the external matching layers. As a consequence, the effect of the bonding film could no longer be neglected in the analysis. For this purpose, we resorted to the generalization of the IEMEN formulation to the case of very thin layers, introduced in Chapter 3, Sec. 3.4. Moreover, the foam used for the external layers resulted to have very poor electromagnetic properties because of its inhomogeneity; therefore, since the permittivity was locally variable, we had to consider an average of the values measured in different samples. New simulations were performed to take into account all these aspects. The experimental validation consisted of reflection and transmission measurements. Since the simulations were performed under the hypothesis that incident, reflected and transmitted waves would be plane, in principle this condition should have been ensured also during the measurements. This would have required placing the FSS panel in the far field of the TX and the RX in the far field of the scattering panel. While the FSS can easily be placed in the far field of the TX, the second requirement, instead, implies either the availability of an enormous anechoic chamber (for a panel of 60 cm x 60 cm the far-field distance from the FSS should be 24 m) or performing the measurements on small panels (but then the edge diffraction would become dominant in the measurements, with or without use of a RAM frame). However, from the comparison between the reflection coefficient measured with the RX in the far field of a FSS subpanel and the one measured with the RX in the near-field of the FSS panel (shown in Fig. 5.8), it seems that the position of the RX with respect to the FSS does not have a significant effect.

These considerations extend also to the transmission measurements, where the RX was placed in the near field of the FSS. In Sec. 4.1.3 we have observed that the frequency behavior of this FSS is almost independent of the angle of incidence of the coming wave. As a consequence, even if the phase front of the impinging wave is not plane, we expect the response of the FSS to be similar to that obtained for plane wave incidence. Therefore,

transmission measurements are reliable even if the FSS is located in the near field of the TX.

The expected performances in terms of transmission coefficient are in excellent agreement with the experimental results, in view of the tolerances in the foam and bonding film permittivities. The reflection coefficient measurements in the pass band were affected by edge diffraction (although more significantly in the far field setup) and by inaccuracies introduced by the measurement setup, especially concerning the calibration with the reference metal plate. However, the difference between simulations and measurements, mainly concerning the pass band, is rather small if we consider the order of magnitude of the values at hand (lower than -20 dB); moreover, the results respect the requirements on the FSS reflection coefficient, which has to be lower than or equal to -10 dB in the pass band. Therefore, the agreement between measured and simulated reflection coefficients is also satisfactory.

From all these considerations, we have concluded that, among the considered setups, the most appropriate experimental verification of an FSS performances was obtained by means of transmission measurements, because:

- the setup is quite simple and limits the possibility of mechanical errors,
- the measurements can be performed in a way to reduce edge diffraction,
- the calibration does not need the use of a reference plate.

Reflection coefficient measurements are also performed by using the waveguide simulator [37,106,117]. They are rather inexpensive and simple to perform, since only one unit cell of the FSS is used. However, this technique does not allow measuring the reflection coefficient in a frequency and angular range, but only for certain pairs of frequency and angle values. This is why measurements in waveguide simulator are mostly used to tune the preliminary design of a periodic structure, while the validation of the final design is usually based on radiation measurements performed in the anechoic chamber.

Finally, we would like to stress the fact that the design and manufacturing of the FSS was aimed to investigate the electromagnetic properties of this multi-layer structure. Therefore, we did not have any technology goal and we have deliberately not considered other aspects, concerning for example mechanical properties dictated by structural and environmental constraints, which would be important in a commercial production of the FSS, but which, in turn, depend on the specific application.

Chapter 6

Reduced kernel integral equation

In Chapter 3, Sec. 3.2 and Sec. 3.3 we have shown that the key innovative notion introduced by the Integral Equation Method for the derivation of Multimode Equivalent Networks (IEMEN), is the formalization of the scattering problem through a single Integral Equation (IE) with reduced kernel and multiple forcing terms, one for each accessible mode. The corresponding reduced Green's Function (GF) appearing in the kernel has been represented as a superposition of Floquet Waves (FW), and the IE has been solved by applying the Method of Moments (MoM) with a Galerkin procedure, and expanding the unknown currents in terms of sub-domain functions. When the frequency filtering performances required from the Frequency Selective Surface (FSS) include steep roll offs and wide scan angles, dielectric slabs with high permittivities are required. Consequently, a larger number of accessible (interacting) modes has to be included in the analysis and it turns out that, for expansions based on sub-domain functions, the MoM matrix tends to become ill conditioned. To overcome this kind of problem, which arises when stringent requirements are set on the FSS, basis functions related to the physics of the problem should be identified. A number of techniques have been presented in the past years for the analysis of large finite arrays. Although we are dealing here with infinite arrays, rather than finite ones, both cases can lead to extremely oscillating kernels and forcing terms, and the techniques used in the analysis of finite arrays to tackle these problems can be extended to the study of infinite arrays when a IEMEN formalism is used. Some of these methods lead to a compression of the MoM size based on physical schemes; approaches which exhibit common features are in [39, 40, 50, 85, 89, 102, 103, 116, 119]. All these techniques attempt to keep explicit information about the multi-scale nature of the solution directly in the representation of the unknown currents. This significantly reduces the number of unknowns associated to the problems at hand. In particular, we have selected truncated

Floquet waves, variations of those proposed in [102] as entire-domain basis functions for the analysis of large finite slot arrays (two-dimensional geometries). The functions introduced here are defined in the periodic cell rather than in all the unit cells, and are equipped with appropriate edge conditions, so that they are different than zero only in the domain of the radiating element.

In Sec. 6.1 a simple two-dimensional array geometry, under TM excitation, is considered. The MoM matrix obtained for this problem is first investigated for the case of sub-domain expansion. It turns out that, already for a small number of accessible modes, the obtained system of linear equations is highly ill conditioned. To reduce the impact of the ill conditioning in the numerical solution, in Sec. 6.2 we have performed a physics-based regularization. This consists in adopting a convenient set of truncated Floquet waves, which, while limiting the solution domain, makes the problem intrinsically well conditioned. Some specific critical test cases are tackled and the results obtained by means of a sub-domain and an entire-domain expansion of the unknown currents are compared. Conclusions are drawn in Sec. 6.3.

6.1 Two-dimensional TM problem

In this section a simple two-dimensional (2D) geometry is specified to introduce the ill conditioning problem that arises when a reduced kernel IE is solved by means of a MoM procedure, and sub-domain basis functions are used to expand the unknown currents.

6.1.1 Geometry and IE formulation

Fig. 6.1 shows the investigated geometry. It consists of an infinite periodic array of metallic strips in free space. The period is d_x and the strips are infinitely long in the y -direction and have width w_x . The incident wave is assumed to be TM polarized with respect to the z -axis, so that the magnetic field is entirely along the y -axis (not shown in the figure) and the electric field has a component along the x -axis. The accessible FW's that appear in the multimode expression of the field can be represented in terms of an equivalent transmission line circuit. A dipole FSS is characterized with respect to this circuit in terms of a shunt discontinuity. As explained in Chapter 3, Sec. 3.2 for a three-dimensional geometry, the FSS equivalent network is obtained from the solution of a reduced kernel IE, derived by applying the IEMEN method and having as forcing terms the transverse modal electric fields associated to the accessible FW's. Fig. 6.2 shows this network, with the localized modes closed on the characteristic admittance.

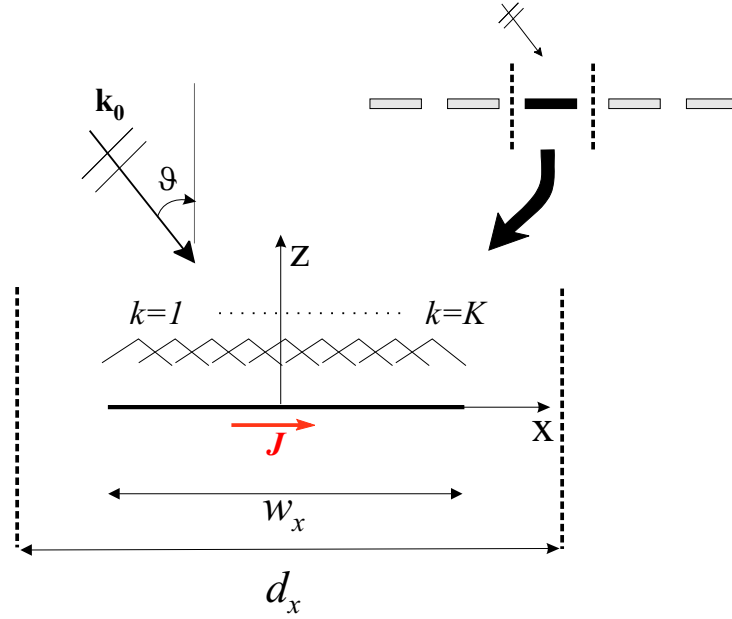


Figure 6.1: Geometry of the investigated two-dimensional problem: infinite periodic array of conducting strips under TM plane-wave incidence.

According to standard array theory (Appendix B, Sec. B.2), the component along the x -direction of the vector mode function for the electric field can be expressed, in case of TM polarization, as:

$$e_i = \frac{1}{\sqrt{d_x}} e^{-j(k_{x_0} - \frac{2\pi i}{d_x})x}, \quad (6.1)$$

where $k_{x_0} = k_0 \sin \vartheta$ is the phase shift of the excitation law in the x direction, $i = -N_a, \dots, N_a$ is the index of the considered accessible mode, and $2N_a + 1$ is the total number of accessible modes and will be indicated from now on as N . Note that the normalization constant appearing in Eq. (6.1) has been derived from the orthogonality condition on the corresponding scalar mode functions, analogously to the three-dimensional (3D) case described in Appendix B. The complete IE in this simple case can then be expressed as:

$$\int_{-w_x/2}^{w_x/2} g_{na}^e(x; x') \cdot j_i(x') dx' = -\frac{1}{\sqrt{d_x}} e^{-jk_{x_i}x}, \quad (6.2)$$

where

$$k_{x_i} = k_{x_0} - \frac{2\pi i}{d_x}$$

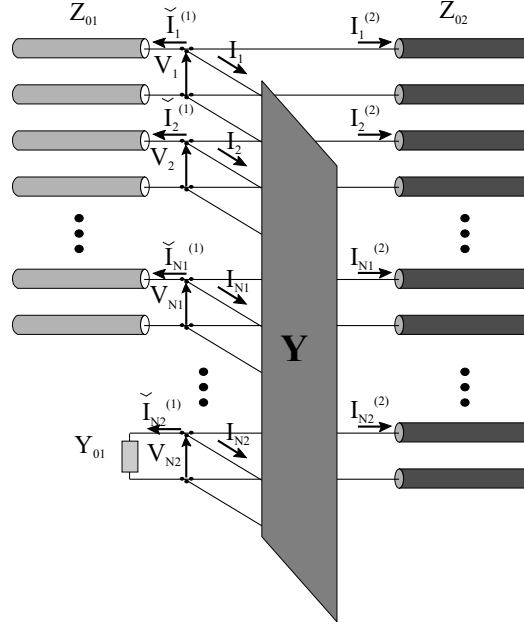


Figure 6.2: Multimode Equivalent Network of an FSS, made of metal patches, for which the patch formulation of the IEMEN method, described in Chapter 3 for a three-dimensional geometry, has been used.

is the modal transverse wavenumber. In Eq. (6.2) $j_i(x')$ are the unknown equivalent currents, induced on the patch by an impressed electric field equal to the i -th Floquet vector mode function. A key aspect characterizing this IE is the fact that the kernel is reduced to the non-accessible portion of the GF $g_{na}^e(x; x')$.

6.1.2 Non-accessible Green's function

The free-space GF for an infinite periodic array of elementary electric currents, with constant amplitude and shifted phase, when the observation is the electric field, can be expressed as:

$$g^e(x; x') = \sum_{m=-\infty}^{\infty} g_m^e(x; x') = C_g \sum_{m=-\infty}^{\infty} \sqrt{k_0^2 - k_{x_m}^2} e^{-jk_{x_m}(x-x')}, \quad (6.4)$$

where $C_g = -(4\pi\omega\varepsilon)^{-1}$ is a constant. The definition introduced in Appendix C, Sec. C.2 for the 3D case leads to the following expression for the non-accessible portion of the GF

due to N accessible modes:

$$g_{na}^e(x; x') = \sum_{m=-\infty}^{\infty} g_m^e(x; x') - \sum_{m=-N_a}^{N_a} g_m^e(x; x'). \quad (6.5)$$

At this point, some considerations on the nature of $g_{na}^e(x; x')$ are needed. For large values of N_a , such that $k_0^2 \ll k_{x(N_a)}^2$, the propagation coefficient figuring in $g_m^e(x; x')$ can be expressed more compactly as:

$$\sqrt{k_0^2 - k_{x_m}^2} = \sqrt{k_0^2 - \left(k_{x_0} - \frac{2\pi m}{d_x}\right)^2} \approx -j \frac{2\pi|m|}{d_x}. \quad (6.6)$$

With this approximation, $g_{na}^e(x, x')$ becomes an almost frequency independent function, as shown in Appendix E, Sec. E.1:

$$\begin{aligned} g_{na}^e(x, x') &\approx j \frac{4\pi}{d_x} e^{-jk_{x_0}(x-x')} \left(\frac{1}{4 \sin^2\left(\frac{\pi}{d_x}(x-x')\right)} + \sum_{m=1}^{N_a} m \cos\left(\frac{2\pi m}{d_x}(x-x')\right) \right) \\ &= j \frac{2\pi}{d_x} e^{-jk_{x_0}(x-x')} \left\{ \frac{\cos\left(\frac{2\pi}{d_x}(N_a+1)(x-x')\right)}{2 \sin^2\left(\frac{\pi}{d_x}(x-x')\right)} + \right. \\ &\quad \left. (N_a+1) \frac{\sin\left(\frac{\pi}{d_x}(2N_a+1)(x-x')\right)}{\sin\left(\frac{\pi}{d_x}(x-x')\right)} \right\}, \end{aligned} \quad (6.7)$$

and results from the superposition of two radically different terms. The first one is oscillating and has a $1/x^2$ singularity, the same kind of singularity that appears in the standard, periodic or non periodic, 2D free-space GF. The second one is also an oscillating term, with amplitude dependent on the number of accessible modes, and the period is equal to the period of the $(2N_a+1)$ -th FW harmonic. Overall it appears that, on the contrary to what the name would suggest, the non-accessible GF is determined by the number of modes extracted from the kernel.

The expression of the non-accessible portion of the field radiated by a periodic array of electric currents, in the approximation of large N_a , has been derived in Appendix E, Sec. E.2:

$$\begin{aligned} \int_{-w_x/2}^{w_x/2} g_{na}^e(x-x') \cdot j_i(x') dx' &= e^{-jk_{x_0}x} \left(\int_{-w_x/2}^{w_x/2} \frac{j_i(x') e^{jk_{x_0}x'}}{\sin^2\left(\frac{\pi}{d_x}(x-x')\right)} dx' \right. \\ &\quad \left. + 2 \sum_{m=1}^{N_a} m \left[e^{j\frac{2\pi m}{d_x}x} \tilde{j}_i(k_{x_m}) + e^{-j\frac{2\pi m}{d_x}x} \tilde{j}_i(k_{x_{-m}}) \right] \right), \end{aligned} \quad (6.8)$$

where $\tilde{j}_i(k_x)$ is the Fourier Transform (FT) of the elementary current distribution $j_i(x)$. A very common choice for the solution of an IE via MoM, is to expand the unknown currents in Eq. (6.2) in terms of piecewise sinusoidal (pws) sub-domain functions [118]:

$$j_i(x') \approx \sum_{k=1}^K I_k^{(i)} \text{pws}(x' - x_k). \quad (6.9)$$

The expression of the pws centered in $x_0 = 0$ is:

$$\text{pws}(x) = \frac{\sin\left(k_{eq} \left(\frac{w}{2} - |x|\right)\right)}{\sin\left(k_{eq} \frac{\ell}{2}\right)} \quad |x| \leq \frac{\ell}{2}, \quad (6.10)$$

where $k_{eq} = k_0 \sqrt{\frac{(\varepsilon_{r1} + \varepsilon_{r2})}{2}}$ is the equivalent wavenumber, ε_{r1} and ε_{r2} are the relative dielectric constants of the medium below and above the FSS, respectively, and in the present context they are supposed to be equal to one, and ℓ is the length of the interval over which the pws function differs from 0.

The FT of the currents in Eq.(6.9), as calculated in Appendix E, Sec. E.3, is:

$$\tilde{j}_i(k_{x_m}) = \sum_{k=1}^K I_k^{(i)} e^{jk_{x_m} x_k} \text{PWS}(k_{x_m}), \quad (6.11)$$

where $\text{PWS}(k_{x_m})$ indicates the FT of a pws centered in $x = 0$:

$$\text{PWS}(k_x) = 2 \frac{\left(k_{eq} \frac{\ell}{2}\right)^2 \left(\cos\left(k_x \frac{\ell}{2}\right) - \cos\left(k_{eq} \frac{\ell}{2}\right)\right)}{k_{eq} \sin\left(k_{eq} \frac{\ell}{2}\right) \left(k_{eq} \frac{\ell}{2}\right)^2 - \left(k_x \frac{\ell}{2}\right)^2}. \quad (6.12)$$

Fig. 6.3 shows parametric curves (for different N_a indices) of the amplitude of the non-accessible fields, generated by a current distributed according to a pws rule.

The calculations have been performed by expressing the non-accessible GF as in Eq. (6.5), without resorting to the approximation in Eq. (6.7). In particular, we have used one pws function, centered in the origin of the reference system in Fig. 6.1, with length $l = 0.01\lambda_0$. The period of the structure is $d_x = 0.6\lambda_0$ and the field is observed on the entire periodic cell. The array is supposed to be radiating broadside, $k_{x_0} = k_0 \sin \theta = 0$ and therefore the entire non-accessible field is purely imaginary. The function is also evidently periodic with period d_x , and only the first period is considered. Both the dominant singularity (in $x = 0$), and the periodic oscillations, appearing explicitly in the approximated expression (6.8), can be recognized. Note that for $N_a = 0$ (fundamental Floquet mode) the radiated field imaginary

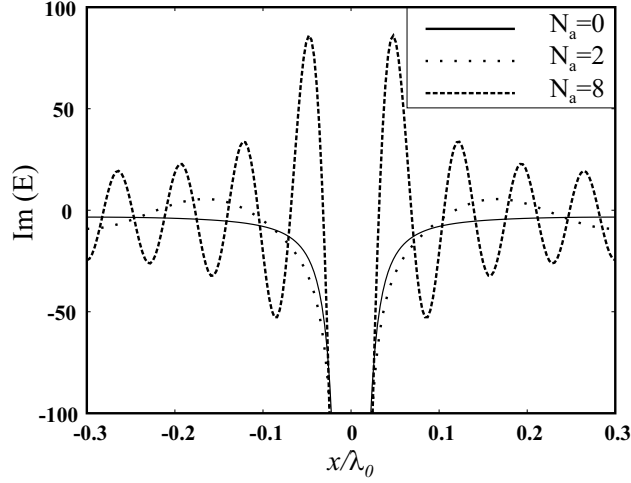


Figure 6.3: Non-accessible Green's function plotted in terms of the x coordinate. The period is $d_x = 0.6\lambda_0$, the pws is $0.01\lambda_0$ wide and it is centered in the origin. The array is supposed to be scanning at broadside. Note that the function is periodic of period d_x and only the first period is shown.

part is equal to the imaginary part of the standard GF. Moreover, for any value of N_a larger than zero, the radiated field shows a slowly decreasing oscillation, whose amplitude and period depend on N_a . It is clear that the asymptotic behavior of the non-accessible GF (for $x \notin$ (source region)) is very different from that of the standard GF. In the following, we will show how this has an impact in the way the IE (6.2) has to be numerically handled.

6.1.3 Ill conditioning of the sub-domain expansion

Piecewise sinusoidal and piecewise linear functions are widely used for studying dipole antennas because they are both very suitable to discretize geometries containing small elements, and their FT is known in close form. In particular, piecewise sinusoidal functions result to be more appropriate than piecewise linear to study configurations where the field varies only in one direction (like for example thin wires, microstrips with thin strips and 2D scattering problems), since their shape is more adequate to follow the variations of the field and therefore, in general, they allow resorting to a discretization of the unknowns with a smaller number of terms. This is a very useful property to calculate the spectral-domain reaction integrals in the MoM solution of the IE. However, the use of these functions to expand the unknown currents in a reduced kernel IE might lead to ill-conditioning problems. Since the forcing terms are periodic functions of x (accessible FW's) the IE's

solution tends also to be highly oscillatory in nature. It turns out that the minimum number of pws's required to obtain an accurate solution depends on the maximum accessible mode index N_a , and at least a few pws's for every possible change of sign in the forcing term must be allowed. This can be regarded as a formulation of the relative convergence problem [95] for the case of reduced IE's and as an alternative form of Shannon's sampling theorem [129]. If we substitute the FT of the unknown currents (6.11) in the expression of the non-accessible radiated field (6.8), the following approximation of the i -th reduced kernel IE, valid for $k_0^2 \ll k_{x_{N_a}}^2$, is obtained:

$$\begin{aligned} \sum_{k=1}^K I_k^{(i)} e^{jk_{x_0} x_k} \int_{-w_x/2}^{w_x/2} \frac{\text{pws}(x') e^{jk_{x_0} x'}}{\sin^2\left(\frac{\pi}{d_x}(x-x'-x_k)\right)} dx' + 2 \sum_{m=1}^{N_a} m \left(e^{j\frac{2\pi m}{d_x} x} \text{PWS}(k_{x_m}) \right. \\ \left. \sum_{k=1}^K I_k^{(i)} e^{jk_{x_m} x_k} + e^{-j\frac{2\pi m}{d_x} x} \text{PWS}(k_{x_{-m}}) \sum_{k=1}^K I_k^{(i)} e^{jk_{x_{(-m)}} x_k} \right) = -j \frac{\sqrt{d_x}}{\pi} e^{j\frac{2\pi i}{d_x} x}. \end{aligned} \quad (6.13)$$

In Appendix E, Sec. E.4 it has been shown that projecting both sides of Eq. (6.13) onto the same functions used for expanding the unknown currents (Galerkin procedure), leads to the system of linear equations:

$$\sum_{k=1}^K I_k^{(i)} Z_{lk} = V_l^{(i)}, \quad (6.14)$$

where the known terms are:

$$V_l^{(i)} = -j \frac{\sqrt{d_x}}{\pi} e^{j\frac{2\pi i}{d_x} x_l} \text{PWS}\left(\frac{2\pi i}{d_x}\right). \quad (6.15)$$

If, for the sake of simplicity, we restrict ourself to the broadside case ($k_0 = 0$), the matrix elements in (6.14) can be written as

$$Z_{lk} \approx \left(S(x_l - x_k) + 4 \sum_{m=1}^{N_a} m \text{PWS}^2\left(\frac{2\pi m}{d_x}\right) \cos\left(\frac{2\pi m}{d_x}(x_l - x_k)\right) \right), \quad (6.16)$$

and they are essentially frequency independent. Even if this approximated expression has been derived for normal incidence or radiation, it provides important qualitative information that is of general validity. The term $S(x_l - x_k)$, which represents the mutual coupling between two pws functions via the singular portion of the kernel only, is equal to:

$$S(x_l - x_k) = \int_{-\ell_x/2}^{\ell_x/2} \int_{-\ell_x/2}^{\ell_x/2} \frac{\text{pws}(x)\text{pws}(x')}{\sin^2\left(\frac{\pi}{d_x}(x-x'+x_l-x_k)\right)} dx' dx, \quad (6.17)$$

where the integral is solved by extracting the singularity corresponding to the self-coupling ($x_l = x_k$). It is dominant for pws functions located close to each other, such that $|x_l - x_k| \rightarrow 0$. For the off-diagonal elements of the MoM matrix in Eq. (6.16), if a relatively large number of accessible modes is retained in the representation (i.e. for large values of N_a), the second term becomes dominant and causes an oscillating behavior. The system (6.14) can be solved via direct inversion of this matrix. More efficiently, other solution techniques exploit the peculiar structure of the MoM matrix, a Toeplitz matrix where each left diagonal is equal to the symmetrical right diagonal (with respect to the main diagonal), from the top-left to the lower-right. While for a general full square matrix of dimension N the inversion requires N^3 steps, for a Toeplitz matrix only N^2 steps are needed [58]. However, since the computational time is mostly associated to the filling of the MoM matrix rather than to its inversion, this aspect has not been further investigated.

Fig. 6.4 shows a parametric study of the condition numbers of the MoM matrix generated when solving the scattering problem of an array of metallic strips under TM incidence. The condition number is plotted as a function of the accessible mode index N_a and for different strip widths. To compare the results, in all cases, 101 pws functions were considered. The strips width ranges from small with respect to the wavelength ($w_x = 0.2\lambda_0$) to a dimension of the order of magnitude of the array period ($w_x = 0.59\lambda_0$). The condition number increases with N_a , as expected. Moreover, one can notice that the growth is much faster when the strip width is comparable with the period. In particular, for $w_x = 0.59\lambda_0$ the sum in the IE kernel did not converge even when the number of expansion functions was increased, and the resulting MoM matrix was always ill-conditioned. The intuitive reason is that the natural modes of the structure tend to resonate with the Floquet modes. In this case, the problem cannot be treated already for $N_a = 1$, while for shorter strips the coherence between Floquet modes and eigenmodes can only occur for larger N_a . In fact, when the strip length tends to coincide with the period, the scattering problem becomes that of an array of magnetic strips having a very small width with respect to the wavelength (point sources), located at the gaps between adjacent strips, and it can be solved more efficiently by means of other techniques.

6.1.4 Eigenvalues and eigenfunctions

The linear Eq. (6.2) is of the type

$$L(\mathbf{x}) = \mathbf{b}, \tag{6.18}$$

where L is an integral operator containing the non-accessible GF, and has been reduced

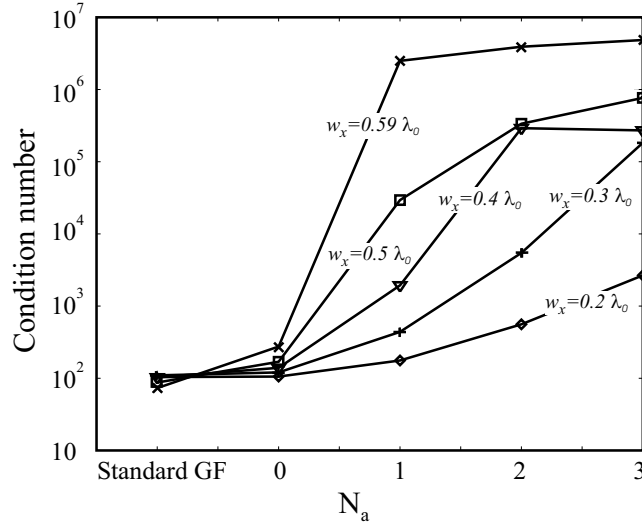


Figure 6.4: Condition number of the MoM matrix obtained for strips of different widths w_x , with lattice period $d_x = 0.6\lambda_0$. In all cases, 101 pws functions were used.

to the matrix equation in (6.14) by applying the MoM. The eigenvalue equation for the operator L is:

$$L\mathbf{v} = \lambda\mathbf{v}, \quad (6.19)$$

where λ are the eigenvalues and \mathbf{v} are the eigenfunctions. As shown in [66], the MoM can be used to discretize this functional equation, in the same way as it is done for the linear Eq. (6.2). If f is a set of basis functions, defined in the domain of L , such that:

$$\mathbf{v} = \sum_n \beta_n f_n, \quad (6.20)$$

and t is a set of testing functions defined in the range of L , Eq. (6.19) becomes:

$$\sum_n \beta_n \langle t_m, Lf_n \rangle = \lambda \sum_n \beta_n \langle t_m, f_n \rangle, \quad m=1,2,\dots, \quad (6.21)$$

which in matrix form becomes:

$$[L][\beta] = \lambda[S][\beta]. \quad (6.22)$$

$[S]$ is the matrix of the scalar products between the basis and the test functions:

$$S_{ij} = \langle t_m, f_n \rangle, \quad (6.23)$$

where the scalar product is defined as $\langle \mathbf{x}, \mathbf{y} \rangle = \int \mathbf{x} \cdot \mathbf{y}^* dS$, where \mathbf{y}^* is the complex conjugate of \mathbf{y} . Eq. (6.22) can be written as:

$$[S]^{-1}[L][\beta] = \lambda[\beta]. \quad (6.24)$$

Therefore, the eigenfunctions of the operator L in Eq. (6.19) can be approximated through Eq. (6.20) by means of a subset of the eigenvectors of the matrix $[S]^{-1}[L]$, and a subset of the eigenvalues of this matrix approximate the operator's eigenvalues. In fact, some of these eigenvalues correspond to non-physical solutions introduced by the discretization.

If, in a MoM-based solution of the IE, the same basis functions can be used to discretize the unknowns and to represent the eigenfunctions of the integral operator, then the eigenvalues of the matrix $[S]^{-1}[L]$ are a better approximation of the eigenvalue spectrum of the operator than those of the MoM matrix $[L]$, and the condition number of $[S]^{-1}[L]$ is relatively independent from the choice of basis and test functions, as argued in [114]. This suggests that, to have a well-conditioned problem, it is necessary that the matrix $[S]$ is well-conditioned. If the matrix $[S]^{-1}[L]$ (and the corresponding discretized problem in Eq. (6.14)) is still poorly conditioned, the conditioning problem resides in the matrix $[L]$ and therefore in the way the IE has been discretized. This fact has been observed when applying the IEMEN formulation and using pws basis functions for a MoM solution of the reduced IE. The $[S]$ matrix is almost diagonal and always well conditioned while the MoM matrix $[L]$ is highly ill conditioned, as seen in Fig. 6.4, and so is the matrix $[S]^{-1}[L]$, which differs from $[L]$ only by a multiplying factor.

Moreover, the matrices $[S]^{-1}[L]$ and $[L]$ have the same eigenvectors and the eigenvalues of the matrix $[S]^{-1}[L]$ can be obtained from those of the matrix $[L]$ by dividing them by a constant factor (equal to the scalar product in Eq. (6.23) for $i = j$). Because of this, the eigenvalues of the matrix $[S]^{-1}[L]$ are harder to distinguish individually, and it is more convenient to present the MoM matrix eigenvalues. All the observed properties can be directly extended to the matrix $[S]^{-1}[L]$ and to the corresponding operator.

The calculation of the $[L]$ matrix eigenvalues and eigenvectors has been carried out for strips of two different widths, small and comparable with the period: $w_x = 0.2\lambda_0$ and $w_x = 0.59\lambda_0$ respectively. The non-accessible kernel is defined by $N_a = 1$, (which corresponds to extracting three FW's from the complete kernel), and the period is again $d_x = 0.6\lambda_0$. The magnitudes of the complete set of eigenvalues are displayed in Fig. 6.5a. There are 101 of them, as many as the originating sub-domain pws functions, and they are ordered according to their magnitude. The eigenvalues are approximately constant, apart for the last three, which are very small and are shown in an expanded scale in Fig. 6.5b. These three eigenvalues are those which mostly change when the strip width is increased from

$w_x = 0.2\lambda_0$ to $w_x = 0.59\lambda_0$. In Fig. 6.6 the smallest eigenvalue is plotted as a function of the strip width w_x/λ_0 . In general, a very small eigenvalue of the matrix $[L]$ is either artificial, due to the discretization of the operator equation, or it is related to the physics of the problem and appears when one of the natural modes of the system is resonant, as shown in [18]. We shall now verify that, for the present problem, the smallest eigenvalue is actually a real one.

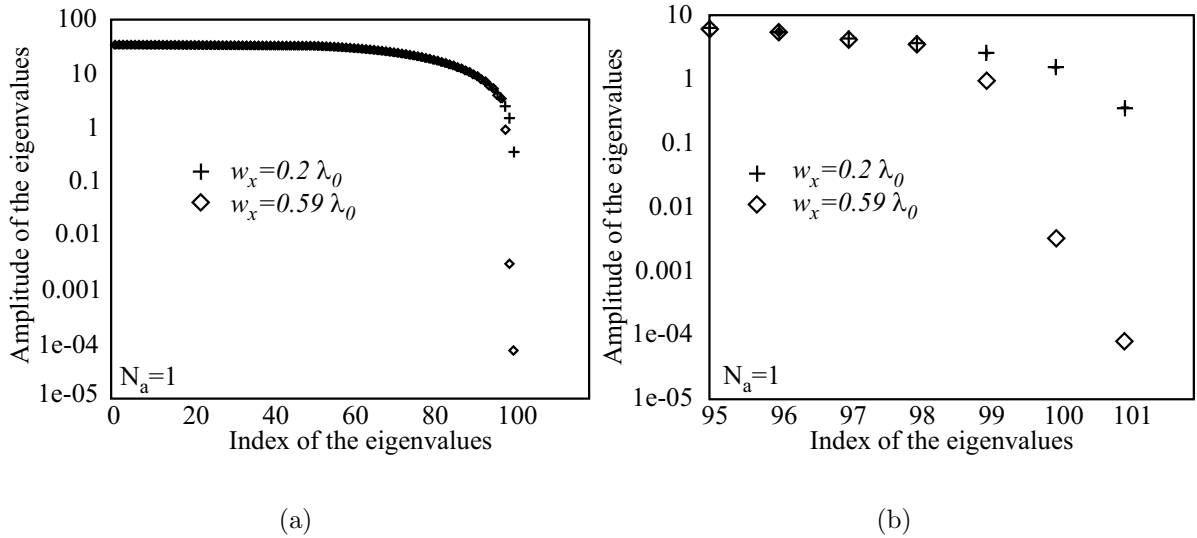


Figure 6.5: Logarithmic plot of the absolute value of the MoM matrix eigenvalues for two different strip widths: $w_x = 0.2\lambda_0$ and $w_x = 0.59\lambda_0$. (a) Complete set of eigenvalues. (b) Smallest three eigenvalues.

With this purpose, from the eigenvectors associated to the smallest eigenvalues in Fig. 6.5 we have derived the corresponding eigenfunctions according to Eq. (6.20), which approximate the eigenfunctions of the integral operator. The imaginary part of these three eigenfunctions is always negligible, while the real part is plotted in Fig. 6.7 for the same two strip widths; in both cases, they go to zero at the end points of the strips, as it follows from the choice of the discretization. For the shorter-strip, the eigenfunctions seem very close to the strip natural modes (pure sines and cosines). Alternatively, they can be seen as FW's defined with respect to the strip's width instead of the array's period. In particular, the first eigenfunction can be expressed as $\cos\left(\frac{\pi}{w_x}x\right)$. Instead, in the longer strip case the 101-th most excited eigenfunction shows a different behavior and it can be written essentially as $\left(1 + \cos\left(\frac{2\pi}{d_x}x\right)\right)$. Thus, when the width of the strip is close to the period of the structure, the eigenfunction associated to the smallest eigenvalue becomes similar to

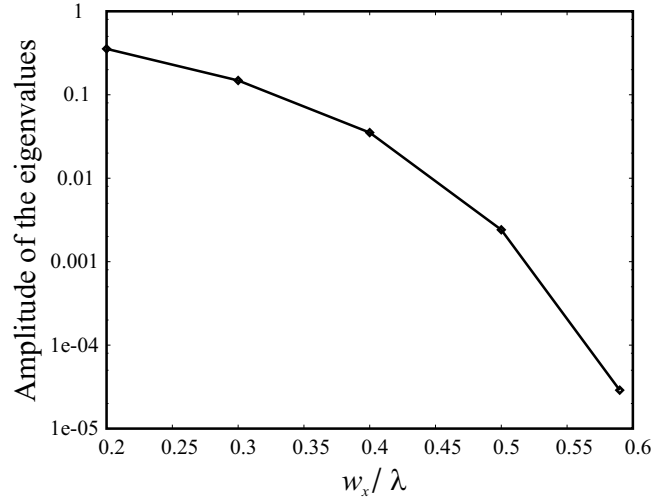


Figure 6.6: Logarithmic plot of the absolute value of the MoM matrix smallest eigenvalue as a function of the strip width.

a a combination of FW's, whose harmonic behavior is governed by the periodicity rather than by the strip's width. Less important, but still visible deviations with respect to the strip natural modes are found also in the other two eigenfunctions plotted in Fig. 6.7b.

From these graphs we can derive some general considerations on the final form of the solutions of IE's with reduced kernels. As a consequence of the extraction of the lower spectral components from the IE kernel, the set of natural modes that mostly contribute to the solution, for different forcing terms, is different (for an in depth discussion about natural modes properties the reader should refer to [136]). In particular, the actual shape of the solutions is dominated by the shape of the most strongly excited eigenfunctions, which are in turn combinations of a few FW's for wider strips, and of FW's truncated at the strip's edges for shorter strips.

6.2 Truncated Floquet waves

In the previous section it was demonstrated that a MoM solution of the reduced kernel IE, obtained by means of the IEMEN method, using sub-domain functions to expand the unknown currents may lead to an ill-conditioned system of linear equations. In particular, for a certain number of accessible modes is extracted from the kernel, the condition number of the MoM matrix increases when the strip width approaches the array period. One way to circumvent this problem consists in the adoption of an appropriate set of entire-domain

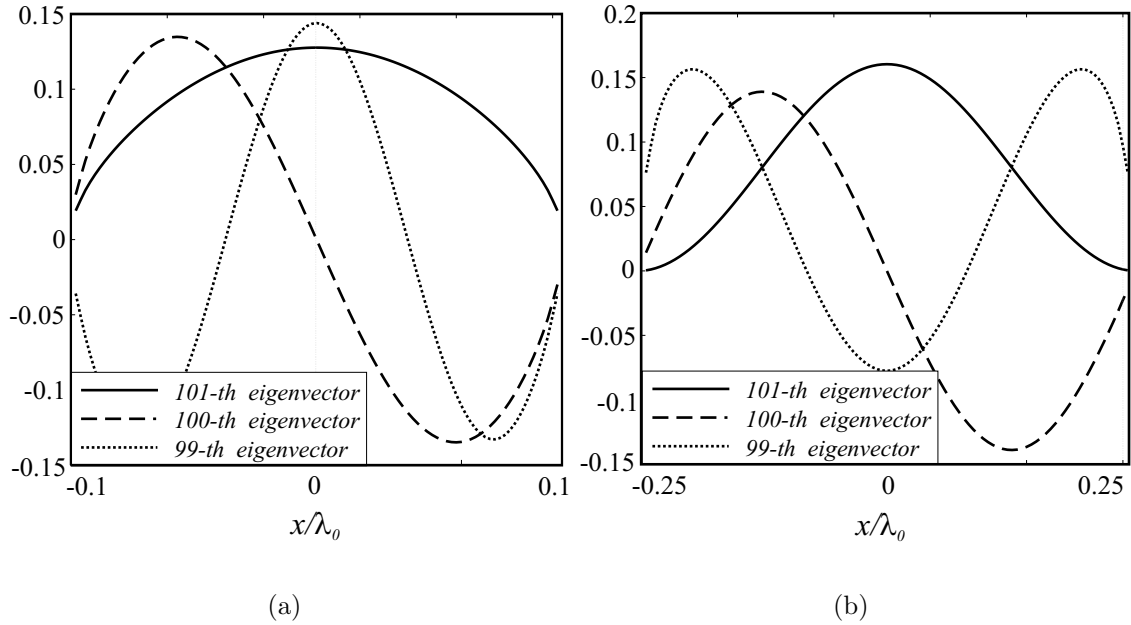


Figure 6.7: Approximated eigenfunctions (real part) of the reduced kernel IE operator, obtained from the eigenvectors of the MoM matrix $[L]$ (and of the $[S]^{-1}[L]$ matrix) for the smallest three eigenvalues. Two different strip width have been considered: (a) $w_x = 0.2\lambda_0$ and (b) $w_x = 0.59\lambda_0$.

basis functions.

A large amount of literature is available on the use of entire-domain basis-functions for antenna array problems. For example, entire-domain functions, based on Tchebychev polynomials with appropriate edge boundary conditions, have been introduced in [1] to study patch based FSS's. In the past, other authors have used the modes of a magnetic wall cavity to generate the basis functions for the surface current on a patch [6, 31, 131, 143]. Entire-domain functions derived from the natural modes of the structure have been proposed in [94] to study dipole-based FSS's. Recently, MoM matrix eigenfunctions obtained from a preliminary sub-domain numerical solution of the scattering problem have been adopted as entire-domain functions in finite array analysis [108].

For the case of reduced kernel IE, we have observed that the eigenfunctions of the reduced integral operator turn out to be similar to combinations of the extracted FW's. This idea, based on the interpretation of Fig. 6.7, is also supported by the observation that the non-accessible GF is dominated, especially for relatively large N_a values, by the Floquet wavenumbers, (see Sec. 6.1.2). Thus, entire-domain functions, derived from FW's, could

be used to reduce the total number of basis functions required in a IEMEN based analysis. This can be seen as a way of regularizing an ill-conditioned problem [104], since the space of the solution would be reduced to a subspace where the small unwanted eigenvalues are avoided. In [102], truncated Floquet waves (tfw) were proposed as entire-domain basis functions for a MoM-based analysis of large finite slot arrays in 2D geometries. The concept was then extended in [39,40,103] to 3D cases, for various types of radiating elements. With respect to these articles, where the functions are non-zero in all cells of the finite-array, the tfw's introduced here are defined in the unit cell and are forced to zero at the edges of the strip. The methodology applied to select a set of these functions, while similar to other techniques, also based on the observation of the eigenfunctions of sub-domain basis functions segmentations [108], does not require the preliminary solution via MoM. Here, the functions are chosen on the basis of priori considerations on the shape of the solution, while the technique described in [108] this would be too onerous because it would require the inversion of a matrix problem for each direction of incidence.

A parallelism with the functions used in [102,103] regards the influence of the end points of the definition domain. In the treatment of large finite arrays, the most appropriate tfw functions are modulated by a junction function derived from the diffraction-like behavior close to the edges. Also in the present case it is convenient to account for appropriate boundary conditions at the end points, but, since the scale of the problem (periodic cell) is typically sub-wavelength, the dominant edge conditions are the quasi-static ones. As a result, the following tfw functions have been adopted here for the MoM solution of Eqs. (6.2):

$$j_i(x) \approx \sum_{k=-K}^K I_k^{(i)} \text{tfw}_k(x), \quad (6.25)$$

where

$$\text{tfw}_k^{TM/TE}(x) = \frac{1}{w_x} \text{rect}(x, w_x) F^{TM/TE}(x, w_x) e^{-j(kx_0 - \frac{2\pi k}{d_x})x}, \quad (6.26)$$

with

$$\begin{pmatrix} F^{TM} \\ F^{TE} \end{pmatrix} = \begin{pmatrix} \left(1 - \left(\frac{2x}{w_x}\right)^2\right)^{1/2} \\ \left(1 - \left(\frac{2x}{w_x}\right)^2\right)^{-1/2} \end{pmatrix} \quad \text{and} \quad \text{rect}(x, w_x) = 1 \quad \forall x \in (-w_x/2, w_x/2), \quad (6.27)$$

and

$$I_k^{(i)} = \int_{-w_x/2}^{w_x/2} \text{tfw}_k(x) j_i(x) dx. \quad (6.28)$$

Fig. 6.8 shows the real and imaginary parts of the tfw's for three different wavenumbers (corresponding to $m = 0$, $m = 3$ and $m = 10$), for both TM and TE polarization. The functions are defined on a strip of width $w_x = 0.5\lambda_0$, for a periodic cell with $d_x = 0.6\lambda_0$ and with $k_{x_0} = 0$. Note that the tfw termination is associated to the presence of the Heaviside unit step function. Thus, also without the specific edge condition it would be appropriate to define tfw's. However, it will be shown in the following that the inclusion of the edge conditions greatly enhances the convergence of the solution.

The FT of a tfw can be obtained analytically and it is indicated as the function $\text{TFW}(k_x)$. After tedious, but straightforward algebraic manipulations (Appendix E, Sec. E.5), we arrive at:

$$\begin{aligned} \begin{pmatrix} \text{TFW}_k^{\text{TM}}(k_x) \\ \text{TFW}_k^{\text{TE}}(k_x) \end{pmatrix} &= FT \begin{pmatrix} \text{tfw}_k^{\text{TM}}(x) \\ \text{tfw}_k^{\text{TE}}(x) \end{pmatrix} \\ &= \begin{pmatrix} \frac{w_x}{4} J_0 \left[\left(k_x - \left(k_{x_0} - \frac{2\pi k}{d_x} \right) \right) \frac{w_x}{2} \right] + J_2 \left[\left(k_x - \left(k_{x_0} - \frac{2\pi k}{d_x} \right) \right) \frac{w_x}{2} \right] \\ \frac{w_x}{2} \pi J_0 \left[\left(k_x - \left(k_{x_0} - \frac{2\pi k}{d_x} \right) \right) \frac{w_x}{2} \right] \end{pmatrix}, \end{aligned} \quad (6.29)$$

where J_0 and J_2 are Bessel functions of the first kind of order 0 and 2 respectively. With the aid of this expression, it is simple to explicitly write the forcing terms and the matrix elements of an appropriate Galerkin-type MoM solution of the IE (6.2). The final linear system of equations is:

$$\sum_{k=-K}^K Z_{lk} I_k^{(i)} = V_l^{(i)}, \quad l = -K, \dots, K, \quad (6.30)$$

where the forcing terms are

$$V_l^{(i)} = \int_{-w_x/2}^{w_x/2} \text{tfw}_k(x) e_i(x) dx = \frac{1}{\sqrt{d_x}} \text{TFW}(-k_{x_i}), \quad (6.31)$$

and the impedance matrix can be expressed as

$$Z_{lk} = C_g \sum_{m=-\infty}^{\infty} \sqrt{k_0^2 - k_{x_m}^2} \text{TFW}_k(k_{x_m}) \text{TFW}_l(-k_{x_m}). \quad (6.32)$$

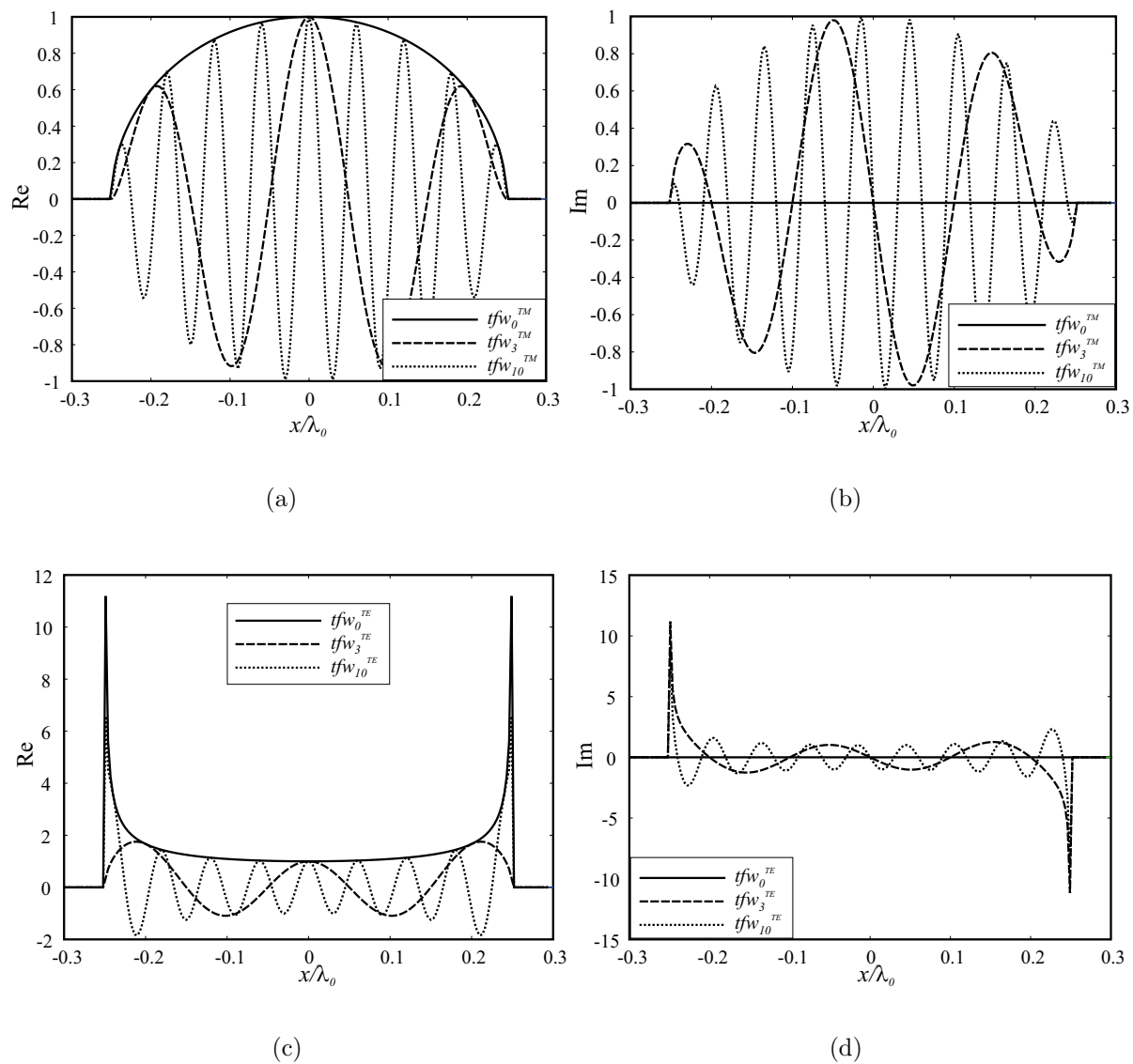


Figure 6.8: Truncated Floquet waves with appropriate boundary conditions for three different wavenumbers (corresponding to the index values $m=0$, $m=3$, $m=10$). a) TM real. b) TM imaginary. c) TE real. d) TE imaginary. In all cases $w_x = 0.5\lambda_0$ and $d_x = 0.6\lambda_0$.

In Fig. 6.9, a comparison between the currents calculated via the MoM, when using pws's and tfw's as basis functions is presented. The strip investigated in this example is $0.2\lambda_0$ wide, with a period $d_x = 0.6\lambda_0$ and $N_a = 2$. Resorting to only three tfw's allows achieving the same accuracy as using 101 pws functions.

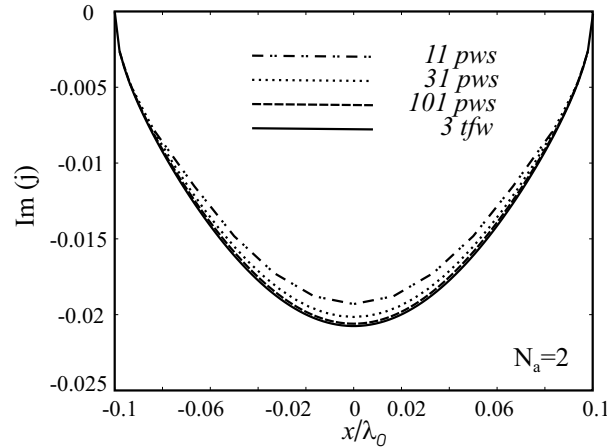


Figure 6.9: Electric currents in the TM case for $w_x = 0.2\lambda_0$, $d_x = 0.6\lambda_0$ and $N_a = 2$. Comparisons between the results obtained using increasing numbers of pws's and those obtained with only three tfw's.

6.2.1 Convergence study

An important advantage of using tfw functions is that they are similar to the forcing terms of the reduced IE, apart for a form factor at the boundaries of the definition domain. As a consequence, a limited number of these functions is sufficient to represent the unknown currents. Instead of the tfw's defined in Eq. (6.26), which are complex, we have used as expansion functions their real and imaginary parts, respectively a cosine and a sine, which will be indicated from now on as real tfw (rtfw) functions. This choice makes the interpretation of the results more straightforward.

A possibility of further improving the condition of the MoM matrix is offered by the distinguishing feature of the IEMEN method: the fact that it resorts to a single IE, with multiple forcing terms and a fixed kernel. This suggests the adoption, for each forcing term (accessible mode), of an ad hoc compact set of rtfw's as expansion functions. The same IE leads then to a different linear system for each forcing term. The computational efficiency is not compromised, since it turns out that only a few of these functions suffice to obtain an accurate result: they are in general the rtfw's having the same index as the forcing term and

those with indices just above and just below. To verify this statement, we have studied the equivalent current associated to each forcing term, in the case of an array of strips with $w_x = 0.2\lambda_0$ and periodicity $dx = 0.6\lambda_0$. The calculations have been performed for different numbers of accessible modes. In Figs. 6.10-6.15 the results obtained using rtfw's are compared with those obtained with pws's. Fig. 6.10 shows the current associated to the forcing term (index 0), when only the fundamental mode TM_0 has been extracted from the kernel; it turns out that the rtfw with index 0 is sufficient to match the result provided by the pws's. In Fig. 6.11 the equivalent current associated to the first forcing term (index 0) is plotted for three accessible modes; in this case, the rtfw with index 0 and those with index ± 1 are needed to obtain a result similar to that of the pws's. The equivalent current associated to the forcing term with index ± 1 is shown in Fig. 6.12; in this case, the rtfw's with index ± 1 are not sufficient to obtain the same solution as with pws's, and the function with index 0 has to be included as well. The so obtained reduced MoM matrix, calculated with a relative precision of 10^{-5} , has a condition number of 36, which implies an accuracy on the final results of 10^{-4} , while the accuracy on the result obtained using 101 pws is 10^{-3} . The same structure has been studied when five accessible modes are extracted from the IE kernel. If the forcing term is the fundamental mode or the first higher-order mode (index ± 1), only the rtfw with index 0 is needed to match the pws's result, as shown in Fig. 6.13 and in Fig. 6.14 respectively. Finally, if the forcing term has index ± 2 , the rtfw's with indices ± 2 and ± 1 have to be included in the analysis as basis and test functions (Fig. 6.15), while the rtfw with index 0 does not significantly influence the result.

6.3 Conclusions

This chapter has been focused on the appropriate choice of basis and test functions, when the IEMEN analysis method is adopted to study scattering problems that require the extraction of a large number of accessible modes from the kernel of the IE. This happens, for example, if the multi-layer FSS contains dielectric slabs with high permittivities. For the sake of simplicity, we have considered a 2D configuration, consisting of an infinite periodic array of metallic strips in free-space, under TM plane wave incidence. For a large number of accessible modes, the (asymptotic) non-accessible GF appears as the superposition of an oscillating singularity (the typical singularity of the standard GF), and another oscillating term, equal to the summation of as many terms as the number of accessible modes extracted from the kernel, with amplitude depending on the mode index and with the same period as the corresponding FW's extracted from the kernel. Moreover, if sub-domain functions

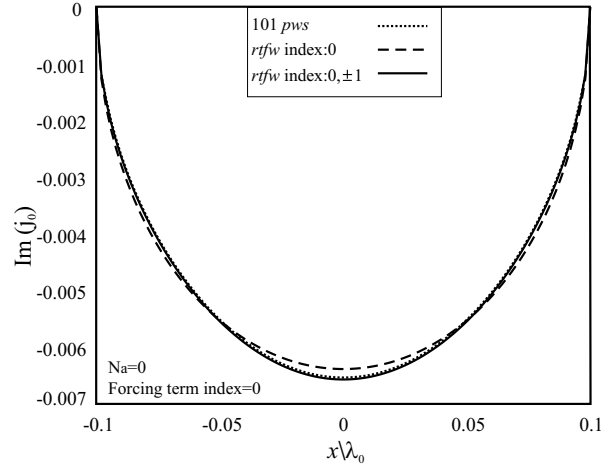


Figure 6.10: Imaginary part of the equivalent electric current associated to the mode with index 0, using rtfw's with indexes 0 and ± 1 , when only one accessible mode is extracted from the kernel. The relevant dimensions are: $w_x = 0.2\lambda_0$, $d_x = 0.6\lambda_0$.

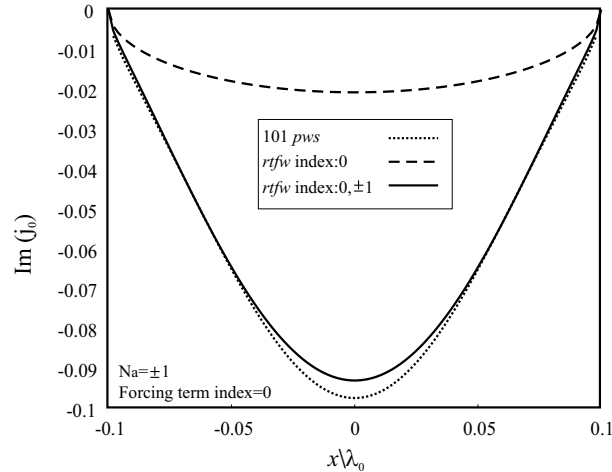


Figure 6.11: Imaginary part of the equivalent electric current associated to the mode with index 0, using rtfw's with indexes 0 and ± 1 , when three accessible modes are extracted from the kernel. The relevant dimensions are: $w_x = 0.2\lambda_0$, $d_x = 0.6\lambda_0$.

are used in a MoM solution of the IE, also the MoM matrix generic element (asymptotic expression) contains a singular term and an oscillating term. The latter prevails when basis and test functions are rather distant and a relatively large number of accessible modes are retained in the analysis; consequently, the off-diagonal elements of the MoM matrix have a non-decreasing and oscillating nature. Moreover, since the forcing terms of the IE's are the

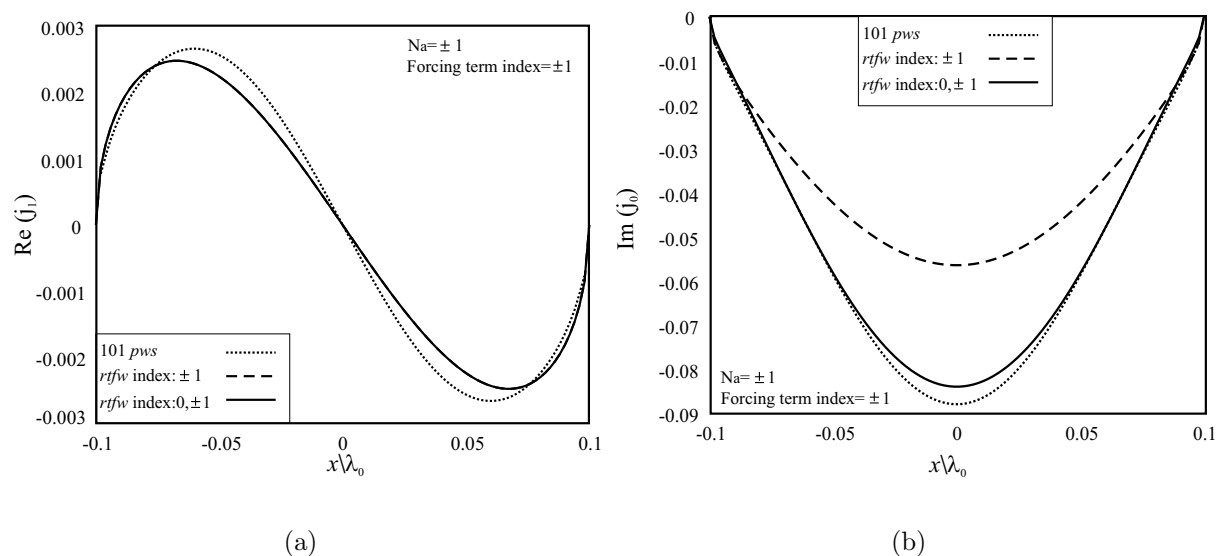


Figure 6.12: Equivalent electric current associated to the modes with index ± 1 , when three accessible modes are extracted from the kernel: comparison between different number and type of expanding functions. (a) Real part. (b) Imaginary part. The relevant dimensions are: $w_x = 0.2\lambda_0$, $d_x = 0.6\lambda_0$.

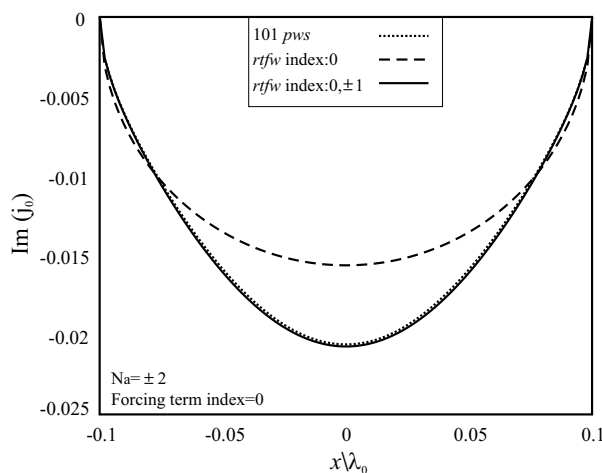


Figure 6.13: Imaginary part of the equivalent electric current associated to the mode with index 0, using rtfw's with indexes 0 and ± 1 , when five accessible modes are extracted from the kernel. The relevant dimensions are: $w_x = 0.2\lambda_0$, $d_x = 0.6\lambda_0$.

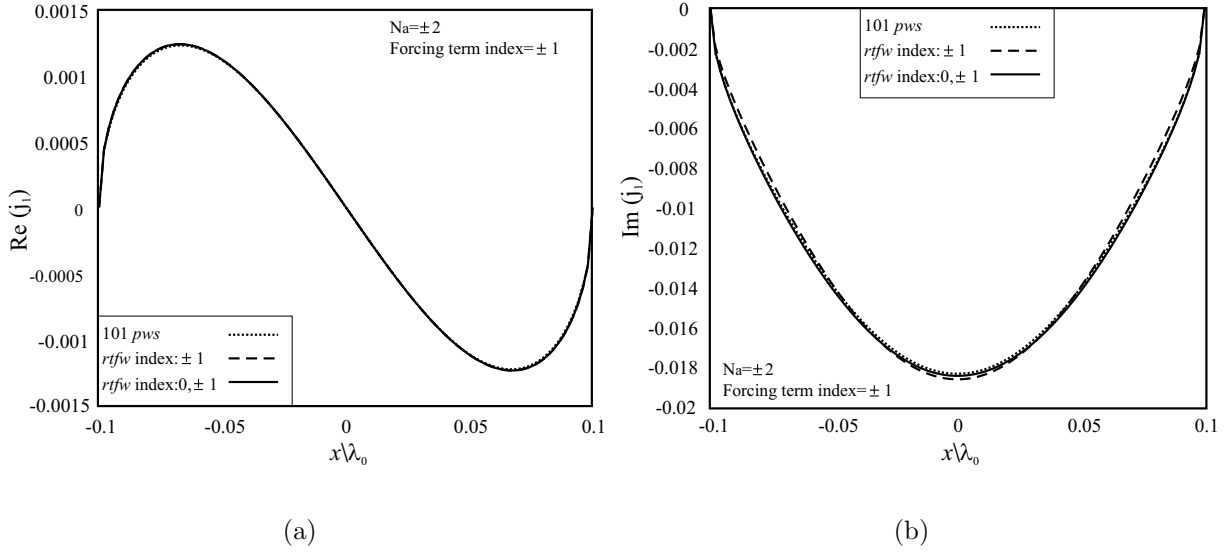


Figure 6.14: Equivalent electric current associated to the modes with index ± 1 , when five accessible modes are extracted from the kernel. (a) Real part. (b) Imaginary part. The dimensions of the structure are: $w_x = 0.2\lambda_0$, $d_x = 0.6\lambda_0$.

accessible Floquet modes, the corresponding solutions have an oscillatory behavior with period depending on the truncation (the number of accessible modes N_a). Therefore, at least a few sub-domain basis functions have to be used for every change of sign of N_a . This can be interpreted in terms of Shannon's sampling theorem [129]. It can also be regarded as a special formulation of the relative convergence problem [95] for the case of reduced IE's. It follows that, when the number of accessible modes to be included in the analysis becomes large, the number of required expansion functions correspondingly increases and the MoM matrix becomes ill conditioned. To prove this statement, the MoM matrix condition number has been plotted as a function of the number of accessible modes N_a and of the strip's width. It results that, for a certain N_a , the wider is the strip the higher is the condition number. The intuitive explanation is that the natural modes of the array have a tendency to resonate with the Floquet modes. The study of the eigenvalue equation associated to the reduced IE operator has confirmed this hypothesis. We have observed that this operator has as many small eigenvalues as the number of extracted accessible modes. Moreover, it turns out that they are not artificial, introduced by the discretization of the operator, but they are actually related to the physics of the problem, and correspond to resonant eigenmodes of strip. The corresponding eigenfunctions are very

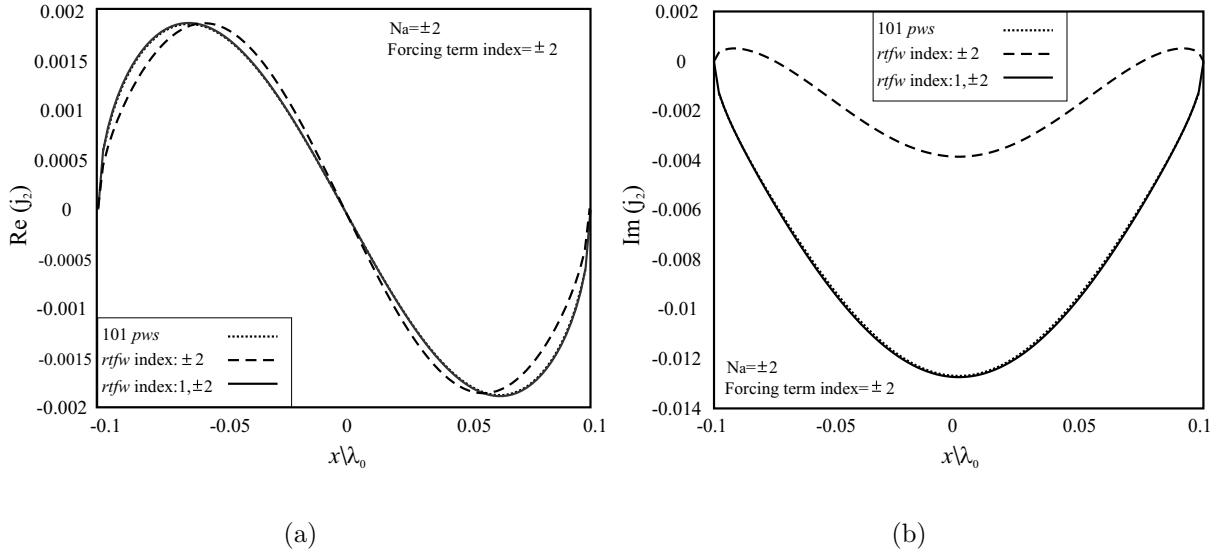


Figure 6.15: Equivalent electric current associated to the modes with index ± 2 , when five accessible modes are extracted from the kernel. (a) Real part. (b) Imaginary part. The dimensions of the structure are: $w_x = 0.2\lambda_0$, $dx = 0.6\lambda_0$.

similar to combinations of the extracted FW's.

It follows that the solution can be represented as a combination of Floquet modes. This corresponds to reduce the space of the solution to a subspace where the small unwanted eigenvalues are avoided, and it can be seen as a way of regularizing the ill-conditioned problem [104]. In particular, we have identified a set of entire-domain basis functions, the truncated Floquet waves (tfw), variations of those proposed in [102] for the analysis of large finite slot arrays (2D geometries). The functions introduced here are defined in the domain of the radiating element inside the periodic cell, rather than in all the unit cells of the finite-array domain, and are supplemented with appropriate edge conditions. In particular, we have used the real and the imaginary part of these functions. At this point the distinguishing feature of the IEMEN method has been exploited: the fact that the formalization of the scattering problem resorts to a single IE, with a fixed kernel and multiple forcing terms. This has suggested the adoption, for each forcing term (accessible mode), of an appropriate compact set of tfw's as expansion functions. In this way, the same IE leads to a different linear system for each forcing term. Although, by implementing this procedure, the number of matrices to be inverted is equal to the number of accessible modes extracted from the kernel of the original IE, the efficiency of the solution is not

compromised. In fact, it turns out that only a few tfw's are needed to obtain an accurate result: they are in general the tfw's having the same index as the forcing term and those with indices just above and just below that function. The corresponding system matrices are always very small and appear in a particularly convenient form of the Toeplitz-type, so that their inversion can be performed very efficiently. The required computation time is then mostly spent in filling the matrix for every set of basis functions. Moreover, these sets of functions overlap because a same tfw is in general used for different forcing terms. This suggests a way to reduce the computational time. First, the couplings between all the basis and test functions are calculated and used to fill a big system matrix, which contains all the information needed to solve the problem for each forcing term. This matrix is then specialized for a specific forcing term through the projection on the corresponding subspace of functions. Such a procedure allows avoiding recomputing the elements of the matrix for each forcing term.

A number of test cases have been presented to demonstrate the efficiency of these basis functions. The results have been validated by comparison with those obtained for a sub-domain expansion of the unknown currents. Because of that, the validation was performed only for the case of narrow strips and a few accessible modes, when the result obtained with by sub-domain functions were still reliable. A further validation, for higher numbers of accessible modes and considering an arbitrary angle of incidence, is postponed to future analysis.

The basis functions identified for this 2D geometry can be used also for more general 3D problems. However, in the 2D case the equivalent tangential current has component along only one direction and a few modes are important. In a 3D problem, instead, the tangential current has an arbitrary orientation; consequently, a larger number of basis functions is needed for the discretization and a larger number of accessible modes has to be included in the analysis. Moreover, if the FSS elements have complex shapes containing internal corners (as it is for the case of a crossed dipole), additional functions to expand the currents at the corners need to be introduced. Functions similar to those defined in [28] could be suitable for this purpose. However, as shown in [59, 140], the identification of a set of functions to represent the unknown surface current density for arbitrary geometries, for example at the internal corners of a crossed dipole, is in general not straightforward.

Finally, we to expect that a procedure analogous to the one adopted for the analysis of waveguide junctions in Chapter 2, where only the dynamic contribution of the accessible modes was extracted from the kernel of the IE, would allow to circumvent the ill-conditioning problem. In the present case, this would correspond to introduce on the left-hand side of Eq. (6.2) a quasi-static summation on the accessible modes.

Chapter 7

Conclusions and recommendations

*I feel that the greatest award for doing
is the opportunity to do more.*
Jonas Salk (1914-1995)

*Show me a thoroughly satisfied man
and I will show you a failure.*
Thomas Edison (1847-1921)

The research work described in this thesis extended a methodology, based on microwave network representations, which was originally presented in [53] for studying waveguide junctions, to the analysis of periodic multi-layer structures, comprising also waveguide array antennas. A software tool was developed that is able to analyze, in the same framework, patch- and slot-based Frequency Selective Surfaces (FSS's), sandwiched between dielectric layers and array antennas, including in the analysis also feeding structures and filtering elements inside the array waveguides. In the present implementation, the radiating elements of the array are rectangular or circular waveguides, as it is typical for radar antennas. Moreover, filtering and feeding elements in the array waveguides can also be accounted for if they can be modeled in terms of waveguides and waveguide junctions. When the feeding network contains more complex components or the used radiating elements are not waveguides and cannot be directly modeled through our approach, an equivalent network representation of these elements is derived by means of commercial packages based on other techniques. In fact, because of the modularity of the IEMEN method, these equivalent matrices can be regarded as building blocks of the whole structure and can be cascaded with the representation of the other structure components, obtained with our approach. This software was used as basis for the design of FSS's integrated with array antennas.

In this thesis, different aspects of the adopted methodology have been highlighted, concerning both the theoretical formulation and its application to the design of FSS's. These aspects will be briefly recalled in Sec. 7.1. On this basis, some recommendations will be given about further developments of this work in Sec. 7.2.

7.1 Conclusions by chapter

Waveguide junctions analysis The Generalized Impedance Matrix (GIM) and the Generalized Admittance Matrix (GAM) are well known representations for waveguide junctions and uniform waveguide sections [5, 61, 67, 90]. In their typical implementation, the number of ports of the corresponding multi-port equivalent network is the same as the number of evanescent modes used to express the fields at the junction in the formalization of the scattering problem. This choice leads to numerical instability when a number of GAM's or GIM's, representing waveguide junctions and waveguide sections, are cascaded. In [5] it was shown that, to prevent this kind of problem, the original GIM has to be reduced to contain only the ports that correspond to the actually interacting (accessible) modes [126]; the matrix operations required for this reduction involve also a matrix inversion.

The distinguishing feature of the adopted methodology, originally proposed in [53] for waveguide junctions, is that it resorts directly to a GIM associated to the accessible modes only, without the need to perform extra matrix inversions. The basic idea is to retain as accessible only those evanescent modes that arrive at the terminal planes with less than a prescribed attenuation. The corresponding modal amplitudes are then identified as the *fundamental unknowns* of the problem, in the sense that all the fields in the discontinuity region between the terminal planes can be expressed as a function of those quantities only. To obtain the GIM representation of the junction, the scattering problem is formulated in terms of a single Integral Equation (IE) with multiple right-hand sides. The IE has a fixed reduced kernel, which contains only the localized modes, and the accessible modes appear as forcing terms. Correspondingly, the adopted methodology has been indicated in this thesis as Integral Equation method for the derivation of Multimode Equivalent Networks (IEMEN). A formulation of the scattering problem at a waveguide junction in terms of reduced kernel IE had already been proposed in [21], where a reduced form of the Generalized Scattering Matrix was derived. However, to achieve this representation four matrix inversions have to be performed, versus only one inversion required by the IEMEN technique. Moreover, the IEMEN formalism allows reusing the reaction integrals that appear in the MoM matrix to build the equivalent network matrix entries, with a consequent

reduction in the computation time. The application of the frequency extraction technique makes the IEMEN approach even more appealing. Therefore, as shown in Chapter 2, the IEMEN method not only allows circumventing the stability problems typical of GIM/GAM representations, but it is computationally efficient compared to other methods and it constitutes in general an appropriate choice for the characterization of a waveguide junction in terms of a reduced multimode equivalent network.

The homogeneous sections of waveguides between two junctions are also characterized in terms of an equivalent GIM. The analysis of cascaded waveguide structures is performed by combining all the corresponding GIM's of junctions and waveguide sections; the result is a banded system of linear equations, which can be solved by means of a recursive technique, which is also efficient. In fact, when waveguides are cascaded, the calculation time that is needed to solve the corresponding linear system of equations depends on the size of the system matrix to be inverted. The IEMEN method resorts to the inversion of the smallest possible matrix.

Infinite waveguide phased array analysis After recalling the relevant theoretical formulation for waveguide junctions, the IEMEN technique has been extended in this thesis to the analysis of an infinite phased array of rectangular waveguides radiating in free space. A solution for this same problem in terms of a GAM representation was also derived in [144], but the obtained network had a large number of ports, while the IEMEN ports resorts to a representation reduced to the accessible modes only. The representation derived for arrays of waveguides has been used for studying aperture-based FSS's, with apertures cut from a thick metal plane, under plane-wave incidence. The application of the IEMEN method to waveguide arrays has been successfully validated against literature results and simulations performed using other methods (direct method described in [144]).

Frequency selective surface analysis The IEMEN method has then been extended to the analysis of FSS's consisting of infinitesimally thin metal elements.

Two formulations were presented for the study of an infinite distribution of patches: the patch and the aperture formulations, which lead to two different types of IE's, where either the induced currents (electric field integral equation - EFIE) on the patches or the tangential electric field (magnetic field integral equation - MFIE) in the complementary apertures, are treated as the unknowns of the problem [62, 106]. In both cases, the equivalent network was in parallel with respect to the transmission lines representing the propagation of the modes in free space, since the electric field and therefore the pertinent modal voltages are continuous at the interface. In the patch formulation, the FSS was characterized in terms

of an equivalent admittance matrix, while in the aperture formulation it was characterized in terms of an equivalent impedance matrix. According to the IEMEN method, the accessible modes were extracted from the kernel of the IE's formalizing the scattering problem, and the information about their behavior in the z -direction was given at transmission-line level, in terms of the equivalent network of the slab. The non-accessible modes, which appear in the kernel of the IE, instead, are localized at the transition and see an infinite transmission line. A Green's Function (GF) formalism was used to express the reduced kernel of the IE, and the corresponding spectral reduced GF was the one associated to two semi-infinite half-spaces in the patch approach and to the infinite space in the aperture approach. When the slabs are very thin, an overwhelming number of modes would be accessible and, if sub-domain basis functions are used to expand the unknowns in a solution of the IE based on the Method of Moments (MoM), also a large number of expansion functions would be required. This leads to an ill-conditioned problem. In these cases, an alternative procedure has been adopted, thanks to the GF formalism. Instead of extracting from the kernel of the IE all the modes that are accessible, we have selected only a few of them, and account for the finiteness of the dielectric layer by calculating a multi-layer spectral GF.

The application of the IEMEN technique to the analysis of FSS's has been successfully validated versus results available in literature.

Frequency selective surface design The IEMEN method, thanks to its modularity, provides a powerful and efficient platform for the design. As an example, in this thesis we have tackled the problem of designing an FSS, which had to be integrated with a waveguide antenna array. The purpose was to prevent interference from an antenna for satellite communications, located in the proximity of the array and operating in a partially overlapping frequency range. The array is similar to those used for the Multi-Frequency Radar mounted on military ship's topsides; in the present case it operates in the X-band and is capable of scanning up to 30° in the H -plane. We have adopted a classical design procedure, which starts with a single-mode design, intuitive and Smith-chart based, to trace the relevant behavior of the structure and to perform a rough tuning of the FSS parameters. This is followed by a refinement phase, which uses full-wave IEMEN-based simulations, including all the relevant accessible modes.

The requirements for the FSS were formulated in terms of bandwidth, roll off and maximum level of the reflection coefficient in pass band, for the given frequency and angular range. The FSS had to realize a stop band in the higher part of the array operating band, with a reflection coefficient lower than the one of the array in pass band. As observed in Chapter

4, the FSS geometry greatly affects its performance. The FSS bandwidth is proportional to the element width and, if the periodicity is small with respect to the wavelength ($< \frac{\lambda}{2}$), not only the grating lobes are delayed, but the FSS bandwidth becomes larger. In view of this, folded dipoles were chosen, arranged in a triangular lattice with the same periodicity as the target array antenna. Moreover, with the simple transmission-line model, it turned out that at least two FSS's had to be used to obtain a fast enough roll off between the pass band and the stop band. According to classical filter theory, the roll off becomes steeper by increasing the number of cascaded FSS's and, if these FSS's are designed to have a slightly different resonance frequency, the bandwidth of the entire structure increases. However, the application of filter theory to FSS design is not straightforward, because it does not account for variations of the resonance behavior with angle of incidence and polarization. Moreover, the total thickness of the FSS is often a sensitive parameter. Therefore, in practical applications, where the design time and the manufacturing costs are an issue, at most three or four FSS's are used [100]. In our case, two equal FSS's, separated by a $\lambda/4$ thick dielectric slab, were sufficient to meet the requirements. The slab, besides working as a $\lambda/4$ transformer, also guarantees that waves, impinging on the FSS with different incidence angles, are reflected in the same direction. To choose the permittivity of the FSS dielectric support, we had also to take into account its effect on the FSS resonance frequency and bandwidth: the larger the permittivity, the lower becomes the resonant frequency and the narrower the FSS bandwidth. In particular, the dielectric constant was selected to achieve angle independence up to 30° , for a rather narrow bandwidth. Moreover, external matching layers were introduced to reduce the effect of "ears" in the pass band (local maximum of the reflection coefficient).

In the first design phase, the patch FSS was represented, with respect to the transmission line equivalent to the main propagating Floquet mode, in terms of its equivalent admittance, calculated by applying the IEMEN method with only one accessible mode, and connected in parallel to the transmission line. This admittance resulted to be a slowly varying function of the frequency, so that it could be calculated in a few frequency points of the operating frequency range and then interpolated. Because of that, the first design phase was very fast. It is important to note that this property holds also when a larger number of accessible modes is retained in the calculations, and is a characterizing feature of the IEMEN method. In fact, all the fast frequency variations are accounted for at transmission-line level and not at equivalent-network level, because the most frequency varying modes have been extracted from the IE's kernel.

The designed FSS was tuned with the array and the results of the IEMEN-based analysis of the whole structure showed very good agreement with those obtained by using HFSS.

Experimental validation The FSS designed by means of the method outlined above was actually manufactured and tested by different experimental procedures. Deviations could be explained from the observation that the material selected for the external matching layers was inhomogeneous, with a locally variable permittivity. Additional in-house dielectric constant tests had to be performed on samples extracted from the manufactured FSS, using a coaxial probe method. Moreover, the materials were not available in the desired thickness. Therefore, three slabs of foam, for each one of the two external matching layers, and two slabs of fiberglass, for the internal $\lambda/4$ transformer, had to be stacked together, and the effect of the bonding film on the electromagnetic performances of the whole structure had to be included in the analysis. Since the chosen materials could not be easily glued together, extra high pressure and temperature was applied during the bonding process, which led to modifications of the thickness and the density of the foam layers. As lessons learned, the materials have to be chosen among those, conceived for electromagnetic applications, which show stable properties in the frequency range where the FSS is used. If different kinds of material have to be glued together, the availability of an adhesive suitable for those materials and such that the bonding process does not affect the mechanical and electromagnetic properties of the structure is essential to the successful completion of the manufacturing.

The experimental validation of the designed FSS consisted of measurements of reflection and transmission coefficients, for different incidence angle configurations. The measurements were performed in one of the microwave anechoic chambers of TNO, using pyramidal horn antennas. Special care was taken to reproduce the same conditions simulated in the calculations: plane-wave incidence on the FSS and on the receiving antenna. Three measurement setups were chosen, two for reflection measurements, and one for transmission measurements.

The reflection measurements were performed with the FSS located in the far field of the transmitting antenna. In the first setup, we considered an FSS subpanel obtained by covering the original one with a frame of absorbing material; this allowed obtaining plane wave incidence also on the receiving antenna, since it could be placed in the far field of the FSS subpanel. In the second setup, instead, we measured the entire FSS panel, with the receiving antenna positioned very close to it. The measurement results obtained using the two setups were compared for the case of broadside incidence, showing a small difference only in the pass band. Moreover, both measurements showed good agreement with the simulations and respected the initial requirements on the FSS reflection coefficient; the differences encountered, mainly concerning the pass band, were rather small with respect to the order of magnitude of the values at hand (lower than -20dB). In view of this, the

achieved accuracy is considered satisfactory.

For the transmission measurements, the receiver was located in the far field of the transmitter and in the near field of the FSS panel. The measured transmission coefficient was in excellent agreement with the theoretical results for all the incidence angles; in fact the small shift in the resonance frequency (about 0.9%) was within the tolerances in the foam and in the bonding film permittivities. Of the three considered setups, the one used for transmission measurements allows the most appropriate experimental verification of an FSS's performance.

The measurements of the electromagnetic performances of an FSS can be done in other ways. Transmission measurements, for example, have also been successfully performed in the near-field range [125]. Reflection coefficient measurements still offer some challenges, especially because of edge diffraction effects and inaccuracies introduced in the calibration with the metal plate. For this reason, waveguide simulator techniques are often preferred [37, 106, 117]. This kind of measurement is inexpensive and simple to perform, because it does not require the availability of an anechoic chamber. By including an appropriate number of unit cells in the cross section of the waveguide, different scan angles can be simulated [64]. Since the result of simulator measurements concerns an infinite array, they are more suitable for comparison with calculations performed in the hypothesis of infinite periodic distribution of radiating elements, without the need to account for edge diffraction. However, the simulator does not allow measuring the FSS performances in a whole frequency or angle range, but only for certain pairs of frequency-angle values, and their interpretation is not straightforward. Simulator measurements are typically used in the first tuning phase, when small, cheap prototypes can be built and measured at almost not cost. Waveguide simulator measurements offer therefore a good option to validate the array-FSS integrated design.

Solution of the reduced kernel IE's In the original implementation of the IEMEN method, the unknown current densities in the IE derived for the analysis of FSS transitions were expanded in terms of sub-domain basis functions, which can be used for an arbitrary form of the FSS elements and allow representing sharp discontinuities. When the element geometry contains corners (for example crosses), a large number of sub-domain basis functions is necessary. Moreover, it has been shown in Chapter 6 that the larger is the number of accessible modes extracted from the kernel, the higher is the spatial variation of the corresponding forcing terms and the larger the number of functions needed to correctly represent the unknowns. In these cases, the reaction integrals involve the calculation of the periodic (non-accessible) GF's for high values of the mode indices. In the present

implementation, these integrals have been greatly accelerated by means of the technique presented in [82], which is based on the Kummer transformation.

If the requirements set on the FSS become very stringent, and ask for a constant behavior for different incidence angles and for a steep roll off, then dielectric slabs with high permittivity have to be used. As a consequence, the number of accessible modes to be included in the simulations increases and, for sub-domain expansion of the unknown currents, the MoM matrix tends to become ill conditioned. For the specific solution that uses the IEMEN formulation, a detailed study has been performed on the non-accessible GF that appears in the reduced kernel IE. With this purpose, we have considered a simple 2D geometry, consisting of an infinite periodic array of metallic strips in free-space, under TM plane wave incidence.

For a sub-domain expansion of the unknowns, an asymptotic expression of the MoM matrix generic element was derived that contains a singular term and an oscillating term. The first prevails when basis and test functions are close to each other; the second becomes dominant when a large number of accessible modes are retained in the analysis, when basis and test functions are rather distant. The non-diagonal elements of the MoM matrix have then a non-decreasing and oscillating nature. Moreover, since the forcing terms of the IE's are periodic functions (they are the accessible Floquet modes), also the corresponding solution tends to be oscillatory with a period depending on the accessible mode index N_a . Therefore, at least a few (sub-domain) expansion functions are needed for every change of sign of N_a . It follows that, when the number of accessible modes to be included in the analysis becomes large, the number of required expansion functions correspondingly increases and the MoM matrix becomes ill conditioned. An analysis of the reduced kernel integral operator has revealed that the resonant eigenmodes can be represented as a combination of the extracted Floquet Waves (FW). This led to the idea of using entire-domain basis functions, with oscillations dominated by the period of the structure and with pertinent boundary conditions to match the local geometrical configurations. We have selected truncated Floquet waves (tfw), variations of those proposed in [102]. These functions are defined only in the domain of the radiating element inside the periodic cell, rather than in the entire finite-array domain, and are equipped with appropriate edge conditions. In this way, the space of the solution is reduced to a subspace where small unwanted eigenvalues are avoided. A possibility of further improving the conditioning of the MoM matrix is offered by the distinguishing feature of the IEMEN method: the fact that the formulation of the scattering problem results in a single IE, with multiple forcing terms and a fixed kernel. This suggests the adoption for each forcing term (accessible mode) of an ad hoc compact set of tfw's as expansion functions. In this way, the same IE leads to different

linear systems for different forcing terms. Although with this procedure the number of system matrices that have to be inverted to solve the problem is linearly proportional to the number of accessible modes extracted from the kernel of the original IE, the efficiency of the solution is not compromised. In fact, it turns out that only a few tfw's are needed to obtain an accurate result: they are in general the tfw having the same index as the forcing term, and the tfw's with indices just above and just below that function. Since the corresponding system matrix is always very small and its inversion cheap, the required computational time is mostly associated to the filling of the matrix for every set of basis functions. However, these sets overlap because the same tfw is in general used for different forcing terms. Therefore, a way to reduce the calculation time should be to first calculate the different elements of all the system matrices and then to combine them to obtain the system matrix corresponding to each forcing term. A number of test cases have been presented in Chapter 6, to demonstrate the efficacy of these basis functions.

7.2 General conclusions and recommendations

The IEMEN method has proved to be very efficient for the analysis of complex structures, involving phased arrays, dielectric radomes and multi-layer FSS's, which consist of patch- and slot-based FSS's sandwiched between dielectric slabs. The theoretical formulation has been implemented in a software tool and successfully tested versus literature results and by means of experimental validations.

The developed tool constitutes a valuable starting point for the design of multi-layer FSS's integrated with waveguide arrays. In the design problem described in Chapter 4, the element shape, a folded dipole, was identified from considerations about the type of behavior required for the FSS and it corresponded to the simplest possible choice. However, for more complex problems, other shapes could be more suitable [100]. In general, to build a real *CAD tool*, the following is needed:

- a catalogue that contains the simulation of the reflection and transmission coefficients of typical FSS elements, for different values of their dimensions and of the lattice geometry;
- an optimization procedure and a sensitivity analysis, to identify which are the most relevant parameters in the design;
- an efficient analysis tool, able to rapidly calculate the reflection and transmission coefficients of the FSS for the different parameter values given in input (typically in

terms of frequency, angle of incidence, geometry).

For the most common geometries, the catalogue can be easily filled up by means the IEMEN-based tool. However, the tool should be completed to cover also other types of geometries, comprising elements with generic shape and multi-layer periodic surfaces with different lattice periods.

Element shape. The meshing procedure used for the MoM-based solution of the IE allows studying only FSS elements obtained as combination of rectangular constituents, placed perpendicularly to each other [121]. Examples are dipoles, Jerusalem crosses, rectangular loops, gangbuster, etc. Other shapes have been proposed in the literature for solving particular problems, which show different characterizing properties (a detailed review can be found in [100]). In view of this, and to have more degrees of freedom in the choice of the elements for design purposes, a meshing procedure should be implemented in our tool that takes into account FSS elements with a generic shape, or the possibility should be considered to adapt to our tool one of the public domain mesh generators.

Lattice period. Our IEMEN-based tool allows studying both arrays with a rectangular and with a triangular lattice. The latter configuration is particularly convenient because it allows packing the elements very close and to delay grating lobes. So far, all the different periodic parts in the analyzed multi-layer structure (antenna and FSS's) have been considered as having the same lattice and the same periods or periods which are integer multiples of each other. However, in the design of FSS's for specific applications the possibility to account for different lattice periods can be very useful. For example, a meander line polarizer is also a periodic structure, but the lattice vectors in general have to form a certain angle with the lattice vectors of the basis array antenna to obtain the desired polarization. As shown in [22, 83], the extension of the theoretical formulation to the case of stacked arrays with different periods is possible if a global period (commensurate system) or a approximate global period (noncommensurate system) can be identified. In this case, a global reference system for all the arrays is defined and a global unit cell, with respect to which the Floquet modes are defined, is identified. From the local equivalent network of each array, calculated with respect to their local reference system (unit cell), the corresponding global network is derived through modal mapping.

The catalogue of FSS elements is used to parameterize the FSS behavior with respect to the element geometry for different lattice periods. In the first phase of the design, the

desired reflection and transmission coefficients are compared with those in the catalogue to identify the most suitable element type. In the second phase, simulations are performed on the chosen FSS geometry, varying the relevant element dimensions and applying a curve fitting algorithm between the obtained and the desired reflection coefficient until agreement is found within the tolerances given as input. Usually, the performances of the structure should be guaranteed in a *certain frequency and angle range*. Therefore, the simulations have to be repeated for different frequencies and angles, and the analysis tool used to perform these simulations should be very efficient. In this respect, the IEMEN method is an appropriate choice for a number of reasons. First, the number of operations required to obtain the network representation of a single FSS layer and to characterize the entire multi-layer FSS is small compared to other microwave network techniques. Second, the solution of the pertinent IE has been accelerated by applying frequency extraction techniques based on the Kummer transformation. Third, in Chapter 4 it was shown that the FSS equivalent matrix derived by means of the IEMEN method varies very slowly with the frequency and therefore, it could be calculated only in a few frequency points of the operating frequency range and then interpolated. This last feature should be actively exploited by identifying and implementing the appropriate interpolation algorithm. Last but not least, recently, techniques have been proposed for the parametrization of the MoM-based solution of an IE with respect to relevant physical constants, which in a scattering problem are frequency, angle of incidence and geometry of the radiating element. The implementation of these techniques in our tool is very important to efficiently use it as basis for a real CAD tool. This activity has already been started in the frame of an international cooperation.

Moreover, the *losses of the materials* play an important role in the performances of an FSS consisting of many dielectric layers, as seen in Chapter 5, and therefore should be taken into account since the very beginning of the design. At the moment, our tool can only account for real permittivities. The updating of the tool for complex values is merely a programming problem and does not require further development of the theory.

The IEMEN-based tool allows simulating only *infinite structures* and does not account for the effect of finiteness of the array antenna and of the FSS's. For a large well-designed array antenna, operating in a frequency range and for scan angles such that grating lobes are far from excitation, the analysis of the corresponding infinite array is sufficient to retrieve its relevant behavior in terms of the input impedance [102, 103]. In this case, windowing techniques [7] would help gaining a feeling about the performances of a finite number of array elements starting from the knowledge of the reflection coefficient of the infinite

array. The design of the multi-layer FSS presented in Chapter 4 was performed under the hypothesis of infinite periodicity of the array, and the agreement with the measurements of the manufactured panel was satisfactory, although the effect of edge diffraction could be observed. However, for small arrays or when higher-order modes are close to cut off, the effects of the finiteness is not negligible. Some recent applications exploit the fact that FSS's can be seen as frequency-dependent ground planes and used to obtain multi/wide-frequency antennas. FSS's could also be used to load the elements of an array of horns to increase the effective area: this allows making the horn's cross section smaller and therefore placing the feeds closer to the focal point. In all these cases the FSS is very small. The computational effort required to include the effect of the edges in full-wave calculations is often way to heavy with respect to the gained information. At the moment, our tool is used to perform a first design in the infinite array approximation, but it could be extended to include the effects of the finiteness for studying small arrays.

In this thesis we concentrated on the analysis of *planar structures*, which correspond to the configuration most widely available on the market. However, for some applications conformal structures are required. For example, FSS's can be used to reduce the Radar Cross Section (RCS) of an antenna located in the nose of a military aircraft or in the mast of a ship (although in this last case the planar configuration is at the moment the most used one). The IEMEN method has been applied to study cylindrical arrays of waveguides and can also be used for multi-layer structures consisting of thick cylindrical FSS's and dielectric slabs [56]. The application of the method to the analysis of infinitesimally thin patch- and slot-based conformal FSS will be therefore a natural extension of our tool.

As already observed, the distinguishing feature of the IEMEN method is that it formulates the scattering problem in terms of a single IE with fixed reduced kernel and multiple forcing terms. However, if the unknowns are expanded in terms of *sub-domain functions* in a MoM based solution approach, for a relatively large number of accessible modes extracted from the kernel a large number of basis functions is required and the problem turns out to be ill-conditioned. Since from physical arguments we could image the solution to be representable as a combination of Floquet's modes, we have restricted the domain of the solution to a subspace where the ill-conditioning problem could be avoided. This was demonstrated in a two-dimensional problem. The extension of this approach to three-dimensional geometries, however, requires the introduction of additional basis functions to expand the unknown currents at the corners of the radiating elements. The functions introduced in [28] could be suitable for this purpose. However, it has been shown in [59,140]

that the identification of a set of functions to represent the surface current density for example at the internal corners of a cross dipole is not straightforward. In view of this, the investigation of alternative solutions of the ill-conditioning problem in the IEMEN method is essential for its applicability to the analysis and design of multi-layer patch- and slot-based FSS's sandwiched between very thin dielectric slabs with high permittivities, when many accessible modes are needed.

Appendix A

Modal representation of the electromagnetic field

The aim of this appendix is to derive a representation of the electromagnetic field in terms of modes for two cases: propagation in a uniform waveguide and propagation in free space, in proximity of a periodic phased array. For this purpose, we have adopted the formalism originally introduced in [48, 132]. In Sec. A.1 Maxwell's equations are introduced. In Sec. A.2 the modal representation of the field in a generic uniform bounded waveguide is obtained. In Sec. A.3 the derivation is applied to two special cases that are relevant for our design: the propagation of the electromagnetic field in a rectangular waveguide and in free-space; this latter is interpreted as a particular case of guided propagation, where the modes form a continuous set of plane waves.

A.1 Maxwell's equations

In this section, Maxwell's equations are introduced for a medium that is linear, isotropic, locally reacting, stationary, characterized by permittivity ε , permeability μ and conductivity σ .

A.1.1 Time domain

Let us indicate a generic space-time point with (\mathbf{r}, t) , where \mathbf{r} is a three-dimensional vector that characterizes the position of the point with respect to a Cartesian reference system in the space domain: $\mathbf{r} = x\mathbf{u}_x + y\mathbf{u}_y + z\mathbf{u}_z$, at a certain instant t in the time domain. The electromagnetic field is described by the four vector fields $\mathcal{E}(\mathbf{r}, t)$ and $\mathcal{B}(\mathbf{r}, t)$, $\mathcal{D}(\mathbf{r}, t)$

and $\mathcal{H}(\mathbf{r}, t)$, assumed to be finite everywhere, continuous in space and time and with continuous derivatives [132]. The field vectors are defined in terms of the experiments that allow to measure them, and $\mathcal{E}(\mathbf{r}, t)$ and $\mathcal{H}(\mathbf{r}, t)$ are indicated as the intensity of the electric and magnetic field, respectively. $\mathcal{D}(\mathbf{r}, t)$ and $\mathcal{B}(\mathbf{r}, t)$ are the electric and magnetic flux intensities. The source of the electromagnetic field is a distribution of electric charge and current assumed to be continuous in space and time and specified in terms of the density of charge $\rho(\mathbf{r}, t)$ and the vector current density $\mathcal{J}(\mathbf{r}, t)$. The charge density $\rho(\mathbf{r}, t)$ at a point (\mathbf{r}, t) is defined as the average per unit volume in the neighborhood of that point, while the current density $\mathcal{J}(\mathbf{r}, t)$ at a point (\mathbf{r}, t) on a surface orthogonal to the direction of flow of the charge, is defined as a vector having that same direction and magnitude equal to the charge which crosses in an unit time the unit area of the surface in the vicinity of that point.

In a point \mathbf{r} , such that the physical properties of the medium are continuous in its proximity, the field vectors are subject to Maxwell's equations:

$$\nabla \times \mathcal{H}(\mathbf{r}, t) - \frac{\partial \mathcal{D}(\mathbf{r}, t)}{\partial t} = \mathcal{J}(\mathbf{r}, t), \quad (\text{A.1a})$$

$$\nabla \times \mathcal{E}(\mathbf{r}, t) + \frac{\partial \mathcal{B}(\mathbf{r}, t)}{\partial t} = \mathbf{0}, \quad (\text{A.1b})$$

supplemented by the law of conservation of the charge:

$$\nabla \cdot \mathcal{J}(\mathbf{r}, t) = -\frac{\partial \rho(\mathbf{r}, t)}{\partial t}. \quad (\text{A.2})$$

Moreover, the fields have to adhere to the causality condition: if the source starts at an instant $t = t_0$, then the $\mathcal{E} \equiv 0 \equiv \mathcal{H}$ for $t < t_0$.

Two further conditions for the vector fields can be deduced directly from Maxwell's equations, by taking their divergence and using Eq. (A.2):

$$\nabla \cdot \mathcal{D}(\mathbf{r}, t) = \rho(\mathbf{r}, t), \quad (\text{A.3a})$$

$$\nabla \cdot \mathcal{B}(\mathbf{r}, t) = \mathbf{0}. \quad (\text{A.3b})$$

Of all previous equations on the five vectors $\mathcal{E}, \mathcal{D}, \mathcal{H}, \mathcal{B}, \mathcal{J}$ only the first two Eqs. (A.1) with the law of conservation of the charge Eq. (A.2) are independent; therefore, to find an unique solution, Maxwell's equations have to be supplemented with additional relations: the boundary conditions and the constitutive relations. The latter can be obtained in a particularly handy form in the frequency domain, by applying a Fourier transformation with respect to the time coordinate.

A.1.2 Frequency domain

The definition of *temporal Fourier transformation* used in this thesis is:

$$F(\mathbf{r}, \omega) = \int \mathcal{F}(\mathbf{r}, t) e^{-j\omega t} dt, \text{ direct Fourier transformation,} \quad (\text{A.4a})$$

$$\mathcal{F}(\mathbf{r}, t) = \int F(\mathbf{r}, \omega) e^{j\omega t} \frac{d\omega}{2\pi}, \text{ inverse Fourier transformation,} \quad (\text{A.4b})$$

where $\mathcal{F}(\mathbf{r}, t)$ is a function absolute integrable in t and the integration is extended to all real frequencies ω . If $\mathcal{F}(\mathbf{r}, t)$ is a signal with a finite duration in time, the transformation exist for all complex values of ω . If ω is complex, then the transform exists only for $\text{Im}(\omega) < 0$. The Fourier transformed Maxwell's equations are:

$$\nabla \times \mathbf{H}(\mathbf{r}, \omega) - j\omega \mathbf{D}(\mathbf{r}, \omega) = \mathbf{J}(\mathbf{r}, \omega), \quad (\text{A.5a})$$

$$\nabla \times \mathbf{E}(\mathbf{r}, \omega) + j\omega \mathbf{B}(\mathbf{r}, \omega) = \mathbf{0}, \quad (\text{A.5b})$$

with the law of conservation of the charge

$$\nabla \cdot \mathbf{J}(\mathbf{r}, \omega) = -j\omega \rho(\mathbf{r}, \omega), \quad (\text{A.6})$$

and the additional equations:

$$\nabla \cdot \mathbf{D}(\mathbf{r}, \omega) = \rho(\mathbf{r}, \omega), \quad (\text{A.7a})$$

$$\nabla \cdot \mathbf{B}(\mathbf{r}, \omega) = \mathbf{0}. \quad (\text{A.7b})$$

If the vector fields have a steady-state sinusoidal time dependence, then a phasor representation can be used. For example, the electric field can be expressed as:

$$\mathcal{E}(\mathbf{r}, t) = \text{Re} \left[\mathbf{E}(\mathbf{r}) e^{j\omega t} \right]. \quad (\text{A.8})$$

In this case, the frequency dependence of the vector fields in Eqs.(A.5) is contained in the factor $e^{j\omega t}$, which occurs in all terms and therefore can be omitted. From now on in this Appendix we will consider only vector fields with this harmonic time dependence.

The constitutive relations are relations between the vector fields, which depend on the properties of the medium. For a linear, isotropic, locally reacting, stationary medium they are expressed as:

$$\mathbf{D}(\mathbf{r}, \omega) = \varepsilon(\mathbf{r}, \omega) \mathbf{E}(\mathbf{r}, \omega), \quad (\text{A.9a})$$

$$\mathbf{B}(\mathbf{r}, \omega) = \mu(\mathbf{r}, \omega) \mathbf{H}(\mathbf{r}, \omega), \quad (\text{A.9b})$$

$$\mathbf{J}(\mathbf{r}, \omega) = \sigma(\mathbf{r}, \omega) \mathbf{E}(\mathbf{r}, \omega), \quad (\text{A.9c})$$

with

$$\varepsilon(\mathbf{r}, \omega) = \varepsilon_0 \left(1 + \chi_e(\mathbf{r}, \omega) \right) = \varepsilon_0 \varepsilon_r(\mathbf{r}, \omega), \quad (\text{A.10a})$$

$$\mu(\mathbf{r}, \omega) = \mu_0 (1 + \chi_m(\mathbf{r}, \omega)) = \mu_0 \mu_r(\mathbf{r}, \omega), \quad (\text{A.10b})$$

where $\varepsilon_r(\mathbf{r}, \omega)$ and $\mu_r(\mathbf{r}, \omega)$ are the relative permittivity and permeability of the medium, and ε_0 and μ_0 are the free-space permittivity and permeability. The functions $\chi_e(\mathbf{r}, \omega)$ and $\chi_m(\mathbf{r}, \omega)$ are the electric and magnetic susceptibilities.

Eq. (A.9a) corresponds in the time domain to the following convolution integral:

$$\mathcal{D}(\mathbf{r}, t) = \int_0^\infty \varepsilon(\mathbf{r}, \tau) \mathcal{E}(\mathbf{r}, t - \tau) d\tau. \quad (\text{A.11})$$

In the special case of an instantaneous medium (it reacts instantaneously to the application of a cause and contains no history) the previous relation becomes:

$$\varepsilon(\mathbf{r}, t) = \varepsilon(\mathbf{r}) \delta(t) \quad \Rightarrow \quad \mathcal{D}(\mathbf{r}, t) = \varepsilon(\mathbf{r}) \mathcal{E}(\mathbf{r}, t), \quad (\text{A.12})$$

which in the frequency domain corresponds to a frequency independent permittivity: $\varepsilon_r(\mathbf{r}, \omega) = \varepsilon_r(\mathbf{r})$. The same holds for the permeability, the susceptibilities and the conductivity.

In this thesis we will consider media that are instantaneous and spatially homogeneous, so that the corresponding permittivity and permeability do not depend on the frequency and on the space point at which they are evaluated.

Maxwell's equations characterize the vector fields in a medium whose properties vary continuously. In presence of a surface S which separates medium 1 from medium 2, the vector fields have to adhere to the following boundary conditions at every point in the interface ∂S :

$$(\mathbf{B}_2 - \mathbf{B}_1) \cdot \mathbf{n} = 0, \quad (\mathbf{H}_2 - \mathbf{H}_1) \times \mathbf{n} = \mathbf{J}_s, \quad (\text{A.13a})$$

$$(\mathbf{D}_2 - \mathbf{D}_1) \cdot \mathbf{n} = \rho_s, \quad (\mathbf{E}_2 - \mathbf{E}_1) \times \mathbf{n} = \mathbf{0}, \quad (\text{A.13b})$$

where \mathbf{n} is unit vector normal to ∂S and pointing into medium 2, \mathbf{J}_s is the density of the surface current flowing tangential to ∂S and ρ_s is the surface charge density on ∂S . The vector fields are evaluated in the medium indicated by the subscript, in the limit where the point approaches the interface.

A.1.3 Plane waves

We consider now Maxwell's equations in the absence of sources:

$$\nabla \times \mathbf{H}(\mathbf{r}) = j\omega\varepsilon\mathbf{E}(\mathbf{r}) = j\omega\mathbf{D}(\mathbf{r}), \quad (\text{A.14a})$$

$$\nabla \times \mathbf{E}(\mathbf{r}) = -j\omega\mu\mathbf{H}(\mathbf{r}) = -j\omega\mathbf{B}(\mathbf{r}), \quad (\text{A.14b})$$

with the boundary conditions:

$$(\mathbf{B}_2 - \mathbf{B}_1) \cdot \mathbf{n} = 0, \quad (\mathbf{H}_2 - \mathbf{H}_1) \times \mathbf{n} = 0, \quad (\text{A.15a})$$

$$(\mathbf{D}_2 - \mathbf{D}_1) \cdot \mathbf{n} = 0, \quad (\mathbf{E}_2 - \mathbf{E}_1) \times \mathbf{n} = \mathbf{0}. \quad (\text{A.15b})$$

In case of a stratified medium, where the stratification is defined with respect to the symmetry axis z . To derive the wave equations, it is convenient to express the fields in terms of their longitudinal and transverse components with respect to the axis of symmetry, the z axis:

$$\begin{aligned} \mathbf{E}(\mathbf{r}) &= \mathbf{E}_t(\mathbf{r}) + E_z(\mathbf{r})\mathbf{u}_z, & \mathbf{H}(\mathbf{r}) &= \mathbf{H}_t(\mathbf{r}) + H_z(\mathbf{r})\mathbf{u}_z, \\ \nabla &= \nabla_t + \mathbf{u}_z \frac{\partial}{\partial z}, \end{aligned} \quad (\text{A.16})$$

where ∇_t is the transverse gradient operator.

Eq. (A.14a) becomes:

$$\left(\nabla_t + \mathbf{u}_z \frac{\partial}{\partial z} \right) \times \left(\mathbf{H}_t(\mathbf{r}) + \mathbf{u}_z H_z(\mathbf{r}) \right) = j\omega\varepsilon \left(\mathbf{E}_t(\mathbf{r}) + \mathbf{u}_z E_z(\mathbf{r}) \right), \quad (\text{A.17})$$

in which the transverse part is:

$$\left(\nabla_t \times \mathbf{u}_z H_z(\mathbf{r}) \right) + \left(\mathbf{u}_z \times \frac{\partial}{\partial z} \mathbf{H}_t(\mathbf{r}) \right) = j\omega\varepsilon \mathbf{E}_t(\mathbf{r}), \quad (\text{A.18})$$

and the longitudinal part is:

$$\nabla_t \times \mathbf{H}_t(\mathbf{r}) = j\omega\varepsilon E_z(\mathbf{r})\mathbf{u}_z. \quad (\text{A.19})$$

Similarly, the transverse part of Eq. (A.14b) is:

$$\left(\nabla_t \times \mathbf{u}_z E_z(\mathbf{r}) \right) + \left(\mathbf{u}_z \times \frac{\partial}{\partial z} \mathbf{E}_t(\mathbf{r}) \right) = -j\omega\mu \mathbf{H}_t(\mathbf{r}), \quad (\text{A.20})$$

while the longitudinal part is:

$$\nabla_t \times \mathbf{E}_t(\mathbf{r}) = -j\omega\mu H_z(\mathbf{r})\mathbf{u}_z. \quad (\text{A.21})$$

By taking the transverse curl of Eq. (A.18) we obtain:

$$-\nabla_t^2 \mathbf{u}_z H_z(\mathbf{r}) + \mathbf{u}_z \frac{\partial}{\partial z} (\nabla_t \cdot \mathbf{H}_t(\mathbf{r})) = j\omega\varepsilon (\nabla_t \times \mathbf{E}_t(\mathbf{r})), \quad (\text{A.22})$$

while by taking the transverse divergence of Eq. (A.20) we obtain:

$$(\nabla_t \cdot \mathbf{H}_t(\mathbf{r})) = -\frac{1}{\mu} \frac{\partial}{\partial z} (\mu H_z(\mathbf{r})), \quad (\text{A.23})$$

where we have used the following result from Eq. (A.21):

$$-\frac{\partial}{\partial z} \mathbf{u}_z \cdot (\nabla_t \times \mathbf{E}_t(\mathbf{r})) = \frac{\partial}{\partial z} (j\omega\mu H_z(\mathbf{r})). \quad (\text{A.24})$$

Substitution of Eq. (A.23) and Eq. (A.24) into Eq. (A.22) leads to *the scalar wave equation for $H_z(\mathbf{r})$* :

$$\nabla_t^2 H_z(\mathbf{r}) + \frac{\partial}{\partial z} \left(\frac{1}{\mu} \frac{\partial}{\partial z} (\mu H_z(\mathbf{r})) \right) = -k^2 H_z(\mathbf{r}), \quad (\text{A.25})$$

where

$$k = \omega \sqrt{\varepsilon\mu} = \frac{2\pi}{\lambda} \quad (\text{A.26})$$

is the *wave propagation constant* or *wavenumber* of the electromagnetic field in the medium, with λ the wavelength.

In a similar manner, by taking the transverse curl of Eq. (A.20) we obtain:

$$-\nabla_t^2 \mathbf{u}_z E_z(\mathbf{r}) + \mathbf{u}_z \frac{\partial}{\partial z} (\nabla_t \cdot \mathbf{E}_t(\mathbf{r})) = j\omega\mu (\nabla_t \times \mathbf{H}_t(\mathbf{r})), \quad (\text{A.27})$$

while by taking the transverse divergence of Eq. (A.18) we obtain:

$$(\nabla_t \cdot \mathbf{E}_t(\mathbf{r})) = -\frac{1}{\varepsilon} \frac{\partial}{\partial z} (\varepsilon E_z(\mathbf{r})), \quad (\text{A.28})$$

where we have used Eq. (A.19). Substitution of Eq. (A.28) into Eq. (A.27) leads to *the scalar wave equation for $E_z(\mathbf{r})$* :

$$\nabla_t^2 E_z(\mathbf{r}) + \frac{\partial}{\partial z} \left(\frac{1}{\varepsilon} \frac{\partial}{\partial z} (\varepsilon E_z(\mathbf{r})) \right) = -k^2 E_z(\mathbf{r}). \quad (\text{A.29})$$

In free space $\varepsilon(\mathbf{r}) = \varepsilon_0$, $\mu(\mathbf{r}) = \mu_0$ and the wavenumber is indicated as k_0 , so that Eqs. (A.25)-(A.27) become:

$$\nabla^2 H_z(\mathbf{r}) + k_0^2 H_z(\mathbf{r}) = 0, \quad (\text{A.30a})$$

$$\nabla^2 E_z(\mathbf{r}) + k_0^2 E_z(\mathbf{r}) = 0, \quad (\text{A.30b})$$

with $k_0 = \omega\sqrt{\varepsilon_0\mu_0}$. Analogous equations can be derived for the transverse components of the vector fields.

The wave equation for the total electric field $\mathbf{E}(\mathbf{r})$:

$$\nabla^2\mathbf{E}(\mathbf{r}) + k_0^2\mathbf{E}(\mathbf{r}) = 0, \quad (\text{A.31})$$

has the general solution:

$$\mathbf{E}(\mathbf{r}) = \mathbf{E}_0 e^{-j\mathbf{k}\cdot\mathbf{r}}, \quad (\text{A.32})$$

with

$$\mathbf{E}_0 \cdot \mathbf{k} = 0, \quad (\text{A.33})$$

where $\mathbf{k} = \mathbf{u}_k k_0 = k_x \mathbf{u}_x + k_y \mathbf{u}_y + k_z \mathbf{u}_z$ is the *propagation vector* or *wavevector* that defines the direction of propagation \mathbf{u}_k of the plane wave. For example, if \mathbf{u}_k is oriented as the \mathbf{u}_z unit vector of the reference system, then $\mathbf{E}(\mathbf{r}) = \mathbf{E}_0 e^{-jk_z z}$. Note that, if k_z is complex, then $\text{Re}(k_z) > 0$ for propagating waves to comply with the radiation condition (the wave has to propagate from the source toward infinity and not the opposite, and has to be bounded). If the sources are contained in a finite region, the field at large distances should travel away from that region. In particular, if \mathbf{u}_z is the direction of propagation and the medium is homogeneous and isotropic, at large distances from the source region the transverse field decays like $1/z$ in a spherically diverging wave, and it behaves locally like a plane wave traveling outward in the z direction; therefore, each field component transverse to z behaves like: $e^{-jk_z z}/z$. [48]. Mathematically, the radiation condition is usually expressed as:

$$\lim_{z \rightarrow \infty} z \left(\frac{\partial A}{\partial z} + jkA \right) = 0, \quad (\text{A.34})$$

where A stands for any field component transverse to z and $k = \omega\sqrt{\mu\varepsilon}$ tends to a constant as $z \rightarrow \infty$.

The solution for the the magnetic field is obtained from Maxwell's Eq. (A.14a):

$$\mathbf{H}(\mathbf{r}) = \frac{1}{\zeta} \left(\mathbf{u}_k \times \mathbf{E}(\mathbf{r}) \right), \quad (\text{A.35})$$

where $\zeta = \sqrt{\frac{\mu}{\varepsilon}}$ is the *free-space intrinsic impedance*.

A.2 Electromagnetic field in uniform waveguide regions

Fig. A.1 shows a uniform waveguide with perfectly conducting walls, where S denotes its cross section, transverse to the coordinate z and bounded by the curve \mathcal{C} , and where \mathbf{n} is the unit vector normal to S and lying on the plane of the cross section, and where $\boldsymbol{\tau}$ is the unit vector tangent to the curve \mathcal{C} .

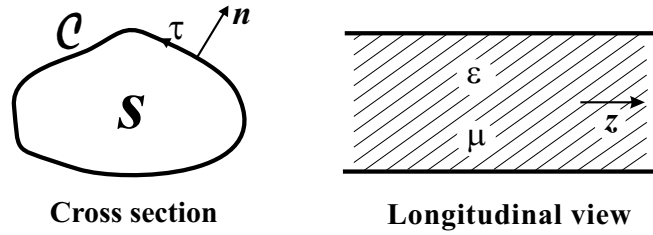


Figure A.1: Uniform waveguide region.

In absence of sources, the electromagnetic vector fields for this problem are described by the homogeneous Maxwell's Eqs. (A.14), with the boundary conditions:

$$\mathbf{n} \times \mathbf{E} = 0, \quad \mathbf{n} \cdot \mathbf{D} = 0, \quad (\text{A.36a})$$

$$\mathbf{n} \times \mathbf{H} = 0, \quad \mathbf{n} \cdot \mathbf{B} = 0. \quad (\text{A.36b})$$

The first boundary condition implies the vanishing of the tangential electric field on the perfectly conducting boundary \mathcal{C} of the waveguide. For an unbounded waveguide (infinite cross section S), it is substituted by the radiation condition. The boundary conditions for the electric field $\mathbf{E}(\mathbf{r})$ and the electric flux $\mathbf{D}(\mathbf{r})$ can be expressed in terms of the transverse field components. The condition on $\mathbf{E}(\mathbf{r})$ is:

$$\mathbf{n} \times \mathbf{E}(\mathbf{r}) = 0 \Rightarrow \begin{cases} \mathbf{n} \times \mathbf{E}_t(\mathbf{r}) = 0 \Leftrightarrow (\boldsymbol{\tau} \cdot \mathbf{E}_t(\mathbf{r})) = 0, \\ E_z(\mathbf{r}) = 0 \Leftrightarrow \nabla_t \cdot (\mathbf{H}_t(\mathbf{r}) \times \mathbf{u}_z) = 0, \end{cases} \quad \text{on } \mathcal{C}, \quad (\text{A.37})$$

where the first condition, substituted in Eq. (A.18), results in:

$$\left[-(\mathbf{n} \cdot \nabla_t) H_z(\mathbf{r}) + \frac{\partial}{\partial z} (\mathbf{n} \cdot \mathbf{H}_t(\mathbf{r})) \right] = 0 \quad \text{on } \mathcal{C}. \quad (\text{A.38})$$

A.2.1 Modal representation of the fields and their sources

According to [48], the electromagnetic field in an uniform perfectly conducting waveguide can be represented in terms of modes and the propagation inside the waveguide can be described using of transmission line theory. The transverse fields are represented in terms of a complete set of transverse vectors (with respect to the z direction) comprising eigenvectors $\mathbf{e}(\mathbf{r}_t)$ for the representation of $\mathbf{E}_t(\mathbf{r})$ and eigenvectors $\mathbf{h}(\mathbf{r}_t)$ for the representation of $\mathbf{H}_t(\mathbf{r})$, where $\mathbf{r} = \mathbf{r}_t + z\mathbf{u}_z$. Since every transverse vector can be expressed as superposition of a solenoidal and a irrotational part, two independent vector mode sets can be identified: $\mathbf{e}^e(\mathbf{r}_t)$ and $\mathbf{e}^h(\mathbf{r}_t)$. The first *vector mode functions* $\mathbf{e}^e(\mathbf{r}_t)$ are irrotational ($\nabla_t \times \mathbf{e}_i^e = 0$ in S) while the second $\mathbf{e}^h(\mathbf{r}_t)$ are solenoidal ($\nabla_t \cdot \mathbf{e}_i^h = 0$ in S). Analogously, we use solenoidal independent vector mode functions $\mathbf{h}^e(\mathbf{r}_t)$ and irrotational independent vector mode functions $\mathbf{h}^h(\mathbf{r}_t)$ to represent the transverse magnetic field \mathbf{H}_t . The functions $\mathbf{e}^e(\mathbf{r}_t)$, $\mathbf{h}^e(\mathbf{r}_t)$ are TM or E vector mode functions and the functions $\mathbf{e}^h(\mathbf{r}_t)$, $\mathbf{h}^h(\mathbf{r}_t)$ are TE or H vector mode functions.

Using these two bases, the transverse electric and magnetic fields can be represented as:

$$\mathbf{E}_t(\mathbf{r}) = \sum_i V_i^e(z) \mathbf{e}_i^e(\mathbf{r}_t) + \sum_i V_i^h(z) \mathbf{e}_i^h(\mathbf{r}_t), \quad (\text{A.39a})$$

$$\mathbf{H}_t(\mathbf{r}) = \sum_i I_i^e(z) \mathbf{h}_i^e(\mathbf{r}_t) + \sum_i I_i^h(z) \mathbf{h}_i^h(\mathbf{r}_t). \quad (\text{A.39b})$$

The longitudinal fields can be obtained by substituting Eqs. (A.39) in Eqs. (A.19) and (A.21):

$$j\omega\varepsilon E_z(\mathbf{r}) = \sum_i I_i^e(z) \nabla_t \cdot \mathbf{e}_i^e(\mathbf{r}_t), \quad (\text{A.40a})$$

$$j\omega\mu H_z(\mathbf{r}) = \sum_i V_i^h(z) \nabla_t \cdot \mathbf{h}_i^h(\mathbf{r}_t), \quad (\text{A.40b})$$

where i is usually a double index and

$$\mathbf{h}_i^\alpha(\mathbf{r}_t) = \mathbf{u}_z \times \mathbf{e}_i^\alpha(\mathbf{r}_t), \quad \text{with } \alpha = e, h. \quad (\text{A.41})$$

These vector mode functions are subject to the following boundary conditions, derived from the conditions for the tangential electric field in Eq. (A.37):

$$\begin{aligned} \mathbf{n} \times \mathbf{e}_i^e &= 0 & \mathbf{n} \times \mathbf{e}_i^h &= 0 & \text{on } \mathcal{C} \\ \nabla_t \cdot (\mathbf{h}_i^e \times \mathbf{u}_z) &= 0 & \nabla_t \cdot (\mathbf{h}_i^h \times \mathbf{u}_z) &= 0 & \text{on } \mathcal{C}. \end{aligned} \quad (\text{A.42})$$

The mode amplitudes in (A.39) can be obtained for both TE and TM modes as:

$$V_i^\alpha(z) = \iint_S \mathbf{E}_t(\mathbf{r}) \cdot \mathbf{e}_i^{\alpha*}(\mathbf{r}_t) d\mathbf{r}_t, \quad (\text{A.43})$$

$$I_i^\alpha(z) = \iint_S \mathbf{H}_t(\mathbf{r}) \cdot \mathbf{h}_i^{\alpha*}(\mathbf{r}_t) d\mathbf{r}_t. \quad (\text{A.44})$$

A mathematical property states that an irrotational vector function can be represented as the gradient of a scalar function, while a solenoidal vector function can be represented as the curl of a scalar function. This property can be applied to express the vector mode functions in terms of two scalar functions $\Phi_i(\mathbf{r}_t)$ and $\Psi_i(\mathbf{r}_t)$:

$$\mathbf{e}_i^e(\mathbf{r}_t) = -\frac{\nabla_t \Phi_i(\mathbf{r}_t)}{k_{t_i}^e}, \quad (\text{A.45a})$$

$$\mathbf{e}_i^h(\mathbf{r}_t) = -\frac{\nabla_t \Psi_i(\mathbf{r}_t)}{k_{t_i}^h} \times \mathbf{z}_0, \quad (\text{A.45b})$$

$$\mathbf{h}_i^e(\mathbf{r}_t) = -\mathbf{z}_0 \times \frac{\nabla_t \Phi_i(\mathbf{r}_t)}{k_{t_i}^e}, \quad (\text{A.45c})$$

$$\mathbf{h}_i^h(\mathbf{r}_t) = -\frac{\nabla_t \Psi_i(\mathbf{r}_t)}{k_{t_i}^h}. \quad (\text{A.45d})$$

The function $\Phi_i(\mathbf{r}_t)$ and $\Psi_i(\mathbf{r}_t)$ are called *scalar mode functions* and are defined by two scalar eigenvalue problems [48]. In particular, the Helmholtz equation for the function $\Phi(\mathbf{r}_t)$ is:

$$\nabla_t^2 \Phi_i(\mathbf{r}_t) + k_{t_i}^{e2} \Phi_i(\mathbf{r}_t) = 0, \quad \text{in } S, \quad (\text{A.46})$$

with the boundary conditions derived from Eqs. (A.42):

$$\begin{aligned} \mathbf{n} \times \mathbf{e}_i^e(\mathbf{r}_t) &= 0 \\ &= \mathbf{e}_i^e(\mathbf{r}_t) \cdot \boldsymbol{\tau} \\ &= -\frac{\nabla_t \Phi_i(\mathbf{r}_t)}{k_{t_i}^e} \cdot \boldsymbol{\tau} \\ &= -\frac{\partial}{\partial l} \Phi_i(\mathbf{r}_t) = 0, \quad \text{on } \mathcal{C} \text{ if } k_{t_i}^e = 0, \end{aligned} \quad (\text{A.47})$$

and

$$\begin{aligned} \nabla_t \cdot (\mathbf{h}_i^e(\mathbf{r}_t) \times \mathbf{u}_z) &= 0 \\ &= \mathbf{u}_z \cdot (\nabla_t \times \mathbf{h}_i^e(\mathbf{r}_t)) \\ &= \mathbf{u}_z \cdot \nabla_t \times \left(\mathbf{u}_z \times \frac{\nabla_t \Phi_i(\mathbf{r}_t)}{k_{t_i}^e} \right) \\ &= \nabla_t^2 \Phi_i(\mathbf{r}_t) = 0 \quad \Rightarrow \Phi_i(\mathbf{r}_t) = 0, \quad \text{on } \mathcal{C} \text{ if } k_{t_i}^e \neq 0. \end{aligned} \quad (\text{A.48})$$

For deriving the first boundary condition, we have used the property that the directional derivative of a scalar function Φ with respect to the distance l along a continuous curve \mathcal{C} having unit tangent vector $\boldsymbol{\tau}$ is: $\frac{d\Phi}{dl} = \nabla_t \Phi \cdot \boldsymbol{\tau}$.

The condition in (A.48) is the Dirichlet condition, while the condition (A.47) identifies a TEM (Transverse ElectroMagnetic) mode, corresponding to $k_{t_i}^e = 0$, as it can be readily verified by substituting the definitions (A.45) in the equations for the longitudinal components of the fields (A.40) and forcing these components to zero. The vector mode functions for the TEM mode can then be redefined by starting from those for the TM modes, in equations (A.45), as:

$$\mathbf{e}_0^e(\mathbf{r}_t) = -\nabla_t \Phi_0(\mathbf{r}_t), \quad (\text{A.49})$$

where Φ_0 is calculated by solving the Helmholtz equation (A.46) with $k_{t_i}^e = 0$:

$$\nabla_t^2 \Phi_0(\mathbf{r}_t) = 0, \quad (\text{A.50})$$

with the boundary condition (A.47) which implies that $\Phi_i(\mathbf{r}_t)$ is constant on each contour. Analogously, the Helmholtz equation for the function $\Psi(\mathbf{r}_t)$ is:

$$\nabla_t^2 \Psi_i(\mathbf{r}_t) + k_{t_i}^{h2} \Psi_i(\mathbf{r}_t) = 0, \quad \text{in } S, \quad (\text{A.51})$$

with the boundary conditions

$$\begin{aligned} \mathbf{n} \times \mathbf{e}_i^h(\mathbf{r}_t) &= 0 \\ &= \mathbf{n} \times \left(\frac{-\nabla_t \Psi_i(\mathbf{r}_t)}{k_{t_i}^h} \times \mathbf{u}_z \right) \\ &= - \left(\mathbf{n} \cdot \frac{-\nabla_t \Psi_i(\mathbf{r}_t)}{k_{t_i}^h} \right) \mathbf{u}_z \\ &= \frac{\partial}{\partial n} \Psi_i(\mathbf{r}_t) = 0, \quad \text{on } \mathcal{C}, \end{aligned} \quad (\text{A.52})$$

and

$$\begin{aligned} \nabla_t \cdot (\mathbf{h}_i^h \times \mathbf{u}_z) &= 0 \\ &= \nabla_t \cdot \left(\frac{\nabla_t \Psi_i(\mathbf{r}_t)}{k_{t_i}^h} \times \mathbf{u}_z \right) \\ &= 0. \end{aligned} \quad (\text{A.53})$$

The first boundary condition is the Neumann condition, while the second boundary condition is always identically verified, and is therefore a trivial one.

Summarizing the previous results, the defining relations for $\Phi_i(\mathbf{r}_t)$ and $\Psi_i(\mathbf{r}_t)$ are:

$$\begin{aligned} \nabla_t^2 \Phi_i + k_{t_i}^{e2} \Phi_i &= 0, & \text{in } S, \\ \Phi_i &= 0, & \text{on } \mathcal{C} \text{ if } k_{t_i}^e \neq 0, \\ \frac{\partial \Phi_i}{\partial l} &= 0, & \text{on } \mathcal{C} \text{ if } k_{t_i}^e = 0 \quad \text{TEM mode,} \end{aligned} \quad (\text{A.54})$$

$$\begin{aligned} \nabla_t^2 \Psi_i + k_{t_i}^{h2} \Psi_i &= 0, & \text{in } S, \\ \frac{\partial \Psi_i}{\partial \mathbf{n}} &= 0, & \text{on } \mathcal{C}. \end{aligned}$$

We shall now show the orthonormality of these scalar mode functions:

$$\iint_S \Phi_m(\mathbf{r}_t) \Phi_n^*(\mathbf{r}_t) d\mathbf{r}_t = \delta_{m,n}, \quad (\text{A.55})$$

$$\iint_S \Psi_m(\mathbf{r}_t) \Psi_n^*(\mathbf{r}_t) d\mathbf{r}_t = \delta_{m,n}. \quad (\text{A.56})$$

We consider the following relation for the function $\Phi(\mathbf{r}_t)$:

$$\nabla_t \cdot [\Phi_m(\mathbf{r}_t) (\nabla_t \Phi_n^*(\mathbf{r}_t)) - (\nabla_t \Phi_m(\mathbf{r}_t)) \Phi_n^*(\mathbf{r}_t)] = (k_{t_n}^{e2} - k_{t_m}^{e2}) \Phi_m(\mathbf{r}_t) \Phi_n^*(\mathbf{r}_t). \quad (\text{A.57})$$

Integrating it over S and using Gauss' Law in two dimensions gives:

$$\oint_{\mathcal{C}} \left(\Phi_m(\mathbf{r}_t) \frac{\partial}{\partial n} \Phi_n^*(\mathbf{r}_t) - \frac{\partial}{\partial n} \Phi_m(\mathbf{r}_t) \Phi_n^*(\mathbf{r}_t) \right) dl = (k_{t_n}^{e2} - k_{t_m}^{e2}) \iint_S (\Phi_m(\mathbf{r}_t) \Phi_n^*(\mathbf{r}_t)) d\mathbf{r}_t. \quad (\text{A.58})$$

Because of the boundary conditions, the first integral is always zero. Therefore, if $k_{t_n}^{e2} \neq k_{t_m}^{e2}$, the integral on the right-hand side must also be zero. If $k_{t_n}^{e2} = k_{t_m}^{e2}$, either $m = n$ or the eigenvalues are degenerated; in this last case, the orthogonality can be organized for example by applying a Gram-Schmidt procedure. This demonstrates the orthogonality of the functions $\Phi_m(\mathbf{r}_t)$, but the same conclusions apply also to the combinations $\Phi_m(\mathbf{r}_t)$, $\Psi_n(\mathbf{r}_t)$ and to the combinations $\Psi_m(\mathbf{r}_t)$, $\Psi_n(\mathbf{r}_t)$.

In view of this, we can prove that the vector mode functions are also orthonormal. For example for the TM functions:

$$\iint_S \mathbf{e}_m^e(\mathbf{r}_t) \cdot \mathbf{e}_n^{e*}(\mathbf{r}_t) d\mathbf{r}_t = \frac{1}{k_{t_m}^e k_{t_n}^e} \iint_S \nabla_t \Phi_m(\mathbf{r}_t) \cdot \nabla_t \Phi_n^*(\mathbf{r}_t) d\mathbf{r}_t. \quad (\text{A.59})$$

If we consider

$$\nabla_t \cdot \left(\Phi_m(\mathbf{r}_t) \nabla_t \Phi_n^*(\mathbf{r}_t) \right) = \nabla_t \Phi_m(\mathbf{r}_t) \cdot \nabla_t \Phi_n^*(\mathbf{r}_t) + \Phi_m(\mathbf{r}_t) \nabla_t^2 \Phi_n^*(\mathbf{r}_t), \quad (\text{A.60})$$

and use Gauss' Law, we obtain:

$$\begin{aligned} \frac{1}{k_{t_m}^e k_{t_n}^e} \iint_S \nabla_t \Phi_m \cdot \nabla_t \Phi_n^* d\mathbf{r}_t &= \frac{1}{k_{t_m}^e k_{t_n}^e} \oint_C \Phi_m \frac{\partial}{\partial n} \Phi_n^* dl \\ &+ \frac{k_{t_n}^{e2}}{k_{t_m}^e k_{t_n}^e} \iint_S \Phi_m \Phi_n^* d\mathbf{r}_t = \delta_{m,n}, \end{aligned} \quad (\text{A.61})$$

where we have used the fact that the first term on the right-hand side is zero because of the boundary condition (A.48).

The orthonormality of the TM vector mode functions with the TE vector mode functions can be demonstrated in a similar way:

$$\iint_S \mathbf{e}_m^e(\mathbf{r}_t) \cdot \mathbf{e}_n^{h*}(\mathbf{r}_t) d\mathbf{r}_t = \frac{-1}{k_{t_m}^e k_{t_n}^h} \iint_S [\nabla_t \Phi_m(\mathbf{r}_t) \cdot (\mathbf{u}_z \times \nabla_t) \Psi_n^*(\mathbf{r}_t)] d\mathbf{r}_t. \quad (\text{A.62})$$

If we consider

$$\begin{aligned} \nabla_t \cdot [\Phi_m(\mathbf{r}_t) (\mathbf{u}_z \times \nabla_t) \Psi_n^*(\mathbf{r}_t)] &= \nabla_t \Phi_m(\mathbf{r}_t) \cdot (\mathbf{u}_z \times \nabla_t) \Psi_n^*(\mathbf{r}_t) \\ &+ \Phi_m(\mathbf{r}_t) \nabla_t \cdot (\mathbf{u}_z \times \nabla_t) \Psi_n^*(\mathbf{r}_t), \end{aligned} \quad (\text{A.63})$$

where the second term on the right-hand side is zero, and use Gauss's theorem, we obtain:

$$\frac{-1}{k_{t_m}^e k_{t_n}^h} \iint_S [\nabla_t \Phi_m(\mathbf{r}_t) \cdot (\mathbf{u}_z \times \nabla_t) \Psi_n^*(\mathbf{r}_t)] d\mathbf{r}_t = \frac{-1}{k_{t_m}^e k_{t_n}^h} \oint_C \Phi_m(\mathbf{r}_t) \mathbf{n} \cdot (\mathbf{u}_z \times \nabla_t) \Psi_n^*(\mathbf{r}_t) dl = 0, \quad (\text{A.64})$$

as a consequence of the boundary condition (A.48) on the TM scalar mode functions.

Finally, the orthonormality of the TE functions

$$\iint_S \mathbf{e}_m^h(\mathbf{r}_t) \cdot \mathbf{e}_n^{h*}(\mathbf{r}_t) d\mathbf{r}_t = \frac{1}{k_{t_m}^h k_{t_n}^h} \iint_S \nabla_t \Psi_m(\mathbf{r}_t) \cdot \nabla_t \Psi_n^*(\mathbf{r}_t) d\mathbf{r}_t, \quad (\text{A.65})$$

can be shown by following the same procedure as for the TM functions.

If we substitute Eqs. (A.45) in the first relations of Eqs. (A.39) and Eqs. (A.40) and we assume that summation and differentiation can be here interchanged, we obtain the following expressions:

$$\mathbf{E}_t(\mathbf{r}) = - \sum_i V_i^e(z) \frac{\nabla_t \Phi_i(\mathbf{r}_t)}{k_{t_i}^e} - \sum_i V_i^h(z) \frac{\nabla_t \Psi_i(\mathbf{r}_t)}{k_{t_i}^h} \times \mathbf{u}_z, \quad (\text{A.66a})$$

$$\mathbf{H}_t(\mathbf{r}) = - \sum_i I_i^e(z) \left(\mathbf{u}_z \times \frac{\nabla_t \Phi_i(\mathbf{r}_t)}{k_{t_i}^e} \right) - \sum_i I_i^h(z) \frac{\nabla_t \Psi_i(\mathbf{r}_t)}{k_{t_i}^h}, \quad (\text{A.66b})$$

$$j\omega \varepsilon E_z(\mathbf{r}) = \sum_i I_i^e(z) k_{t_i}^e \Phi_i(\mathbf{r}_t), \quad (\text{A.66c})$$

$$j\omega \mu H_z(\mathbf{r}) = \sum_i V_i^h(z) k_{t_i}^h \Psi_i(\mathbf{r}_t). \quad (\text{A.66d})$$

We verify now that these expressions satisfy the homogeneous version of Maxwell's Eqs. (A.14), both for the TE and TM contributions. By doing this, we will derive the transmission line equations for the modal voltages and currents, according to the formulation presented in [138].

The constituent of the electric and magnetic fields associated to the i -th TM mode is:

$$\mathbf{E}_{t_i}^e(\mathbf{r}) = -V_i^e(z) \frac{\nabla_t \Phi_i(\mathbf{r}_t)}{k_{t_i}^e}, \quad (\text{A.67a})$$

$$\mathbf{H}_{t_i}^e = -I_i^e(z) \left(\mathbf{u}_z \times \frac{\nabla_t \Phi_i(\mathbf{r}_t)}{k_{t_i}^e} \right), \quad (\text{A.67b})$$

$$j\omega\epsilon E_{z_i}^e(\mathbf{r}) = I_i^e(z) k_{t_i}^e \Phi_i(\mathbf{r}_t), \quad (\text{A.67c})$$

$$H_{z_i}^e(\mathbf{r}) = 0. \quad (\text{A.67d})$$

Substituting Eq. (A.67a) in Eq. (A.18) results in:

$$\frac{\partial}{\partial z} I_i^e(z) \nabla_t \frac{\Phi_i(\mathbf{r}_t)}{k_{t_i}^e} = j\omega\epsilon V_i^e(z) \frac{-\nabla_t \Phi_i(\mathbf{r}_t)}{k_{t_i}^e}, \quad (\text{A.68})$$

which leads to the *first transmission line equation*:

$$\frac{\partial}{\partial z} I_i^e(z) = -j\omega\epsilon V_i^e(z). \quad (\text{A.69})$$

Substituting Eqs. (A.67a)–(A.67c) in Eq. (A.20) results in:

$$\begin{aligned} -\frac{k_{t_i}^e}{j\omega\epsilon} I_i^e(z) (\mathbf{u}_z \times \nabla_t) \Phi_i(\mathbf{r}_t) - \frac{\partial}{\partial z} V_i^e(z) (\mathbf{u}_z \times \nabla_t) \frac{\Phi_i(\mathbf{r}_t)}{k_{t_i}^e} &= \\ &= j\omega\mu I_i^e(z) (\mathbf{u}_z \times \nabla_t) \frac{\Phi_i(\mathbf{r}_t)}{k_{t_i}^e}, \end{aligned} \quad (\text{A.70})$$

which leads to the *second transmission line equation*:

$$\frac{\partial}{\partial z} V_i^e(z) = -j\omega\mu \frac{(k^2 - k_{t_i}^{e2})}{k^2} I_i^e(z). \quad (\text{A.71})$$

We shall now introduce some definitions:

$$\kappa_i^e = \sqrt{k^2 - k_{t_i}^{e2}} = -j\sqrt{k_{t_i}^{e2} - k^2}, \quad (\text{A.72})$$

is the *modal wavenumber* or *modal propagation constant* [48] (also indicated as *guide wavenumber* in [88]) and it is the wavenumber of the electromagnetic field along z , where the sign of the square root is chosen to satisfy the radiation condition. The eigenvalue of

the Helmholtz problem k_{t_i} is also indicated as *cut-off wavenumber* or *transverse wavenumber*. The *modal characteristic impedance* Z_i^e and the *modal characteristic admittance* Y_i^e are defined as:

$$Z_i^e = \frac{1}{Y_i^e} = \frac{\kappa_i^e}{\omega \varepsilon} = \zeta \frac{k}{\kappa_i^e}. \quad (\text{A.73})$$

With these definitions, the transmission line Eqs. (A.69) and (A.71) can be written as:

$$\frac{\partial}{\partial z} I_i^e(z) = -j \kappa_i^e Y_i^e V_n^e(z), \quad (\text{A.74a})$$

$$\frac{\partial}{\partial z} V_i^e(z) = -j \kappa_i^e Z_i^e I_i^e(z). \quad (\text{A.74b})$$

Following the same procedure for the constituent of the electric and magnetic fields (A.66) associated to the i -th TE mode:

$$\mathbf{E}_{ti}^e(\mathbf{r}) = -V_i^h(z) \frac{\nabla_t \Psi_i(\mathbf{r}_t)}{k_{t_i}^h}, \quad (\text{A.75a})$$

$$\mathbf{H}_{ti}^e = -I_i^h(z) (\mathbf{u}_z \times \frac{\nabla_t \Psi_i(\mathbf{r}_t)}{k_{t_i}^h}), \quad (\text{A.75b})$$

$$j\omega\mu H_z(\mathbf{r}) = \sum_i V_i^h(z) k_{t_i}^h \Psi_i(\mathbf{r}_t), \quad (\text{A.75c})$$

leads to the transmission line equations:

$$\frac{\partial}{\partial z} I_i^h(z) = -j \kappa_i^h Y_i^h V_i^h(z), \quad (\text{A.76a})$$

$$\frac{\partial}{\partial z} V_i^h(z) = -j \kappa_i^h Z_i^h I_i^h(z), \quad (\text{A.76b})$$

where the modal propagation constant κ_n^h and the modal characteristic impedance Z_i^h and admittance Y_i^h are still defined according to Eqs. (A.72) and (A.73), respectively. Therefore, in absence of sources, the mode amplitude functions $V_n(z)$ and $I_n(z)$ in the field representation (A.39) can be calculated by means of Eqs. (A.74a)-(A.74b) and Eqs. (A.76a)-(A.76b) for TM and TE modes respectively.

Electric source

We shall now introduce an electric source $\mathbf{J}(\mathbf{r})$. The pertinent Maxwell's equations that describe the fields in the uniform waveguide are the inhomogeneous ones Eqs. (A.5). The source can also be written in terms of longitudinal and transverse components:

$$\mathbf{J}(\mathbf{r}) = \mathbf{J}_t(\mathbf{r}) + J_z(\mathbf{r}) \hat{\mathbf{u}}_z. \quad (\text{A.77})$$

Accordingly, Eq. (A.5a) becomes:

$$\left(\nabla_t + \mathbf{u}_z \frac{\partial}{\partial z} \right) \times \left(\mathbf{H}_t(\mathbf{r}) + \mathbf{u}_z H_z(\mathbf{r}) \right) = j\omega\varepsilon \left(\mathbf{E}_t(\mathbf{r}) + \mathbf{u}_z E_z(\mathbf{r}) \right) + \mathbf{J}_t(\mathbf{r}) + \mathbf{u}_z J_z(\mathbf{r}), \quad (\text{A.78})$$

in which the transverse part is:

$$\left(\nabla_t \times \mathbf{u}_z H_z(\mathbf{r}) \right) + \left(\mathbf{u}_z \times \frac{\partial}{\partial z} \mathbf{H}_t(\mathbf{r}) \right) = j\omega\varepsilon \mathbf{E}_t(\mathbf{r}) + \mathbf{J}_t(\mathbf{r}), \quad (\text{A.79})$$

and the longitudinal part is:

$$\nabla_t \times \mathbf{H}_t(\mathbf{r}) = j\omega\varepsilon \mathbf{u}_z E_z(\mathbf{r}) + \mathbf{u}_z J_z(\mathbf{r}). \quad (\text{A.80})$$

The projection of Maxwell's Eq. (A.5b) in transverse and longitudinal coordinates is still given by Eqs. (A.20) and (A.21).

The modal representation of the transverse field is still given by Eqs. (A.39), while for the longitudinal components we introduce a representation in terms of the longitudinal components of the vector mode functions [48] $e_{zi}^\alpha(\mathbf{r}_t)$ and $h_{zi}^\alpha(\mathbf{r}_t)$ ($\alpha = e, h$):

$$E_z(\mathbf{r}) = \sum_i I_i^e(z) Z_i^e e_{zi}^e(\mathbf{r}_t) - \frac{J_z(\mathbf{r})}{j\omega\varepsilon}, \quad (\text{A.81a})$$

$$= \sum_i f_i(z) \Phi_i(\mathbf{r}_t), \quad (\text{A.81b})$$

$$H_z(\mathbf{r}) = \sum_i V_i^h(z) Y_i^h h_{zi}^h(\mathbf{r}_t), \quad (\text{A.81c})$$

where $f_i(z)$ are amplitude functions to be determined.

If we now substitute the expressions of the transverse fields (A.39a) and (A.39b) and of the longitudinal magnetic field (A.81c) in Eq. (A.79), we obtain:

$$\sum_i V_i^h(z) \frac{jk_{t_i}^{h2}}{\omega\mu} (\mathbf{u}_z \times \nabla_t) \frac{\Psi_i(\mathbf{r}_t)}{k_{t_i}^{h2}} - \sum_\alpha \sum_i I_i^\alpha(z) \mathbf{e}_i^\alpha(\mathbf{r}_t) = j\omega\varepsilon \sum_\alpha \sum_i V_i^\alpha(z) \mathbf{e}_i^\alpha(\mathbf{r}_t) + \mathbf{J}_t(\mathbf{r}), \quad (\text{A.82})$$

with $\alpha = e, h$. Taking the inner product with $\mathbf{e}_i^\alpha(\mathbf{r}_t)$, results in the new transmission line equation:

$$-\frac{\partial}{\partial z} I_i^\alpha(z) = j\kappa_i^\alpha Y_i^\alpha V_i^\alpha(z) + i_i^\alpha(z), \quad (\text{A.83})$$

where the scalar sources $i_i^\alpha(z)$ have been defined as:

$$i_i^\alpha(z) = \iint_S \mathbf{J}_t(\mathbf{r}) \cdot \mathbf{e}_i^{\alpha*}(\mathbf{r}_t) d\mathbf{r}_t. \quad (\text{A.84})$$

Substituting the expression of the transverse magnetic field (A.39b) and of the longitudinal electric field (A.81b) into Eq. (A.80) results in:

$$\sum_{\alpha} \sum_i I_i^{\alpha}(z) \left(\nabla_t \times \mathbf{h}_i^{\alpha}(\mathbf{r}_t) \right) = j\omega\varepsilon \sum_i f_i(z) \Phi_i(\mathbf{r}_t) + J_z(\mathbf{r}). \quad (\text{A.85})$$

Noting that

$$\nabla_t \times \mathbf{h}_i^{\alpha}(\mathbf{r}_t) = \begin{cases} -\mathbf{u}_z k_{t_i}^{e2} \Phi_i(\mathbf{r}_t) & , \quad \alpha = e, \\ 0 & , \quad \alpha = h, \end{cases} \quad (\text{A.86})$$

and taking the inner product of both sides of Eq. (A.85) with the n -th function $\Phi_n(\mathbf{r}_t)$ leads to:

$$f_n(z) = \frac{1}{j\omega\varepsilon} \left\{ -k_{t_n}^e I_n^e(z) - \iint_S J_z(\mathbf{r}) \Phi_n^*(\mathbf{r}_t) d\mathbf{r}_t \right\}. \quad (\text{A.87})$$

We substitute now the expressions of the transverse fields (A.39a), (A.39b) and of the longitudinal field (A.81b) in Eq. (A.20) and use the definition of $\mathbf{h}_i^e(\mathbf{r}_t)$ in Eqs. (A.45):

$$\sum_i f_i(z) k_{t_i}^e \mathbf{h}_i^e(\mathbf{r}_t) + \sum_{\alpha} \sum_i \frac{\partial}{\partial z} V_i^{\alpha}(z) \mathbf{h}_i^e(\mathbf{r}_t) = -j\omega\mu \sum_{\alpha} \sum_i I_i^{\alpha}(z) \mathbf{h}_i^{\alpha}(\mathbf{r}_t). \quad (\text{A.88})$$

In this expression, we introduce the definition of $f_n(z)$ in Eq. (A.87). For the case of TM modes, we calculate the inner product with the i -th vector mode function $\mathbf{h}_i^e(\mathbf{r}_t)$ and obtain:

$$\frac{k_{t_i}^e}{j\omega\varepsilon} \left\{ -k_{t_i}^e I_i^e(z) - \iint_S J_z(\mathbf{r}) \Phi_i^*(\mathbf{r}_t) d\mathbf{r}_t \right\} + \frac{\partial}{\partial z} V_i^{\alpha}(z) = -j\omega\mu I_n^{\alpha}(z). \quad (\text{A.89})$$

Introducing the definition:

$$v_i^e(z) = -j \frac{k_{t_i}^e}{\omega\varepsilon} \iint_S J_z(\mathbf{r}) \Phi_i^*(\mathbf{r}_t) d\mathbf{r}_t, \quad (\text{A.90})$$

leads to the transmission line equation:

$$-\frac{\partial}{\partial z} V_i^e = j\kappa_i^e Z_i^e I_i^e(z) + v_i^e(z). \quad (\text{A.91})$$

For TE modes, the first term in Eq. (A.88) does not give contribution and the corresponding transmission line equation becomes:

$$-\frac{\partial}{\partial z} V_i^h = j\kappa_i^h Z_i^h I_n^i(z). \quad (\text{A.92})$$

Summarizing, the modal transmission line equations that allow calculating the mode amplitude functions for the transverse fields in Eqs. (A.39) $V_i^\alpha(z)$ and $I_i^\alpha(z)$, with $\alpha = e, h$, in presence of an electric current $\mathbf{J}(\mathbf{r})$ are:

$$-\frac{\partial}{\partial z} I_i^\alpha(z) = j\kappa_i^\alpha Y_i^\alpha V_i^\alpha(z) + i_i^\alpha(z), \quad (\text{A.93a})$$

$$-\frac{\partial}{\partial z} V_i^\alpha = j\kappa_i^\alpha Z_i^\alpha I_i^\alpha(z) + v_i^\alpha(z), \quad (\text{A.93b})$$

where the scalar sources are:

$$v_i^e(z) = -j \frac{k_{t_i}^e}{\omega \varepsilon} \iint_S J_z(\mathbf{r}) \Phi_i^*(\mathbf{r}_t) d\mathbf{r}_t, \quad v_i^h(z) = 0, \quad (\text{A.94a})$$

$$i_i^\alpha(z) = \iint_S \mathbf{J}_t(\mathbf{r}) \cdot \mathbf{e}_i^{\alpha*}(\mathbf{r}_t) d\mathbf{r}_t. \quad (\text{A.94b})$$

A magnetic source distribution can be included by following exactly the same procedure.

A.2.2 Solution of the uniform transmission-line equations

The solution of the homogeneous Maxwell equations for the electromagnetic field in a source-free uniform bounded waveguide region requires calculating the scalar eigenfunctions Φ_i and Ψ_i and the corresponding eigenvalues k_{t_i} from the eigenvalue problems in the transverse domain (A.54). The modal voltage and current amplitudes, $V_i(z)$ and $I_i(z)$, are obtained by solving the differential transmission line Eqs. (A.74) and (A.76). The solution of this equations can be represented in a traveling-wave or standing-wave form [48]. In the following we report the most common expressions, where the modal subscript i has been omitted.

Traveling-wave form

$$\begin{aligned} V(z) &= V_{\text{inc}}(z') e^{-jk_z(z-z')} + V_{\text{refl}}(z') e^{jk_z(z-z')} \\ &= V_{\text{inc}}(z') [e^{-jk_z(z-z')} + \Gamma(z') e^{jk_z(z-z')}], \\ I(z) &= Y [V_{\text{inc}}(z') e^{-jk_z(z-z')} - V_{\text{refl}}(z') e^{jk_z(z-z')}] \\ &= Y V_{\text{inc}}(z') [e^{-jk_z(z-z')} - \Gamma(z') e^{jk_z(z-z')}], \end{aligned} \quad (\text{A.95})$$

where $V_{\text{inc}}(z')$ and $V_{\text{refl}}(z')$ are the complex amplitudes of the incident and reflected field at a point z' of the transmission line and $\Gamma(z)$ is the voltage reflection coefficient defined as:

$$\Gamma(z) = \frac{V_{\text{refl}}(z)}{V_{\text{inc}}(z)} = \Gamma(z') e^{j2k_z(z-z')}, \quad (\text{A.96})$$

as shown in Fig. A.2.

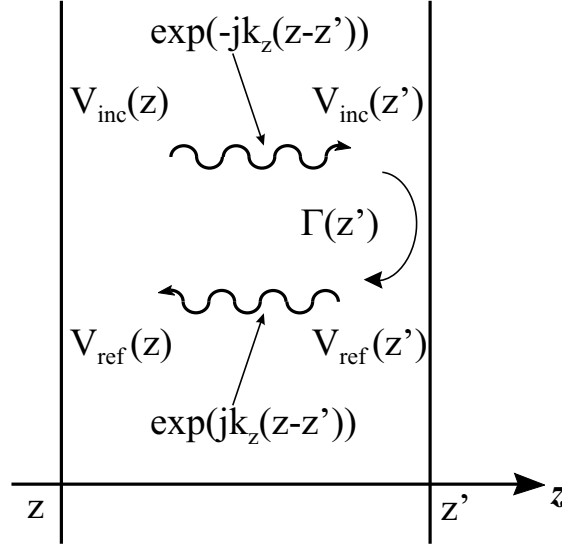


Figure A.2: Traveling-wave representation of the modal voltages, according to Eqs. (A.95).

Standing-wave form

$$\begin{aligned} V(z) &= V(z') \cos k_z(z - z') - jZI(z') \sin k_z(z - z'), \\ I(z) &= I(z') \cos k_z(z - z') - jYV(z') \sin k_z(z - z'). \end{aligned} \quad (\text{A.97})$$

The relation between the standing-wave and the traveling-wave formulations is given by:

$$V(z) = V_{\text{inc}}(z) + V_{\text{refl}}(z), \quad V_{\text{inc}}(z) = \frac{1}{2}[V(z) + ZI(z)], \quad (\text{A.98a})$$

$$ZI(z) = V_{\text{inc}}(z) - V_{\text{refl}}(z), \quad V_{\text{inc}}(z) = \frac{1}{2}[V(z) - ZI(z)]. \quad (\text{A.98b})$$

A.3 Application of the modal representation

The modal representation of the field in a uniform bounded waveguide, derived in Sec. A.2, is here applied to two particular cases that are relevant for the problems considered in this thesis: the propagation of the electromagnetic field in a rectangular waveguide and in free-space.

A.3.1 Homogeneously filled rectangular waveguide

Fig. A.3 shows the cross section of a uniform rectangular waveguide and the pertinent reference system.

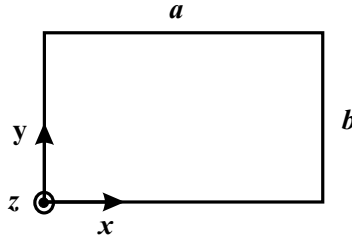


Figure A.3: Cross section of a rectangular waveguide

In Cartesian coordinates the Laplace operator can be written as $\nabla_t^2 = \frac{\partial^2}{\partial x^2} + \frac{\partial^2}{\partial y^2}$, and the two scalar eigenvalue problems in Eq. (A.54) can be solved by applying the method of separation of variables:

$$\Phi_i(\mathbf{r}_t) = \Phi_{k_x}(x)\Phi_{k_y}(y), \quad \Phi_i(\mathbf{r}_t) = 0 \quad \text{on } \mathcal{C}. \quad (\text{A.99})$$

where the transverse wavenumber k_t has been written in terms of the separation constants k_x and k_y : $k_t^2 = k_x^2 + k_y^2$. The Helmholtz Eq. (A.54) for *TM modes* becomes:

$$\left(\frac{d^2}{dx^2} + k_x^2 \right) \Phi_{k_x}(x) = 0, \quad \Phi_{k_x}(0) = \Phi_{k_x}(a) = 0, \quad (\text{A.100a})$$

$$\left(\frac{d^2}{dy^2} + k_y^2 \right) \Phi_{k_y}(y) = 0, \quad \Phi_{k_y}(0) = \Phi_{k_y}(b) = 0, \quad (\text{A.100b})$$

and the solutions are

$$\Phi_{k_x}(x) = \sqrt{\frac{2}{a}} \sin(k_x x), \quad k_x = \frac{m\pi}{a}, \quad m = 1, 2, 3... \quad (\text{A.101a})$$

$$\Phi_{k_y}(y) = \sqrt{\frac{2}{b}} \sin(k_y y), \quad k_y = \frac{n\pi}{b}, \quad n = 1, 2, 3... \quad (\text{A.101b})$$

where the multiplicative constant is chosen to normalize the modes:

$$\int_0^a \Phi_{k_x}(x)\Phi_{k'_x}(x)dx = \delta_{k_x k'_x} = \begin{cases} 1 & , \quad k_x = k'_x, \\ 0 & , \quad k_x \neq k'_x, \end{cases} \quad (\text{A.102})$$

and a similar condition for $\Phi_{k_y}(y)$.

The total solution of the first of Eqs. (A.54) for the case rectangular waveguide is:

$$\Phi_i(\mathbf{r}_t) = \frac{2}{\sqrt{ab}} \sin \frac{m\pi x}{a} \sin \frac{n\pi y}{b}, \quad m, n = 1, 2, 3... \quad (\text{A.103})$$

where the index i corresponds to the double index (m, n) .

The orthonormality of the two-dimensional set $\Phi_i(\mathbf{r}_t)$ is assured from that of Φ_{k_x} and Φ_{k_y} :

$$\iint_S \Phi_i(\mathbf{r}_t) \Phi_j(\mathbf{r}_t) d\mathbf{r}_t = \delta_{ij}. \quad (\text{A.104})$$

The Helmholtz Eq. (A.54) for *TE modes* becomes:

$$\left(\frac{d^2}{dx^2} + k_x^2 \right) \Psi_{k_x}(x) = 0, \quad \frac{\partial \Psi_{k_x}}{\partial x} \Big|_{x=0,a}, \quad (\text{A.105a})$$

$$\left(\frac{d^2}{dy^2} + k_y^2 \right) \Psi_{k_y}(y) = 0, \quad \frac{\partial \Psi_{k_y}}{\partial y} \Big|_{y=0,b}, \quad (\text{A.105b})$$

where we have assumed a solution of the type

$$\Psi_i(\mathbf{r}_t) = \Psi_{k_x}(x) \Psi_{k_y}(y), \quad \frac{\partial \Psi_i}{\partial l} = 0 \quad \text{on } \mathcal{C}. \quad (\text{A.106})$$

The two-dimensional mode functions that solve this problem are:

$$\Psi_i(\mathbf{r}_t) = \sqrt{\frac{\epsilon_m \epsilon_n}{ab}} \cos \frac{m\pi x}{a} \cos \frac{n\pi y}{b}, \quad m, n = 0, 1, 2, 3, \dots \quad \text{mode } m = n = 0 \text{ excluded}, \quad (\text{A.107})$$

where the function ϵ is defined as

$$\epsilon_m = \begin{cases} 1 & , \quad \text{if } m = 0, \\ 2 & , \quad \text{if } m \geq 1. \end{cases} \quad (\text{A.108})$$

The eigenvalues are still those in (A.101).

The transverse wavenumber and the the cut-off wavelength are defined as:

$$k_{t_i}^2 = \left(\frac{m\pi}{a} \right)^2 + \left(\frac{n\pi}{b} \right)^2, \quad (\text{A.109})$$

$$\lambda_i = \frac{2\pi}{k_{t_i}} = \frac{2\pi}{\sqrt{\left(\frac{m\pi}{a} \right)^2 + \left(\frac{n\pi}{b} \right)^2}}, \quad (\text{A.110})$$

$$\begin{aligned} \text{where } & m, n = 1, 2, 3, \dots & , & \text{TM modes,} \\ & m, n = 0, 1, 2, 3, \dots \text{ but not } (m = n = 0) & , & \text{TE modes.} \end{aligned} \quad (\text{A.111})$$

The vector mode functions can be obtained by substituting the expressions of the scalar mode functions (A.103) and (A.107) in Eqs. (A.45), while the modal amplitudes are calculated as described in Sec. A.2.2. Substituting these quantities in Eqs. (A.40) and (A.39),

leads to the following expressions for the electric and magnetic field of the i -th (mn -th) mode [48]:

TM modes

$$E_x^e(x, y, z) = -V_i^e(z) \frac{2}{\sqrt{ab}} \frac{m\pi}{k_{t_i} a} \cos \frac{m\pi}{a} x \sin \frac{n\pi}{b} y, \quad (\text{A.112a})$$

$$E_y^e(x, y, z) = -V_i^e(z) \frac{2}{\sqrt{ab}} \frac{n\pi}{k_{t_i} b} \sin \frac{m\pi}{a} x \cos \frac{n\pi}{b} y, \quad (\text{A.112b})$$

$$E_z^e(x, y, z) = I_i^e(z) \frac{1}{j\omega\epsilon} \frac{2}{\sqrt{ab}} k_{t_i} \sin \frac{m\pi}{a} x \sin \frac{n\pi}{b} y, \quad (\text{A.112c})$$

$$H_x^e(x, y, z) = I_i^e(z) \frac{2}{\sqrt{ab}} \frac{n\pi}{k_{t_i} b} \sin \frac{m\pi}{a} x \cos \frac{n\pi}{b} y, \quad (\text{A.112d})$$

$$H_y^e(x, y, z) = -I_i^e(z) \frac{2}{\sqrt{ab}} \frac{m\pi}{k_{t_i} a} \cos \frac{m\pi}{a} x \sin \frac{n\pi}{b} y, \quad (\text{A.112e})$$

$$H_z^e(x, y, z) = 0. \quad (\text{A.112f})$$

TE modes

$$E_x^h(x, y, z) = V_i^h(z) \sqrt{\frac{\epsilon_m \epsilon_n}{ab}} \frac{n\pi}{k_{t_i} b} \cos \frac{m\pi}{a} x \sin \frac{n\pi}{b} y, \quad (\text{A.113a})$$

$$E_y^h(x, y, z) = -V_i^h(z) \sqrt{\frac{\epsilon_m \epsilon_n}{ab}} \frac{m\pi}{k_{t_i} a} \sin \frac{m\pi}{a} x \cos \frac{n\pi}{b} y, \quad (\text{A.113b})$$

$$E_z^h(x, y, z) = 0, \quad (\text{A.113c})$$

$$H_x^h(x, y, z) = I_i^h(z) \sqrt{\frac{\epsilon_m \epsilon_n}{ab}} \frac{m\pi}{k_{t_i} a} \sin \frac{m\pi}{a} x \cos \frac{n\pi}{b} y, \quad (\text{A.113d})$$

$$H_y^h(x, y, z) = -I_i^h(z) \sqrt{\frac{\epsilon_m \epsilon_n}{ab}} \frac{n\pi}{k_{t_i} b} \cos \frac{m\pi}{a} x \sin \frac{n\pi}{b} y, \quad (\text{A.113e})$$

$$H_z^h(x, y, z) = V_i^h(z) \frac{1}{j\omega\mu} \sqrt{\frac{\epsilon_m \epsilon_n}{ab}} k_{t_i} \cos \frac{m\pi}{a} x \cos \frac{n\pi}{b} y. \quad (\text{A.113f})$$

These expressions are also reported in [88], although there a different normalization has been used for the scalar mode functions ($\Phi_{\text{Marcuvitz}} = \Phi_{\text{Felsen}}/k_{t_i}$).

A.3.2 Electromagnetic field in free space

It has been shown in [48,88] that, from the point of view of characterizing the propagation of the electromagnetic field, free space can be regarded as an uniform waveguide with infinite cross sectional dimensions. A description of the fields in terms of transmission line can still be developed in a manner similar to the previous section, using the same reference system and letting $a \rightarrow \infty$ and $b \rightarrow \infty$. In absence of periodicity requirements on the

fields, the eigenvalues form a continuous spectrum and the modes form a continuous set of plane waves characterized by the wavenumber \mathbf{k}_t containing the information about the direction of propagation and wavelength. The TM and TE scalar eigenfunctions $\Phi_i(\mathbf{r}_t)$ and $\Psi_i(\mathbf{r}_t)$ are identical:

$$\Phi(\mathbf{k}_t; \mathbf{r}_t) = \Psi(\mathbf{k}_t; \mathbf{r}_t) = \frac{1}{2\pi} e^{-j(\mathbf{k}_t \cdot \mathbf{r}_t)}, \quad (\text{A.114})$$

where $\mathbf{k}_t = k_x \mathbf{u}_x + k_y \mathbf{u}_y$ and $-\infty < k_x < \infty$, $-\infty < k_y < \infty$.

The orthonormality relation

$$\iint_{-\infty}^{\infty} \Phi_i(\mathbf{k}_t; \mathbf{r}_t) \Phi_i^*(\mathbf{k}'_t; \mathbf{r}_t) = \frac{1}{4\pi^2} \iint_{-\infty}^{\infty} e^{j(\mathbf{k}'_t - \mathbf{k}_t) \cdot \mathbf{r}_t} = \delta(\mathbf{k}'_t - \mathbf{k}_t), \quad (\text{A.115})$$

is the continuous equivalent of the orthonormality relation for guided modes in a bounded medium.

Space domain

The definition of *spatial Fourier transformation* used in this thesis is:

$$\tilde{F}(\mathbf{k}_t, \omega; z) = \iint F(\mathbf{r}_t, \omega; z) e^{j(\mathbf{k}_t \cdot \mathbf{r}_t)} d\mathbf{r}_t, \text{ direct Fourier transformation,} \quad (\text{A.116a})$$

$$F(\mathbf{r}_t, \omega; z) = \iint \tilde{F}(\mathbf{k}_t, \omega; z) e^{-j(\mathbf{k}_t \cdot \mathbf{r}_t)} \frac{d\mathbf{k}_t}{4\pi^2}, \text{ inverse Fourier transformation,} \quad (\text{A.116b})$$

where $F(\mathbf{r}_t, \omega; z)$ is a function square integrable in \mathbf{r}_t .

In a stratified medium with symmetry axis z , the vector fields can be expressed by means of Eqs. (A.116) as a combination of plane waves with transverse wavenumber \mathbf{k}_t : $e^{-j(\mathbf{k}_t \cdot \mathbf{r}_t)} e^{-jk_z z}$ where $k_z = \sqrt{k^2 - k_x^2 - k_y^2}$. For complex values of k_z , the imaginary part is chosen with a negative sign according to the radiation condition.

Appendix B

Electromagnetic field in proximity of a periodic array

For the purpose of characterizing the electromagnetic field in proximity of an infinite phased array, free space can be regarded as a uniform waveguide having cross sectional dimensions equal to those of the array unit cell [88]. As shown in [7], the pertinent eigenvalue problem is periodic and can be solved by applying the Bloch-Floquet theorem, which was originally formulated in solid state physics for the study of crystals [26, 49]. In this way, the electromagnetic field in proximity of the array is expressed in terms of Floquet modes, defined with respect to the direction perpendicular to the unit cell, and the propagation is still described through transmission line theory [48].

B.1 Bloch-Floquet theorem for crystals

The study of wave propagation in three-dimensional periodic media (in particular crystals) was pioneered by Bloch [26], who in 1928 extended unknowingly the theorem formulated in 1883 by Floquet [49] for the one-dimensional case. Bloch proved that in such media, eigenstates exist that are periodic except a phase factor.

B.1.1 Some basics about crystals

A crystal is obtained by repeating the basis at every Bravais lattice point. The *basis* can be an atom or a molecule and is the unit that is repeated in the crystal. The *Bravais lattice point* is the point that identifies the position of the basis in the crystal. The repetition or displacement of the basis is made along the lattice vector $\mathbf{R} = n_1\mathbf{a}_1 + n_2\mathbf{a}_2 + n_3\mathbf{a}_3$, where

n_1, n_2, n_3 are integer numbers and $\mathbf{a}_1, \mathbf{a}_2, \mathbf{a}_3$ are independent vectors called the *primitive vectors* of the lattice. The result of this repetition is an infinite array of points, called *Bravais lattice* or *space lattice*. The *unit cell* is a volume which fills the space completely when shifted by some subset of the lattice vectors. It contains an integer number of lattice points, as shown in Fig. B.1. The *primitive unit cell* or primitive cell is a volume which fills the space completely without overlapping if shifted by all the lattice vectors. A primitive unit cell contains just one lattice point and is the smallest possible unit cell. The volume identified by the primitive vectors is one possible primitive cell, as indicated in Fig. B.1. Common choice of primitive cell is the Wigner-Seitz cell, defined as the volume closer to a given Bravais lattice point than to any other lattice point.

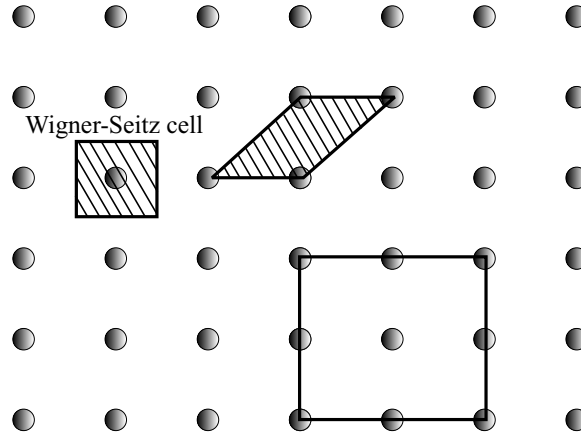


Figure B.1: Examples of possible choices of unit cell in a two-dimensional Bravais lattice. The primitive cells are hatched.

The so defined lattice is the *direct lattice*. The concept of *reciprocal lattice* has been introduced to study the diffraction of waves. If $\mathbf{k} = \frac{2\pi}{\lambda}\mathbf{u}_k$ is the wavevector, pointing at the direction of propagation of the wave, then there are three equivalent definitions of reciprocal lattice:

1. a collection of all wavevectors \mathbf{k} that yield plane waves with a period of the Bravais lattice;
2. a collection of vectors $\mathbf{B} : \mathbf{B} \cdot \mathbf{R} = 2\pi n$ or $e^{-j\mathbf{B} \cdot \mathbf{R}} = 1$;
3. the space spanned by the following primitive vectors, obtained by applying the second definition:

$$\mathbf{b}_1 = 2\pi \frac{\mathbf{a}_2 \times \mathbf{a}_3}{V}, \mathbf{b}_2 = 2\pi \frac{\mathbf{a}_3 \times \mathbf{a}_1}{V}, \mathbf{b}_3 = 2\pi \frac{\mathbf{a}_1 \times \mathbf{a}_2}{V}, \quad (\text{B.1})$$

where $V = \mathbf{a}_1 \cdot (\mathbf{a}_2 \times \mathbf{a}_3)$. The volume of the unit cell in the reciprocal lattice is $\frac{(2\pi)^3}{V}$. Note that the reciprocal of a Bravais lattice is also a Bravais lattice, but in general with a different symmetry.

B.1.2 The Bloch-Floquet theorem

The discussion reported here closely follows [14]. We shall consider an electron moving in a static periodic potential $V(\mathbf{r}) = V(\mathbf{r} + \mathbf{R})$, in a perfect crystal where \mathbf{R} is the Bravais lattice vector. As a consequence, in the corresponding Schrödinger equation:

$$\left[-\frac{\hbar^2}{2m} \nabla^2 + V(\mathbf{r}) \right] \psi(\mathbf{r}) = E\psi(\mathbf{r}), \quad (\text{B.2})$$

if $\psi(\mathbf{r})$ is a solution then $\psi(\mathbf{r} + \mathbf{R})$ is also a solution. Moreover, it can be shown that [14]:

$$\psi(\mathbf{r} + \mathbf{R}) = e^{-j\mathbf{k} \cdot \mathbf{R}} \psi(\mathbf{r}), \quad (\text{B.3})$$

which is also known as *Bloch-type boundary condition at the boundary of the unit cell*. The *Bloch-Floquet theorem* states that the general solution $\psi(\mathbf{r})$ of a periodic eigenproblem of periodicity \mathbf{R} that adheres to the condition (B.3) can be written as the product of a periodic function of the same periodicity of the problem, $u(\mathbf{r})$, and a phase factor $e^{-j(\mathbf{k} \cdot \mathbf{r})}$:

$$\psi(\mathbf{r}) = e^{-j\mathbf{k} \cdot \mathbf{r}} u(\mathbf{r}), \quad (\text{B.4})$$

where

$$u(\mathbf{r}) = e^{-j(\mathbf{k} \cdot \mathbf{r})} \psi(\mathbf{r}) = u(\mathbf{r} + \mathbf{R}). \quad (\text{B.5})$$

The wavevector \mathbf{k} can be expressed as

$$\mathbf{k} = q_1 \mathbf{b}_1 + q_2 \mathbf{b}_2 + q_3 \mathbf{b}_3, \quad (\text{B.6})$$

where q_i are integer numbers and the vectors \mathbf{b}_i are a basis for the reciprocal lattice, defined such that

$$\mathbf{b}_i \cdot \mathbf{a}_j = 2\pi \delta_{ij} \quad \Rightarrow \quad \mathbf{B} \cdot \mathbf{R} = 2\pi n, \quad (\text{B.7})$$

with n an integer and \mathbf{B} the reciprocal lattice vector:

$$\mathbf{B} = m_1 \mathbf{b}_1 + m_2 \mathbf{b}_2 + m_3 \mathbf{b}_3, \quad (\text{B.8})$$

with m_i integers. Note that different wavevectors \mathbf{k} and \mathbf{k}' do not always correspond to distinct eigenfunctions. In particular, if $\mathbf{k}' = \mathbf{k} + \mathbf{B}$, the wavevectors \mathbf{k} and \mathbf{k}' are said to

be equivalent and the corresponding eigenfunctions $\psi_{\mathbf{k}}(\mathbf{r})$ and $\psi_{\mathbf{k}'}(\mathbf{r})$ are the same. The reciprocal space spanned by the wavevectors \mathbf{k} , is divided into classes of equivalence $[\mathbf{k}]$, each one pointing to a different solution. The representative of each class is called *Bloch vector* and it is usually taken as the smallest element in modulus. The ensemble of all the Bloch vectors for the considered eigenproblem defines the *first Brillouin zone*, which is obtained by cutting the reciprocal space by planes perpendicular to the primitive vectors and distant $|\mathbf{b}_i/2|$ from the origin of the reference system. The first Brillouin zone is therefore the Wigner-Seitz cell in the reciprocal lattice (see Fig. B.1). For example, in a one-dimensional system, where $R_1 = a$ for some periodicity a , then $b_1 = 2\pi/a$ and the first Brillouin zone is the region $-\frac{\pi}{a} < k \leq \frac{\pi}{a}$.

An important consequence of the Bloch-Floquet theorem (B.4) follows from the fact that, since the function $u(\mathbf{r})$ is periodic, it can be expressed as Fourier series:

$$u(\mathbf{r}) = \sum_{\mathbf{B}} \check{u}_{\mathbf{B}} e^{-j(\mathbf{B} \cdot \mathbf{r})} = \sum_{m_1} \sum_{m_2} \sum_{m_3} \check{u}_{m_1 m_2 m_3} e^{-j(m_1 \mathbf{b}_1 \cdot \mathbf{r} + m_2 \mathbf{b}_2 \cdot \mathbf{r} + m_3 \mathbf{b}_3 \cdot \mathbf{r})}. \quad (\text{B.9})$$

Therefore, the solution $\psi(\mathbf{r})$ can be written explicitly as linear combination of plane waves:

$$\begin{aligned} \psi(\mathbf{r}) &= e^{-j\mathbf{k} \cdot \mathbf{r}} u(\mathbf{r}) \\ &= \sum_{\mathbf{B}} \check{u}_{\mathbf{B}, \mathbf{k}} e^{-j(\mathbf{B} + \mathbf{k}) \cdot \mathbf{r}} \\ &= e^{-j\mathbf{k} \cdot \mathbf{r}} \sum_{m_1} \sum_{m_2} \sum_{m_3} \check{u}_{m_1 m_2 m_3} e^{-j(m_1 \mathbf{b}_1 \cdot \mathbf{r} + m_2 \mathbf{b}_2 \cdot \mathbf{r} + m_3 \mathbf{b}_3 \cdot \mathbf{r})}. \end{aligned} \quad (\text{B.10})$$

B.2 Bloch-Floquet theorem for periodic phased arrays

Some of the results obtained for infinite periodic crystals can be applied to the study of an infinite periodic phased array. In the periodic phased array of waveguides shown in Fig. B.2, the Bravais lattice is two-dimensional. As lattice point we have chosen the center of a radiating element and the primitive vectors are identified as those connecting two neighboring lattice points. The lattice vector is $\mathbf{R} = d_1 \mathbf{a}_1 + d_2 \mathbf{a}_2$ and a primitive unit cell can then be readily identified and is hatched in Fig. B.2.

In a phased array the radiating elements are excited with an uniform amplitude and a linearly varying phase; for example, the (m_1, n_1) -th waveguide, located at $\mathbf{R}_{m_1 m_2} = m_1 d_1 \mathbf{a}_1 + m_2 d_2 \mathbf{a}_2$, is excited by one of its modes such that:

$$V_{m_1 m_2} = V_{00} e^{-j(\mathbf{k}_0 \cdot \mathbf{R}_{m_1 m_2})}, \quad (\text{B.11})$$

where, with respect to the Cartesian reference system in Fig. B.5, $\mathbf{k}_0 = k_{x0}\mathbf{u}_x + k_{y0}\mathbf{u}_y + k_{z0}\mathbf{u}_z = \mathbf{k}_{t0} + k_{z0}\mathbf{u}_z$ is the wavevector of the plane wave radiated by the array in free space, evaluated in its far-field.

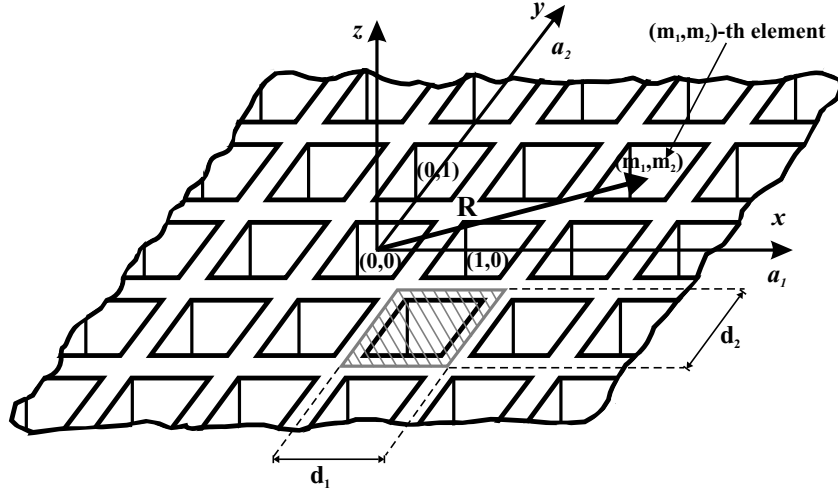


Figure B.2: Geometry of an infinite array of waveguides when the direct lattice is rectangular. The lattice vector \mathbf{R} and a primitive unit cell (hatched) are also indicated.

We want to derive an expression for the fields in region $z \geq 0$ in the vicinity of the array. It has been shown in [44, 88] that, in the proximity of the array, free space can be regarded as a uniform waveguide having cross sectional dimensions equal to those of the unit cell. Therefore, as shown in Appendix A, Sec. A.2.1, a transmission line description of the fields can be developed, where \mathbf{u}_z is the propagation direction. The pertinent vector mode functions for the field representation in Eqs. (A.39) and (A.40) are calculated by solving the homogeneous Helmholtz Eqs. (A.54) for the TM and TE modes, in the scalar eigenfunctions $\Phi_i(\mathbf{r}_t)$ and $\Psi_i(\mathbf{r}_t)$ respectively. Since the operator $\nabla^2 + k_{t_i}^2$ is periodic with period \mathbf{R} , the Helmholtz equations are now supplemented with a Bloch-type periodic boundary condition. Considering for example the TM case, the eigenvalue problem is defined by:

$$\begin{aligned} \nabla_t^2 \Phi_i(\mathbf{r}_t) + k_{t_i}^2 \Phi_i(\mathbf{r}_t) &= 0, & \text{in } S, \\ \Phi(\mathbf{r}_t + \mathbf{R}) &= e^{-j(\mathbf{k}_{t0} \cdot \mathbf{R})} \Phi(\mathbf{r}_t), & \text{in } S, \end{aligned} \quad (\text{B.12})$$

where S is the cross section of the unit cell and $\mathbf{r} = x\mathbf{u}_x + y\mathbf{u}_y + z\mathbf{u}_z = \mathbf{r}_t + z\mathbf{u}_z$. The transverse free-space propagation vector \mathbf{k}_{t0} is defined in the reciprocal space according to equation (B.6). The general solution of this problem for a certain value of \mathbf{k}_{t0} , as shown in [7], follows from the application of Bloch-Floquet theorem to this two-dimensional

problem:

$$\begin{aligned}
\Phi_{\mathbf{k}_{t_0}}(\mathbf{r}_t) &= e^{-j\mathbf{k}_{t_0} \cdot \mathbf{r}_t} \sum_{m_1} \sum_{m_2} \check{\phi}_{m_1 m_2} e^{-j(m_1 \mathbf{b}_1 \cdot \mathbf{r}_t + m_2 \mathbf{b}_2 \cdot \mathbf{r}_t)} \\
&= e^{-j(k_{x_0} x + k_{y_0} y)} \sum_{m_1} \sum_{m_2} \check{\phi}_{m_1 m_2} e^{-j(m_1 \mathbf{b}_1 \cdot \mathbf{r}_t + m_2 \mathbf{b}_2 \cdot \mathbf{r}_t)} \\
&= \phi_{\mathbf{k}_{t_0} m_1 m_2}(\mathbf{r}_t),
\end{aligned} \tag{B.13}$$

where

$$\phi_{\mathbf{k}_{t_0} m_1 m_2}(\mathbf{r}_t) = \check{\phi}_{m_1 m_2} e^{-j(\mathbf{k}_{t_0} \cdot \mathbf{r}_t + m_1 \mathbf{b}_1 \cdot \mathbf{r}_t + m_2 \mathbf{b}_2 \cdot \mathbf{r}_t)}, \tag{B.14}$$

is the contribution of the (m_1, m_2) -th mode to the general solution corresponding to the transverse wavevector \mathbf{k}_{t_0} . Note that \mathbf{k}_{t_0} is the transverse propagation vector of the plane wave radiated by the array in the array far-field, while $\mathbf{k}_{t_i} = m_1 \mathbf{b}_1 + m_2 \mathbf{b}_2$ is the transverse propagation vector of the i -th Floquet mode identified by the indices (m_1, m_2) . The normalization amplitudes

$$\check{\phi}_{m_1 m_2} = \frac{1}{\sqrt{\mathbf{a}_1 \cdot (\mathbf{a}_2 \times \mathbf{u}_z)}}, \tag{B.15}$$

are calculated by evaluating the integral

$$\iint_{U_c} \Phi_{\mathbf{k}_{t_0}}(\mathbf{r}_t) e^{-j(m_1 \mathbf{b}_1 \cdot \mathbf{r}_t + m_2 \mathbf{b}_2 \cdot \mathbf{r}_t)} \check{\phi}_{m_1 m_2} d\mathbf{r}_t = \check{\phi}_{m_1 m_2} (\mathbf{a}_1 \cdot (\mathbf{a}_2 \times \mathbf{u}_z)), \tag{B.16}$$

where U_c is the unit cell. From this result we obtain the orthogonality condition for the functions $\phi_{\mathbf{k}_{t_0} m_1 m_2}(\mathbf{r}_t)$ in Eq. (B.14) corresponding to the same transverse wavevector:

$$\iint_{U_c} \phi_{\mathbf{k}_{t_0} m_1 m_2}(\mathbf{k}_{t_0}, \mathbf{r}_t) \phi_{\mathbf{k}_{t_0} n_1 n_2}^*(\mathbf{k}_{t_0}, \mathbf{r}_t) d\mathbf{r}_t = \delta_{m_1 n_1}(\mathbf{k}_{t_0}) \delta_{m_2 n_2}(\mathbf{k}_{t_0}), \tag{B.17}$$

while the orthogonality condition for the eigenfunctions corresponding to different wavevectors as been shown in [137]. It can be verified that the functions (B.13) are also solution of the Helmholtz problem for TE eigenfunctions.

In common phased arrays the elements can be arranged to obtain two type of configurations: the rectangular lattice and the triangular lattice. Form now on to simplify the notation we will indicate the coordinates of the reciprocal lattice vector as (m, n) instead of (m_1, n_1) .

B.2.1 Rectangular lattice

In the rectangular lattice the primitive vectors are orthogonal to each other and parallel to the axis of the Cartesian reference system, as shown in Fig. B.3a. The direct lattice vector is: $\mathbf{R} = d_1\mathbf{u}_x + d_2\mathbf{u}_y$ and the reciprocal lattice vector \mathbf{B} can be derived from the definitions in Eq. (B.1):

$$\mathbf{b}_1 = \frac{2\pi}{d_1}\mathbf{u}_x, \quad \mathbf{b}_2 = \frac{2\pi}{d_2}\mathbf{u}_y. \quad (\text{B.18})$$

Fig. B.3a shows the primitive vectors for the direct and Fig. B.3b for the reciprocal lattice. The unit cell is indicated in gray. The scalar eigenfunctions for TM and TE modes pertinent to this configuration can be obtained by substituting the expression of \mathbf{B} given by (B.18) and the expression of \mathbf{R} in the general solution (B.13), with the amplitudes given by Eq. (B.15):

$$\begin{aligned} \Phi_{\mathbf{k}_t}(\mathbf{r}_t) &= e^{-j(k_{x_0}x + k_{y_0}y)} \sum_{m_1} \sum_{m_2} \frac{1}{\sqrt{d_1 d_2}} e^{j\left(\frac{2\pi m_1}{d_1}x + \frac{2\pi m_2}{d_2}y\right)} \\ &= \sum_{m_1} \sum_{m_2} \frac{1}{\sqrt{d_1 d_2}} e^{-j\left(k_{x_0} - \frac{2\pi m_1}{d_1}\right)x} e^{-j\left(k_{y_0} - \frac{2\pi m_2}{d_2}\right)y}. \end{aligned} \quad (\text{B.19})$$

B.2.2 Triangular lattice

If the direct lattice is triangular, the primitive vectors are not orthogonal as shown in Fig. B.4a and they can be expressed in terms of the basis vectors of the Cartesian reference system in this figure, \mathbf{u}_x , \mathbf{u}_y , \mathbf{u}_z as:

$$\mathbf{a}_1 \equiv (d_1, 0, 0) \quad \mathbf{a}_2 \equiv (d_2 \cos \Omega, d_2 \sin \Omega, 0), \quad (\text{B.20})$$

where Ω is the skew angle. Using the definitions of primitive vectors for the reciprocal lattice given by equations (B.1), we obtain:

$$\mathbf{b}_1 = \frac{2\pi}{d_1}\mathbf{u}_x - \frac{2\pi}{d_1 \tan \Omega}\mathbf{u}_y, \quad \mathbf{b}_2 = \frac{2\pi}{d_2 \sin \Omega}\mathbf{u}_y. \quad (\text{B.21})$$

Fig. B.4b shows the primitive vectors in the reciprocal lattice. The scalar eigenfunctions (B.13) are here:

$$\Phi_{\mathbf{k}_0}(\mathbf{r}_t) = \sum_m \sum_n \frac{1}{\sqrt{d_1 d_2 \sin \Omega}} e^{-j\left(k_{x_0} - \frac{2\pi m}{d_1}\right)x} e^{-j\left(k_{y_0} + \frac{2\pi m}{d_1 \tan \Omega} - \frac{2\pi n}{d_2 \sin \Omega}\right)y}. \quad (\text{B.22})$$

The rectangular lattice expression can be obtained as a particular case of the triangular one, when the skew angle between the primitive vectors of the direct lattice is $\Omega = 90^\circ$.

Note that, in the case depicted in Fig. B.4, the unit cell does not contain a single complete waveguide aperture, but it intercepts parts of other waveguides. It has been demonstrated in [7] that the orthonormality and completeness of the set of Floquet modes can be preserved over a deformed unit cell containing a single waveguide, provided that the area of the unit cell stays the same and that the deformation is obtained by translations of integer multiples of d_1 and d_2 along the axes \mathbf{a}_1 and \mathbf{a}_2 respectively. This is a consequence of the fact that there are different possible choices for the primitive unit cell of an array. For example, in Fig. B.4a the original parallelogram unit cell (indicated in gray) has been continuously deformed to a rectangular unit cell (indicated with hatching).

The transverse propagation constant of the i -th (mn -th) Floquet mode can be expressed in the Cartesian reference system in terms of its projections k_{x_i} and k_{y_i} along the x and y directions:

$$k_{t_i} = \sqrt{k_{x_i}^2 + k_{y_i}^2} = \sqrt{\left(k_{x_0} - \frac{2\pi m}{d_1}\right)^2 + \left(k_{y_0} + \frac{2\pi m}{d_1 \tan \Omega} - \frac{2\pi n}{d_2 \sin \Omega}\right)^2}. \quad (\text{B.23})$$

If we now express the transverse propagation vector \mathbf{k}_0 in terms of polar coordinates with respect to the reference system in Fig. B.5:

$$k_{x_0} = k_0 \sin \vartheta \cos \varphi = k_0 T_x, \quad \tan \varphi = \frac{k_{y_0}}{k_{x_0}}, \quad (\text{B.24a})$$

$$k_{y_0} = k_0 \sin \vartheta \sin \varphi = k_0 T_y, \quad \sin \vartheta = \frac{k_{t_0}}{k_0}, \quad (\text{B.24b})$$

$$k_{z_0} = k_0 \cos \vartheta = k_0 T_z, \quad (\text{B.24c})$$

where $k_0 = \omega \sqrt{\varepsilon \mu}$ is the propagation constant and where T_x , T_y and T_z are the directional cosines of \mathbf{k} with respect to the x , y and z axes, then we obtain the following definitions:

$$k_{x_i} = k_{x_0} - \frac{2\pi m}{d_1} = k_0 \sin \vartheta \cos \varphi - \frac{2\pi m}{d_1} = k_0 T_x - \frac{2\pi m}{d_1}, \quad (\text{B.25a})$$

$$\begin{aligned} k_{y_i} &= k_{y_0} + \frac{2\pi m}{d_1 \tan \Omega} - \frac{2\pi n}{d_2 \sin \Omega} = k_0 \sin \vartheta \sin \varphi + \frac{2\pi m}{d_1 \tan \Omega} - \frac{2\pi n}{d_2 \sin \Omega} \\ &= k_0 T_y + \frac{2\pi m}{d_1 \tan \Omega} - \frac{2\pi n}{d_2 \sin \Omega}, \end{aligned} \quad (\text{B.25b})$$

where the angle ϑ is referred to as the *angle of incidence* of the plane wave and φ defines the orientation of the *plane of incidence*.

Introducing the expression of the scalar eigenfunctions (B.22) in Eq. (A.45), we obtain the corresponding vector mode functions. The z -dependence of the modes is determined by the transmission-line behavior of the modal voltage V_i and current I_i . For a uniform

waveguide the phase factor is of the type $e^{-j\kappa_i z}$ where

$$\begin{aligned}\kappa_i &= \sqrt{k_0^2 - k_{t_i}^2} = \sqrt{k_0^2 - k_{x_i}^2 - k_{y_i}^2} \\ &= \sqrt{k_0^2 - \left(k_0 T_x - \frac{2\pi m}{d_1}\right)^2 - \left(k_0 T_y + \frac{2\pi m}{d_1 \tan \Omega} - \frac{2\pi n}{d_2 \sin \Omega}\right)^2}.\end{aligned}\quad (\text{B.26})$$

When κ_i is imaginary, the corresponding Floquet mode is evanescent. In this case, the square root in Eq. (B.26) has to be taken with negative sign: $\kappa_i = -j\sqrt{k_{t_i}^2 - k_0^2}$ to guarantee that the electromagnetic field does not exponentially increase while the wave is moving from the observation point toward infinity. Each mode for which κ_i is real corresponds to a radiated plane wave of the phased array. In particular, the plane wave with indices $m = 0, n = 0$ identifies the main beam, while those with indices $m \neq 0$ or $n \neq 0$ correspond to radiated *grating lobes*. The *grating lobe diagram* can be obtained as a function of T_x and T_y by setting $\kappa_i = 0$, as presented in [7]:

$$\begin{aligned}k_0^2 &= \left[\left(k_0 T_x - \frac{2\pi m}{d_1}\right)^2 - \left(k_0 T_y + \frac{2\pi m}{d_1 \tan \Omega} - \frac{2\pi n}{d_2 \sin \Omega}\right)^2 \right] \\ &= k_0^2 \left[\left(T_x - \frac{\lambda m}{d_1}\right)^2 + \left(T_y + \frac{\lambda m}{d_1 \tan \Omega} - \frac{\lambda n}{d_2 \sin \Omega}\right)^2 \right] \\ \Rightarrow 1 &= \left[\left(T_x - \frac{\lambda m}{d_1}\right)^2 + \left(T_y - \left(\frac{\lambda n}{d_2 \sin \Omega} - \frac{\lambda m}{d_1 \tan \Omega}\right)\right)^2 \right].\end{aligned}\quad (\text{B.27})$$

The last equation defines a family of circles of unit radius and center $\left(\frac{\lambda m}{d_1}, \left(\frac{\lambda n}{d_2 \sin \Omega} - \frac{\lambda m}{d_1 \tan \Omega}\right)\right)$, with respect to T_x and T_y . This grating lobe diagram is shown in Fig. B.6 for the case of a triangular lattice. Note that in this case the primitive vectors of the reciprocal axes are normalized with respect to k_0 , to show in the same drawing both the grating lobe diagram and the triangular lattice geometry, as proposed in [7]:

$$\mathbf{b}_1 = \frac{2\pi}{d_1} \mathbf{u}_x - \frac{2\pi}{d_1 \tan \Omega} \mathbf{u}_y = k_0 \left(\frac{\lambda}{d_1} \mathbf{u}_x\right) - k_0 \left(\frac{\lambda}{d_1 \tan \Omega} \mathbf{u}_y\right), \quad (\text{B.28a})$$

$$\mathbf{b}_2 = k_0 \left(\frac{\lambda}{d_2 \sin \Omega} \mathbf{u}_y\right). \quad (\text{B.28b})$$

Substituting the vector mode functions and the modal amplitudes in Eqs. (A.39) and (A.40), we obtain the expressions for the the electric and magnetic field of the i -th (mn -th) mode, for the general case of triangular lattice, as reported in [88].

TM modes

The vector mode functions are:

$$\mathbf{e}_i = \frac{1}{k_{t_i}} \frac{1}{\sqrt{d_1 d_2 \sin \Omega}} (k_{x_i} \mathbf{u}_x + k_{y_i} \mathbf{u}_y) e^{-j(mk_{x_i}x + nk_{y_i}y)}, \quad (\text{B.29a})$$

$$\mathbf{h}_i = \frac{1}{k_{t_i}} \frac{1}{\sqrt{d_1 d_2 \sin \Omega}} (-k_{y_i} \mathbf{u}_x + k_{x_i} \mathbf{u}_y) e^{-j(mk_{x_i}x + nk_{y_i}y)}. \quad (\text{B.29b})$$

Consequently the fields components are:

$$E_x(x, y, z) = V_i^e(z) \frac{k_{x_i}}{k_{t_i}} \frac{1}{\sqrt{d_1 d_2 \sin \Omega}} e^{-j(mk_{x_i}x + nk_{y_i}y)}, \quad (\text{B.30a})$$

$$E_y(x, y, z) = V_i^e(z) \frac{k_{y_i}}{k_{t_i}} \frac{1}{\sqrt{d_1 d_2 \sin \Omega}} e^{-j(mk_{x_i}x + nk_{y_i}y)}, \quad (\text{B.30b})$$

$$E_z(x, y, z) = \frac{I_i'}{\omega \varepsilon} k_{t_i} \frac{1}{\sqrt{d_1 d_2 \sin \Omega}} e^{-j(mk_{x_i}x + nk_{y_i}y)}, \quad (\text{B.30c})$$

$$H_x(x, y, z) = -I_i^e(z) \frac{k_{y_i}}{k_{t_i}} \frac{1}{\sqrt{d_1 d_2 \sin \Omega}} e^{-j(mk_{x_i}x + nk_{y_i}y)}, \quad (\text{B.30d})$$

$$H_y(x, y, z) = I_i^e(z) \frac{k_{x_i}}{k_{t_i}} \frac{1}{\sqrt{d_1 d_2 \sin \Omega}} e^{-j(mk_{x_i}x + nk_{y_i}y)}, \quad (\text{B.30e})$$

$$H_z(x, y, z) = 0. \quad (\text{B.30f})$$

TE modes

The vector mode functions are:

$$\mathbf{e}_i = \frac{1}{k_{t_i}} \frac{1}{\sqrt{d_1 d_2 \sin \Omega}} (k_{y_i} \mathbf{u}_x - k_{x_i} \mathbf{u}_y) e^{-j(mk_{x_i}x + nk_{y_i}y)}, \quad (\text{B.31a})$$

$$\mathbf{h}_i = \frac{1}{k_{t_i}} \frac{1}{\sqrt{d_1 d_2 \sin \Omega}} (k_{x_i} \mathbf{u}_x + k_{y_i} \mathbf{u}_y) e^{-j(mk_{x_i}x + nk_{y_i}y)}. \quad (\text{B.31b})$$

Consequently the field components are:

$$E_x(x, y, z) = V_i^h(z) \frac{k_{y_i}}{k_{t_i}} \frac{1}{\sqrt{d_1 d_2 \sin \Omega}} e^{-j(mk_{x_i}x + nk_{y_i}y)}, \quad (\text{B.32a})$$

$$E_y(x, y, z) = -V_i^h(z) \frac{k_{x_i}}{k_{t_i}} \frac{1}{\sqrt{d_1 d_2 \sin \Omega}} e^{-j(mk_{x_i}x + nk_{y_i}y)}, \quad (\text{B.32b})$$

$$E_z(x, y, z) = 0, \quad (\text{B.32c})$$

$$H_x(x, y, z) = I_i^h(z) \frac{k_{x_i}}{k_{t_i}} \frac{1}{\sqrt{d_1 d_2 \sin \Omega}} e^{-j(mk_{x_i}x + nk_{y_i}y)}, \quad (\text{B.32d})$$

$$H_y(x, y, z) = I_i^h(z) \frac{k_{y_i}}{k_{t_i}} \frac{1}{\sqrt{d_1 d_2 \sin \Omega}} e^{-j(mk_{x_i}x + nk_{y_i}y)}, \quad (\text{B.32e})$$

$$H_z(x, y, z) = \frac{V_i^h(z)}{\omega \mu} k_{t_i} \frac{1}{\sqrt{d_1 d_2 \sin \Omega}} e^{-j(mk_{x_i}x + nk_{y_i}y)}. \quad (\text{B.32f})$$

These vector mode functions can be interpreted as a discrete set of plane waves, whose wavevectors \mathbf{k} point in the directions identified by the angles ϑ and φ , as shown in Fig. B.5. In the case of the main beam, corresponding to the plane wave with indices $m = n = 0$, the normalized transverse components of \mathbf{k} are:

$$\frac{k_{x_i}}{k_{t_i}} = \frac{k_0 \sin \vartheta \cos \varphi}{\sqrt{(k_0 \sin \vartheta \cos \varphi)^2 + (k_0 \sin \vartheta \sin \varphi)^2}} = \cos \varphi,$$

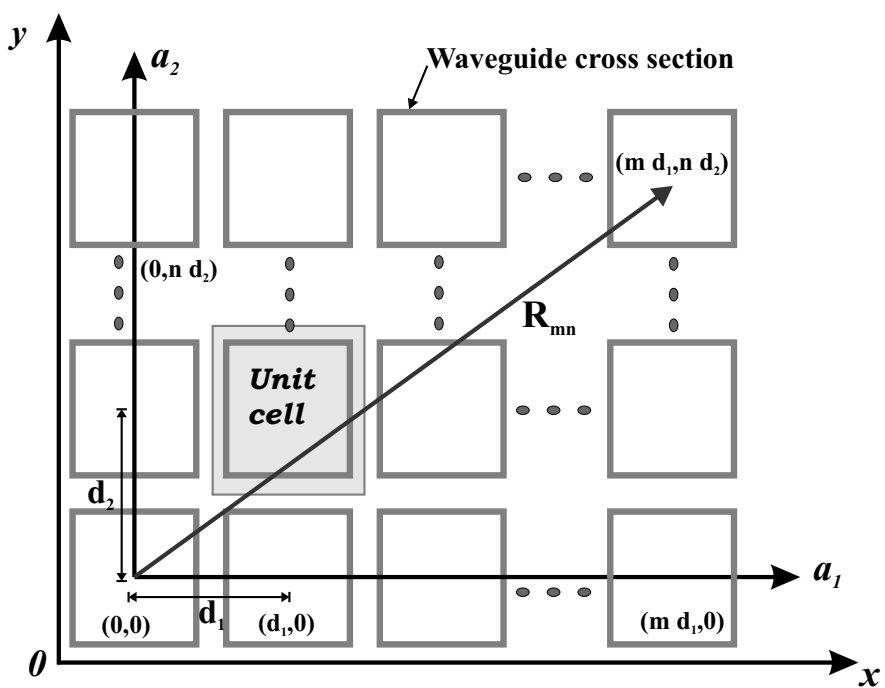
$$\frac{k_{y_i}}{k_{t_i}} = \frac{k_0 \sin \vartheta \sin \varphi}{\sqrt{(k_0 \sin \vartheta \cos \varphi)^2 + (k_0 \sin \vartheta \sin \varphi)^2}} = \sin \varphi,$$

and the vector mode functions become:

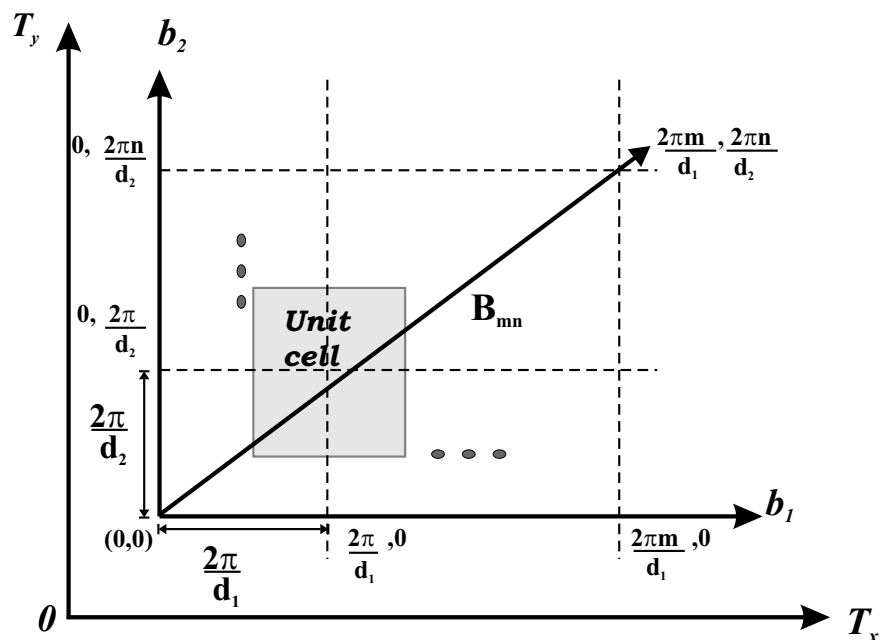
$$\mathbf{e}_{t_{00}} = \frac{1}{\sqrt{d_1 d_2 \sin \Omega}} e^{-j(mk_{x_i}x + nk_{y_i}y)} \begin{cases} (\sin \varphi \mathbf{u}_x - \cos \varphi \mathbf{u}_y) & \text{TE modes,} \\ (\cos \varphi \mathbf{u}_x + \sin \varphi \mathbf{u}_y) & \text{TM modes,} \end{cases} \quad (\text{B.33})$$

$$\mathbf{h}_{t_{00}} = \frac{1}{\sqrt{d_1 d_2 \sin \Omega}} e^{-j(mk_{x_i}x + nk_{y_i}y)} \begin{cases} (\cos \varphi \mathbf{u}_x + \sin \varphi \mathbf{u}_y) & \text{TE modes,} \\ (-\sin \varphi \mathbf{u}_x + \cos \varphi \mathbf{u}_y) & \text{TM modes.} \end{cases} \quad (\text{B.34})$$

For normal incidence, $\vartheta = 0 \Rightarrow k_{t_i} = 0$, this plane wave corresponds to a TEM mode. The electric and magnetic field associated to this mode can be represented using the vector mode functions for TM modes indicated in Eqs. (B.33) and (B.34). The phase contribution is constant on each transverse plane.

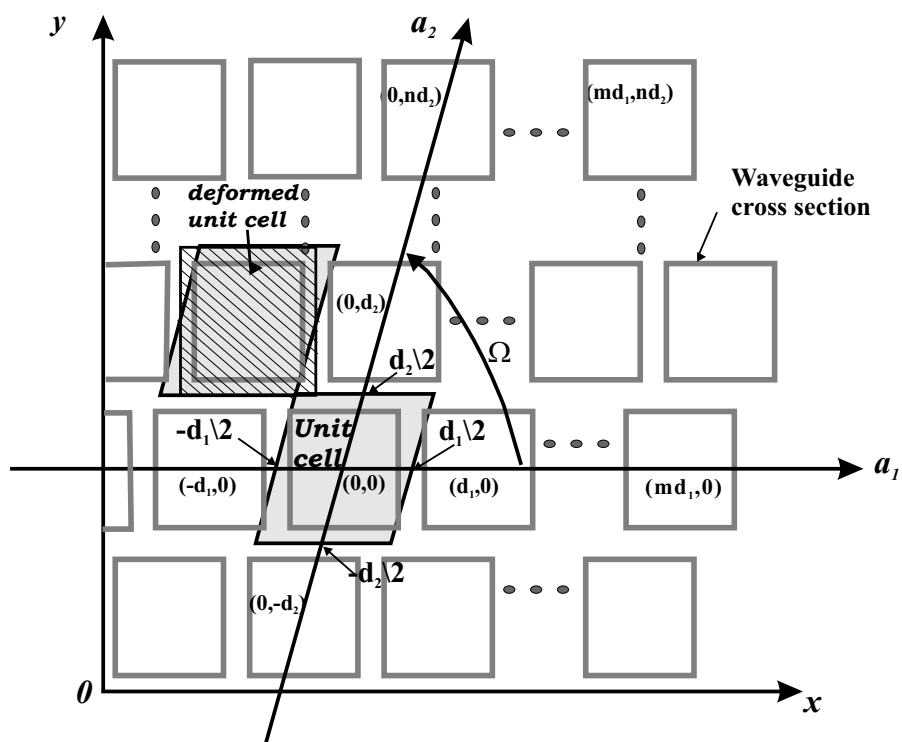


(a)

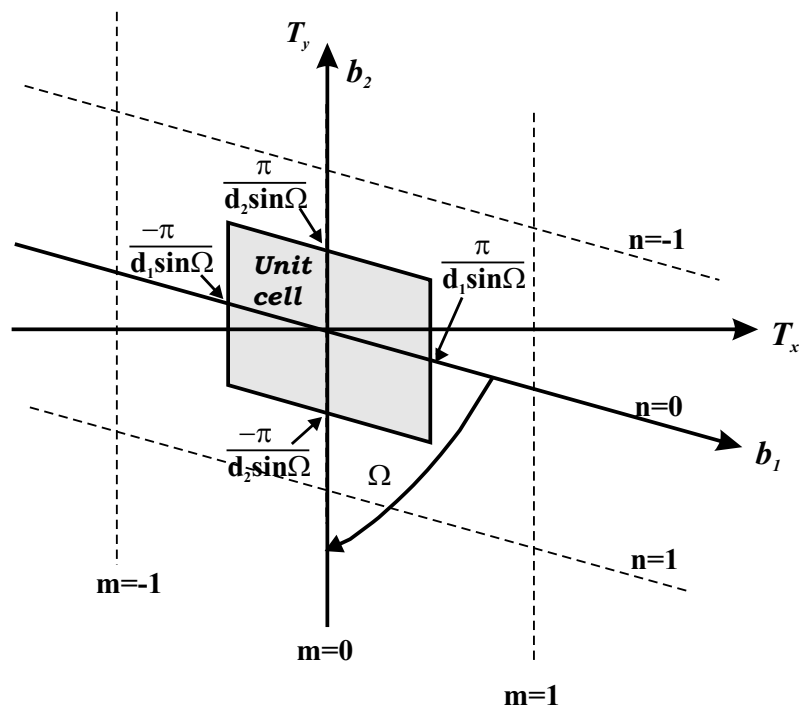


(b)

Figure B.3: Geometry of the rectangular lattice: (a) direct lattice and (b) corresponding reciprocal lattice.



(a)



(b)

Figure B.4: Geometry of the triangular lattice: (a) direct lattice and (b) corresponding reciprocal lattice.

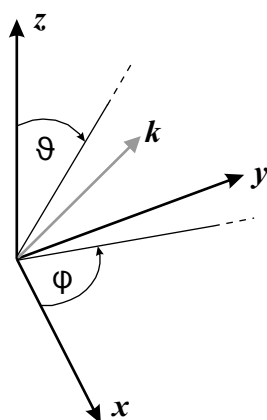


Figure B.5: Cartesian reference system used to express the transverse wavenumber.

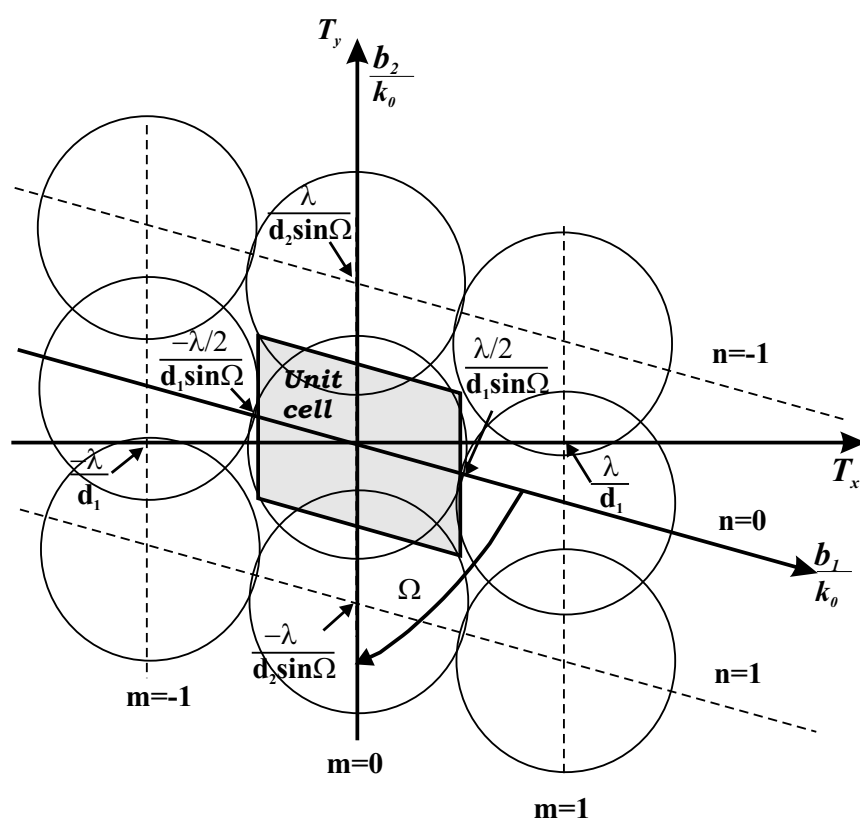


Figure B.6: Grating lobe diagram in reciprocal lattice coordinates [7].

Appendix C

Infinite array Green's function in a periodic environment

In this appendix we will derive the infinite array Green's Function (GF) for a periodic distribution of dipoles printed at the interface between two semi-infinite dielectric layers. The dual case, a periodic distribution of slots, will also be briefly considered. The expression of the GF will then be written in terms of Floquet modes. Finally, the non-accessible GF will be defined.

C.1 General formulation

In this section, we will derive the periodic GF for two cases: the dyadic GF for electric source and electric observation, which will be indicated with $\bar{\mathbf{G}}^e(x, y; x', y'; z, z')$, and the dyadic GF for the magnetic source and magnetic observation, which will be indicated with $\bar{\mathbf{G}}^h(x, y; x', y'; z, z')$. In particular, since we will consider source and observation located at $z' = z = 0$, the z -dependence will be dropped and we will use the following notation: $\bar{\mathbf{G}}^e(x, y; x', y')$ and $\bar{\mathbf{G}}^h(x, y; x', y')$. A detailed derivation will be performed for the electric case only, from which the expression of the magnetic GF can also be deduced in a straightforward way. For the basic GF theory the reader can refer to [71].

Electric source and electric observation

Let us consider the doubly infinite periodic dipole array in Fig. C.1 having rectangular lattice with periods d_x and d_y along the axes x and y of the indicated Cartesian reference system. The dipole width along x is l_x and along y is l_y . Note that in this thesis we intend

as dipole a strip of finite length, having width smaller than the length. The array separates two different half-spaces, indicated with region 1 ($z < 0$) and region 2 ($z > 0$) respectively.

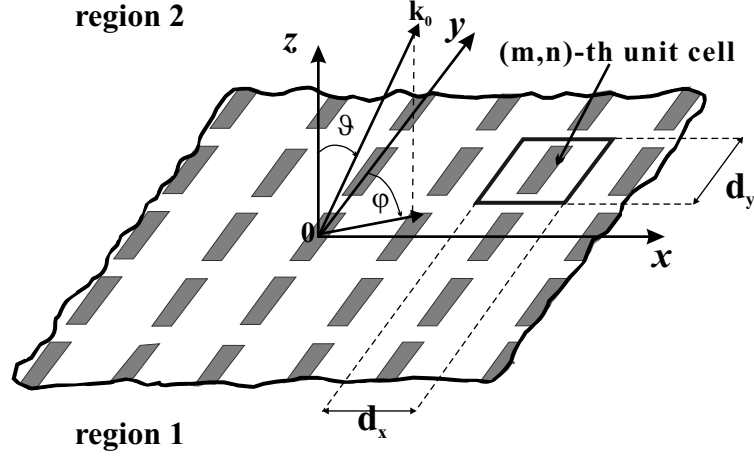


Figure C.1: Infinite periodic dipole array geometry.

The Electric Field Integral Equation (EFIE) for the tangential electric field is:

$$\mathbf{E}_{t,tot}(x, y, 0) = \mathbf{0} \Rightarrow \mathbf{E}_t^i(x, y, 0) = -\mathbf{E}_t^s(x, y, 0), \quad \text{on each dipole,} \quad (\text{C.1})$$

where \mathbf{E}^i is the incident electric field and \mathbf{E}^s is the scattered electric field and the subscript t refers to the transverse component of the field with respect to the z -axis, (but for sake of simplicity this subscript will be omitted from now on). The application of the equivalence theorem in the region just above and below the FSS plane ($z = 0$) allows substituting the dipoles with an unknown electric current distribution equal to the sum of the currents induced on both sides of the dipoles:

$$\mathbf{J}(x, y) = \mathbf{u}_z \times \left(\mathbf{H}_t^{(2)}(x, y, 0^-) - \mathbf{H}_t^{(1)}(x, y, 0^+) \right), \quad (\text{C.2})$$

where $\mathbf{H}_t^{(1)}$ and $\mathbf{H}_t^{(2)}$ are the tangential magnetic fields in region 1 and region 2 respectively. From now we will consider only the transverse component of the vector fields on the plane $z = 0$ and we will omit both the subscript t and the z -dependence to simplify the notation. We chose the center of the dipole at the origin of the reference system in Fig. C.1. The transverse component of the scattered electric field due to the equivalent electric current $\mathbf{J}_{00}(x', y')$ on the dipole can then be written in terms of the dyadic GF of an electric dipole in free space, evaluated on the plane $z = 0$, $\bar{\mathbf{G}}_{00}^e(x, y; x', y')$:

$$\mathbf{E}^s(x, y) = \int_{-\frac{l_x}{2}}^{\frac{l_x}{2}} \int_{-\frac{l_y}{2}}^{\frac{l_y}{2}} \bar{\mathbf{G}}_{00}^e(x, y; x', y') \cdot \mathbf{J}_{00}(x', y') dx' dy'. \quad (\text{C.3})$$

Because of the array periodicity, we can apply the Bloch-Floquet theorem (see Section B.2), which states that the current distribution on a dipole located at distance (md_x, nd_y) from the origin of the reference system in Fig. C.1, $\mathbf{J}_{mn}(x', y')$, differs from the current distribution on the dipole located at the origin $\mathbf{J}_{00}(x', y')$ only by a phase term:

$$\mathbf{J}_{mn}(x', y') = \mathbf{J}_{00}(x' - md_x, y' - nd_y) e^{-j(mk_{x_0}d_x + nk_{y_0}d_y)}, \quad (\text{C.4})$$

where k_{x_0} and k_{y_0} are the transverse components of the free-space propagation vector \mathbf{k}_0 and $\mathbf{J}_{00}(x' - md_x, y' - nd_y)$ is the current distribution on the dipole centered in the origin of the reference system translated to the point (md_x, nd_y) .

The total current distribution on the array is then:

$$\mathbf{J}_{tot}(x', y') = \sum_{m=-\infty}^{\infty} \sum_{n=-\infty}^{\infty} \mathbf{J}_{mn}(x', y'), \quad (\text{C.5})$$

where the current distribution $\mathbf{J}_{mn}(x', y')$ is non-zero for $x' \in (md_x - l_x/2, md_x + l_x/2)$ and $y' \in (md_y - l_y/2, md_y + l_y/2)$.

The total scattered electric field results to be

$$\begin{aligned} \mathbf{E}^s(x, y) &= \int_{-\infty}^{\infty} \int_{-\infty}^{\infty} \bar{\mathbf{G}}_{tot}^e(x, y; x', y') \cdot \mathbf{J}_{tot}(x', y') dx' dy' \\ &= \sum_{m=-\infty}^{\infty} \sum_{n=-\infty}^{\infty} \int_{md_x - l_x/2}^{md_x + l_x/2} \int_{md_y - l_y/2}^{md_y + l_y/2} \bar{\mathbf{G}}_{tot}^e(x, y; x', y') \cdot \mathbf{J}_{mn}(x', y') dx' dy'. \end{aligned} \quad (\text{C.6})$$

If we now substitute Eq. (C.4), we obtain:

$$\begin{aligned} \mathbf{E}^s(x, y) &= \sum_{m=-\infty}^{\infty} \sum_{n=-\infty}^{\infty} \int_{md_x - l_x/2}^{md_x + l_x/2} \int_{md_y - l_y/2}^{md_y + l_y/2} \bar{\mathbf{G}}_{tot}^e(x, y; x', y') \cdot \\ &\quad \mathbf{J}_{00}(x' - md_x, y' - nd_y) e^{-j(mk_{x_0}d_x + nk_{y_0}d_y)} dx' dy'. \end{aligned} \quad (\text{C.7})$$

Applying the change of variable $x'' = x' - md_x$ and $y'' = y' - nd_y$ where $x'' \in (-l_x/2, l_x/2)$ and $y'' \in (-l_y/2, +l_y/2)$ results in:

$$\begin{aligned} \mathbf{E}^s(x, y) &= \sum_{m=-\infty}^{\infty} \sum_{n=-\infty}^{\infty} \int_{-\frac{l_x}{2}}^{\frac{l_x}{2}} \int_{-\frac{l_y}{2}}^{\frac{l_y}{2}} \bar{\mathbf{G}}^e(x, y; x'' + md_x, y'' + nd_y) \cdot \\ &\quad \mathbf{J}_{00}(x'', y'') e^{-j(mk_{x_0}d_x + nk_{y_0}d_y)} dx'' dy''. \end{aligned} \quad (\text{C.8})$$

Using the definition of spatial Fourier transform in Eq. (A.116a) of Appendix A:

$$\int_{-\frac{l_x}{2}}^{\frac{l_x}{2}} \int_{-\frac{l_y}{2}}^{\frac{l_y}{2}} \mathbf{J}_{00}(x'', y'') e^{jk_x x''} e^{jk_y y''} dx'' dy'' = \tilde{\mathbf{J}}_{00}(k_x, k_y), \quad (\text{C.9})$$

and using the expression of the GF as inverse Fourier transform of its spectral form:

$$\bar{\mathbf{G}}^e(x, y; x'', y'') = \left(\frac{1}{2\pi}\right)^2 \int_{-\infty}^{\infty} \int_{-\infty}^{\infty} \tilde{\mathbf{G}}^e(k_x, k_y) e^{-jk_x(x-x'')} e^{-jk_y(y-y'')} dk_x dk_y, \quad (\text{C.10})$$

leads to:

$$\begin{aligned} \mathbf{E}^s(x, y) &= \left(\frac{1}{2\pi}\right)^2 \int_{-\infty}^{\infty} \int_{-\infty}^{\infty} \tilde{\mathbf{G}}^e(k_x, k_y) \cdot \hat{\mathbf{J}}_{00}(k_x, k_y) \\ &\quad \sum_{m=-\infty}^{\infty} \sum_{n=-\infty}^{\infty} e^{-jk_x x} e^{-jk_y y} e^{-j(mk_{x0}d_x + mk_{y0}d_y)} e^{j(mk_x d_x + nk_y d_y)} dk_x dk_y, \end{aligned} \quad (\text{C.11})$$

where $\tilde{\mathbf{G}}^e(k_x, k_y) = \tilde{\mathbf{G}}^e(k_x, k_y, z = 0)$.

The Poisson summation formula:

$$\sum_{m=-\infty}^{\infty} f(m) = \sum_{p=-\infty}^{\infty} F(2\pi p), \quad (\text{C.12})$$

is then applied to the exponential functions in equation (C.11) both for the x -dependence and for the y -dependence:

$$\sum_{m=-\infty}^{\infty} e^{jmd_x(k_x - k_{x0})} = \sum_{p=-\infty}^{\infty} 2\pi \delta(d_x(k_x - k_{x0}) + 2\pi p) = \frac{2\pi}{d_x} \sum_{p=-\infty}^{\infty} \delta(k_x - k_{xp}), \quad (\text{C.13a})$$

$$\sum_{m=-\infty}^{\infty} e^{jmd_y(k_y - k_{y0})} = \sum_{p=-\infty}^{\infty} 2\pi \delta(d_y(k_y - k_{y0}) + 2\pi p) = \frac{2\pi}{d_y} \sum_{p=-\infty}^{\infty} \delta(k_y - k_{yp}), \quad (\text{C.13b})$$

where δ is the well known Dirac distribution and $k_{xp} = k_{x0} - \frac{2\pi p}{d_x}$, $k_{yp} = k_{y0} - \frac{2\pi p}{d_y}$.

Substituting this result in (C.11) leads to

$$\begin{aligned} \mathbf{E}^s(x, y) &= \left(\frac{1}{2\pi}\right)^2 \frac{2\pi}{d_x} \frac{2\pi}{d_y} \int_{-\infty}^{\infty} \int_{-\infty}^{\infty} \tilde{\mathbf{G}}^e(k_x, k_y) \cdot \tilde{\mathbf{J}}_{00}(k_x, k_y) \\ &\quad \sum_{m=-\infty}^{\infty} \sum_{n=-\infty}^{\infty} e^{-jk_x x} \delta(k_x - k_{xm}) e^{-jk_y y} \delta(k_y - k_{yn}) dk_x dk_y, \end{aligned} \quad (\text{C.14})$$

which, using the properties of the distribution δ , leads to:

$$\mathbf{E}^s(x, y) = \frac{1}{d_x d_y} \sum_{m=-\infty}^{\infty} \sum_{n=-\infty}^{\infty} \tilde{\mathbf{G}}^e(k_{xm}, k_{yn}) \cdot \tilde{\mathbf{J}}_{00}(k_{xm}, k_{yn}) e^{-jk_{xm}x} e^{-jk_{yn}y}. \quad (\text{C.15})$$

If the source, the equivalent current distribution $\mathbf{J}_{00}(x'', y'') = \boldsymbol{\delta}(x'', y'')$ is a unitary pulse located at the dipole center ($x_c = 0, y_c = 0$) and having unit Fourier transform, the

convolution product in (C.15) gives the infinite array periodic GF for electric source and electric observation:

$$\bar{\mathbf{G}}^e(x, y; x_c = 0, y_c = 0) = \frac{1}{d_x d_y} \sum_{m=-\infty}^{\infty} \sum_{n=-\infty}^{\infty} \tilde{\mathbf{G}}^e(k_{x_m}, k_{y_n}) e^{-jk_{x_m}x} e^{-jk_{y_n}y}. \quad (\text{C.16})$$

If the source is a unitary pulse centered on a generic point (x_c, y_c) , then $\mathbf{J}(x'' - x_c, y'' - y_c) = \delta(x'' - x_c, y'' - y_c)$ and the infinite array GF becomes

$$\bar{\mathbf{G}}^e(x, y; x_c, y_c) = \frac{1}{d_x d_y} \sum_{m=-\infty}^{\infty} \sum_{n=-\infty}^{\infty} \tilde{\mathbf{G}}^e(k_{x_m}, k_{y_n}) e^{-j(k_{x_m}x + k_{y_n}y)} e^{j(k_{x_m}x_c + k_{y_n}y_c)}. \quad (\text{C.17})$$

Magnetic source and magnetic observation

We shall now consider the dual problem, an infinite periodic distribution of slots with a geometry analogous to the one indicated in Fig. C.1 for the array of dipoles. The total tangential scattered magnetic field in the apertures can be obtained by applying the equivalence theorem and subsequently the image theorem in the region just under (region 1 for $z < 0$) and above (region 2 for $z > 0$) the transition plane. This results in transforming the original problem of apertures between two semi-infinite media in two separate problems, for two homogeneous infinite regions, corresponding to region 1 and region 2, where the aperture has been substituted by an unknown transverse magnetic current distribution, $2\mathbf{M}^{(1)}(x, y)$ and $2\mathbf{M}^{(2)}(x, y)$ respectively.

Fig. C.2a shows one unit cell of the slot array under plane wave incidence. We shall apply the equivalence theorem separately for $z > 0$ for $z < 0$.

For $z > 0$, the electromagnetic field of the plane wave (the source) is equivalent to the field produced by an electric and a magnetic current distribution on a planar surface located at $z = 0^+$ and it is zero under this surface ($\mathbf{H}^{(2)}(x, y, z)|_{z < 0^+} = 0$ and $\mathbf{E}^{(2)}(x, y, z)|_{z < 0^+} = 0$):

$$\begin{aligned} \mathbf{u}_z \times (\mathbf{H}^{(2)}(x, y, z)|_{z > 0^+} - \mathbf{H}^{(2)}(x, y, z)|_{z < 0^+}) &= \mathbf{u}_z \times \mathbf{H}^{(2)}(x, y, z)|_{z > 0^+} = -\mathbf{J}^{(2)}(x, y), \\ \mathbf{u}_z \times (\mathbf{E}^{(2)}(x, y, z)) &= \mathbf{M}^{(2)}(x, y), \end{aligned} \quad (\text{C.18})$$

where the orientation of the vector fields is defined with respect to the reference systems indicated Fig. C.2a. The tangential electric field vanishes on a perfect electric conductor (PEC); therefore, on the metallic screen only the surface electric currents $\mathbf{J}^{(2)}$ are present, while on the aperture there are both electric and magnetic surface currents $\mathbf{J}^{(2)}$ and $\mathbf{M}^{(2)}$ (Fig. C.2b).

For $z < 0$ the field of the plane wave is equivalent to the field produced by an electric and a magnetic current distribution on a planar surface located just under the discontinuity

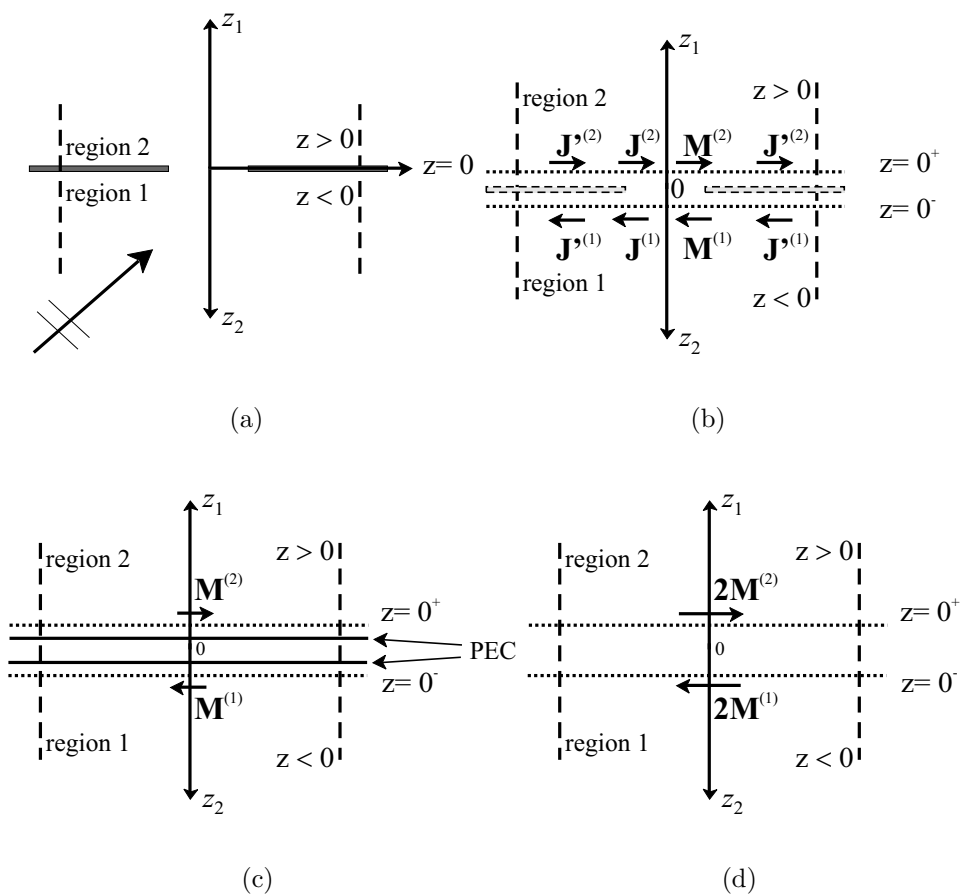


Figure C.2: Equivalence theorem applied to a unit cell of the slot array. (a) unit cell of the array; (b) result of the application of the equivalence theorem; (c) result of the application of the consequence of the equivalence theorem; (d) result of the application of the image theorem.

$z = 0^-$ and it is zero above this surface ($\mathbf{H}^{(1)}(x, y, z)|_{z>0^-} = 0$ and $\mathbf{E}^{(1)}(x, y, z)|_{z>0^-} = 0$):

$$\begin{aligned} \mathbf{u}_z \times (\mathbf{H}^{(1)}(x, y, z)|_{z<0^-} - \mathbf{H}^{(1)}(x, y, z)|_{z>0^-}) &= \mathbf{u}_z \times \mathbf{H}^{(1)}(x, y, z)|_{z<0^-} = -\mathbf{J}^{(1)}(x, y), \\ \mathbf{u}_z \times (\mathbf{E}(x, y, z)^{(1)} &= \mathbf{M}^{(1)}(x, y). \end{aligned} \quad (\text{C.19})$$

Analogously to region 1, on the PEC there are only surface electric currents $\mathbf{J}^{(1)}$, while on the aperture there are both electric and magnetic surface currents $\mathbf{J}^{(1)}$ and $\mathbf{M}^{(1)}$. A consequence of the equivalence theorem is that if we put a PEC just under the plane at $z = 0^+$ for the case $z > 0$ and a PEC just above the plane at $z = 0^-$ for the case $z < 0$, the total electromagnetic field outside the surface does not change. Only the contribution to this field given by the magnetic and electric current distribution are changed. In fact, only the (new) equivalent magnetic current distribution contributes to the field, as shown in Fig. C.2c.

Applying the image theorem separately to each magnetic current distribution and to the corresponding PEC with respect to the indicated reference system, we can substitute the PEC with another magnetic current having the same orientation as the starting one. Therefore, the initial scattering problem for a slot etched on a PEC between two half spaces is reduced to two separate problems of a (double) magnetic current distribution $2\mathbf{M}^{(\gamma)}$, with $\gamma = 1, 2$ radiating in a homogeneous infinite space (Fig. C.2d).

Eventually, the scattered tangential magnetic field in the aperture centered at the origin of the reference system is found as:

$$\mathbf{H}^{s(1)}(x, y) = \int_{-\frac{l_x}{2}}^{+\frac{l_x}{2}} \int_{-\frac{l_y}{2}}^{+\frac{l_y}{2}} \bar{\mathbf{G}}^{h(1)}(x, y; x', y') \cdot 2\mathbf{M}^{(1)}(x', y') dx' dy', \quad (\text{C.20a})$$

$$\mathbf{H}^{s(2)}(x, y) = \int_{-\frac{l_x}{2}}^{+\frac{l_x}{2}} \int_{-\frac{l_y}{2}}^{+\frac{l_y}{2}} \bar{\mathbf{G}}^{h(2)}(x, y; x', y') \cdot 2\mathbf{M}^{(2)}(x', y') dx' dy', \quad (\text{C.20b})$$

where $\bar{\mathbf{G}}^{h(1)}$ is the GF for an homogeneous infinite space having the electromagnetic properties of region 1, and $\bar{\mathbf{G}}^{h(2)}$ is the GF for an homogeneous infinite space having the electromagnetic properties of region 2. The equivalent magnetic currents, $\mathbf{M}^{(1)}(x, y)$ and $\mathbf{M}^{(2)}(x, y)$ are opposite in sign, as indicated in Fig. C.2, and we can use the substitution: $2\mathbf{M}^{(1)} = -2\mathbf{M}^{(2)} = 2\mathbf{M}$. By following the same procedure that was described for the patch transition, the scattered magnetic field can be expressed in terms of the equivalent magnetic current as:

$$\begin{aligned} \mathbf{H}^{s(\gamma)}(x, y) &= \frac{1}{d_x d_y} \sum_{m=-\infty}^{\infty} \sum_{n=-\infty}^{\infty} \tilde{\mathbf{G}}^{h(\gamma)}(k_{x_m}, k_{y_n}) \cdot 2\mathbf{M}(-1)^{(\gamma+1)}(k_{x_m}, k_{y_n}) \\ &e^{-jk_{x_m}x} e^{-jk_{y_n}y}, \end{aligned} \quad (\text{C.21})$$

where $\gamma = 1, 2$. If the source corresponding to each aperture is a unitary pulse at the center of the aperture ($x_c = 0, y_c = 0$): $2\mathbf{M}^{(\gamma)}(x', y') = (-1)^{(\gamma+1)}2\delta(x', y')$ then the periodic GF will assume the form

$$\bar{\mathbf{G}}^{h(\gamma)}(x, y; x_c = 0, y_c = 0) = \frac{2}{d_x d_y} \sum_{m=-\infty}^{\infty} \sum_{n=-\infty}^{\infty} \tilde{\mathbf{G}}^{h(\gamma)}(k_{x_m}, k_{y_n}) e^{-jk_{x_m}x} e^{-jk_{y_n}y}. \quad (\text{C.22})$$

If the source is located in a point $(x_c, y_c, 0)$ the periodic GF becomes:

$$\bar{\mathbf{G}}^e(x, y; x_c, y_c) = \frac{2}{d_x d_y} \sum_{m=-\infty}^{\infty} \sum_{n=-\infty}^{\infty} \tilde{\mathbf{G}}^{h(\gamma)}(k_{x_m}, k_{y_n}) e^{-j(k_{x_m}x + k_{y_n}y)} e^{+j(k_{x_m}x_c + k_{y_n}y_c)}. \quad (\text{C.23})$$

C.2 Green's function in terms of Floquet modes

In Appendix B we have seen that the transverse components of electric and magnetic fields, in proximity of a infinite periodic structure, can be expressed as a linear combination of Floquet vector mode functions, defined with respect to the z axis of a given reference system. Moreover, the propagation of each Floquet mode along the z direction can be characterized in terms of an equivalent transmission line circuit. The spectral dyadic Green's function for a two-layered dielectric medium is obtained by applying the spectral domain immittance approach described in [71].

Electric source and electric observation

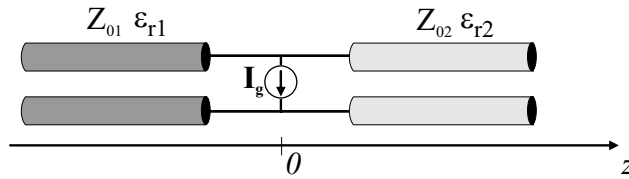


Figure C.3: Equivalent transmission line circuit for a Floquet mode in presence of dipole array used for the definition of the GF for electric source and electric observation.

The equivalent circuit for a Floquet mode in presence of a dipole array between two semi-infinite half spaces consists of a current generator in parallel with the transmission lines representing the propagation of the Floquet mode in the two half-spaces, as shown in

Fig. C.3 [48]. With respect to the polar basis identified by the unit vectors $\hat{\mathbf{k}}_t$, $\hat{\boldsymbol{\alpha}}$ and \mathbf{u}_z :

$$\begin{aligned}\mathbf{k}_t &= k_x \mathbf{u}_x + k_y \mathbf{u}_y, & \hat{\mathbf{k}}_t &= \frac{1}{k_t} (k_x \mathbf{u}_x + k_y \mathbf{u}_y), & \text{with } k_t &= \sqrt{k_x^2 + k_y^2}, \\ \hat{\boldsymbol{\alpha}} &= \mathbf{u}_z \times \hat{\mathbf{k}}_t = \frac{1}{k_t} (k_x \mathbf{u}_y - k_y \mathbf{u}_x),\end{aligned}\tag{C.24}$$

in the spectral domain the strength of the current generator I_g is the component along the direction of $\hat{\mathbf{k}}_t$ of the Fourier transform of the induced current distribution \mathbf{J} [37]. If the current generator I_g has unit amplitude, then the expression for the spectral dyadic GF, for an electric source and electric observation at the same height ($z = z' = 0$), is:

$$\tilde{\mathbf{G}}^e(k_x, k_y) = G_{\text{TM}}^e(k_x, k_y) \hat{\mathbf{k}}_t \hat{\mathbf{k}}_t + G_{\text{TE}}^e(k_x, k_y) \hat{\boldsymbol{\alpha}} \hat{\boldsymbol{\alpha}},\tag{C.25}$$

where $\tilde{\mathbf{G}}^e(k_x, k_y) = \tilde{\mathbf{G}}^e(k_x, k_y, z = 0)$, and

$$G_{\text{TM}}^e(k_x, k_y) = -Z_{\text{TM}}(\mathbf{k}_t) \quad G_{\text{TE}}^e(k_x, k_y) = -Z_{\text{TE}}(\mathbf{k}_t),\tag{C.26}$$

with $Z_{\text{TM}}(\mathbf{k}_t) = Z_{\text{TM}}(\mathbf{k}_t, z = 0)$ and $Z_{\text{TE}}(\mathbf{k}_t) = Z_{\text{TE}}(\mathbf{k}_t, z = 0)$ are the impedances at the section $z = 0$ in the equivalent circuit of Fig. C.3 for the TM and TE transmission lines, respectively. These impedances can be interpreted as the parallel of the characteristic impedances of the two media:

$$G_{\text{TM}}^e(k_x, k_y) = -Z_{\text{TM}}(\mathbf{k}_t) = -\frac{Z_{01}^{\text{TM}} Z_{02}^{\text{TM}}}{Z_{01}^{\text{TM}} + Z_{02}^{\text{TM}}},\tag{C.27a}$$

$$G_{\text{TE}}^e(k_x, k_y) = -Z_{\text{TE}}(\mathbf{k}_t) = -\frac{Z_{01}^{\text{TE}} Z_{02}^{\text{TE}}}{Z_{01}^{\text{TE}} + Z_{02}^{\text{TE}}},\tag{C.27b}$$

where

$$Z_0^{\text{TM}} = \frac{\zeta}{k_0} \frac{\kappa}{\varepsilon_r} \quad Z_0^{\text{TE}} = \zeta \frac{k_0}{\kappa}.\tag{C.28}$$

With this formalism, the GF in (C.16) can be expressed more explicitly as:

$$\begin{aligned}\bar{\mathbf{G}}^e(x, y; x', y') &= \frac{1}{d_x d_y} \sum_{m=-\infty}^{\infty} \sum_{n=-\infty}^{\infty} - \left(Z_{\text{TM}}(\mathbf{k}_{t_i}) \hat{\mathbf{k}}_t \hat{\mathbf{k}}_t \right. \\ &\quad \left. + Z_{\text{TE}}(\mathbf{k}_{t_i}) \hat{\boldsymbol{\alpha}} \hat{\boldsymbol{\alpha}} \right) e^{-j(k_{xm} x + k_{yn} y)} e^{+j(k_{xm} x' + k_{yn} y')} \\ &= \frac{1}{d_x d_y} \sum_{i=1}^{\infty} \left(G_{\text{TM}}^e(\mathbf{k}_{t_i}) \hat{\mathbf{k}}_t \hat{\mathbf{k}}_t + G_{\text{TE}}^e(\mathbf{k}_{t_i}) \hat{\boldsymbol{\alpha}} \hat{\boldsymbol{\alpha}} \right) e^{-j\mathbf{k}_{t_i} \cdot (\mathbf{r}_t - \mathbf{r}'_t)},\end{aligned}\tag{C.29}$$

where the index i refers to the (m, n) -th unit cell.

If we now introduce the definitions (C.24) in the Floquet wave definitions given in Appendix 2 Sec. B.2, we can observe for the electric field vector mode function \mathbf{e}_i that

$$\begin{aligned}\mathbf{e}_i &= \frac{1}{k_{t_i}} \frac{1}{\sqrt{d_x d_y} \sin \Omega} e^{-j(mk_{x_i}x + nk_{y_i}y)} \begin{pmatrix} (k_{x_i} \mathbf{u}_x + k_{y_i} \mathbf{u}_y) & ; & \text{TM} \\ (k_{y_i} \mathbf{u}_x - k_{x_i} \mathbf{u}_y) & ; & \text{TE} \end{pmatrix} \\ &= \frac{1}{\sqrt{d_x d_y} \sin \Omega} e^{-j(mk_{x_i}x + nk_{y_i}y)} \begin{pmatrix} \hat{\mathbf{k}}_{t_i} & ; & \text{TM} \\ -\hat{\boldsymbol{\alpha}} & ; & \text{TE} \end{pmatrix}.\end{aligned}$$

The infinite GF for the electric field in equation (C.29) can then be written in terms of Floquet's modes as

$$\bar{\mathbf{G}}^e(\mathbf{r}_t, \mathbf{r}'_t) = - \sum_{i=-\infty}^{\infty} \left(Z_{\text{TM}}(\mathbf{k}_{t_i}) \mathbf{e}_i(\mathbf{r}_t) \mathbf{e}_i^*(\mathbf{r}'_t) + Z_{\text{TE}}(\mathbf{k}_{t_i}) \mathbf{e}_i(\mathbf{r}_t) \mathbf{e}_i^*(\mathbf{r}'_t) \right), \quad (\text{C.31})$$

where $\mathbf{r}_t = x\mathbf{u}_x + y\mathbf{u}_y$ and $\mathbf{r}'_t = x'\mathbf{u}_x + y'\mathbf{u}_y$.

Non-accessible Green's Function The infinite array GF in (C.31), for a infinite periodic distribution of dipoles, when the observation is the electric field tangential to the dipoles ($z = z' = 0$), can be written in a more compact form by not explicitly distinguishing TM and TE modes:

$$\bar{\mathbf{G}}^e(\mathbf{r}_t, \mathbf{r}'_t) = - \sum_{i=1}^{\infty} \left(Z_i(\mathbf{k}_{t_i}) \mathbf{e}_i(\mathbf{r}_t) \mathbf{e}_i^*(\mathbf{r}'_t) \right), \quad (\text{C.32})$$

where $Z_i = Z_{\text{TE}} + Z_{\text{TM}}$. At this point, we can use the concept of accessible modes introduced in [126] and separate in this expression the contribution due to the first N accessible modes from the one due to the localized modes:

$$\begin{aligned}\bar{\mathbf{G}}^e(\mathbf{r}_t, \mathbf{r}'_t) &= - \left\{ \sum_{i=1}^N Z_i(\mathbf{k}_{t_i}) \mathbf{e}_i(\mathbf{r}_t) \mathbf{e}_i^*(\mathbf{r}'_t) + \sum_{i=N+1}^{+\infty} Z_i(\mathbf{k}_{t_i}) \mathbf{e}_i(\mathbf{r}_t) \mathbf{e}_i^*(\mathbf{r}'_t) \right\} \\ &= \bar{\mathbf{G}}_a^e(\mathbf{r}_t, \mathbf{r}'_t) + \bar{\mathbf{G}}_{na}^e(\mathbf{r}_t, \mathbf{r}'_t),\end{aligned} \quad (\text{C.33})$$

where

$$\bar{\mathbf{G}}_a^e(\mathbf{r}_t, \mathbf{r}'_t) = - \sum_{i=1}^N \left(Z_i(\mathbf{k}_{t_i}) \mathbf{e}_i(\mathbf{r}_t) \mathbf{e}_i^*(\mathbf{r}'_t) \right), \quad \text{accessible GF}, \quad (\text{C.34a})$$

$$\bar{\mathbf{G}}_{na}^e(\mathbf{r}_t, \mathbf{r}'_t) = - \sum_{i=N+1}^{\infty} \left(Z_i(\mathbf{k}_{t_i}) \mathbf{e}_i(\mathbf{r}_t) \mathbf{e}_i^*(\mathbf{r}'_t) \right), \quad \text{non-accessible GF}. \quad (\text{C.34b})$$

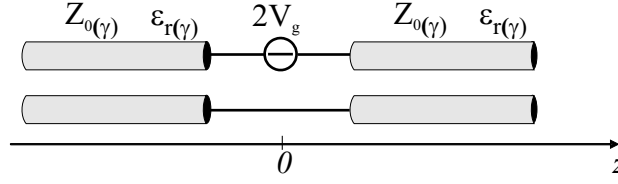


Figure C.4: Equivalent transmission line circuit for a Floquet mode in presence of slot array used for the definition of the GF for magnetic source and magnetic observation.

Magnetic source and magnetic observation

The equivalent network for a Floquet mode in presence of a slot array, shown in Fig. C.4, consists of voltage generator in series with the transmission lines representing the propagation of the mode in one of the two regions [48]. The strength of the voltage generator is the component of the magnetic current distribution along the direction of \mathbf{k}_t in the spectral domain reference system [37] and $Z_0^{(\gamma)}$ is the modal characteristic impedance in region $\gamma = 1, 2$. This network is used to determine the GF for the case of magnetic source and magnetic observation. If we proceed in the same way as for the case of electric source and electric observation, we obtain the expression:

$$\bar{\mathbf{G}}^{h^{(\gamma)}}(\mathbf{r}_t, \mathbf{r}'_t) = \frac{2}{d_x d_y} \sum_{i=1}^{\infty} \left(G_{TM}^{h^{(\gamma)}}(\mathbf{k}_{t_i}) \hat{\mathbf{k}}_t \hat{\mathbf{k}}_t + G_{TE}^{h^{(\gamma)}}(\mathbf{k}_{t_i}) \hat{\boldsymbol{\alpha}} \hat{\boldsymbol{\alpha}} \right) e^{-j\mathbf{k}_{t_i} \cdot (\mathbf{r}_t - \mathbf{r}'_t)}, \quad (\text{C.35})$$

where $G_{TE}^{h^{(\gamma)}}(\mathbf{k}_{t_i}, 0) = Y_{inTE}^{(\gamma)}$ and $G_{TM}^{h^{(\gamma)}}(\mathbf{k}_{t_i}, 0) = Y_{inTM}^{(\gamma)}$. In these expressions, the input admittances are defined with respect to Fig. C.4 as $Y_{inTE}^{(\gamma)} = 1/(2Z_{0TE}^{(\gamma)})$ and $Y_{inTM}^{(\gamma)} = 1/(2Z_{0TM}^{(\gamma)})$, where $Z_{0TE}^{(\gamma)}$ and $Z_{0TM}^{(\gamma)}$ are modal characteristic impedances in region (γ) for the TE and TM polarizations. Eq. (C.35) can be written in compact form as:

$$\bar{\mathbf{G}}^{h^{(\gamma)}}(\mathbf{r}_t, \mathbf{r}'_t) = -2 \sum_{i=1}^{\infty} \left(Y_i^{(\gamma)}(\mathbf{k}_{t_i}) \mathbf{h}_i(\mathbf{r}_t) \mathbf{h}_i^*(\mathbf{r}'_t) \right), \quad (\text{C.36})$$

where $Y_i^{(\gamma)} = 1/(2Z_i^{(\gamma)})$ and $Z_i^{(\gamma)} = Z_{TE}^{(\gamma)} + Z_{TM}^{(\gamma)}$. In this case $Z_{TE}^{(\gamma)}$ and $Z_{TM}^{(\gamma)}$ are the modal characteristic impedances for the TE and TM modes in regions $\gamma = 1, 2$.

Non-accessible Green's Function Separating accessible and localized modes in each region yields:

$$\bar{\mathbf{G}}_a^{h(\gamma)}(\mathbf{r}_t, \mathbf{r}'_t) = -2 \sum_{i=1}^{N(\gamma)} \left(Y_i^{(\gamma)}(\mathbf{k}_{t_i}) \mathbf{h}_i(\mathbf{r}_t) \mathbf{h}_i^*(\mathbf{r}'_t) \right), \quad \text{accessible GF}, \quad (\text{C.37a})$$

$$\bar{\mathbf{G}}_{na}^{h(\gamma)}(\mathbf{r}_t, \mathbf{r}'_t) = -2 \sum_{i=N(\gamma)+1}^{\infty} \left(Y_i^{(\gamma)}(\mathbf{k}_{t_i}) \mathbf{h}_i(\mathbf{r}_t) \mathbf{h}_i^*(\mathbf{r}'_t) \right), \quad \text{non-accessible GF}. \quad (\text{C.37b})$$

C.3 Green's function in Cartesian coordinates

If a plane wave is impinging on the array with an angle of incidence φ , the components of the vector \mathbf{k}_t in Eq. (C.24) become

$$k_x = k_t \cos \varphi, \quad k_y = k_t \sin \varphi, \quad (\text{C.38})$$

$$\cos^2 \varphi = \left(\frac{k_x^2}{k_x^2 + k_y^2} \right), \quad \sin^2 \varphi = \left(\frac{k_y^2}{k_x^2 + k_y^2} \right). \quad (\text{C.39})$$

Therefore the dyads $\hat{\mathbf{k}}_t \hat{\mathbf{k}}_t$ and $\hat{\boldsymbol{\alpha}} \hat{\boldsymbol{\alpha}}$ can be expressed in terms of the basis of the Cartesian system in Fig. C.1 as:

$$\hat{\mathbf{k}}_t \hat{\mathbf{k}}_t = \cos^2 \varphi \mathbf{u}_x \mathbf{u}_x + \cos \varphi \sin \varphi \mathbf{u}_x \mathbf{u}_y + \cos \varphi \sin \varphi \mathbf{u}_y \mathbf{u}_x + \sin^2 \varphi \mathbf{u}_y \mathbf{u}_y, \quad (\text{C.40a})$$

$$\hat{\boldsymbol{\alpha}} \hat{\boldsymbol{\alpha}} = \sin^2 \varphi \mathbf{u}_x \mathbf{u}_x - \cos \varphi \sin \varphi \mathbf{u}_x \mathbf{u}_y - \cos \varphi \sin \varphi \mathbf{u}_y \mathbf{u}_x + \cos^2 \varphi \mathbf{u}_y \mathbf{u}_y. \quad (\text{C.40b})$$

If we now substitute in Eq. (C.35), we obtain the following expression for the components of the dyadic GF:

$$g_{xx}(\mathbf{r}_t, \mathbf{r}'_t) = \frac{1}{d_x d_y} \sum_{i=1}^{+\infty} \left(G_{\text{TM}}(\mathbf{k}_{t_i}) \frac{k_{x_i}^2}{k_{x_i}^2 + k_{y_i}^2} + G_{\text{TE}}(\mathbf{k}_{t_i}) \frac{k_{y_i}^2}{k_{x_i}^2 + k_{y_i}^2} \right) e^{-j\mathbf{k}_{t_i} \cdot (\mathbf{r}_t - \mathbf{r}'_t)}, \quad (\text{C.41a})$$

$$\begin{aligned} g_{xy}(\mathbf{r}_t, \mathbf{r}'_t) &= \frac{1}{d_x d_y} \sum_{i=1}^{+\infty} \left(\frac{k_{x_i} k_{y_i}}{k_{x_i}^2 + k_{y_i}^2} \right) (G_{\text{TM}}(\mathbf{k}_{t_i}) - G_{\text{TE}}(\mathbf{k}_{t_i})) e^{-j\mathbf{k}_{t_i} \cdot (\mathbf{r}_t - \mathbf{r}'_t)} \\ &= g_{yx}(\mathbf{r}_t, \mathbf{r}'_t), \end{aligned} \quad (\text{C.41b})$$

$$g_{yy}(\mathbf{r}_t, \mathbf{r}'_t) = \frac{1}{d_x d_y} \sum_{i=1}^{+\infty} \left(G_{\text{TM}}(\mathbf{k}_{t_i}) \frac{k_{y_i}^2}{k_{x_i}^2 + k_{y_i}^2} + G_{\text{TE}}(\mathbf{k}_{t_i}) \frac{k_{x_i}^2}{k_{x_i}^2 + k_{y_i}^2} \right) e^{-j\mathbf{k}_{t_i} \cdot (\mathbf{r}_t - \mathbf{r}'_t)}, \quad (\text{C.41c})$$

where we have omitted the superscripts e and h , since these equations are valid both for the electric source/electric observation GF and for the magnetic source/magnetic observation GF. However, in the latter case a factor 2 appears and the infinite-space GF must be considered instead of the semi-infinite half-space GF for the electric source/electric observation case.

Considering the particular case of electric source/electric observation, and introducing the expressions (C.27a) for G_{TM}^e and G_{TE}^e in (C.41a), leads to the following explicit form for the GF:

$$\begin{aligned} G_{xx} &= G_{\text{TM}}^e(\mathbf{k}_{t_i}) \frac{k_{x_i}^2}{k_{x_i}^2 + k_{y_i}^2} + G_{\text{TE}}^e(\mathbf{k}_{t_i}) \frac{k_{y_i}^2}{k_{x_i}^2 + k_{y_i}^2} \\ &= -\frac{\zeta}{k_0} \left(\frac{k_0^2}{\kappa_{1i} + \kappa_{2i}} - \frac{k_{x_i}^2}{\kappa_{1i}\varepsilon_{r2} + \kappa_{2i}\varepsilon_{r1}} \right), \end{aligned} \quad (\text{C.42a})$$

$$\begin{aligned} G_{xy} &= \left(\frac{k_{x_i} k_{y_i}}{k_{x_i}^2 + k_{y_i}^2} \right) \left(G_{\text{TM}}^e(\mathbf{k}_{t_i}) - G_{\text{TE}}^e(\mathbf{k}_{t_i}) \right) \\ &= -\frac{\zeta}{k_0} \left(\frac{-k_{x_i} k_{y_i}}{\kappa_{1i}\varepsilon_{r2} + \kappa_{2i}\varepsilon_{r1}} \right), \end{aligned} \quad (\text{C.42b})$$

$$\begin{aligned} G_{yy} &= G_{\text{TM}}^e(\mathbf{k}_{t_i}) \frac{k_{y_i}^2}{k_{x_i}^2 + k_{y_i}^2} + G_{\text{TE}}^e(\mathbf{k}_{t_i}) \frac{k_{x_i}^2}{k_{x_i}^2 + k_{y_i}^2} \\ &= -\frac{\zeta}{k_0} \left(\frac{k_0^2}{\kappa_{1i} + \kappa_{2i}} - \frac{k_{y_i}^2}{\kappa_{1i}\varepsilon_{r2} + \kappa_{2i}\varepsilon_{r1}} \right). \end{aligned} \quad (\text{C.42c})$$

Appendix D

Measurement of the dielectric properties of the foam Bisco HT-820

The dielectric properties of the foam Bisco HT-820 have been measured by the material manufacturer, Rogers Corporation, and they are reported in Sec. D.1. Moreover, since the manufacturing process of the FSS required applying high pressure and temperature on the foam slabs, and therefore affected their density and dielectric constant, we have performed an extra in-house test on the permittivity of foam samples obtained from the manufactured FSS. The results of these measurements are described in Sec. D.2.

D.1 Rogers measurements

Fig. D.1 shows the results of the dielectric-constant and dissipation-factor measurements performed by Rogers Corp. using the test method IPC TM 650 2.5.5.5.1 [69]. The test required building a stripline resonator about 15 cm long. The accuracy of this test method in the determination of the dielectric constant for solid dielectrics is about ± 0.01 . Foams, however, always show a certain variation in the density, which yields a corresponding variation of the dielectric constant. Taking into account the 320.37-512.59 kg/m³ total density range of the HT-820 material, Rogers expected the permittivity to assume values between 1.52 and 1.76, with 1.64 the mean value of this range. The tests were performed in the frequency range 0.78-14 GHz, on two samples 152.4 mm wide, 3.175 mm long with thickness 2.3622 mm and 3.175 mm respectively. The average of the measured dielectric constant values in the range 7-12 GHz was 1.6 while the average of the dissipation factor values was $\tan \delta = 0.00981$. From Fig. D.1, it is observed that the two tested samples have quite different dielectric properties, due to inhomogeneity of the material. A summary of

the results is reported in Tab. D.1.

Bisco HT-820		
Nominal Density (PCF ¹)	24	24
Measured Density (PCF ¹)	22.97	22.99
Thickness (mm)	2.3622	3.175
ϵ_r at 1 GHz	1.62	1.6
$\tan \delta$ at 1 GHz	0.0053	0.0062
ϵ_r at 10 GHz	1.6	1.59
$\tan \delta$ at 10 GHz	0.0091	0.0092

Table D.1: Summary result of the test performed by Rogers Corp. on the dielectric properties of the Bisco HT-820

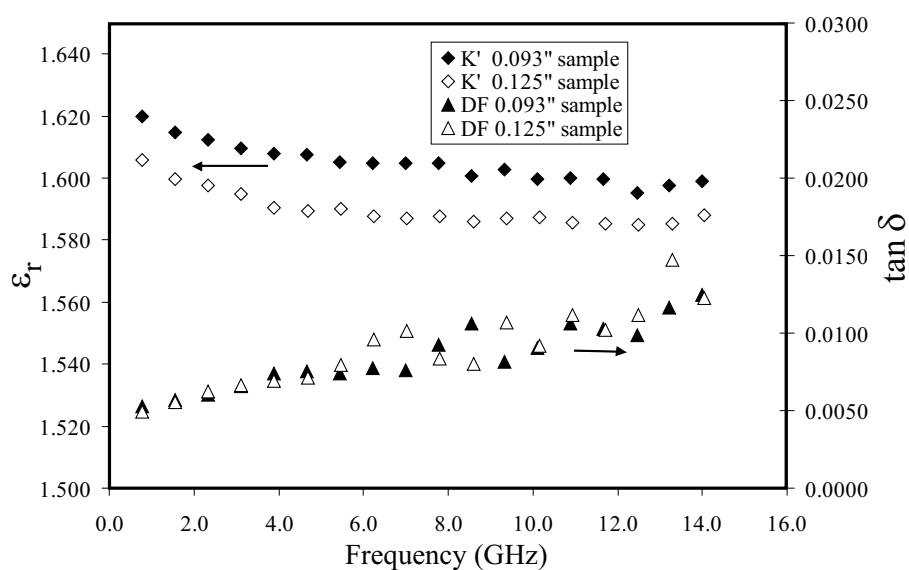


Figure D.1: Dielectric constant and dissipation factor of Bisco HT-820 foam versus frequency as measured by Rogers Corp. by applying the procedure IPC TM 650 2.5.5.5.1.

From these tests we can conclude that the Bisco Cellular Silicone shows quite high losses

¹1 Pound/Cubic Foot=16.018463 kg/cubic meters

in comparison with materials typically used for microwave applications and a dielectric constant that, although rather stable in the frequency range of interest, is spatially variable, depending on the local density of the material.

D.2 Coaxial probe measurements

The dielectric constant and the dissipation factor of a material can be measured in a non-destructive way by using an open-ended coaxial probe. The material sample is placed on the probe and the reflection coefficient is measured. From the relation between reflection coefficient (input admittance of the probe) and permittivity of the material it is possible to calculate its dielectric properties.

For our test, we have used the Hewlett Packard coaxial probe kit HP85070A, which allows to measure with a nominal accuracy (as indicated in the technical sheet) of $\pm 5\%$ on the dielectric constant and $\pm 0.05\%$ on the dissipation factor. However, the method does not give reliable results for dissipation factors lower than 0.01. The software provided with the coaxial probe allows to improve the accuracy on the measurements by using a sample of material of known dielectric properties as reference for calibration purposes. In particular, for this test rexolite was used (permittivity 2.55 and dissipation factor 0.00047, rather constant in the frequency range 2-12 GHz). This kind of test is sensitive to the flatness of the material surface, which has to adhere to the opening of the coaxial probe. To guaranty adhesion, some pressure was applied to the foam samples.

Fig. D.2 shows the results of the measurement of two samples, one consisting of a single layer of foam and the other consisting of a double layer with the bonding film in between. In both cases, the measurements were performed with and without applying pressure on the sample. Fig. D.2 also shows the average measured permittivity for every frequency point; the medium value in the frequency range 2-12 GHz turns out to be 1.67, which, if we account for a calibration error of about 2%, is in agreement with the value of 1.64 estimated on the basis of the density range.

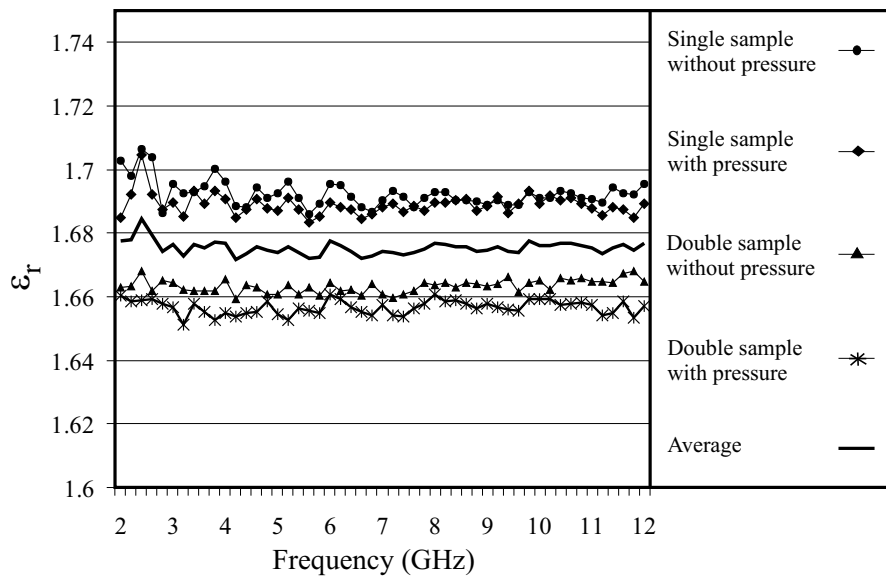


Figure D.2: Dielectric constant and dissipation factor of Bisco HT-820 foam versus frequency as measured in TNO using the coaxial probe kit HP85070A.

Appendix E

Non-accessible Green's function

In this appendix, the compact approximated expressions of the two-dimensional (2D) non-accessible Green's Function g_{na} and of the non-accessible field, used in Chapter 6, are derived in Sec E.1 and in Sec. E.2 respectively. These expressions are then inserted in the kernel of the Integral Equation (IE), obtained when resorting to the IE formulation for the derivation of Multimode Equivalent Networks (IEMEN). The equation is solved by applying the MoM with a Galerkin procedure, and an approximated expression of the MoM matrix elements is derived in Sec. E.4 for the case of sub-domain functions used to expand the unknown currents (the Fourier transform of these currents is derived in Sec. E.3). In Sec. E.5 the Fourier transform of a truncated Floquet wave is calculated.

E.1 Approximated g_{na} for large N_a

The approximated expression of g_{na} , obtained from the general definition in Eq. (6.5) of Chapter 6 for moderately large values of the accessible mode index N_a , is:

$$g_{na}^e(x; x') \approx -j \left(\sum_{m=-\infty}^{-N_a-1} \frac{2\pi|m|}{d_x} e^{-j(k_{x_0} - \frac{2\pi m}{d_x})(x-x')} + \sum_{m=N_a+1}^{\infty} \frac{2\pi m}{d_x} e^{-j(k_{x_0} - \frac{2\pi m}{d_x})(x-x')} \right). \quad (\text{E.1})$$

We shall now demonstrate that this expression is equivalent to the following two expres-

sions:

$$g_{na}^e(x; x') \approx j \frac{2\pi}{d_x} e^{-jk_{x_0}(x-x')} \left\{ \frac{\cos\left(\frac{2\pi}{d_x}(N_a+1)(x-x')\right)}{2 \sin^2\left(\frac{\pi}{d_x}(x-x')\right)} + (N_a+1) \frac{\sin\left(\frac{\pi}{d_x}(2N_a+1)(x-x')\right)}{\sin\left(\frac{\pi}{d_x}(x-x')\right)} \right\}, \quad (\text{E.2})$$

$$g_{na}^e(x; x') \approx j \frac{4\pi}{d_x} e^{-jk_{x_0}(x-x')} \left(\frac{1}{4 \sin^2\left(\frac{\pi}{d_x}(x-x')\right)} + \sum_{m=1}^{N_a} m \cos\left(\frac{2\pi m}{d_x}(x-x')\right) \right). \quad (\text{E.3})$$

Demonstration 1

We first derive the equivalent form (E.2). For this purpose, we rewrite Eq. (E.1) as:

$$g_{na}^e(x; x') \approx -j \left(\sum_{m=N_a+1}^{\infty} \frac{2\pi m}{d_x} e^{-j(k_{x_0} + \frac{2\pi m}{d_x})(x-x')} + \sum_{m=N_a+1}^{\infty} \frac{2\pi m}{d_x} e^{-j(k_{x_0} - \frac{2\pi m}{d_x})(x-x')} \right), \quad (\text{E.4})$$

and consider the two sums in Eq. (E.4) separately. We introduce the variable transformation $m = N_a + 1 + m'$ in the second sum

$$\sum_{m=N_a+1}^{\infty} \frac{2\pi m}{d_x} e^{-j(k_{x_0} - \frac{2\pi m}{d_x})(x-x')}, \quad (\text{E.5})$$

and obtain

$$\frac{2\pi}{d_x} e^{-jk_{x_0}(x-x')} e^{j\frac{2\pi(N_a+1)}{d_x}(x-x')} \sum_{m'=0}^{\infty} (N_a+1+m') e^{j\frac{2\pi m'}{d_x}(x-x')}. \quad (\text{E.6})$$

This sum can be broken up into two sums:

$$(N_a+1) \sum_{m'=0}^{\infty} e^{j\frac{2\pi m'}{d_x}(x-x')} + \sum_{m'=0}^{\infty} m' e^{j\frac{2\pi m'}{d_x}(x-x')}, \quad (\text{E.7})$$

which are calculated by using the following results:

$$\sum_{m=0}^{\infty} e^{j\beta m} = \lim_{\alpha \downarrow 0} \sum_{m=0}^{\infty} e^{(-\alpha m + j\beta m)} = \lim_{\alpha \downarrow 0} \frac{1}{1 - e^{(-\alpha + j\beta)}} = \frac{1}{1 - e^{j\beta}}, \quad (\text{E.8})$$

$$\sum_{m=0}^{\infty} m e^{j\beta m} = \frac{1}{j} \frac{\partial}{\partial \beta} \sum_{m=0}^{\infty} e^{j\beta m} = \frac{1}{j} \frac{\partial}{\partial \beta} \frac{1}{1 - e^{j\beta}} = \frac{-1}{4 \sin^2(\beta/2)}, \quad (\text{E.9})$$

with $\beta \neq 2n\pi$, $n = 0, 1, \dots$. The sum (E.5) thus becomes:

$$\begin{aligned} & \sum_{m=N_a+1}^{\infty} \frac{2\pi m}{d_x} e^{-j(k_{x_0} - \frac{2\pi m}{d_x})(x-x')} = \\ & = \frac{2\pi}{d_x} e^{-jk_{x_0}(x-x') - \frac{2\pi(N_a+1)}{d_x}(x-x')} \left[\frac{N_a+1}{1 - e^{j\frac{2\pi}{d_x}(x-x')}} - \frac{1}{4 \sin^2\left(\frac{\pi}{d_x}(x-x')\right)} \right]. \end{aligned} \quad (\text{E.10})$$

By applying this same procedure to the first sum in Eq. (E.4), we obtain:

$$\begin{aligned} & \sum_{m=N_a+1}^{\infty} \frac{2\pi m}{d_x} e^{-j(k_{x_0} + \frac{2\pi m}{d_x})(x-x')} = \\ & = \frac{2\pi}{d_x} e^{-jk_{x_0}(x-x') + \frac{2\pi(N_a+1)}{d_x}(x-x')} \left[\frac{N_a+1}{1 - e^{-j\frac{2\pi}{d_x}(x-x')}} - \frac{1}{4 \sin^2\left(\frac{\pi}{d_x}(x-x')\right)} \right]. \end{aligned} \quad (\text{E.11})$$

Now we perform some straightforward algebraical manipulations in the approximated expression of g_{na} (E.4) and obtain:

$$\begin{aligned} g_{na}^e(x, x') & \approx -j \frac{2\pi}{d_x} e^{-jk_{x_0}(x-x')} \left\{ e^{j\frac{2\pi(N_a+1)}{d_x}(x-x')} \left[\frac{N_a+1}{1 - e^{j\frac{2\pi}{d_x}(x-x')}} - \frac{1}{4 \sin^2\left(\frac{\pi}{d_x}(x-x')\right)} \right] + \right. \\ & \left. + e^{-j\frac{2\pi(N_a+1)}{d_x}(x-x')} \left[\frac{N_a+1}{1 - e^{-j\frac{2\pi}{d_x}(x-x')}} - \frac{1}{4 \sin^2\left(\frac{\pi}{d_x}(x-x')\right)} \right] \right\} \\ & = j \frac{2\pi}{d_x} e^{-jk_{x_0}(x-x')} \left\{ \frac{2 \cos\left(\frac{2\pi}{d_x}(N_a+1)(x-x')\right)}{4 \sin^2\left(\frac{\pi}{d_x}(x-x')\right)} + \right. \\ & \left. + (N_a+1) \frac{e^{j\frac{\pi}{d_x}(2N_a+1)(x-x')}}{2 \sin\left(\frac{\pi}{d_x}N_a(x-x')\right)} - (N_a+1) \frac{e^{-j\frac{\pi}{d_x}(2N_a+1)(x-x')}}{2 \sin\left(\frac{\pi}{d_x}N_a(x-x')\right)} \right\} \\ & = j \frac{2\pi}{d_x} e^{-jk_{x_0}(x-x')} \left\{ \frac{\cos\left(\frac{2\pi}{d_x}(N_a+1)(x-x')\right)}{2 \sin^2\left(\frac{\pi}{d_x}(x-x')\right)} + \right. \\ & \left. + (N_a+1) \frac{\sin\left(\frac{\pi}{d_x}(2N_a+1)(x-x')\right)}{\sin\left(\frac{\pi}{d_x}(x-x')\right)} \right\}, \end{aligned} \quad (\text{E.12})$$

which leads to the desired result.

Demonstration 2

We shall now derive the second approximated expression of g_{na} in Eq. (E.3). This expression will be used in Sec. E.2 to calculate the reduced kernel of the IE. From Eq. (E.4) we obtain:

$$\begin{aligned}
g_{na}^e(x, x') &\approx -j \left(\sum_{m=N_a+1}^{\infty} \frac{2\pi m}{d_x} e^{-j(k_{x_0} + \frac{2\pi m}{d_x})(x-x')} + \sum_{m=N_a+1}^{\infty} \frac{2\pi m}{d_x} e^{-j(k_{x_0} - \frac{2\pi m}{d_x})(x-x')} \right) \\
&= -j \sum_{m=N_a+1}^{\infty} \frac{2\pi m}{d_x} \left(e^{-j(k_{x_0} - \frac{2\pi m}{d_x})(x-x')} + e^{-j(k_{x_0} + \frac{2\pi m}{d_x})(x-x')} \right) \\
&= -j e^{-jk_{x_0}(x-x')} \sum_{m=N_a+1}^{\infty} \frac{2\pi m}{d_x} \left(e^{j\frac{2\pi m}{d_x}(x-x')} + e^{-j\frac{2\pi m}{d_x}(x-x')} \right) \\
&= -2j e^{-jk_{x_0}(x-x')} \sum_{m=N_a+1}^{\infty} \frac{2\pi m}{d_x} \cos\left(\frac{2\pi m}{d_x}(x-x')\right) \\
&= -2j e^{-jk_{x_0}(x-x')} \left(\sum_{m=1}^{\infty} \frac{2\pi m}{d_x} \cos\left(\frac{2\pi m}{d_x}(x-x')\right) - \sum_{m=1}^{N_a} \frac{2\pi m}{d_x} \cos\left(\frac{2\pi m}{d_x}(x-x')\right) \right).
\end{aligned}$$

Using the result in [34, page 811]:

$$\sum_{n=1}^{\infty} n \cos(n\alpha) = -\frac{1}{4} \frac{1}{\sin^2(\alpha/2)}, \quad (\text{E.13})$$

we obtain the desired expression of the approximated g_{na} :

$$g_{na}^e(x, x') \approx \frac{4\pi}{d_x} j e^{-jk_{x_0}(x-x')} \left(\frac{1}{4 \sin^2\left(\frac{\pi}{d_x}(x-x')\right)} + \sum_{m=1}^{N_a} m \cos\left(\frac{2\pi m}{d_x}(x-x')\right) \right). \quad (\text{E.14})$$

E.2 Approximated non-accessible field for large N_a

In this section we shall demonstrate that, as indicated in Eq. (6.8) of Chapter 6, the approximated expression of the scattered field due to only the non-accessible modes, for

moderately large values of N_a is:

$$\int_{-w_x/2}^{w_x/2} g_{na}^e(x-x') \cdot j_m(x') dx' = e^{-jk_{x_0}x} \left(\int_{-w_x/2}^{w_x/2} \frac{j_i(x') e^{jk_{x_0}x'}}{\sin^2\left(\frac{\pi}{d_x}(x-x')\right)} dx' + \right. \\ \left. + 2 \sum_{m=1}^{N_a} m \left(e^{j\frac{2\pi m}{d_x}x} \tilde{j}_i(k_{x_m}) + e^{-j\frac{2\pi m}{d_x}x} \tilde{j}_i(k_{x_{-m}}) \right) \right), \quad (\text{E.15})$$

Demonstration

The non-accessible GF can be approximated, for moderately large values of the number of accessible modes N_a , by using Eq. (E.3). Substituting in the Left-Hand Side (LHS) of Eq. (E.15) leads to:

$$\int_{-w_x/2}^{w_x/2} g_{na}^e(x-x') \cdot j_m(x') dx' \\ \approx \int_{-w_x/2}^{w_x/2} \frac{4\pi}{d_x} j e^{-jk_{x_0}(x-x')} \cdot \left(\frac{1}{4 \sin^2\left(\frac{\pi}{d_x}(x-x')\right)} + \sum_{m=1}^{N_a} m \cos\left(\frac{2\pi m}{d_x}(x-x')\right) \right) \cdot j_i(x') \\ \approx \frac{\pi}{d_x} j e^{-jk_{x_0}x} \int_{-w_x/2}^{w_x/2} j_i(x') e^{jk_{x_0}x'} \frac{1}{\sin^2\left(\frac{\pi}{d_x}(x-x')\right)} dx' + \\ + \frac{4\pi}{d_x} j e^{-jk_{x_0}x} \int_{-w_x/2}^{w_x/2} j_i(x') e^{jk_{x_0}x'} \sum_{m=1}^{N_a} m \cos\left(\frac{2\pi m}{d_x}(x-x')\right) dx'. \quad (\text{E.16})$$

The second term in the Right Hand Side (RHS) of this last equation can be written as:

$$\frac{2\pi}{d_x} j e^{-jk_{x_0}x} \int_{-w_x/2}^{w_x/2} j_i(x') e^{jk_{x_0}x'} \sum_{m=1}^{N_a} m \left(e^{j\frac{2\pi m}{d_x}(x-x')} + e^{-j\frac{2\pi m}{d_x}(x-x')} \right) dx' \\ = \frac{2\pi}{d_x} j e^{-jk_{x_0}x} \sum_{m=1}^{N_a} m \left(e^{j\frac{2\pi m}{d_x}x} \int_{-w_x/2}^{w_x/2} j_i(x') e^{jk_{x_0}x'} e^{j\frac{2\pi-m}{d_x}x'} dx' + \right. \\ \left. + e^{-j\frac{2\pi m}{d_x}x} \int_{-w_x/2}^{w_x/2} j_i(x') e^{jk_{x_0}x'} e^{j\frac{2\pi m}{d_x}x'} dx' \right). \quad (\text{E.17})$$

Using this result in (E.16), we obtain:

$$\int_{-w_x/2}^{w_x/2} g_{na}^e(x-x') \cdot j_m(x') dx' = e^{-jk_{x_0}x} \left(\int_{-w_x/2}^{w_x/2} \frac{j_i(x') e^{jk_{x_0}x'}}{\sin^2\left(\frac{\pi}{d_x}(x-x')\right)} dx' + \right. \\ \left. + 2 \sum_{m=1}^{N_a} m \left(e^{j\frac{2\pi m}{d_x}x} \tilde{j}_i(k_{x_m}) + e^{-j\frac{2\pi m}{d_x}x} \tilde{j}_i(k_{x_{-m}}) \right) \right). \quad (\text{E.18})$$

E.3 Fourier transform of pws-shaped currents

The Fourier transform of the equivalent electric current expressed in terms of piecewise sinusoidal (pws) functions:

$$j_i(x') \approx \sum_{k=1}^K I_k^{(i)} \text{pws}(x' - x_k), \quad (\text{E.19})$$

is:

$$\tilde{j}_i(k_{x_m}) = \sum_{k=1}^K I_k^{(i)} e^{jk_{x_m}x_k} \text{PWS}(k_{x_m}), \quad (\text{E.20})$$

where we have indicated with $\text{PWS}(k_x)$ the Fourier transform of a $\text{pws}(x)$ centered in $x_c = 0$.

Demonstration

$$\begin{aligned} \tilde{j}_i(k_{x_m}) &= \int_{-w_x/2}^{w_x/2} \sum_{k=1}^K I_k^{(i)} \text{pws}(x' - x_k) e^{jk_{x_m}x'} dx' \\ &= \sum_{k=1}^K I_k^{(i)} \int_{x_k-w_x/2}^{x_k+w_x/2} \text{pws}(x' - x_k) e^{jk_{x_m}x'} dx' \\ &= \sum_{k=1}^K I_k^{(i)} e^{jk_{x_m}x_k} \int_{-w_x/2}^{+w_x/2} \text{pws}(x') e^{jk_{x_m}x'} dx' \\ &= \sum_{k=1}^K I_k^{(i)} e^{jk_{x_m}x_k} \text{PWS}(k_{x_m}). \end{aligned} \quad (\text{E.21})$$

E.4 Approximated integral equation for large N_a

In this section we shall demonstrate that the approximated integral equation (6.13) introduced in Chapter 6 for moderately large values of N_a , such that $k_0^2 \ll k_{x(N_a)}^2$:

$$\begin{aligned} &\sum_{k=1}^K I_k^{(i)} e^{jk_{x_0}x_k} \int_{-w_x/2}^{w_x/2} \text{pws}(x') e^{jk_{x_0}x'} \frac{1}{\sin^2\left(\frac{\pi}{d_x}(x - x' - x_k)\right)} dx' + \\ &+ 2 \sum_{m=1}^{N_a} m \left(e^{j\frac{2\pi m}{d_x}x} \text{PWS}(k_{x_m}) \sum_{k=1}^K I_k^{(i)} e^{jk_{x_m}x_k} + \right. \\ &\left. + e^{-j\frac{2\pi m}{d_x}x} \text{PWS}(k_{x_{-m}}) \sum_{k=1}^K I_k^{(i)} e^{jk_{x_{-m}}x_k} \right) = -j \frac{\sqrt{d_x}}{\pi} e^{j\frac{2\pi i}{d_x}x}, \end{aligned} \quad (\text{E.22})$$

can be expressed as

$$\sum_{k=1}^K I_k^{(i)} Z_{lk} = V_l^{(i)}, \quad (\text{E.23})$$

where

$$Z_{lk} \approx \left(S(x_l - x_k) + 4 \sum_{m=1}^{N_a} m \text{PWS}^2 \left(\frac{2\pi m}{d_x} \right) \cos \left(\frac{2\pi m}{d_x} (x_l - x_k) \right) \right), \quad (\text{E.24})$$

and

$$V_l^{(i)} = -j \frac{\sqrt{d_x}}{\pi} e^{j \frac{2\pi i}{d_x} x_l} \text{PWS} \left(\frac{2\pi i}{d_x} \right). \quad (\text{E.25})$$

Demonstration

To obtain a set of algebraic equations, we project both the LHS and the RHS of Eq. (E.22) into the same expansion functions (Galerkin procedure):

$$\int_{x_l - w_x/2}^{x_l + w_x/2} \text{pws}(x - x_l) \text{LHS}(x) dx = \int_{x_l - w_x/2}^{x_l + w_x/2} \text{pws}(x - x_l) \text{RHS}(x) dx. \quad (\text{E.26})$$

We will now compute the pertinent results.

E.4.1 Right hand side

For the RHS of Eq. (E.26) we obtain:

$$\int_{x_l - w_x/2}^{x_l + w_x/2} \text{pws}(x - x_l) \text{RHS}(x) dx = -j \frac{\sqrt{d_x}}{\pi} e^{j \frac{2\pi i}{d_x} x_l} \text{PWS} \left(\frac{2\pi i}{d_x} \right). \quad (\text{E.27})$$

Demonstration

$$\begin{aligned} \int_{x_l - w_x/2}^{x_l + w_x/2} \text{pws}(x - x_l) \text{RHS}(x) dx &= -j \frac{\sqrt{d_x}}{\pi} \int_{x_l - w_x/2}^{x_l + w_x/2} \text{pws}(x - x_l) e^{j \frac{2\pi i}{d_x} x} dx \\ &= -j \frac{\sqrt{d_x}}{\pi} e^{j \frac{2\pi i}{d_x} x_l} \int_{-w_x/2}^{+w_x/2} \text{pws}(x) e^{j \frac{2\pi i}{d_x} x} dx \\ &= -j \frac{\sqrt{d_x}}{\pi} e^{j \frac{2\pi i}{d_x} x_l} \text{PWS} \left(\frac{2\pi i}{d_x} \right). \end{aligned} \quad (\text{E.28})$$

E.4.2 Left hand side

The LHS of Eq. (E.26) implies the summation of two contributions:

$$\int_{x_l-w_x/2}^{x_l+w_x/2} \text{pws}(x-x_l) (\text{LHS}_1(x) + \text{LHS}_2(x)) dx. \quad (\text{E.29})$$

We calculate now two terms LHS_1 and LHS_2 .

Left hand side -1

The term corresponding to LHS_1 in Eq. (E.29) results to be:

$$\begin{aligned} & \int_{x_l-w_x/2}^{x_l+w_x/2} \text{pws}(x-x_l) \text{LHS}_1(x) dx \\ &= \sum_{k=1}^K I_k^{(i)} e^{jk_{x_0}x_k} \int_{-w_x/2}^{+w_x/2} \text{pws}(x') e^{jk_{x_0}x'} \int_{-w_x/2}^{+w_x/2} \frac{\text{pws}(x)}{\sin^2\left(\frac{\pi}{d_x}(x-x'+x_l-x_k)\right)} dx dx'. \end{aligned} \quad (\text{E.30})$$

Demonstration

$$\begin{aligned} & \int_{x_l-w_x/2}^{x_l+w_x/2} \text{pws}(x-x_l) \text{LHS}_1(x) dx \\ &= \int_{x_l-w_x/2}^{x_l+w_x/2} \text{pws}(x-x_l) \sum_{k=1}^K I_k^{(i)} e^{jk_{x_0}x_k} \int_{-w_x/2}^{+w_x/2} \text{pws}(x') e^{jk_{x_0}x'} \frac{1}{\sin^2\left(\frac{\pi}{d_x}(x-x'-x_k)\right)} dx dx' \\ & \quad + \sum_{k=1}^K I_k^{(i)} e^{jk_{x_0}x_k} \int_{-w_x/2}^{+w_x/2} \text{pws}(x') e^{jk_{x_0}x'} \int_{-w_x/2}^{+w_x/2} \frac{\text{pws}(x-x_l)}{\sin^2\left(\frac{\pi}{d_x}(x-x'-x_k)\right)} dx dx' \\ &= \sum_{k=1}^K I_k^{(i)} e^{jk_{x_0}x_k} \int_{-w_x/2}^{+w_x/2} \text{pws}(x') e^{jk_{x_0}x'} \int_{-w_x/2}^{+w_x/2} \frac{\text{pws}(x)}{\sin^2\left(\frac{\pi}{d_x}(x-x'+x_l-x_k)\right)} dx dx', \end{aligned} \quad (\text{E.31})$$

Left hand side - 2

The term corresponding to LHS_2 in Eq. (E.29) results to be:

$$\begin{aligned} & \int_{x_l-w_x/2}^{x_l+w_x/2} \text{pws}(x-x_l) \text{LHS}_2(x) dx \\ &= \sum_{k=1}^K I_k^{(i)} e^{jk_{x_0} x_k} 2 \sum_{m=1}^{N_a} m \text{PWS} \left(\frac{2\pi m}{d_x} \right) \left(\text{PWS}(k_{x_m}) e^{j \frac{2\pi m}{d_x} (x_l-x_k)} + \right. \\ & \quad \left. + \text{PWS}(k_{x_{-m}}) e^{-j \frac{2\pi m}{d_x} (x_l-x_k)} \right). \end{aligned} \quad (\text{E.32})$$

Demonstration

$$\begin{aligned} & \int_{x_l-w_x/2}^{x_l+w_x/2} \text{pws}(x-x_l) \text{LHS}_2(x) dx \\ &= \int_{x_l-w_x/2}^{x_l+w_x/2} \text{pws}(x-x_l) 2 \sum_{m=1}^{N_a} m \left(e^{j \frac{2\pi m}{d_x} x} \text{PWS}(k_{x_m}) \sum_{k=1}^K I_k^{(i)} e^{jk_{x_m} x_k} + \right. \\ & \quad \left. + e^{-j \frac{2\pi m}{d_x} x} \text{PWS}(k_{x_{-m}}) \sum_{k=1}^K I_k^{(i)} e^{jk_{x_{-m}} x_k} \right) dx \\ &= 2 \sum_{m=1}^{N_a} m \text{PWS}(k_{x_m}) \sum_{k=1}^K I_k^{(i)} e^{jk_{x_m} x_k} \int_{-w_x/2}^{+w_x/2} \text{pws}(x) e^{j \frac{2\pi m}{d_x} (x+x_l)} dx \\ & \quad + 2 \sum_{m=1}^{N_a} m \text{PWS}(k_{x_{-m}}) \sum_{k=1}^K I_k^{(i)} e^{jk_{x_{-m}} x_k} \int_{-w_x/2}^{+w_x/2} \text{pws}(x) e^{-j \frac{2\pi m}{d_x} (x+x_l)} dx \\ &= 2 \sum_{m=1}^{N_a} m \text{PWS}(k_{x_m}) \sum_{k=1}^K I_k^{(i)} e^{jk_{x_m} x_k} e^{j \frac{2\pi m}{d_x} x_l} \text{PWS} \left(\frac{2\pi m}{d_x} \right) + \\ & \quad + 2 \sum_{m=1}^{N_a} m \text{PWS}(k_{x_{-m}}) \sum_{k=1}^K I_k^{(i)} e^{jk_{x_{-m}} x_k} e^{-j \frac{2\pi m}{d_x} x_l} \text{PWS} \left(-\frac{2\pi m}{d_x} \right) \\ &= \sum_{k=1}^K I_k^{(i)} e^{jk_{x_0} x_k} 2 \sum_{m=1}^{N_a} m \text{PWS} \left(\frac{2\pi m}{d_x} \right) \left(\text{PWS}(k_{x_m}) e^{j \frac{2\pi m}{d_x} (x_l-x_k)} + \right. \\ & \quad \left. + \text{PWS}(k_{x_{-m}}) e^{-j \frac{2\pi m}{d_x} (x_l-x_k)} \right). \end{aligned} \quad (\text{E.33})$$

E.4.3 Summary

The RHS and LHS of Eq. (E.26) have been calculated. For the RHS we have obtained:

$$\int_{x_l-w_x/2}^{x_l+w_x/2} \text{pws}(x-x_l) \text{RHS}(x) dx = -j \frac{\sqrt{d_x}}{\pi} e^{j \frac{2\pi i}{d_x} x_l} \text{PWS} \left(\frac{2\pi i}{d_x} \right), \quad (\text{E.34})$$

while the LHS implies the summation of two contributions:

$$\int_{x_l-w_x/2}^{x_l+w_x/2} \text{pws}(x-x_l) (\text{LHS}_1(x) + \text{LHS}_2(x)) dx. \quad (\text{E.35})$$

The first term leads to:

$$\begin{aligned} \int_{x_l-w_x/2}^{x_l+w_x/2} \text{pws}(x-x_l) \text{LHS}_1(x) dx &= \sum_{k=1}^K I_k^{(i)} e^{jk_{x_0} x_k} \int_{-w_x/2}^{+w_x/2} \text{pws}(x') e^{jk_{x_0} x'} \\ &\int_{-w_x/2}^{+w_x/2} \frac{\text{pws}(x)}{\sin^2\left(\frac{\pi}{d_x}(x-x'+x_l-x_k)\right)} dx dx', \end{aligned} \quad (\text{E.36})$$

while the second term becomes:

$$\begin{aligned} &\int_{x_l-w_x/2}^{x_l+w_x/2} \text{pws}(x-x_l) \text{LHS}_2(x) dx \\ &= \sum_{k=1}^K I_k^{(i)} e^{jk_{x_0} x_k} 2 \sum_{m=1}^{N_a} m \text{PWS}\left(\frac{2\pi m}{d_x}\right) \left(\text{PWS}(k_{x_m}) e^{j\frac{2\pi m}{d_x}(x_l-x_k)} + \right. \\ &\quad \left. + \text{PWS}(k_{x_{-m}}) e^{-j\frac{2\pi m}{d_x}(x_l-x_k)} \right). \end{aligned} \quad (\text{E.37})$$

To interpret these expressions we consider the simple case of normal plane wave incidence. Introducing $k_{x_0} = 0$ in Eqs. (E.36),(E.37) leads to the compact form of Eq. (E.22):

$$\begin{aligned} &\sum_{k=1}^K I_k^{(i)} \left(S(x_l-x_k) + 2 \sum_{m=1}^{N_a} m \text{PWS}^2\left(\frac{2\pi m}{d_x}\right) 2 \cos\left(\frac{2\pi m}{d_x}(x_l-x_k)\right) \right) \\ &= -j \frac{\sqrt{d_x}}{\pi} e^{j\frac{2\pi i}{d_x} x_l} \text{PWS}\left(\frac{2\pi i}{d_x}\right), \end{aligned} \quad (\text{E.38})$$

where

$$S(x_l-x_k) = \int_{-w_x/2}^{+w_x/2} \int_{-w_x/2}^{+w_x/2} \frac{\text{pws}(x)\text{pws}(x')}{\sin^2\left(\frac{\pi}{d_x}(x-x'+x_l-x_k)\right)} dx dx'. \quad (\text{E.39})$$

This equation can be written in algebraic form

$$\sum_{k=1}^K I_k^{(i)} Z_{lk} = V_l^{(i)}, \quad (\text{E.40})$$

where Z_{lk} and $V_l^{(i)}$ are given by Eq. (E.24) and Eq. (E.25).

E.5 Fourier transform of truncated Floquet waves

We shall derive here the Fourier transform of a tfw (truncated Floquet wave) centered in $x_c = 0$, defined in Chapter 6, Sec. 6.2. We consider both the tfw's used for the case of TM plane wave incidence and those used for the case of TE plane wave incidence.

TM case The Fourier transform of a $\text{tfw}(x)$, indicated in Chapter 6, Sec. 6.2 as $\text{TFW}(k_x)$, is:

$$\begin{aligned} FT \left(e^{-j(k_{x0} - \frac{2\pi n}{d_x})x} \sqrt{1 - \left(\frac{2x}{w_x}\right)^2} \right) &= \frac{w_x}{4} \pi J_0 \left[\left(k_x - \left(k_{x0} - \frac{2\pi n}{d_x} \right) \right) \frac{w_x}{2} \right] \\ &+ \frac{w_x}{4} \pi J_2 \left[\left(k_x - \left(k_{x0} - \frac{2\pi n}{d_x} \right) \right) \frac{w_x}{2} \right], \end{aligned} \quad (\text{E.41})$$

where J_0 and J_2 are Bessel functions of the first kind of order 0 and 2 respectively.

Demonstration

We shall first derive the Fourier transform for the case of normal incidence ($k_{x0} = 0$):

$$FT \left(e^{-j\frac{2\pi n}{d_x}x} \sqrt{1 - \left(\frac{2x}{w_x}\right)^2} \right) = \frac{w_x}{4} \pi J_0 \left[\left(k_x - \frac{2\pi n}{d_x} \right) \frac{w_x}{2} \right] + \frac{w_x}{4} \pi J_2 \left[\left(k_x - \frac{2\pi n}{d_x} \right) \frac{w_x}{2} \right]. \quad (\text{E.42})$$

Using the definition of spatial Fourier transformation, introduced in Appendix 1, Eq. (A.116), we obtain:

$$\begin{aligned} &FT \left(e^{-j\frac{2\pi n}{d_x}x} \sqrt{1 - \left(\frac{2x}{w_x}\right)^2} \right) \\ &= \int_{-w_x/2}^{+w_x/2} e^{-j\frac{2\pi n}{d_x}x} \sqrt{1 - \left(\frac{2x}{w_x}\right)^2} e^{jk_x x} dx \\ &= \int_{-w_x/2}^{+w_x/2} e^{j(k_x - \frac{2\pi n}{d_x})x} \left[\frac{1}{\sqrt{1 - \left(\frac{2x}{w_x}\right)^2}} - \frac{\left(\frac{2x}{w_x}\right)^2}{\sqrt{1 - \left(\frac{2x}{w_x}\right)^2}} \right] dx. \end{aligned} \quad (\text{E.43})$$

Introducing the variable transformation $\frac{2x}{w_x} = \cos \phi$ leads to

$$\begin{aligned}
& \int_{\pi}^0 e^{j(k_x - \frac{2\pi n}{d_x}) \frac{w_x}{2} \cos \phi} \frac{1}{\sqrt{1 - \cos^2 \phi}} \frac{w_x}{2} \sin \phi \, d\phi - \int_{\pi}^0 e^{j(k_x - \frac{2\pi n}{d_x}) \frac{w_x}{2} \cos \phi} \\
& \quad \frac{\cos^2 \phi}{\sqrt{1 - \cos^2 \phi}} \frac{w_x}{2} \cos \phi \, d\phi \\
& = \frac{w_x}{2} \int_{\pi}^0 e^{j(k_x - \frac{2\pi n}{d_x}) \frac{w_x}{2} \cos \phi} \, d\phi - \frac{w_x}{2} \int_{\pi}^0 e^{j(k_x - \frac{2\pi n}{d_x}) \frac{w_x}{2} \cos \phi} \cos^2 \phi \, d\phi.
\end{aligned} \tag{E.44}$$

The first integral is trivial, since it represents a Bessel function:

$$\int_{-1}^{+1} e^{j\Omega x} \frac{1}{\sqrt{1 - x^2}} \, dx = \int_{\pi}^0 e^{j\Omega \cos \alpha} \, d\alpha = \pi J_0(\Omega), \tag{E.45}$$

and the second integral can be solved using this same transformation:

$$\int_{-1}^{+1} e^{j\Omega x} \frac{x^2}{\sqrt{1 - x^2}} \, dx = \int_{\pi}^0 e^{j\Omega \cos \alpha} \cos^2 \alpha \, d\alpha = \frac{1}{2} \pi (J_0(\Omega) - J_2(\Omega)). \tag{E.46}$$

With this procedure, the Fourier transform (E.42) is calculated and from this result the transform (E.41) follows also immediately.

TE case For the sake of completeness, we also present the final result for the TE case, which is derived in a completely analogous manner as for the TM case:

$$FT \left(e^{-j \frac{2\pi n}{d_x} x} \frac{1}{\sqrt{1 - \left(\frac{2x}{w_x}\right)^2}} \right) = \frac{w_x}{2} \pi J_0 \left(\left(k_x - \frac{2\pi n}{d_x} \right) \frac{w_x}{2} \right). \tag{E.47}$$

Bibliography

- [1] C. K. Aanandan, P. Debernardi, R. Orta, R. Tascone, and D. Trincherio, "Problem-matched basis functions for moment method analysis - An application to reflection gratings," *IEEE Trans. Antennas and Propagation*, vol. 48, no. 1, pp. 35–40, 2000.
- [2] M. Abramowitz and I. Stegun, *Handbook of Mathematical Functions*. New York: Dover, 1964.
- [3] Agilent Technologies. (2005) RF and microwave instruments and systems. [Online]. Available: <http://www.home.agilent.com/NLdut/nav/-11882.0/pc.html>
- [4] V. D. Agrawal and W. A. Imbriale, "Design of a dichroic cassegrain subreflector," *IEEE Trans. Antennas and Propagation*, vol. 27, no. 4, pp. 466–473, 1979.
- [5] F. Alessandri, G. Bartolucci, and R. Sorrentino, "Admittance matrix formulation of waveguide discontinuity problems: computer-aided design of branch guide directional couplers," *IEEE Trans. Microwave Theory and Techniques*, vol. 36, no. 2, pp. 394–403, 1988.
- [6] S. M. Ali, W. C. Chew, and J. A. Kong, "Vector Hankel transform analysis of annular-ring microstrip antenna," *IEEE Trans. Antennas and Propagation*, vol. 30, no. 4, pp. 637–645, 1982.
- [7] N. Amitay, V. Galindo, and C. P. Wu, *Theory and Analysis of Phased Array Antennas*. New York: John Wiley and Sons, 1972.
- [8] I. Anderson, "On the theory of self-resonant grids," *Bell Syst. Tech. J.*, no. 54, pp. 1725–1731, 1975.
- [9] M. Ando, K. Ueno, H. Kumazawa, and K. Lagoshima, "AK/C/S band satellite antenna with frequency selective surface," *Electronics and Communication in Japan*, vol. 66-B, no. 5, pp. 27–66, 1983.

-
- [10] *Ansoft Designer. Electromagnetically Charged EDA Software v1.1. Getting Started Guide*, Ansoft Corporation, 2003.
- [11] *HFSS v9.0. Getting Started with HFSS*, Ansoft Corporation, 2003.
- [12] Arlon. (2003) Materials for electronics. [Online]. Available: <http://www.arlon-med.com>
- [13] F. Arndt, R. Beyer, J. M. Reiter, T. Sieverding, and T. Wolf, “Automated design of waveguide components using hybrid mode-matching/numerical EM building-blocks in optimization-oriented CAD frameworks. State-of-the-art and recent advances,” *IEEE Trans. Microwave Theory and Techniques*, vol. 45, no. 5, pp. 747–760, 1997.
- [14] N. W. Ashcroft and N. D. Mermin, *Solid State Physics*. Saunders College, Philadelphia: International Edn, 1976.
- [15] C. A. Balanis, *Antenna Theory. Analysis and Design*. New York: John Wiley and Sons, 1997.
- [16] S. Bastonero, O. A. Peverini, R. Orta, and R. Tascone, “Anisotropic surface relief diffraction gratings under arbitrary plane wave incidence,” *Optical and Quantum Electronics*, no. 32, pp. 1013–1025, 2000.
- [17] F. Baumann, W. A. B. Jr., A. Naweed, W. D. Goodhue, and A. J. Gatesman, “Wet-etch optimization of free-standing Terahertz frequency selective structures,” *Opt. Lett.*, vol. 28, no. 11, pp. 938–940, 2003.
- [18] D. Bekers, “Finite Antenna Arrays: An Eigencurrents Approach.” Ph.D. dissertation, Technical University of Eindhoven, Eindhoven, The Netherlands, 2004.
- [19] P. Besso, M. Bozzi, L. Perregri, L. Drioli, and W. Nickerson, “Deep-space antenna for Rosetta mission: design and testing of the S/X band dichroic mirror,” *IEEE Trans. Antennas and Propagation*, vol. 51, no. 3, pp. 388–394, 2003.
- [20] A. K. Bhattacharyaa, “Multimode moment method formulation for waveguide discontinuities,” *IEEE Trans. Antennas Propagat.*, vol. 42, no. 8, pp. 1567–1571, 1994.
- [21] A. K. Bhattacharyaa, “A numerical model for multilayered microstrip phased-array antennas,” *IEEE Trans. Antennas Propagat.*, vol. 44, no. 10, pp. 1386–1393, 1996.

- [22] A. K. Bhattacharyaa, "Analysis of multilayer infinite periodic array structures with different periodicities and axes orientations," *IEEE Trans. Antennas Propagat.*, vol. 49, no. 3, pp. 357–369, 2000.
- [23] A. K. Bhattacharyaa, "On the convergence of MoM and mode matching solutions for infinite array and waveguide problems," *IEEE Trans. Antennas Propagat.*, vol. 51, no. 7, pp. 1599–1606, 2003.
- [24] P. Bielli, R. Campo, S. Contu, D. Forigo, P. C. Massaglia, D. Savini, and R. Tascone, "Frequency selective surface design capability programme. Part 1-Theory and Measurements. Final report," CSELT, Torino, Italy, Tech. Rep. 4828/81/NL/MS (SC), mar 1983.
- [25] T. S. Bird, "Analysis of mutual coupling in finite arrays of different-sized rectangular waveguides," *IEEE Trans. Antennas and Propagation*, vol. 38, no. 2, pp. 166–172, 1990.
- [26] F. Bloch, "Über die Quantenmechanik der Electronen in Kristallgittern," *Z. Physik*, no. 52, pp. 555–600, 1928.
- [27] V. E. Boria, G. Gerini, and M. Guglielmi, "An efficient inversion technique for banded linear systems," in *IEEE Microwave Theory and Tech. Int. Symp. 1997 Dig.*, Boston, MA, June 1997, pp. 1567–1570.
- [28] S. Bruni, N. Llombart, A. Neto, G. Gerini, and S. Maci, "Problem-matched basis functions for microstrip coupled slot arrays based on transmission line Green's functions," *IEEE Trans. Antennas and Propagation*, accepted for publication.
- [29] H. A. Burger, "A dual polarized antenna system using a meanderline polarizer," in *New Mexico State Univ. Proc. of the 1978 Syn. Aperture Radar Technol. Conf.*, 1978.
- [30] R. Cahill, E. A. Parker, and C. Antonopoulous, "Design of multilayer frequency selective surface for diplexing two closely spaced channels," *Microwave and Optical Technology Letters*, vol. 8, pp. 293–296, 1995.
- [31] K. R. Carver and J. W. Mink, "Microstrip antenna technology," *IEEE Trans. Antennas and Propagation*, vol. 29, pp. 2–24, 1981.
- [32] C. H. Chan and R. Mittra, "On the analysis of frequency-selective surfaces using subdomain basis functions," *IEEE Trans. Antennas and Propagation*, vol. 38, no. 1, pp. 40–50, 1990.

- [33] C. C. Chen, "Transmission through a conducting screen perforated periodically with apertures," *IEEE Trans. Microwave Theory and Techniques*, vol. 18, pp. 627–632, 1970.
- [34] R. E. Collin, *Field Theory of Guided Waves - 2nd ed.* New York: IEEE Press, 1991.
- [35] R. E. Collin, *Foundations for Microwave Engineering.* New York: McGraw Hill, 1992, pp. 230–232.
- [36] G. Conciauro, M. Guglielmi, and R. Sorrentino, *Advanced Modal Analysis.* Chichester: John Wiley and Sons, 2000.
- [37] S. Contu and R. Tascone, "Scattering from passive arrays in plane stratified regions," *Electromagnetics*, vol. 5, no. 4, pp. 285–306, 1985.
- [38] C. Craeye, A. G. Tijhuis, and D. H. Schaubert, "An efficient MoM formulation for finite-by-infinite arrays of two-dimensional antennas arranged in a three-dimensional structure," *IEEE Trans. Antenna Propagat.*, vol. 52, no. 1, pp. 271–282, 2004.
- [39] A. Cucini, M. Albani, and S. Maci, "Truncated Floquet wave full-wave analysis of large phased arrays of open-ended waveguides with a nonuniform amplitude excitation," *IEEE Trans. Antennas and Propagation*, vol. 51, no. 6, pp. 1386–1394, 2003.
- [40] A. Cucini, M. Albani, and S. Maci, "Truncated Floquet wave full-wave (T(FW)²) analysis of large periodic arrays of rectangular waveguides," *IEEE Trans. Antennas and Propagation*, vol. 51, no. 6, pp. 1373–1385, 2003.
- [41] T. Cwik, R. Mittra, K. Lang, and T. Wu, "Frequency selective screens," *IEEE Antennas and Propagation Society Newsletter*, vol. 29, no. 2, pp. 5–10, 1987.
- [42] V. J. Dicaudo, *Radar Handbook.* New York: McGraw-Hill, 1970, pp. 14.1–14.32.
- [43] B. Dunnebier, "Integrated Topside Design - Progress Report 2002," TNO-FEL, The Hague, The Netherlands, Tech. Rep. FEL-03-A045, aug 2003.
- [44] S. Edelberg and A. A. Oliner, "Mutual coupling effects in large antenna arrays: part I-Slot arrays," *IEEE Trans. Antennas and Propagation*, vol. 8, no. 3, pp. 286–297, 1960.
- [45] T. F. Eibert, Y. Erdemli, and J.L.Volakakis, "Upgrading the hybrid finite element-boundary integral method using multilayer periodic Green's functions," in *IEEE*

- Antennas and Propagation Soc. Int. Symp. 2002 Dig.*, San Antonio, Texas, June 2002.
- [46] J. J. Epis, "Broadband antenna polarizer," *U.S. Patent 3,754,271*, 1973.
- [47] Y. E. Erdemli, K. Sertel, R. A. Gilbert, D. E. Wright, and J. L. Volakis, "Frequency-selective surfaces to enhance performance of broad-band reconfigurable arrays," *IEEE Trans. Antennas and Propagation*, vol. 50, no. 12, pp. 1716–1724, 2002.
- [48] L. B. Felsen and N. Marcuvitz, *Radiation and Scattering of Waves*. New York: IEEE Press, 1994.
- [49] G. Floquet, "Sur les équations différentielles linéaires à coefficients périodiques," *Ann. École Norm. Sup.*, no. 12, pp. 47–88, 1883.
- [50] P. Focardi, A. Freni, S. Maci, and G. Vecchi, "Efficient analysis of arrays of rectangular corrugated horns: the synthetic aperture function approach," *IEEE Trans. Antennas and Propagation*, vol. 53, no. 2, pp. 601–607, 2000.
- [51] P. R. Franchi and R. J. Mailloux, "Theoretical and experimental study of metal grid angular filters for sidelob suppression," *IEEE Trans. Antenna Propagat.*, vol. 31, no. 3, pp. 445–450, 1983.
- [52] G. Gerini and M. Guglielmi, "Full-wave CAD of a rectangular waveguide filter with integrated coaxial excitation," *IEEE Trans. Microwave Theory Tech.*, vol. 49, no. 5, pp. 986–989, 2001.
- [53] G. Gerini, M. Guglielmi, and G. Lastoria, "Efficient integral equation formulations for admittance or impedance representations of planar waveguide junctions," *Recent Res. Devel. Microwave Theory Tech.*, no. 1, pp. 199–206, 1999.
- [54] G. Gerini, S. Monni, and L. Zappelli, "Arbitrary shaped aperture/patch FSS's in planar phased arrays. Full-domain and sub-domain basis functions," in *IEEE Antennas and Propagation Soc. Int. Symp. 2003 Dig.*, Columbus, Ohio, June 2003.
- [55] G. Gerini and L. Zappelli, "CAD of multilayer conformal cylindrical arrays," in *IEEE Antennas and Propagation Soc. Int. Symp. 2001 Dig.*, Boston, MA, June 1999, pp. 216–219.

- [56] G. Gerini and L. Zappelli, "Phased arrays of rectangular apertures on conformal cylindrical surfaces: a multimode equivalent network approach," *IEEE Trans. Antennas and Propagation*, vol. 52, no. 7, pp. 1843–1850, 2004.
- [57] B. Gimeno, J. L. Cruz, E. A. Navarro, and V. Such, "A polarizer rotator system for three dimensional oblique incidence," *IEEE Trans. Antennas and Propagation*, vol. 42, no. 7, pp. 912–919, 1994.
- [58] G. H. Golub and C. F. van Loan, *Matrix Computations*. Baltimore, MD: John Hopkins University Press, 1996.
- [59] R. D. Graglia, D. R. Wilton, and A. F. Peterson, "Higher order interpolatory vector bases for computational electromagnetics," *IEEE Trans. Antennas and Propagation*, vol. 45, no. 3, pp. 329–342, 1997.
- [60] M. Guglielmi, "Simple CAD procedure for microwave filters and multiplexers," *IEEE Trans. Microwave Theory and Techniques*, vol. 42, no. 7, pp. 1347–1352, 1994.
- [61] M. Guglielmi, G. Gheri, M. Calamia, and G. Pelosi, "Rigorous multimode network numerical representation of inductive step," *IEEE Trans. Microwave Theory and Techniques*, vol. 42, no. 2, pp. 317–326, 1995.
- [62] M. Guglielmi and A. A. Oliner, "Multimode network description of a planar periodic metal-strip grating at a dielectric interface - Part I: rigorous network formulations," *IEEE Trans. Microwave Theory Tech.*, vol. 37, no. 3, pp. 534–541, 1989.
- [63] M. Guglielmi and A. A. Oliner, "Multimode network description of a planar periodic metal-strip grating at a dielectric interface - Part II: small-aperture and small-obstacle solutions," *IEEE Trans. Microwave Theory Tech.*, vol. 37, no. 3, pp. 542–552, 1989.
- [64] P. W. Hannan and M. A. Balfour, "Simulation of a phased array antenna in waveguide," *IEEE Trans. Antenna Propagat.*, vol. 13, pp. 342–252, 1965.
- [65] R. C. Hansen, *Microwave Scanning Antennas. Vol. II*. New York: McGraw-Hill, 1966.
- [66] R. F. Harrington, *Field Computation by Moment Methods*. Malabar, Florida: Robert E. Krieger Publishing Company, 1968.

- [67] W. Hauth, R. Keller, U. Papziner, R. Ihmels, T. Sieverding, and F. Arndt, "Rigorous CAD of multiport coupled rectangular waveguide components," in *Proc. 23rd European Microwave Conf.*, Madrid, Spain, sep 1993, pp. 611–614.
- [68] C. M. Horvitz, "A new solar selective surface," *Opt. Commun.*, vol. 11, no. 2, pp. 210–212, 1974.
- [69] I. A. C. E. Industries. (2004) Electrical test methods. [Online]. Available: <http://www.ipc.org/contentpage.asp?PageID=4.1.0.1.1.5>
- [70] International Electrotechnical Commission. (2004) International Electrotechnical Vocabulary (IEV) online database. [Online]. Available: <http://dom2.iec.ch/iev>
- [71] T. Itoh, "Spectral domain immitance approach for dispersion characteristics of generalized printed transmission lines," *IEEE Trans. Microwave Theory Tech.*, vol. 28, no. 7, pp. 733–736, 1980.
- [72] T. Itoh, *Numerical Techniques for Microwave and Millimeter-Wave Passive Structures*. New York: John Wiley and Sons, 1989.
- [73] E. M. T. Jones, S. B. Cohn, and L. A. Robinson, "Wide band radomes matched by reactive walls," in *Proc. OSU-WADC Radome Symp.*, June 1955, pp. 52–67.
- [74] R. B. Kiebertz and A. Ishimaru, "Scattering by a periodically apertured conducting screen," *IRE Trans. Antenna Propagat.*, vol. 9, pp. 506–514, 1961.
- [75] D. Kinowski and M. Guglielmi, "Multimode equivalent numerical representation for the scattering from multistrip gratings," *IEEE Trans. Antennas and Propagation*, vol. 43, no. 6, pp. 597–603, 1995.
- [76] D. Kinowski, M. Guglielmi, and A. G. Roederer, "Angular bandpass filters: an alternative viewpoint gives improved design flexibility," *IEEE Trans. Antennas and Propagation*, vol. 43, no. 4, pp. 390–395, 1995.
- [77] R. J. Langley and E. A. Parker, "Equivalent circuit model for arrays of square loops," *Electronics Letters*, vol. 18, no. 7, pp. 294–296, 1982.
- [78] R. J. Langley and E. A. Parker, "Double square frequency-selective surfaces and their equivalent circuit," *Electronics Letters*, vol. 19, no. 17, pp. 675–677, 1983.

- [79] C. K. Lee and R. J. Langley, "Equivalent-circuit for frequency-selective surfaces at oblique angles of incidence," *IEE Proceedings*, vol. 132, no. 6, pp. 395–399, 1985.
- [80] S.-W. Lee, "Scattering by dielectric-loaded screen," *IEEE Trans. Antennas Propagat.*, vol. 19, no. 5, pp. 656–665, 1971.
- [81] L. Lewin, *Theory of Waveguides*. New York: John Wiley and Sons, 1974.
- [82] N. Llombart-Juan, "Development of integrated printed array antennas using EBG substrates," Ph.D. dissertation, Departamento de Comunicaciones, Universidad Politecnica de Valencia, Valencia, Spain, 2005.
- [83] J.-F. Ma, R. Mittra, and N. T. Huang, "Analysis of multiple FSS screens of unequal periodicity using an efficient cascading technique," *IEEE Antennas and Propagation Society Newsletter*, vol. 53, no. 4, pp. 1401–1414, 2005.
- [84] S. Maci, M. Caiazzo, A. Cucini, and M. Casaletti, "A pole-zero matching method for EBG surfaces composed of a dipole FSS printed on grounded dielectric slab," *IEEE Trans. Antennas Propagat.*, vol. 53, no. 1, pp. 70–81, 2005.
- [85] S. Maci, G. Vecchi, and A. Freni, "Matrix compression and supercompression techniques for large arrays," in *IEEE Antennas and Propagation Soc. Int. Symp. 2003 Dig.*, Columbus, Ohio, June 2003, pp. 1064–1067.
- [86] E. Magill and H. Wheeler, "Wide-angle impedance matching of a planar array antenna by a dielectric sheet," *IEEE Trans. Antennas Propagat.*, vol. 14, no. 1, pp. 49–53, 1996.
- [87] R. J. Mailloux, "Synthesis of spatial filters with Chebyshev characteristics," *IEEE Trans. Antenna Propagat.*, vol. 24, no. 2, pp. 174–181, 1976.
- [88] N. Marcuvitz, *Waveguide Handbook*. New York: McGraw-Hill, 1951.
- [89] L. Matekovits, G. Vecchi, G. Dassano, and M. Orefice, "Synthetic function analysis of large printed structures: the solution space sampling approach," in *IEEE Antennas and Propagation Soc. Int. Symp. 2003 Dig.*, Boston, Massachusetts, July 2001, pp. 568–571.
- [90] A. A. Melcon, G. Connor, and M. Guglielmi, "New simple procedure for the computation of the multimode admittance or impedance matrix of planar waveguide

- junctions,” *IEEE Trans. Microwave Theory and Techniques*, vol. 44, no. 3, pp. 413–418, 1996.
- [91] C. Mias, C. Tsakonas, and C. Oswald, “An investigation into the feasibility of designing frequency selective windows employing periodic structures,” Nottingham University, Nottingham, UK, Tech. Rep. AY3992, 2002.
- [92] W. H. Miller, G. D. Bernard, and J. L. Allen, “The optics of insect compound eyes,” *Science*, vol. 162, pp. 760–767, 1968.
- [93] R. Mittra, “A look at some challenging problems in computational electromagnetics,” *IEEE Antennas and Propagation Magazine*, vol. 46, no. 5, pp. 18–32, 2004.
- [94] R. Mittra, C. H. Chan, and T. Cwik, “Techniques for analyzing frequency selective surfaces. A review,” *Proceedings of the IEEE*, vol. 76, no. 12, 1988.
- [95] R. Mittra, T. Itoh, and T.-S. Li, “Analytical and numerical studies of the relative convergence phenomena arising in the solution of an integral equation by the moment method,” *IEEE Trans. Microwave Theory Tech.*, vol. 20, no. 2, pp. 96–104, 1972.
- [96] R. Mittra and S. W. Lee, *Analytical Techniques in the Theory of Guided Waves*. New York: MacMillan, 1971.
- [97] R. Mittra and J. Pace, “A new technique for solving a class of boundary value problems,” Antenna Laboratory, University of Illinois, Urbana, Tech. Rep. Rep. 72, 1963.
- [98] B. Monacelli, J. B. Pryor, B. A. Munk, D. Kotter, and G. D. Boreman, “Infrared frequency selective surface based on circuit-analog square loop design,” *IEEE Trans. Antennas Propagat.*, vol. 53, no. 2, pp. 745–752, 2005.
- [99] S. Monni and G. Gerini, “A novel technique for the design of frequency selective structures integrated with a waveguide array,” in *IEEE Antennas and Propagation Soc. Int. Symp. 2004 Dig.*, Monterrey, California, June 2004.
- [100] B. A. Munk, *Frequency Selective Surfaces: Theory and Design*. USA: John Wiley and Sons, 2000.
- [101] A. Neto and J. J. Lee, ““Infinite bandwidth” long slot array antenna,” *IEEE Antenna Wireless Propagation Letters*, vol. 4, pp. 75–78, 2005.

- [102] A. Neto, S. Maci, G. Vecchi, and M. Sabbadini, "A truncated Floquet wave diffraction method for the full-wave analysis of large phased arrays. Part I: basic principle and 2-D case," *IEEE Trans. Antennas and Propagation*, vol. 48, no. 4, pp. 594–600, 2000.
- [103] A. Neto, S. Maci, G. Vecchi, and M. Sabbadini, "A truncated Floquet wave diffraction method for the full-wave analysis of large phased arrays. Part II: generalization to 3-D cases," *IEEE Trans. Antennas and Propagation*, vol. 48, no. 4, pp. 601–611, 2000.
- [104] A. I. Nosich, "The method of analytical regularization in wave-scattering and eigenvalue problems: foundations and review of solutions," *IEEE Antennas Propagat. Mag.*, vol. 41, no. 3, pp. 34–49, 1999.
- [105] A. S. Omar and K. Schunemann, "Transmission matrix representation of finline discontinuities," *IEEE Trans. Microwave Theory and Techniques*, vol. 9, no. 3, pp. 462–471, 1985.
- [106] R. Orta, R. Tascone, and R. Zich, "A unified formulation for the analysis of general frequency selective surfaces," *Electromagnetics*, vol. 5, no. 4, pp. 307–329, 1985.
- [107] R. H. Ott, R. G. Kouyoumajian, and L. P. Jr., "Scattering by a two dimensional periodic array of narrow plates," *Radio Science*, vol. 2, pp. 1347–1359, 1967.
- [108] L. M. P. Pirinoli, G. Vecchi, "Multiresolution analysis of printed antennas and circuits: a dual-isoscalar approach," *IEEE Trans. Antennas and Propagation*, vol. 49, no. 6, pp. 858–874, 2001.
- [109] I. Palocz and A. A. Oliner, "Equivalent network of multimode planar grating," *IEEE Trans. Microwave Theory Tech.*, vol. 18, no. 5, pp. 244–252, 1970.
- [110] U. Papziner and F. Arndt, "Field theoretical computer-aided design of rectangular or circular waveguide cavity filters," *IEEE Trans. Microwave Theory and Techniques*, vol. 41, pp. 462–471, 1988.
- [111] U. Papziner and F. Arndt, "Field theoretical computer-aided design of rectangular and circular iris coupled rectangular or circular waveguide cavity filters," *IEEE Trans. Microwave Theory and Techniques*, vol. 4, no. 3, pp. 462–471, 1993.
- [112] H. Patzelt and F. Arndt, "Double-plane steps in rectangular waveguides and their applications for transformers, irises and filters," *IEEE Trans. Microwave Theory and Techniques*, vol. 30, no. 5, pp. 771–776, 1982.

- [113] E. L. Pelton and B. A. Munk, "A streamlined metallic radome," *IEEE Trans. Antennas Propagat.*, vol. 22, no. 6, pp. 799–803, 1974.
- [114] A. E. Peterson, C. F. Smith, and R. Mittra, "Eigenvalues of the moment-method matrix and their effect on the convergence of the conjugate gradient algorithm," *IEEE Trans. Antennas and Propagation*, vol. 36, no. 8, pp. 1177–1179, 1988.
- [115] A. F. Peterson, S. L. Ray, and R. Mittra, *Computational Methods for Electromagnetics*. Pennsylvania State University: IEEE Press, 1998.
- [116] P. Pirinoli, L. Matekovits, G. Vecchi, F. Vipiana, and M. Orefice, "Synthetic functions, multiscale MoM analysis of arrays," in *IEEE Antennas and Propagation Soc. Int. Symp. 2003 Dig.*, Columbus, Ohio, jun 2003, pp. 799–802.
- [117] R. Pous and D. M. Pozar, "A frequency-selective surface using aperture-coupled microstrip patches," *IEEE Trans. Antennas Propagat.*, vol. 8, no. 3, 1960.
- [118] D. M. Pozar and D. H. Schaubert, "Scan blindness in infinite phased arrays of printed dipoles," *IEEE Trans. Antennas Propagat.*, vol. 32, no. 6, 1984.
- [119] V. V. S. Prakash and R. Mittra, "Characteristic basis function method: a new technique for fast solution of integral equations," *Microwave Optical Technology Letters*, pp. 95–100, 2003.
- [120] Y. Rahmat-Samii and A. N. Tulintseff, "Diffraction analysis of frequency selective reflector antennas," *IEEE Trans. Antennas and Propagation*, vol. 41, pp. 476–487, 1993.
- [121] S. M. Rao, D. R. Wilton, and A. W. Glisson, "Electromagnetic scattering by surfaces of arbitrary shape," *IEEE Trans. Antennas Propagat.*, vol. 30, no. 3, pp. 409–418, 1982.
- [122] J. M. Reiter and F. Arndt, "Rigorous analysis of arbitrarily shaped H and E-plane discontinuities in rectangular waveguides by a full-wave boundary contour mode-matching method," *IEEE Trans. Microwave Theory Tech.*, vol. 43, no. 4, pp. 796–801, 1995.
- [123] Rogers Corporation. (2004) High performance foams. [Online]. Available: <http://www.rogers-corp.com/hpf/il/bisco/products.htm>

- [124] Rogers Corporation. (2005) High frequency laminates and flexible circuit materials. [Online]. Available: <http://www.rogerscorporation.com/acm/index.htm>
- [125] J. Romeu and Y. Rahmat-Samii, "Fractal FSS: a novel dual-band frequency selective surface," *IEEE Trans. Antennas and Propagation*, vol. 48, no. 7, pp. 1097–1105, 2000.
- [126] T. E. Rozzi and W. F. G. Mecklenbrauker, "Wide-band network modeling of interacting inductive irises and steps," *IEEE Trans. Microwave Theory Tech.*, vol. 23, pp. 235–244, 1975.
- [127] G. H. Schennum, "Frequency-selective surfaces for multiple frequency antennas," *Microwave Journal*, no. May, pp. 55–57, 1973.
- [128] Seavey Engineering/ARA. (2005) Meanderline polarizers. [Online]. Available: <http://www.seaveyantenna.com/catalog/p112/pg112.htm>
- [129] C. E. Shannon, "A mathematical theory of communication," *Bell System Tech. J.*, vol. 27, pp. 379–423, 623–656, 1948.
- [130] S. Singh, W. Richards, J. Zinecker, and R. Wilton, "Accelerating the convergence of series representing the free space periodic Greens function," *IEEE Trans. Antennas and Propagation*, vol. 38, no. 12, pp. 1958–1962, 1990.
- [131] B. Smolders, "Microstrip phased-array antennas: a finite-array approach," Ph.D. dissertation, Technical University of Eindhoven, Eindhoven, The Netherlands, 1994.
- [132] J. A. Stratton, *Electromagnetic Theory*. New York: McGraw-Hill, 1941.
- [133] W. L. Stutzman and G. A. Thiele, *Antenna Theory and Design*. New York: John Wiley and Sons, 1998.
- [134] Taconic Advanced Dielectric Division. (2005) TLY RF and microwave laminate. [Online]. Available: <http://www.taconic-add.com/en/products-tly-1.php>
- [135] G. C. Temes and J. W. L. Patra, *Circuit Synthesis and Design*. Tokyo: McGraw-Hill Kogakusha, LTD., 1977.
- [136] A. G. Tijhuis, *Electromagnetic Inverse Profiling: Theory and Numerical Implementation*. Utrecht: VNU Science Press, 1987.

-
- [137] A. G. Tijhuis, "Plane-wave excitation of two-dimensionally periodic metallized structures in plane-stratified dielectric media," Eindhoven University of Technology, Eindhoven, The Netherlands, Tech. Rep. WDC262A, jan 2002.
- [138] A. G. Tijhuis and A. Rubio-Bretones, "Transient excitation of a layered dielectric medium by a pulsed electric dipole," *IEEE Trans. Antenna Propagat.*, vol. 48, no. 10, pp. 1673–1684, 2000.
- [139] R. Ulrich, T. J. Bridges, and M. A. Pollack, "Variable metal mesh coupler for far infrared lasers," *Appl. Opt.*, vol. 9, no. 11, p. 25112516, 1970.
- [140] M. C. van Beurden, "Integro-Differential Equations for Electromagnetic Scattering: Analysis and Computation for Objects with Electric Contrast." Ph.D. dissertation, Technical University of Eindhoven, Eindhoven, The Netherlands, 2003.
- [141] L. van Ewijk, "Shape, dimension and construction technique of the polarising radome," TNO-FEL, The Hague, The Netherlands, Tech. Rep. FEL-01-1243, oct 2001.
- [142] J. C. Vardaxoglou, *Frequency Selective Surfaces - Analysis and Design*. UK: John Wiley and Sons, 1997.
- [143] G. Vecchi, L. Matekovits, P. Pirinoli, and M. Orefice, "Hybrid spectral-spatial method for the analysis of printed antennas," *Radio Sci. (Special Issue Computat. Electromagn.)*, vol. 31, no. 5, pp. 1263–1270, 1996.
- [144] H. J. Visser and M. Guglielmi, "CAD of waveguide array antennas based on "filter" concepts," *IEEE Trans. Antennas and Propagation*, vol. 47, no. 3, pp. 542 – 548, 1999.
- [145] T. K. Wu, "Cassini frequency selective surface development," *J. Electromagn. Waves Applicat.*, vol. 8, no. 12, pp. 1547–1561, 1994.

Summary

Frequency Selective Surfaces (FSS's) are periodic arrays of patches and/or slots etched on a metal plate, having frequency and angular filtering properties. The FSS response to an excitation (for example a plane wave) is characterized in terms of its reflection and transmission coefficient, and depends on the element type (slot or patch), the element shape (loop, cross, ...) and the array grid (rectangular or triangular). Cascading a number of FSS's to each other allows achieving larger bandwidths and steeper roll offs. The angle dependence of the response can be reduced by sandwiching the FSS's between dielectric slabs. As a special application, the (multi-layer) selective structure is integrated with an array antenna: for example to reduce the antenna's radar cross section or to obtain wideband/multi-frequency antennas.

The analysis and the design of a multi-layer FSS, possibly integrated with an antenna, requires the availability of a CAD package based on an efficient analysis methodology. In this respect, microwave network techniques constitute an appropriate choice because of their modularity. Originally introduced for the analysis of waveguides, they have been extended to periodic structures. The basic idea is to derive a representation of layers and transitions between adjacent layers in terms of equivalent networks. The entire structure is then represented by the cascade of these networks. Different choices of parameters to characterize the structure lead to different types of equivalent network: for example, scattering parameters are used to derive the generalized scattering matrix. The adjective 'generalized' refers to the fact that the input and output ports correspond not only to the propagating modes but also to the evanescent ones. In the conventional approaches, the number of these ports is equal to the number of modes used to represent the electromagnetic field at the transition. From this general equivalent network, a reduced form can be derived, which includes only the modes that actually contribute to the electromagnetic interaction between two successive transitions (accessible modes). If the structure consists of many layers, this reduced form is convenient to limit the calculation time, and it is necessary for some types of network representations to avoid the instability problem that arises when

many networks are cascaded to each other.

The distinguishing feature of the Integral Equation method for the derivation of Multimode Equivalent Networks (IEMEN), described in detail in this thesis, is that it resorts directly to an equivalent network representation in terms of the accessible modes only. The innovative idea is to retain as accessible, in the analysis of a certain transition, only those evanescent modes that arrive at the terminal planes with an attenuation factor that is smaller than a chosen maximum tolerance. The corresponding modal amplitudes are then identified as the fundamental unknowns of the problem, in the sense that all the fields in the region between the terminal planes can be expressed as a linear combination of those quantities only. This results in the formulation of the scattering problem in terms of a single integral equation with reduced kernel, and corresponding reduced Green's function, and multiple forcing terms, one for each accessible mode. The formulation has been extended to efficiently analyze structures containing thin layers, as for example bond films.

The IEMEN method has been implemented in a software tool and its analysis capabilities have been demonstrated for some representative examples presented in literature, and by comparing with analysis results obtained by means of commercial software. The tool is also a reliable and flexible instrument for the design and it has been successfully used to solve a realistic design problem, consisting of an FSS to be integrated with a waveguide phased array. The FSS had to prevent interference between the array and a satellite communication antenna, located in its proximity. A dipole-based FSS was identified as suitable geometry to meet the requirements.

A classical design procedure has been adopted. It starts with a single-mode design, intuitive and Smith-chart based, to trace the relevant behavior of the structure and to perform a rough tuning of the FSS parameters. With respect to the transmission line corresponding to the main propagating Floquet mode, the FSS was characterized by a simple shunt equivalent admittance. The actual value of this admittance, as a function of the frequency, was obtained by means of the IEMEN approach.

This initial design phase was followed by a refinement phase, in which full-wave IEMEN-based simulations, including all the relevant accessible modes, were used. It should be noted that, since the patch admittance is a slowly varying function of the frequency, it can be linearly approximated near the resonance. As a consequence, the first design phase was very fast. This property holds also for the elements of the equivalent admittance matrix of a patch FSS, when a larger number of accessible modes is retained in the calculations, and it is a characterizing feature of the IEMEN method. In fact, all the fast frequency

variations are accounted for at transmission-line level and not at equivalent-network level, because the modes that vary most rapidly with the frequency have been extracted from the IE kernel. The designed FSS has been manufactured and measured using different setups.

Subsequently, the properties of the reduced kernel integral equation have been investigated for an expansion of the unknown current by means of sub-domain basis functions. To comply with very stringent requirements set on the FSS, in terms of incidence angles and roll off, dielectric slabs with high permittivity are required. As a consequence, the number of accessible modes to be included in the simulations increases and, for a sub-domain expansion of the unknown currents, the Method of Moments (MoM) matrix becomes ill conditioned.

In particular, we have considered a simple two-dimensional geometry, consisting of an infinite periodic array of metallic strips in free space under TM plane wave incidence. An asymptotic expression of the non-accessible Green's function has been derived where, besides the typical singularity, an oscillating term can be recognized. The amplitude of this term depends on the number of accessible modes extracted from the complete kernel and the period is the same as that of the Floquet waves with index equal to the index of the highest-order accessible mode.

From a parametric study, it is observed that, if sub-domain functions are used to expand the unknowns, the MoM matrix condition number increases with the number of accessible modes and with the strip width. The intuitive explanation is that the natural modes of the array resonate with the Floquet modes. The study of the eigenvalue equation associated to the reduced IE operator has confirmed this hypothesis. In fact, its eigenfunctions appear to be similar to combinations of the extracted Floquet waves. Consequently, the solution can be represented as a combination of Floquet modes. This confines the solution to a subspace of the solution space where the small unwanted eigenvalues are avoided. Thus, using a limited number of global basis functions can be seen as a way of regularizing an ill-conditioned problem.

In particular, we have selected truncated Floquet waves (tfw), variations of those proposed in literature as entire domain basis functions for the analysis of large finite slot arrays. Furthermore, the particular formulation of the IEMEN approach, with a single IE and different forcing terms, suggests the adoption, for each specific forcing term, of a different compact set of tfw's, which can be used to solve the integral equation. This implies that a different matrix has to be inverted for each accessible mode. Since only a few basis functions are needed to solve the problem corresponding to a given forcing term, the computational time is related to the calculation of the MoM matrix elements, rather than to the matrix

inversion. Therefore, the efficiency of the method of solution is not compromised.

A number of test cases has been presented, demonstrating the advantage of using tfw's as basis functions instead of sub-domain functions, as well as a discussion on the nature of the eigenvalues of the reduced kernel IE.

Samenvatting

Frequency Selective Surfaces (FSSen) zijn periodieke arrays van patches en of slots, geëtst in een metalen plaat, die als filter werken voor een invallend elektromagnetisch veld, afhankelijk van de frequentie en de hoek. De respons van een FSS op een excitatie (bijvoorbeeld een invallende vlakke golf) wordt gekarakteriseerd in termen van de reflectiecoëfficiënt, en hangt af van het type element (slot of patch), de vorm (lus, kruis, ...) en het rooster (rechthoekig of driehoekig). Met een cascade van een aantal frequency selective surfaces kan een grotere bandbreedte en een steilere roll off worden bereikt. De hoekafhankelijkheid van de respons neemt af als de FSS'en met diëlektrische lagen worden omringd. Een speciale toepassing is de integratie van de gelaagde, selectieve structuur met een (array) antenne. Hiermee wordt bijvoorbeeld de radar cross section (RCS) van de antenne beperkt of wordt een breedbandige multi-frequente antenne verkregen.

Voor de analyse en het ontwerp van een multi-laag FSS, eventueel geïntegreerd met een antenne, moet een CAD pakket beschikbaar zijn dat gebaseerd is op een efficiënte rekenmethode. Microgolf netwerk technieken zijn hiervoor een geschikte keus vanwege hun modulariteit. Deze technieken zijn oorspronkelijk ingevoerd voor de analyse van golfgeleiders en daarna uitgebreid tot periodieke structuren. Het achterliggende idee is om lagen en overgangen voor te stellen in termen van equivalente netwerken. De gehele structuur wordt dan voorgesteld als een cascade van dergelijke netwerken. Verschillende keuzes voor de parameters waarmee de structuur wordt gekarakteriseerd leiden tot verschillende soorten equivalente netwerken. Zo worden verstrooiingsparameters bijvoorbeeld gebruikt om de gegeneraliseerde verstrooiingsmatrix te bepalen. De aanduiding “gegeneraliseerd” slaat op de omstandigheid dat de input en output terminals niet alleen corresponderen met propagerende modi, maar ook met dempende. In de gebruikelijke aanpak is het aantal terminals gelijk aan het aantal modi dat wordt gebruikt om het elektromagnetische veld bij de overgang te benaderen. Uit dit algemene equivalente netwerk kan een gereduceerde vorm worden afgeleid, waarin alleen modi voorkomen die daadwerkelijk bijdragen aan de elektromagnetische wisselwerking tussen twee achtereenvolgende overgangen (toegankelijke

of accessible modi). Deze vorm is handig om de rekentijd te beperken als de configuratie uit veel lagen bestaat en is noodzakelijk om stabiliteitsproblemen te voorkomen als veel netwerken worden gecombineerd.

De karakteristieke eigenschap van de integraalvergelijking (Integral Equation) methode voor het bepalen van Multimode Equivalente Netwerken (IEMEN), zoals die in detail in dit proefschrift wordt beschreven, is dat deze direct een beroep doet op een equivalente netwerkrepresentatie in termen van alleen de toegankelijke modi. Het vernieuwende idee is om in de analyse alleen die dempende (evanescent) modi te behouden die op de grensvlakken aankomen met een dempingsfactor die kleiner is dan een gekozen tolerantie. De corresponderende modale amplitudes worden dan beschouwd als de fundamentele onbekenden van het probleem, wat betekent dat alle velden tussen beide grensvlakken kunnen worden uitgedrukt als een lineaire combinatie van alleen deze grootheden. Dit leidt tot de formulering van het verstrooiingsprobleem in termen van één enkele integraalvergelijking met een gereduceerde kern en bijbehorende Greense functie, en meerdere drijvende termen, een voor elke toegankelijke modus. De formulering is uitgebreid om ook structuren met dunne lagen, zoals lijmlagen, efficiënt te kunnen analyseren.

De IEMEN methode is geïmplementeerd in een software tool en de analyse mogelijkheden ervan zijn gedemonstreerd voor enkele representatieve voorbeelden uit de literatuur en door vergelijking met resultaten verkregen met behulp van commerciële software. Het programma is een betrouwbaar en flexibel ontwerpgereedschap en is met succes gebruikt om een realistisch ontwerpprobleem op te lossen, voor de integratie van een FSS en een golfpijp array. De FSS moest de interferentie voorkomen tussen het array en een antenne voor satellietcommunicatie, die in de nabijheid is geplaatst en die in een gedeeltelijk overlappende frequentieband werkt. Een dipool-gebaseerde FSS bleek geschikt om aan de ontwerp eisen te voldoen.

Een klassieke ontwerpprocedure werd gevolgd. Deze begon met een single-mode ontwerp, intuïtief en gebaseerd op de Smith kaart, om het relevante gedrag van de structuur te volgen en een ruwe afstemming van de FSS parameters uit te voeren. In relatie tot de transmissielijn die met de belangrijkste Floquet modus correspondeert werd het FSS gekarakteriseerd door een eenvoudige parallelle equivalente impedantie. De werkelijke waarde van deze impedantie, als functie van de frequentie, werd bepaald door middel van de IEMEN aanpak.

De eerste ontwerpstep werd gevolgd door een verfijnings step, waarbij volledige IEMEN simulaties werden gebruikt, waarin alle relevante toegankelijke modi werden meegenomen. Hierbij moet worden opgemerkt dat de admittantie van de patch een langzaam variërende functie van de frequentie is, die in de buurt van de resonantie kan worden gelineariseerd.

Daardoor kon de eerste ontwerpstep zeer snel worden uitgevoerd. Deze eigenschap geldt ook voor de elementen van de equivalente admittantiematrix voor een patch FSS, wanneer een groter aantal toegankelijke modi wordt meegenomen in de berekeningen, en is kenmerkend voor de IEMEN methode. In feite worden alle snelle frequentievariëaties in rekening gebracht op transmissielijn niveau en niet in de equivalente netwerken, omdat de modi waarvan het gedrag het sterkst afhankelijk is van de frequentie uit de kern van de integraalvergelijking zijn gehaald. Het ontworpen FSS is gerealiseerd en doorgemeten in verschillende opstellingen.

In het vervolg van het proefschrift zijn de eigenschappen van de gereduceerde integraalvergelijking onderzocht voor het geval waarin de onbekende stroom wordt ontwikkeld in subdomein basisfuncties. Om aan de zeer strikte eisen voor het FSS te voldoen, in termen van hoek van inval en roll off, zijn diëlektrische lagen met een hoge permittiviteit nodig. Hierdoor neemt het aantal toegankelijke modi toe dat moet worden meegenomen in de simulaties en krijgt de systeemmatrix in de momentenmethode (MoM) voor subdomein basisfuncties een slechte conditie.

Als speciaal geval is een eenvoudige tweedimensionale geometrie beschouwd, bestaande uit een periodiek array van metalen strips in de vrije ruimte die worden geëxciteerd door een invallende transversaal magnetische (TM) vlakke golf. Een asymptotische uitdrukking voor de Greense functie is afgeleid, waarin naast de typische singulariteit een oscillerende term kan worden herkend. De amplitude van deze term is afhankelijk van het aantal toegankelijke modi dat van de volledige kern wordt afgesplitst en de periode correspondeert met die van de laatste Floquet golf.

Uit een parameterstudie bleek dat, als de onbekende stroom door subdomein (lokale) ontwikkelingsfuncties werd benaderd, het conditiegetal van de MoM matrix toenam met het aantal toegankelijke modi en met de breedte van de strips. De gevoelsmatige uitleg is dat de natuurlijke trillingen van het array resoneren met de Floquet modi. Bestuderen van de eigenwaardevergelijking die samenhangt met de gereduceerde integraalvergelijking bevestigt deze hypothese. De eigenfuncties van de gereduceerde integraalvergelijking lijken zelfs op combinaties van de afgesplitste Floquet golven. Bijgevolg kan de oplossing van deze vergelijking als zo'n combinatie worden geschreven. Dit beperkt de oplossing tot een deelruimte van de oplossingsruimte waarin de kleine, ongewenste eigenwaarden worden vermeden. Zo kan het gebruik van een beperkt aantal globale basisfuncties worden opgevat als een manier om een slecht gesteld probleem te regulariseren.

Wij hebben gekozen voor afgekorte Floquet golven (truncated Floquet waves, tfw), variaties op de globale basisfuncties die in de literatuur zijn voorgesteld voor grote eindige slot arrays. Verder suggereert de speciale formulering van de IEMEN aanpak, met een

enkele integraalvergelijking en verschillende drijvende termen, de keuze voor een verschillende compacte verzameling van tfw's in de oplossing van de integraalvergelijking voor elke drijvende term. Dit betekent dat een nieuwe matrix moet worden geïnverteerd voor elke toegankelijke modus. Omdat slechts enkele basisfuncties nodig zijn om het probleem voor een gegeven drijvende term op te lossen wordt de rekentijd bepaald door de berekening van de MoM matrixelementen, en niet door de matrixinversie. De efficiëntie van de methode wordt hierdoor niet aangetast.

Tot besluit is een aantal testen gepresenteerd die het voordeel van het gebruik van de tfw's als basisfuncties aantonen, en wordt de aard van de eigenwaarden van de gereduceerde integraalvergelijking bediscussieerd.

Biography

Stefania Monni was born in Cagliari, Italy, on July 4, 1974. After graduating from the secondary school in 1993 at the Liceo Scientifico Pacinotti in Cagliari, she enrolled as a student in Electronic Engineering at the University of Cagliari. In December 1999 she started to work on her final project in collaboration with the Department of Biophysical and Electronic Engineering at the University of Genoa in Italy, and with the Payload Systems Division (currently TEC-ET) of ESTEC (European Space and Technology Center) in The Netherlands. At the University of Genoa, where she spent about four months, she studied SAR interferometry and signal processing. She had the chance to apply this knowledge during an internship in ESTEC, from March to July 1999, where she finalized her M.Sc. Thesis on SAR interferometry for flood damage assessment. In October 1999 she received the M.Sc. degree (cum laude) in Electronic Engineering. In April 2000 the Comitato Elettrotecnico Italiano (Italian Electrotechnical Committee) awarded her the Prize for the best M.Sc. Thesis of the year. From November 1999 to November 2000 she was back in ESTEC as Young Graduate Trainee, where she improved her competencies in SAR remote sensing, interferometry and polarimetry. Captured by the subject and willing to better understand the function of the sensors, she started a Ph.D. in electromagnetics with the Eindhoven University of Technology in February 2001, under the supervision of prof. dr. A.G. Tijhuis. She was given the opportunity to carry out her research on frequency selective surfaces in the Radar Group of TNO-FEL (currently TNO Defence, Security and Safety) guided by dr. ir. G. Gerini and dr. ir. A. Neto. In addition to her Ph.D. research, she was involved in a four-year research project in the framework of the Integrated Topside Design program of the Royal Dutch Navy, for which she performed also project management tasks. Since February 2005 she is employed in TNO as research scientist in the field of antennas.

Acknowledgements

This thesis is the result of four years of work at TNO and living in a foreign country. Many persons have contributed directly or indirectly to the successful outcome of my Ph.D. project.

First of all, I would like to thank the four people who made this Ph.D. possible.

Dr. ir. Andrea Neto, playfully called "the guru" of the antenna group, who managed to convince me to start a Ph.D. in antennas and has been coaching me during the last three years. Besides being a reference point for any theoretical matter, he also cheers us up through his contagious enthusiasm on electromagnetic research and the entertaining lunch discussions about the very deep meanings of life.

Dr. ir. Giampiero Gerini, the responsible of the antenna activities at TNO, who entrusted me the project on Frequency Selective Surfaces and guided my research at TNO during the last four years. I am grateful to him for always supporting my work and for sitting next to me to tackle some nasty problems even when his agenda was full.

Prof. dr. Anton Tjihuis, the chief of the Electromagnetic group at the Technical University of Eindhoven, who took on the responsibility of supervising my work at TNO. I would like to thank him for always maintaining a critical look to my research work, which helped me clarifying many points. I am especially indebted with him for the long time he invested in reading this thesis, even during week-ends and Christmas holidays, and for taking care of all the bureaucratic aspects connected to the organization of the defense.

Ir. Frank van den Bogaart, the head of the Integrated Front-End Solutions section (currently Business Unit manager knowledge, observation systems with TNO Defence Security and Safety) who gave me the possibility to undertake this Ph.D. project and who always trusted my work.

I would also like to thank the Dutch Ministry of Defense for providing the financial support. A special thanks goes to ir. Bas Dunnebier and ir. Lucas van Ewijk, responsible of the Integrated Topside Design program, for their comments and their supportive attitude with respect to the project on FSS's. Moreover, I would like to thank ir. Albert Huizing

for the interesting discussions on interference problems between different sensors and for providing me with the specifications on the FSS that have been used as starting point for the design described in this thesis.

I am especially indebted to ing. Frans Nennie, the TNO microwave measurements expert and my officemate in the last one and half year. Frans, thank you for performing the FSS measurements, also when the budget of the project was finished and this meant working systematically over time for many days. But above all thank you for your constant help in the every day life at TNO and for always having a listening ear.

Thank you very much to all my colleagues of the former Integrated Front-End Solutions group at TNO, for making life in the corridor very nice. In particular, I am indebted to ir. Simona Bruni and ir. Nuria Llombart, colleagues, car pooling mates but above all friends. Simona, thank you above all for helping me taming L^AT_EX. Nuria, thank you for your valuable contributions to the IEMEN-based tool, especially for what concerns the acceleration technique. I would also like to thank ir. Roland Bolt, who has always been available for discussions and dr. ir. Dave Bekers, for his help in mathematical matters. Thanks to dr. ir. Frank van Vliet for his useful comments.

Thank you very much also to all the Electromagnetic group at the Technical University of Eindhoven. I am particularly grateful to dr. ir. Bas De Hone for his tips on L^AT_EX and for providing me with very interesting references on the microwave network techniques, and to dr. ir. Martijn van Beurden for looking at the properties of the reduced kernel Integral Equation.

A very special thanks goes to dr. ir. Thomas Bertuch, for his priceless advise on all aspects related to the design, manufacture and measurements of FSS's. Moreover, my gratitude goes to dr. ir. Leonardo Zappelli for introducing me to the BCMM method and for letting me comparing my results with his. A special thanks also to dr. ir. Marco Guglielmi for his suggestions concerning different aspects of the IEMEN method.

I would like to express my gratitude to prof. dr. ir. Stefano Maci and prof. dr. ir. Giuseppe Vecchi for the very helpful discussions we had on the topics covered by this thesis. In particular, thanks to prof. dr. ir. Stefano Maci and prof. dr. ir. Angelo Freni who patiently attended a long presentation on the methodology described in this thesis and provided interesting comments.

Moreover, I thank all the members of the reading commission for their remarks and suggestions, and in particular prof. dr. ir. Guy Vandenbosch, prof. dr. ir. Peter Zwamboorn and prof. dr. ir. Peter van den Berg.

I am very grateful to prof. dr. ir. Gianni Vernazza, dean of the Engineering Faculty at

the University of Genoa and supervisor of my M.Sc. Thesis: he gave me the possibility to perform part of my work at the European Space Agency and if it was not for him I would maybe never have come to The Netherlands.

I would like to thank all my friends for their support, especially in the last period of my Ph.D. A special thanks goes to ir. Alfonso Martinez-Vicente and ir. Maria Garcia-Lorrade for their bravery in volunteering reading the first draft of this thesis and for providing me with very interesting comments and original points view, which helped me reformulating some concepts in a (I hope) clearer form.

I would like to thank my parents Carmen and Eligio and my brother Fabrizio for their constant loving support, even from faraway. I am really indebted to my boyfriend Michel for his patience and understanding, especially during this last year, and for always encouraging me in the most difficult moments encountered during this project.

A personal note

Since you survived reading this thesis, you deserve a nice recipe.

Sebadas (typical sardinian desert)

Ingredients: 600g of flour, 150g of butter, 400g of fresh sardinian cheese, 2 oranges, water, salt, sugar or honey.

Mix the flour with some lukewarm water and salt in a bowl. Add the melted butter and knead the dough until it becomes firm and smooth. Cover it and let it rest in a warm area. Prepare the filling with the cheese and the skin of the oranges, both rasped very thin. Knead the dough again a little bit, then make a thin sheet from which you cut circles of 15 cm diameter. In each of them put some of the filling, then fold one half over the other and push the borders closed. Fry the sebadas in boiling oil, until they become gold colored on both sides. Serve them warm covered with honey or sugar.

Enjoy!!!